



Universiteit
Leiden
The Netherlands

Cochlear implants: Modeling electrophysiological responses

Gendt, M.J. van

Citation

Gendt, M. J. van. (2021, March 25). *Cochlear implants: Modeling electrophysiological responses*. Retrieved from <https://hdl.handle.net/1887/3149359>

Version: Publisher's Version

License: [Licence agreement concerning inclusion of doctoral thesis in the Institutional Repository of the University of Leiden](#)

Downloaded from: <https://hdl.handle.net/1887/3149359>

Note: To cite this publication please use the final published version (if applicable).

Cover Page



Universiteit Leiden



The handle <http://hdl.handle.net/1887/3149359> holds various files of this Leiden University dissertation.

Author: Gendt, M.J. van

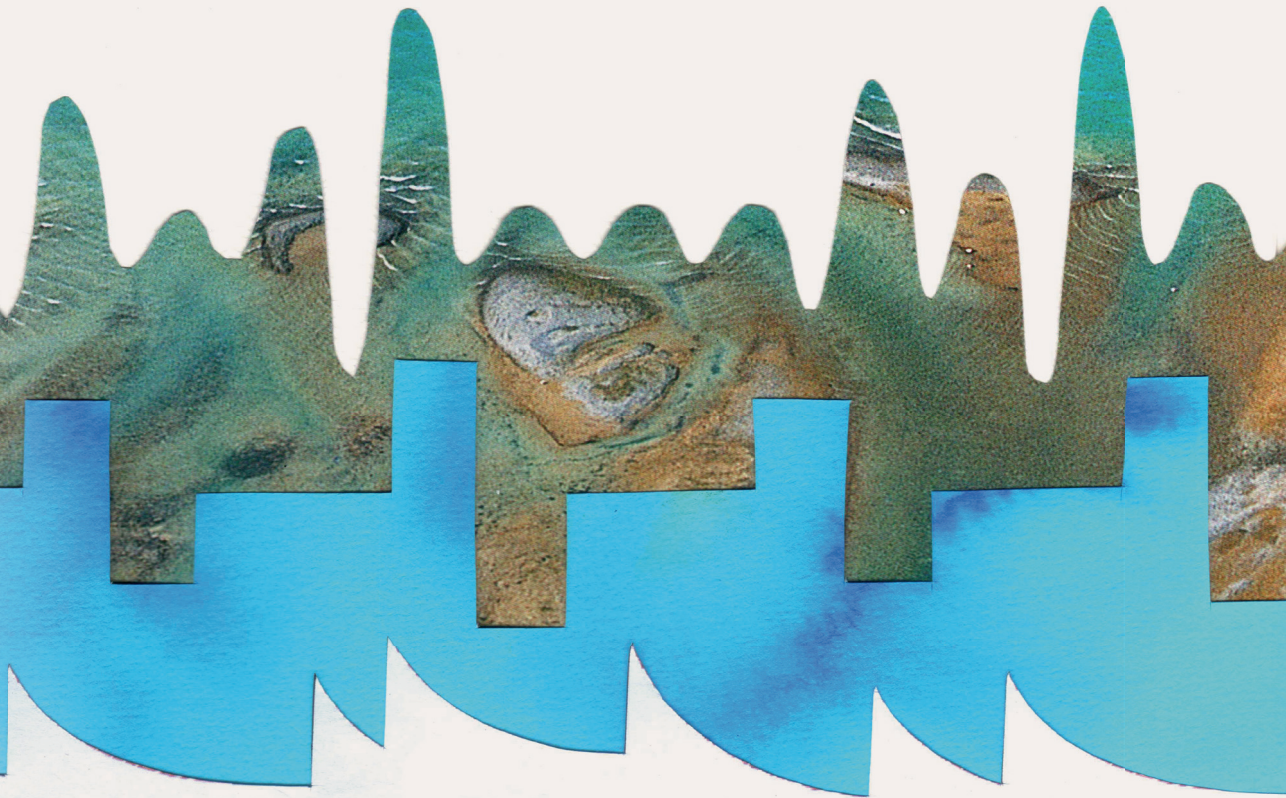
Title: Cochlear implants: Modeling electrophysiological responses

Issue date: 2021-03-25

Cochlear Implants

Modeling electrophysiological responses

Margriet van Gendt



Cochlear Implants

Modeling electrophysiological responses

Margriet Jessica van Gendt

© copyright Margriet Jessica van Gendt, 2021

Cover: Esther Hoogendijk

Printing: ProefschriftMaken || www.proefschriftmaken.nl

ISBN 978 94 6423 107 6

All rights reserved. No part of this publication may be reproduced, stored in a retrieval system or transmitted, in any form or by any means, electronic, mechanical, photocopying, recording or otherwise, without prior permission of the author or the copyright-owning journals for previous published chapters.

This research was funded by:
Advanced Bionics Corporation
Stichting het Heinsius-Houbolt fonds

This thesis was financially supported by:
Advanced Bionics, Cochlear, Med-EL, Oticon, Pedagogische Praktijk, Chipsoft, Amplifon –
Beter Horen

Cochlear Implants

Modeling electrophysiological responses

PROEFSCHRIFT

ter verkrijging van de graad van Doctor
aan de Universiteit Leiden, op gezag van
Rector Magnificus prof.dr.ir. H. Bijl,
volgens besluit van het College voor Promoties
te verdedigen op
donderdag 25 maart 2021 klokke 15:00 uur

door

Margriet Jessica Bekkering - van Gendt
geboren te Alphen aan den Rijn in 1984

Promotor: Prof. dr. ir. J.H.M. Frijns

Copromotor: Dr. ir. J.J. Briaire

Leden promotiecommissie:

Prof. dr. P.P.B. van Benthem

Prof. dr. P. van Dijk

Prof. dr. J.H. Meijer

Dr. H. Versnel

Rijksuniversiteit Groningen

Universiteit Utrecht

Aan mijn ouders

Aan alle CI-dragers

Table of contents

CHAPTER 1	Introduction	9
CHAPTER 2	A fast, stochastic, and adaptive model of auditory nerve responses to cochlear implant stimulation	21
CHAPTER 3	Modeled auditory nerve responses to amplitude modulated cochlear implant stimulation	51
CHAPTER 4	Short and long-term adaptation in the auditory nerve stimulated with high-rate electrical pulse trains are better described by a power law	83
CHAPTER 5	Effect of neural adaptation and degeneration on pulse-train eCAPs: a model study	107
CHAPTER 6	Simulating intracochlear electrocochleography with a combined model of acoustic hearing and electric current spread in the cochlea	131
CHAPTER 7	Discussion	153
CHAPTER 8	Summary (Nederlandstalig)	167
	Bibliography	173
	List of publications	191
	Acknowledgements	195
	Curriculum Vitae	199

CHAPTER 1

Introduction

1 Introduction

Cochlear implants are implantable hearing devices for individuals with severe to profound hearing loss. Since its introduction in the clinics in the 1980s many people have benefited from these devices and valuable adjustments to the design of the hardware and software have been implemented (Zeng et al., 2008). Over recent years however, in spite of considerable efforts, development of sound coding strategies has stagnated. The drawbacks and restrictions related to testing of new coding strategies in patients require innovative ways to evaluate sound coding developments. One such approach is the computational evaluation of sound coding in the implanted ear. The digital age, with its powerful computers and recent developments in information theory, provides all necessary means for the development of appropriate models and interpretation of their output. In this thesis, computational models of the implanted auditory periphery's response to sound are described. This introduction will explain the basic functioning of the auditory system, the working mechanism of cochlear implants and the state of the art of cochlear implant sound coding modeling.

1.1 The ear & hearing

In a healthy ear, sound travels through the outer ear (pinna and ear canal) and the middle ear (tympanic membrane and the middle ear ossicles) to the inner ear from where sound is transmitted to the auditory nerve. The purpose of the outer and middle ears is to focus the pressure of the sound wave on the oval window, a membrane that separates the middle ear from the cochlear endolymphatic fluid, figure 1.1A&B. The inner ear, or cochlea, is part of the vestibulocochlear organ depicted in figure 1.1A. Located in the scala media of the cochlea is the organ of Corti, shown in figure 1.1C. This is the actual hearing organ where hair cells located on the basilar membrane convert mechanical energy of the resonating membrane to an electric signal reaching the auditory nerve through synapses. The cochlea is a marvelous organ, it is tonotopically organized to fulfill its frequency-analyzing function. It contains active elements (outer hair cells) increasing its sensitivity and selectivity, and has nonlinearity in both inner and outer hair cell sensitivities to efficiently transduce relevant sounds. By virtue of these factors, the human ear is most sensitive to frequencies present in human speech and is optimized to analyze the dynamic range of speech. The auditory nerve is just as wonderful, it preserves the frequency-selectivity by both place- and time coding and sophisticatedly encodes loudness by an associated spiking pattern in the auditory nerve. Because of spontaneous activity in both types of hair cells and in the auditory neurons, the auditory system is 'alert' and sensitive to sudden and soft sounds. Although the peripheral auditory system is very intriguing, the real magic happens higher up in the auditory system. Different relay stations, where information is sorted and processed, send the signal towards the brain. The most important relay stations are the cochlear nuclei, olivary nuclei located in the lateral lemniscus, the inferior colliculi and the medial geniculate bodies (the auditory portion of the thalamus).

After this, the signal reaches the auditory cortices. Information processing follows in a bottom-up approach (the afferent system), and is controlled and attuned by a top-down approach (efferent system). There are connections between the differently leveled and lateralized nuclei, which is a prerequisite for, amongst others purposes, our specific localization abilities. The further up in the system you go, the more complex the processing becomes. Attention, association, learning, memorizing and emotion, and other related connections with the limbic system are of essence to our perception of sound.

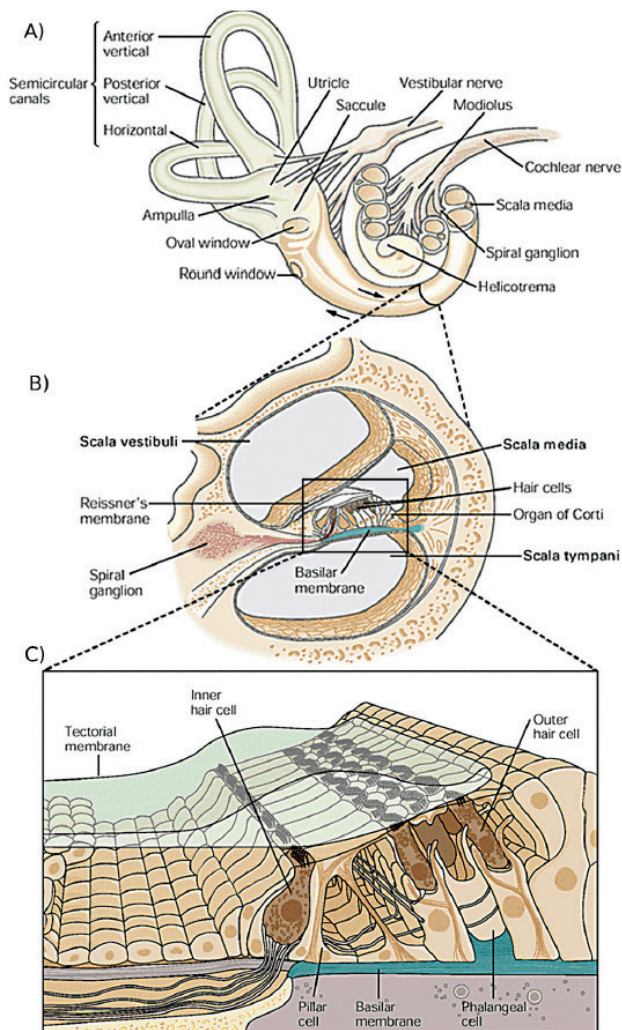


Figure 1.1 Anatomy of the inner ear. A) Vestibulocochlear organ; showing the semicircular canals, utricle and saccule of the vestibular organ and the spiraling cochlea; B) a cross-section of the cochlea showing the scala media; C) zoomed in at the organ of corti visualizing the inner and outer hair cells and the basilar membrane [Adopted from Kandel and Schwartz (2000), copyright McGraw-Hill Education]

1.2 Hearing loss and rehabilitation

Malfunctioning of (part of) the hearing system causes hearing loss. Conductive hearing loss is a consequence of damage to the outer or middle ear and can lead to a hearing loss of up to 60 dB. Damage to the inner ear, referred to as perceptive hearing loss, manifests as a hearing loss with a severity ranging from mild to profound. Auditory problems originating higher up in the auditory system, e.g. auditory neuropathy or auditory processing disorders, are much less common. Prevalence of disabling hearing loss is estimated by the WHO in 2018 at 6.1% of the world's population, when defined as a loss of more than 40 dB in the better hearing ear in adults and 30 dB in children (<https://www.who.int/pbd/deafness/estimates/en/>). Congenital hearing losses are hereditary, can be caused by infectious diseases, or due to prenatal complications. Acquired hearing losses can have hereditary or infectious causes but can also, and with increasing prevalence, be concomitant with age or manifest as a consequence of noise exposure.

The perception of sound is important for communication with others and for awareness of the world around us. Hearing rehabilitation is developed to disburden those suffering from hearing loss. It can come in the form of a hearing aid, a bone conduction device or a cochlear implant. A hearing aid amplifies sound before it enters the ear canal. A bone conduction device transfers the sound directly to the inner ear through mechanical vibration of the skull. In a cochlear implant (CI) the auditory nerve is directly activated through electrical stimulation by an electrode placed in the cochlea, see figure 1.2. Sign language provides a means of communication for those who cannot use, or are not sufficiently rehabilitated by a hearing device.

1.3 Cochlear Implants

The CI is the designated rehabilitation device for those with severe to profound hearing loss. As of 2016 an estimated 600 000 devices were implanted worldwide (The Ear Foundation, UK). Currently, in the Netherlands, people with rehabilitated speech perception scores, scored by phonemes correct, of lower than 70% for speech presented at a level of 65 dB_{HL} are considered eligible for implantation. The functional benefits brought about by CIs range from mere detection of environmental sounds to restoration of speech perception scores of over 90% in quiet surroundings. The prognosis for the functional outcome depends on the hearing loss history, etiology, age at implantation, cognitive abilities and electrode position (Holden et al., 2013), but the exact relation between patient characteristics and perceptual outcomes are not understood well enough to exactly predict outcomes. Due to this complexity, the question whether or not cochlear implantation is the optimal treatment for an individual patient should be carefully considered by a multidisciplinary team (involving an audiologist, speech therapist, ENT-surgeon, and social worker) in consultation with the patient.

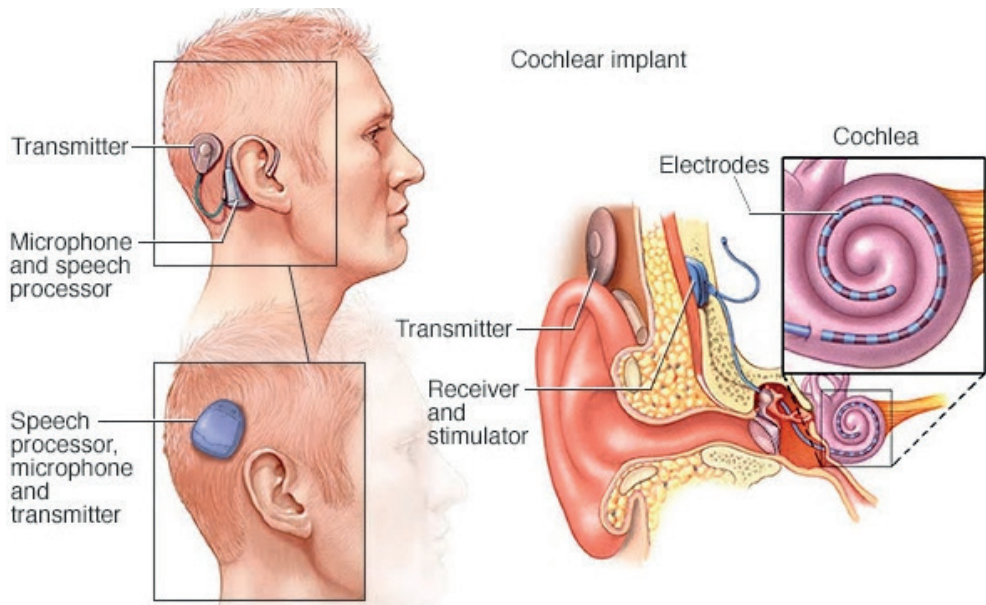


Figure 1.2. Configuration of the external (transmitter, microphone, speech processor) and internal parts (stimulator and electrodes) of the cochlear implant (Reprinted with permission of Mayo Foundation for Medical Education and Research, all rights reserved.)

The first attempts to restore hearing with electrical stimulation were done in the late sixties and early seventies (Djourno and Eyries, 1957; Doyle et al., 1964; Simmons et al., 1964) but due to skepticism and safety issues it was not until 1984 that Food and Drug Administration (FDA) approval opened up the road for development of the CIs. The House 3M single-electrode device (House and Urban, 1973) was the first CI available on the market, and was followed in the years after by multichannel electrodes (Loeb, 1990). The CI consists of an external processor that detects and manipulates sound and a coil, connected via a magnet to the internal part, that sends the signal to the electrode placed in the inner ear (figure 1.2). Currently, CI electrodes contain between 12 and 24 electrode-contacts (depending on the manufacturer) located alongside one-another. Each electrode-contact stimulates a different part of the tonotopically organized auditory nerve, thereby making use of place-coding to provide frequency-specific information.

1.4 Sound coding in cochlear implants

The first cochlear implants used compressed analog techniques in which the electrical equivalent of the sound pressure was administered continuously to frequency-specific electrode-contacts. In 1991, the continuous interleaved sampling (CIS) technique was introduced, which employs consecutive stimulation of the different electrode-contacts. With this type of coding strategy, speech perception and safety improved and the clinical implementation of CIs gained momentum (Wilson et al., 1991). In CIs, the auditory nerve is

excited by biphasic (charge-balanced) electrical stimulation from each electrode contact. Loudness is encoded by either increasing the width of the phases or the amplitude of the transferred current. Since the introduction of CIS, numerous researchers worked on further improvement of perception with and usability of CIs (Wouters et al., 2015). To save battery-life and to minimize electrode interactions, peak-picking strategies are combined with CIS, e.g. MP3000. To increase the number of stimulation contacts, 'virtual' electrodes are used in HiRes, in which, via current steering, the neural region in between physical electrode-contacts is stimulated. CIs are designed to encode speech in an optimized and efficient way, for this purpose they discard fine-structure to a large extent. In Fine-Structure Processing (FSP) strategies, the timing of stimulation is dependent on zero-crossings of the sound signal in a particular frequency band to maintain the fine structure of that band. However, even for such strategies, speech understanding in noise, tonal perception, voice recognition and music appreciation are often unsatisfactory. Despite all efforts, speech perception tests show that since the introduction of CIS, new strategies have not led to further improvement of speech scores, which have stagnated, on average, around 80% (Zeng, 2004).

Evaluation of new sound coding strategies is challenging for three reasons: it involves time- and energy consuming patient-testing, the study power is usually limited by group size, because only a restricted pool of patients is able to perform the tests and lastly a large patient-variability leads to negligible improvement on a group level, or may even cancel out opposing effects from different sub-groups. Alternatively, objective measurements, such as Evoked Compound Action Potential (eCAP) recordings, can also be used to test the performance of CIs. However, similarly to the difficulties of evaluating new coding strategies laid out above, the relationship between objective measures, individual fittings and performance are difficult to establish (de Vos et al., 2017; McKay et al., 2013). Parallel to the development of sound coding strategies, efforts to improve performance and subjective satisfaction with CIs were directed at electrode design (Dhanasingh and Jolly, 2017), musical therapy training (Fuller et al., 2014), bilateral implantation (van Schoonhoven et al., 2013), and electroacoustic stimulation (EAS) (Talbot and Hartley, 2008). EAS systems are designed for patients with residual hearing, so that they can benefit from the combination of acoustic and electrical hearing in the same ear.

1.5 Recording peripheral responses to sound segments

There are different objective measures that record the responses of the electrically stimulated peripheral auditory system to sound segments. Three such measures are introduced in this section. One example of an objective measure, in response to long duration electrical stimulation, is the single fiber action potential (SFAP). In the SFAP, responses to pulse trains in the electrically stimulated ear are recorded invasively from single neurons in animals. By doing so, exact spike timings of the neuron under test are recorded. From these spike times, average spike rates, or times between subsequent action potentials, can be calculated and plotted in a post-stimulus time histogram (PSTH) or interspike interval histograms (IH) respectively. When periodically amplitude modulated pulse

trains are used, the spike times relative to the stimulus period yield the period histograms (PH), and modulation-following behavior can be calculated with the Vector Strength (VS). These responses all provide detailed information about how the neuron responds to stimulation. Due to its intrusiveness, the SFAP has only been recorded in animals. Animals' auditory nerve fibers are morphologically and physiologically somewhat different from human auditory nerve fibers, for instance in diameter and myelination (Liu et al., 2015; Paintal, 1966; Spoenclin and Schrott, 1989).

In contrast to the SFAP, which is recorded only from animals, the eCAP is the best available method to measure neural responses from human CI users. These recordings are therefore, very valuable to validate the simulated responses for the human situation. Moreover eCAP responses have been obtained in both humans and animals with different degrees of hearing loss. This provides the possibility to evaluate the effect of hearing loss on neural behavior. ECAPs in response to single or double pulses are studied extensively (Briaire and Frijns, 2005; Miller et al., 1999), but they can also be obtained in response to pulse trains (Wilson et al., 1997).

For the purpose of EAS, electrocochleography (ECoChG), which goes way back as an objective tool in the diagnosis of hearing loss (Eggermont, 2017), recently found its place to objectively measure acoustic hearing during cochlear implant surgery and fitting (Koka et al., 2017). With this method responses of the implanted auditory periphery to acoustic sound segments can be recorded. In ECoChG, electrical potentials generated by hair cell and neural activity in response to sound stimulation are recorded by an electrode, usually placed close to the round window. Nowadays, through the use of the reverse telemetry functionality of cochlear implants, ECoChG could readily be recorded intracochlearly. In intracochlear ECoChG recordings, cochlear potentials in response to acoustic stimulation are recorded by the cochlear implant electrode. This has recently been suggested as a tool to detect hair cell damage (Koka et al., 2017b).

1.6 Modeling cochlear implant sound coding

To improve our understanding of objective measures, computational models can be used. Through the use of such models the effect of individual differences in the auditory system, perhaps related to hearing loss, can be investigated. Responses of the implanted auditory system can be modeled to gain more insight in interpatient-differences and to predict functional outcomes with different stimulation strategies. Such models can be built using either a biophysical or phenomenological approach.

In a biophysical model, expressions to describe behavior of physiological elements of the auditory neuron are based on voltage clamp recordings, usually made from laboratory animals. For an overview of existing models view O'Brien et al. (2016). Hodgkin and Huxley were the first to quantitatively describe nerve membrane behavior in response to an induced membrane current (Hodgkin and Huxley, 1952). Later, these differential equations were adjusted to describe myelinated and mammalian nerve fibers (Frankenhaeuser and

Huxley, 1964; Schwarz and Eikhof, 1987). To calculate responses to an external electrical stimulus, a cable model was required that calculates potentials at several nodes (McNeal, 1976), that was based on a realistic nerve morphology (Frijns et al., 1994; Frijns and ten Kate, 1994) and described the effects of the spatial distribution of currents outside the membrane (Reilly et al., 1985). It was shown that a multiple non-linear node model was required to accurately model stimulus repetition rates, as limits to these rates were caused by nerve fiber conduction properties rather than by single-node frequency-following behavior. In the later published generalized Schwarz-Eikhof-Frijns (GSEF) model, kinetics were based on mammalian fibers and generalized for different diameters. In the LUMC, a realistic 3D model of the intracochlear potentials and a multi-nodal active-cable model of the auditory nerve with GSEF characteristics has been developed and validated for evaluation of current spread and spread of excitation in response to single pulses (Dekker et al., 2014; Frijns et al., 2001, 1995; Kalkman et al., 2015, 2014). The model reproduced deterministic threshold characteristics and refractory behavior for different pulse shapes. Unfortunately, biophysical models often do not include stochasticity or long temporal effects, which are required for modeling long duration segments of stimulation. Inclusion of these factors while taking a biophysical approach would require a large number of parameters. Moreover, calculation of responses of a large number of nerve fibers to long duration segments would require tremendous computational power.

Phenomenological model types predict the neural response with a simplified description of neural behavior. The characteristics of phenomena are deduced from single fiber action potential (SFAP) recordings, gross potential recordings such as eCAPs or psychophysical measurements. For a review of phenomenological models of responses of the auditory periphery to electrical stimulation see Takanen et al. (2016). Phenomena related to electrical stimulation include refractoriness, adaptation after long duration of spiking, accommodation to prolonged stimulation (irrespective of the neural response), facilitation (increased firing in response to specific rates), latency, jitter and stochasticity in the neural responses. In most of these models, initial thresholds are determined with a statistical process (point-process) (Goldwyn et al., 2010, 2012), or with a simple electrical network such as the leaky integrate-and-fire (LIF) models (Bruce et al., 1999b, 1999a; Fredelake and Hohmann, 2012; Hamacher, 2004; Horne et al., 2016; Macherey et al., 2007). Both point process and LIF models can be extended with the spike-history and stochastic effects described here.

For both types of models, to calculate responses of the complete auditory nerve, a realistic distribution of current spread within the cochlea is required. So as to simulate responses to pulse trains, a 3D model should be combined with pulse-dependent thresholds, stochastic effects and long temporal components, all preferably minimizing the computational power, so that speech-relevant sections of sound can be modeled with reasonable amounts of computation.

2 Aims and method

The aim of the current research is to better understand how the implanted auditory periphery responds to sound, to

1. aid in the evaluation of sound coding
2. gain more understanding of inter-patient differences

To do this, models of responses to sound of the implanted auditory periphery were developed. Models of responses to sound in cochlear implant subjects can function as digital test-boards for sound coding strategies and recordings from the implant, thereby speeding up developments in CI design. Moreover, they can be used to relate interpatient differences from objective recordings to differences in behavior of the auditory peripheral system. Requirements for such models include accurate and fast simulations in response to a wide range of stimuli.

In this thesis, a model of responses to electrical stimulation was developed that combined a biophysical and phenomenological approach. Thresholds dependent on current distribution and different pulse shapes were pre-calculated with the detailed 3D cochlear model and the biophysical multi-nodal cable- neuron model and stored in a database. Parameters of neural behavior that required too much computational time, or with the biophysical model too many fitting parameters, were implemented using a phenomenological approach. Phenomena related to electrical stimulation include temporal and stochastic effects in the neural responses. The deterministic thresholds were adjusted according to phenomenological parameters to describe stochasticity, refractoriness, accommodation and adaptation. In this manner, a model that was fast enough to simulate responses to pulse trains, and detailed enough to simulate responses to all sorts of pulse shapes was developed.

A model of responses of the implanted auditory periphery to sound was also developed. This model had to include hair cell activation evoked by sound and was based on a previously developed model (Zilany et al., 2014). In addition, spatial spread of electrical currents evoked by hair cell activation had to be calculated. This was done with the 3D model describing electrical conductivities in the auditory periphery. By combining these, responses to acoustic stimulation could be modeled at the electrode locations for EAS-subjects.

The responses of both models were validated by comparison to objective recordings. Recorded inter-patient differences were explored by model parameter variations.

3 Outline of this thesis

Chapters 2 and 3 describe the neural model in detail and validate the models' responses to constant amplitude electric pulse trains and amplitude modulated electric pulse trains respectively. The work covers durations of several hundreds of milliseconds and with rates up to 5000 pps. **Chapter 4** shows that power-law adaptation is a required adjustment to the model when simulations with durations of seconds up to several minutes are required. In **chapter 5** the model is used to simulate eCAP responses to pulse trains. Previously published data of pulse-train recordings in humans are correctly replicated, indicating that the model is a reliable tool to evaluate human neural responses. Moreover, the pulse-train eCAP can be used as a tool to test inter-patient differences in their temporal responses. For the purpose of evaluating electroacoustic stimulation, and aid in the interpretation of ECoChG recordings made intra- and post-operatively, **chapter 6** shows validation of a model that simulates recordings with the cochlear implant of hair cell responses to sound. An overall discussion of the outline, results, clinical relevance and future directions of the presented work is given in **chapter 7**.

CHAPTER 2

A fast, stochastic, and adaptive model of auditory nerve responses to cochlear implant stimulation

Margriet J. van Gendt

Jeroen J. Briaire

Randy K. Kalkman

Johan H.M. Frijns

Abstract

Cochlear implants (CIs) rehabilitate hearing impairment through direct electrical stimulation of the auditory nerve. New stimulation strategies can be evaluated using computational models. In this study, a computationally efficient model that accurately predicts auditory nerve responses to CI pulse train input was developed. A three-dimensional volume conduction and active nerve model developed at Leiden University Medical Center was extended with stochasticity, adaptation, and accommodation. This complete model includes spatial and temporal characteristics of both the cochlea and the auditory nerve. The model was validated by comparison with experimentally measured single fiber action potential responses to pulse trains published in the literature. The effects of pulse rate and pulse amplitude on spiking patterns were investigated. The modeled neural responses to CI stimulation were very similar to the single fiber action potential measurements in animal experiments. The model's responses to pulse train stimulation with respect to spatial location were also investigated. Adaptation was stronger at the borders of the stimulated area than in the center. By combining spatial details with long-term temporal components and a broad implementation of stochasticity a comprehensive model was developed that was validated for long duration electric stimulation of a wide range of pulse rates and amplitudes. The model can be used to evaluate auditory nerve responses to cochlear implant sound coding strategies.

1 Introduction

Cochlear implants (CIs) are implantable devices that partially restore auditory perception in individuals who have severe to profound hearing loss. CIs generally provide good speech understanding in quiet and have become the established mode of rehabilitation for adults with severe to profound hearing loss (Clark and Clark, 2013). However, CI users still experience difficulties understanding speech in noisy (real life) situations and suboptimal encoding of pitch accents due to limited transfer of the fine spectrotemporal details of the sound (Wouters et al., 2015). Many different sound-coding strategies have been introduced in the last decade to overcome this challenge, but no major advances have been made since the introduction of the Continuous Interleaved Sampling (CIS) strategy (Wilson et al., 1991; Zeng et al., 2008). New stimulation strategies are commonly investigated in psychophysical experiments and clinical trials, which is time-consuming for both the patient and researcher. Alternatively, strategies can be evaluated with the use of computational models. The present study presents a computationally efficient model that accurately predicts auditory nerve responses to arbitrary CI input signals.

A comprehensive computational model of the response of the auditory nerve to CI stimulation should include a realistic distribution of thresholds of all nerve fibers, and take into account both stochastic behavior and history effects. Stochasticity generally plays a role in the human sensory system (Verveen and Derksen, 1968) and is present in the auditory nerve's responses to electrical stimulation (Rubinstein, 1995). Animal experiments have demonstrated variance in neural responses to different pulses in a pulse train (Bruce et al., 1999a, 1999b; Dynes and Delgutte, 1992; Miller et al., 1999a; Shepherd and Javel, 1997). In addition, animal experiments (Cartee et al., 2000; Litvak et al., 2001; Miller et al., 2008; Zhang et al., 2007) have shown a dependency of auditory nerve behavior on previous neural spikes and pulses, referred to as the history effects. Here, history effects include refractoriness, facilitation, adaptation, and accommodation. Refractoriness is the diminished excitability of the nerve immediately following an action potential. Facilitation is a threshold decrease caused by a preceding sub-threshold pulse. Adaptation refers to a threshold increase caused by long-term firing of the neuron. Accommodation refers to a threshold increase caused by a long-term stimulation current and occurs when the membrane slowly depolarizes due to the stimulus. Accommodation and adaptation recently received increased attention as important aspects in neural responses to long duration electrical stimulation (Hay-McCutcheon et al., 2005; Hughes et al., 2012; Liu and Wang, 2001; Negm and Bruce, 2014, 2008; Woo et al., 2010, 2009). Neural adaptation, a decrease in neural excitability during persistent stimulation, is important for efficient coding of dynamically varying inputs (Bohte, 2012; Drew and Abbott, 2006; Zilany and Carney, 2010). Although some early research was equivocal about the existence of auditory nerve adaptation in response to electrical stimulation (Parkins, 1989), several reports indicate that electrical stimulation leads to adaptation of the auditory nerve (Javel et al., 1987; van den Honert and Stypulkowski, 1987). Several groups have investigated the effects of long duration continuous or pulsatile electrical stimulation on nerve activation

based on single fiber action potential (SFAP) measurements of the auditory nerve (Dynes and Delgutte, 1992; Hartmann et al., 1984; Javel et al., 1987; Shepherd and Javel, 1997; van den Honert and Stypulkowski, 1987). In order to predict the performance of patients with CIs in discrimination tasks, the complete nerve fiber's response has to be predicted. A complete cochlear model is required to investigate the responses of the auditory nerve in both the spatial and temporal domain. A model of the whole nerve is needed to investigate the influence of the spatial location of auditory nerve fibers on temporal response patterns.

Different types of models are available to predict nerve responses to electrical stimulation. A major distinction can be made between the biophysical and phenomenological type of models. Biophysical models quantitatively describe nerve membrane behavior in response to an induced membrane current and have been shown to correctly predict membrane responses to single pulses and reasonably predict latencies, refraction, and facilitation effects (Frijns et al., 1994; Frijns and ten Kate, 1994; Reilly et al., 1985; Schwarz and Eikhof, 1987). These models can be combined with 3D volume conduction models of the cochlea to predict auditory nerve responses to electrical pulses as reported by Kalkman et al. (2015). Biophysical model parameters are based on patch-clamp single fiber recordings, from which high order effects, required to model responses to long duration pulse trains, are difficult to obtain. In addition, the calculation of responses to long duration pulse trains using these models requires long computational times. Phenomenological models directly relate empirical observations to expected neural output. Such models have been used to efficiently predict responses to sustained stimulation by direct implementation of stochastic and temporal behavior (Bruce et al., 1999a, 1999b; Chen and Zhang, 2007; Litvak et al., 2003a; Macherey et al., 2007; Stocks et al., 2002; Xu and Collins, 2007). All proposed phenomenological approaches modeled auditory nerve fibers as single nodes and incorporated at most 20,000 fibers. The models that included a geometric current spread all modeled the electrode contacts as point sources located in homogeneous media. Phenomenological models that simulate thresholds are only capable of dealing with pre-defined pulse shapes.

The goal of the current study was to develop a hybrid model that incorporates spatial and pulse-shape effects from a biophysical model, as well as temporal effects and stochastic responses from a phenomenological model. The model had to be computationally efficient in order to predict whole nerve responses to long duration pulse trains. By merging the biophysical and phenomenological approaches in a compound model, we utilized the merits of both methods and minimized their disadvantages. The model was validated by comparison with experimentally measured SFAP responses to pulse trains published in the literature. The model's output with regards to discharge rate, rate variances, rate decreases, and pulse intervals was evaluated for pulse trains with different rates and amplitudes. For clarity the comparison between model predictions and animal data from the literature will be given directly in the results section. In the discussion section the

similarities and differences between predictions and data will be interpreted and analyzed in terms of model parameters.

2 Materials and methods

2.1 Model

The model presented in this paper builds on the previously published 3D volume conduction model of the cochlea and deterministic cable model of the human auditory nerve (Kalkman et al., 2015). The cochlear geometry is based on micro-CT data, the electrode array geometry is based on the HiFocus1J, modelled in lateral position. The model presented in this paper extends the deterministic thresholds from active GSEF nerve fibers (Briaire and Frijns, 2005; Frijns et al., 2000) with stochastic behavior and history effects (Figure 2.1). Deterministic thresholds are obtained at 3200 spatially different locations using the 3D volume conduction model, an overview of the model is shown in Figure 2.2; for details of its implementation we refer to Kalkman et al. (2015). At each of these locations, 10 different nerve fibers are modeled. Thus, the model of the whole auditory nerve effectively incorporates a total of 32,000 different auditory nerve fibers. The deterministic thresholds of the 3D model are used as input to the phenomenological model extension; only the thresholds of entire fibers are taken into account, and not the individual thresholds of each Ranvier node. For each nerve fiber, stochasticity is induced by adding a relative spread (RS) to the deterministic thresholds. To account for refractoriness these stochastic thresholds are elevated depending on the time since the last spike relative to refractory period. Spike adaptation (SA) and accommodation are included by increasing the threshold after each spike and pulse.

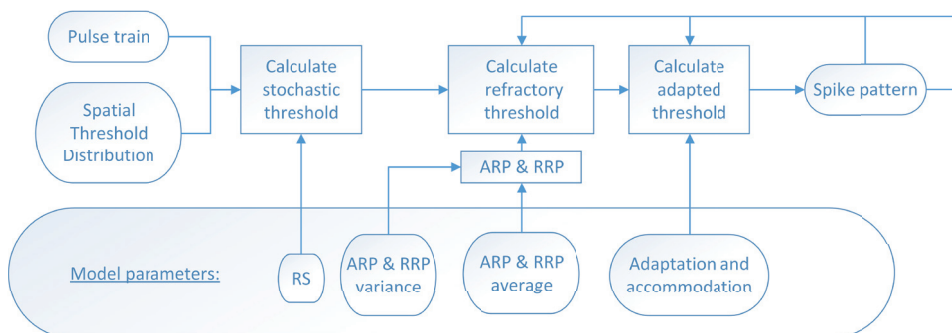


Figure 2.1. Model flow-chart per fiber. The deterministic threshold is input to the model that includes a relative spread, refractoriness, adaptation and accommodation. The final calculated thresholds are compared to the stimulus input to predict whether or not an action potential has occurred.

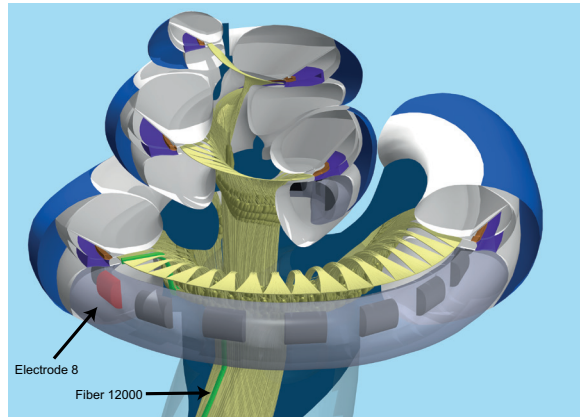


Figure 2.2. 3D model overview. Unless stated otherwise, the simulations were done by stimulating the electrode located at roughly 175 degrees from the round window, here highlighted in red. Most of the simulations were done on fiber 12000 (fiber 1200 in the 3D model), here highlighted in green; fibers are counted from basal to apical cochlear locations. The tip of this fiber is located roughly at the same cochlear angle as the stimulated electrode.

In order to develop a model that predicts neural responses to situations different than the ones exactly replicated during the validation, model parameters were based on physiological data. For every parameter the values and references are described below. A distinction can be made between parameters for which the values could be drawn directly from the literature (refractoriness, stochasticity and the adaptation time constant) and parameters which were based on fits to experimental data (adaptation and accommodation amplitudes). Because of this approach the model predictions are generalizable to other experiments than the ones presented in this paper. The mean and variance of the model parameters RS, absolute refractory period (ARP), and relative refractory period (RRP) are based on the literature. For each fiber, a specific value is drawn from these normal distributions. For the simulations in this paper, monopolar stimulation with cathodic-first biphasic pulses and a pulse width of $18 \mu\text{s}$ was used and is the stimulus was strong enough an action potential was assumed to occur during the anodic phase. The model uses time steps in the size of the pulse width; in other words, in the presented simulations every $18 \mu\text{s}$ the model calculates which fibers are expected to fire. The extended temporal and stochastic model was developed in Matlab (Mathworks, Inc.). The configuration of stimulation and measurement in the model is shown in figure 2.2. The electrode contact coloured red is the stimulating contact in the simulations presented in the paper. Most of the recordings are done on a fiber at the location coloured green. In the simulations the action potential is recorded at the end of the fiber to exclude effects of aborted spikes (Frijns et al., 1994). Typical inputs and outputs to this extension of the complete model are shown in figure 2.3. Figure 2.3A shows the typical stimulation waveform, where in the presented simulations the Phase Duration (PD) was set to $18 \mu\text{s}$ and amplitudes were variable. Figure 2.3B shows an example neural excitation threshold

distribution as obtained using the 3D volume conduction and active nerve fiber model. Figure 2.3C and 2.3D show an example spike pattern and its corresponding Post Stimulus Time Histogram. This example is obtained by measuring the response at fiber 12000.

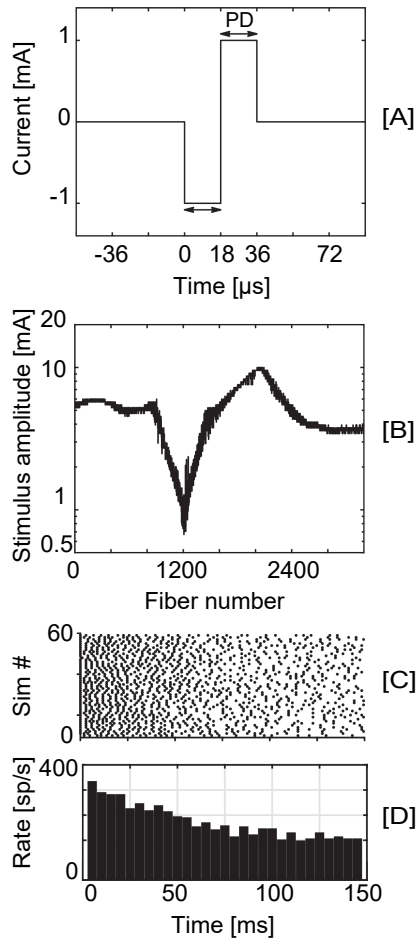


Figure 2.3. Model input and output. An example of the stimulating waveform used in the current simulations is shown in [A]. The deterministic threshold of all fibers was calculated using the 3D model and the active nerve model. An example of the threshold waveform, in the spatial dimension, in response to stimulation of one electrode is shown in [B]. The output of the model is a spiking pattern. An example of spike patterns in 50 different trials to an identical stimulus (1000 pps, 150 ms, amplitude 0.85 mA) is shown in [C] and its corresponding Post Stimulus Time Histogram in [D].

Relative spread of thresholds

A measure of the variability of spike initiation is the RS, which is defined as the standard deviation (SD) of the underlying Gaussian distribution divided by its mean (Verveen and Derksen, 1968). The SD of the normal distribution around the deterministic threshold is defined as: $SD = I_{det} \cdot RS$, where I_{det} is the deterministic single pulse threshold for an individual fiber. I_{det} is the minimal current required on the selected electrode to elicit an action potential in the fiber that is strong enough to run all the way to the end of the modelled axon, regardless of the node at which the fiber was excited initially. I_{det} was calculated using the 3D volume conduction and the deterministic nerve model. Using the RS, the spiking probability can be calculated using a phenomenological approach, similar to Bruce et al. (1999b). After each pulse, the stochastic threshold is obtained from the normal distribution, $N(I_{det}, SD)$. The RS, an estimate of the stochastic behavior of the auditory nerve, is obtained from measurements of the SFAP (Bruce et al., 1999b; Javel et al., 1987; Miller et al., 1999a). An overview of RS values described in the literature is given in table 2.1. In the model, the RS is set to 0.06 with a SD of 0.04 and a minimum of 0, within the range of the various distributions found in the literature for comparable pulse widths.

Table 2.1. Relative Spread (RS) estimates obtained from SFAP measurements published in literature, PD = Phase Duration, RS = Relative Spread, SD = Standard Deviation

Author (year)	Stimulus	RS (SD)
Bruce et al. (1999b) from Javel et al (1987)	PD 200 us, biphasic	0.12 (0.05)
	PD 400 us, biphasic	0.11 (0.04)
Bruce et al. (1999b) from Dynes (1996)	PD 100-200 us, cathodic	0.12 (0.06)
Miller et al. (1999)	PD = 26 us, cathodic	0.06 (0.03)
	PD = 26 us, anodic	0.06 (0.04)
	PD = 39 us, cathodic	0.06 (0.04)
	PD = 39 us, anodic	0.07 (0.07)

Refractoriness

The ARP is the period immediately following an action potential during which the neural membrane is unable to fire again. The ARP is followed by the RRP, during which only a greater than normal stimulus can induce a response. Refractoriness can be implemented as a threshold increase following an action potential. The refractoriness factor, R , is calculated using equation 2.1:

$$R = \frac{1}{1 - e^{-\frac{(t - \tau_{ARP})}{\tau_{RRP}}}} \quad (\text{Eq. 2.1})$$

where τ_{ARP} and τ_{RRP} are the time constants for the ARP and RRP, and t is the time since the last action potential. Equation 2.4 below shows how R is used to calculate the final threshold. Estimates for the ARP and RRP of the auditory nerve can be obtained directly using the SFAP (Dynes, 1996; Miller et al., 2001, 1999a), extracted from model data (Bruce et al., 1999a) or estimated based on human electrically evoked Compound Action Potential (ECAP) measurements (Cartee et al., 2000; Stypulkowski and Van den Honert,

1984). Figures 2.4A and 2.4B show the estimates for τ_{ARP} and τ_{RRP} , respectively. The average values and SDs for τ_{ARP} and τ_{RRP} were chosen so they closely mimic the range of values found in the literature (figure 2.4). τ_{ARP} is set to 0.4 ms (SD 0.1 ms) and τ_{RRP} to 0.8 ms (SD 0.5 ms). For each of the 32,000 modeled fibers, values for τ_{ARP} and τ_{RRP} were randomly chosen from the normal distribution. Additional randomness is applied to the refractoriness by choosing the final ARP and RRP at every time point from a distribution with a SD of 5% of the average (Hamacher, 2004). If the value obtained for one of the refractory parameters is less than zero, its value is set to zero.

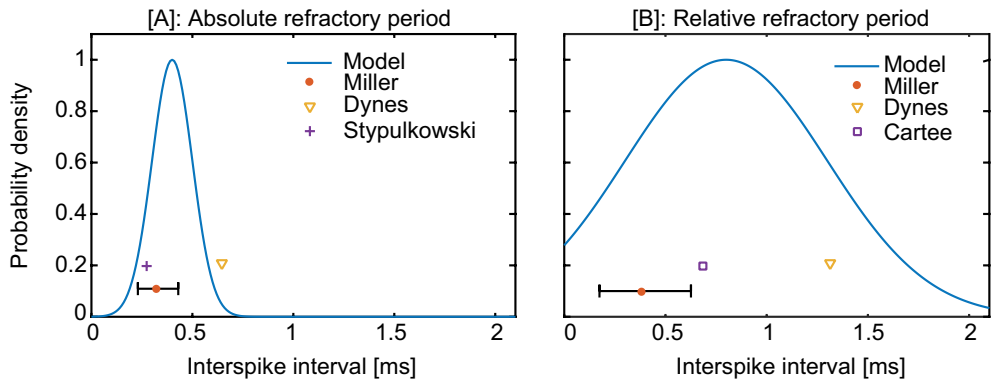


Figure 2.4. Absolute [A] and relative [B] refractory periods. The blue lines indicate the distribution of both model parameters as used in the proposed model. The other symbols indicate values published in the literature for both model parameters. If a standard deviation was also reported this is included as an error bar.

Spike adaptation and accommodation

The model extension described in this paper includes both firing-dependent adaptation and stimulus-dependent adaptation, with the latter referred to as accommodation. As first described by Litvak et al. (2001), auditory nerve responses exhibit larger adaptation in response to higher rate pulse trains. In order to obtain a stronger reduction in spike rates with higher stimulus rates, regardless of the initial discharge rate, an adapting parameter had to be introduced into the model that depends on pulse history, not on spiking history. To account for this effect, the accommodation parameter is included. The fiber adapts after each spike and accommodates after each pulse given. The spike adaptation (SA) is calculated as in equation 2.2, where i are all previous spikes, t is the current time, and t_i is the time since spike i .

$$SA = \sum_i \text{ampl}_{adap} \cdot e^{\frac{t-t_i}{\tau_{adap}}} \quad (\text{Eq. 2.2})$$

The adaptation amplitude is taken from a normal distribution with an average of 1.0% of the threshold and a SD of 0.6% of the threshold.

The accommodation (acco) is calculated as in equation 2.3, where p are all previous pulses, t is the current time, and t_p is the time since pulse p .

$$Acco = \sum_p 0.03\% \cdot I \cdot \frac{I_{\min}(electrode)}{I(electrode, fiber)} \cdot e^{\frac{t-t_p}{\tau_{adap}}} \quad (\text{Eq. 2.3})$$

The accommodation parameter is modeled as a threshold increase after each pulse as large as 0.03% of the given stimulus current multiplied by a spatial factor. The spatial factor for each fiber and electrode is the minimum current required to elicit a spike on any of the fibers using the concerned electrode, divided by the current required to elicit a spike in the simulated fiber with this electrode: $\frac{I_{\min}(electrode)}{I(electrode, fiber)}$. Thus, the accommodation is strongest at the fibers with the lowest thresholds. Both the accommodation and the adaptation parameter are forced to have a positive value for every fiber.

Dynes and Delgutte (1992) suggested that adaptation to electric sinusoids follows a single negative exponential course across several hundreds of milliseconds. More recently, several research groups studied the adaptation of responses to high-rate biphasic electrical stimulation with CIs (Litvak et al., 2001; Miller et al., 2008; Zhang et al., 2007). Litvak et al. (2001) found a short-term (< 150 ms) adaptation that is dependent on pulse rate. Investigating spike rates for pulse trains up to 5000 Hz, Zhang et al. (2007) and Miller et al. (2008) found asymptotic values within 300 ms of stimulation. The amount of adaptation was affected by pulse rates and stimulus levels and fit to an exponential decaying model with two different time constants: a rapid adaptation of 10 ms and a short-term adaptation of 100 ms. In the current model, both spike adaptation and accommodation are modeled as decaying exponentially with a time constant of 100 ms.

Final threshold

For every fiber, the final adjusted threshold (I_{adj}) is calculated as in equation 2.4.

$$I_{adj} = N(I_{det}, \sigma) \cdot R + SA + Acco \quad (\text{Eq. 2.4})$$

A spike is assumed to occur if: $I_{given} > I_{adj}$, where I_{given} is the stimulus current. The overall parameter set used in the model is given in table 2.2.

Table 2.2. Overall parameter set as used in the model

Parameter	Value (\pm SD)
RS	0.06 (\pm 0.04)
T_{ARP}	0.4 (\pm 0.1) ms
T_{RRP}	0.8 (\pm 0.5) ms
Within Refractoriness stochasticity	5% of τ_{ARP} / τ_{RRP}
Adaptation amplitude	1.0 (\pm 0.6)% of threshold
Accommodation amplitude	0.03% of pulse current · spatial factor

2.2 Validation

To validate the outcomes of the model, animal experiments published in the literature were emulated (Javel et al., 1987; Litvak et al., 2001; Miller et al., 2008; Zhang et al., 2007). The experiments were SFAP measurements performed in cats. Unless noted otherwise, the simulations were done by stimulating the electrode located at roughly 175 degrees from the round window. Most of the simulations were done on fiber 12000, fibers are counted from basal to apical cochlear locations. This fiber is located roughly at the same angle as electrode 8, close to its center of stimulation. Both electrode 8 and fiber 12000 (which corresponds to fiber 1200 in the 3D model) are highlighted in figure 2.2. Because of the multitude of different experiments, a variety of set-ups were investigated. In validation experiments that included a group of nerve fibers, the model parameters of the different fibers were randomly drawn from the distributions given in table 2.2. In some of the experimental data only the recordings of a single fiber are shown. The characteristics of the modeled fiber used to reproduce these data were always set to the average value presented in table 2.2. Except for the discharge rate I/O curves, which were calculated by simulating a nerve one time, all outcome measures were obtained by simulating one fiber several times. For the interval histograms (IHs), five averages were used; for all other simulations 30 averages were used.

The effect of stimulus amplitude on overall discharge rate was investigated by evaluating the discharge rate I/O curves using 100 ms pulse trains of different rates: 100, 200, 300, 400, 600, and 800 pulses per second (pps), in accordance with experiments done by Javel et al. (1987). Average discharge rates were calculated over the whole period of stimulation. For this simulation, the average model parameters were used. The animal experiments were previously simulated using a phenomenological model by Bruce et al (1999a). Their results also included normalized values for the first spike of the pulse train. Similar to the approach of Bruce et al, the model was used to predict these by turning off all inter-pulse effects. The variances in the responses are also presented in the paper by Bruce et al. and simulated using the proposed model for rates of 200 and 600 pps.

To emulate the data published by Zhang et al. (2007), post-stimulus time histograms (PSTHs) for a fiber in response to 300 ms pulse trains were modeled. Discharge rates during the complete stimulus, calculated as the number of spikes during small time segments, were plotted in PSTHs with binwidths of 1 ms. Stimulus pulse rates were 250, 1000, 5000, and 10,000 pulses/s. Amplitudes of 0.8, 0.9, and 1 mA were used. For this simulation, all model parameters were set to the average values.

In order to compare to data from Miller et al. (2008), the timing of spikes in response to 300 ms pulse trains at different rates and amplitudes was investigated using IHs, which plot timings between consecutive spikes in response to a pulse train. To investigate changes in inter-spike timings over the duration of the stimulus IHs were obtained for simulated responses to 300 ms pulse trains of 250, 1000, and 5000 pps at three different temporal epochs; 0-12 ms, 4-50 ms, and 200-300 ms.

To investigate how the model accounts for adaptation and accommodation, spike rate decrements in response to pulse trains with different rates were calculated. Group data on spike rate decrements were obtained to replicate the measurements of multiple fibers by Litvak et al. (2001). Discharge rate decrements were obtained by calculating the difference between the final and initial discharge rates in response to 1200 and 4800 pps pulse trains for a large number of fibers. The discharge rate decreases measured for a group of nerve fibers by Zhang et al. (2007) were also simulated. The spike rate decrements at four different stimulus pulse rates (250, 1000, 5000, and 10,000 pps) were calculated.

2.3 Whole nerve simulations

To see the effect of the 3D volume conduction model on discharge rates in the whole nerve, all 32,000 fibers were stimulated for a period of 200 ms. The average discharge rates of all fibers over the duration of the stimulus were compared to the deterministic single pulse thresholds obtained using the 3D volume conduction and active nerve fiber model. Whole nerve simulations were performed to investigate the total nerve activation and the effect of the spatial distribution of nerve fibers relative to the electrode on the temporal response. Simulations were performed with a loud (1.4 mA) continuous pulse train of 150 ms and 5000 pulses/s presented to the stimulating electrode. The temporal spiking pattern of fibers at different geometric locations was investigated.

3 Results

3.1 Spike rate growth I/O curves and variances

Simulated discharge rate I/O curves calculated for different rate pulse trains (figure 2.5A) mimicked animal experiments done by Javel et al. (1987) (figure 2.5B).

The discharge rate in response to the 800 pps pulse train in both simulations and experiments increased from 0 to 700 spikes/s when stimulus amplitude increased with 8 dB. The slopes for lower rate pulse trains were shallower in both the animal data and simulations, which was most clearly visible at 100 pps. To visualize this effect an I/O curve at these lowest rates is obtained for a fiber with all parameters set to average, shown in figure 2.6. As clearly visible in this figure, the rate increases most with amplitudes for higher stimulation rates. In both the animal data and simulations, the I/O curves exhibit a rocky increase in the discharge rate with increasing amplitude. Because the absolute amplitudes are dependent on the electrode configuration and placement, which is very different in the experimental set-up and modeled situation, only relative amplitude differences are relevant.

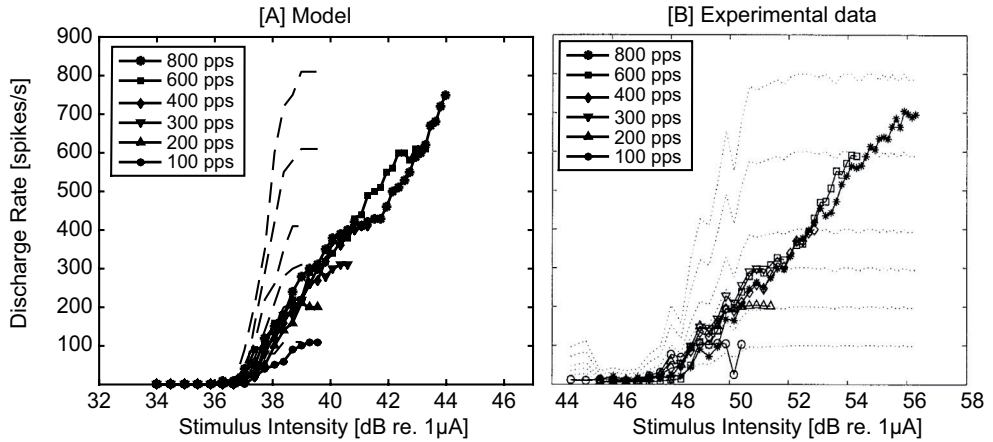


Figure 2.5. Mean discharge rates simulated with the current model [A] and results obtained with animal experiments [B] (Javel et al., 1987, reprinted with permission(1987)), at pulse rates of 100, 200, 300, 400, 600 and 800 pulses/s. Amplitudes used for the simulations ranged from 0.5 to 1.6 mA with a step size of 0.03 mA. Every data point was obtained from a single trial. Once the discharge rate equaled the stimulus rate only a few higher steps in amplitude were simulated, as was done in the animal experiments. Dotted lines indicate normalized values for the first spike of the pulse train. Similar to the approach of Bruce et al, the model was used to predict these by turning off all inter-pulse effects.

The variance measures shown by Bruce et al were also simulated with the proposed model, results are shown in figure 2.7. Larger variance per pulse is seen for the lower pulse rates, especially around 0.5 discharge probability per pulse. At this discharge probability per pulse the variance shows a dip, as is also seen in the animal data. Changing parameters for RS and the refractory periods gives different variability behavior. The refractoriness, as suggested by the authors of the paper of Bruce et al, as well as the RS, influences the shape of these curves.

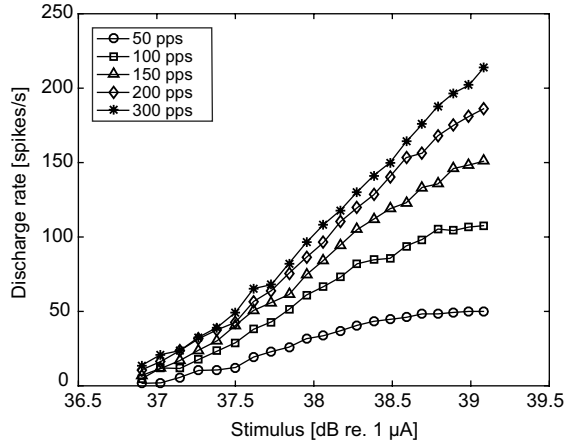


Figure 2.6. I/O-curves of discharge rate increases with increased stimulus amplitude for 5 different pulse rates: 50, 100, 150, 200 and 300 Hz. The x-axis plots the amplitude in dB relative to 1 μ A, 30 trials were done.

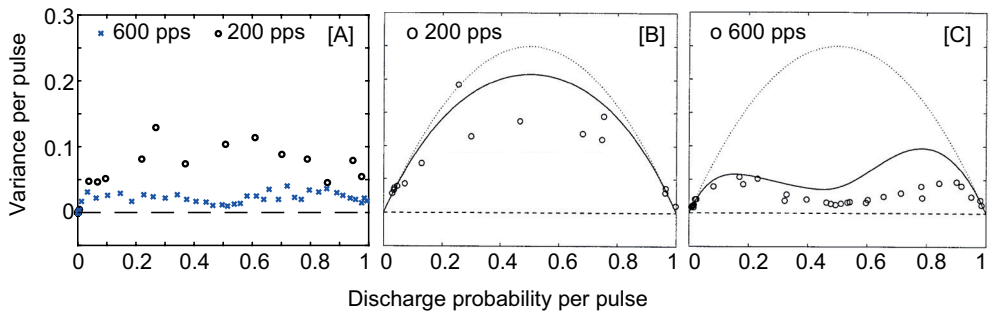


Figure 2.7. Variance per pulse versus discharge rate probability per pulse with the here presented model [A] and previous recordings and models [B and C] (Bruce et al., 1999, reprinted with permission). In [A] simulations are shown with 200 and 600 pps, all model parameters were set to average, amplitudes ranged from 0.5 to 1.5 with a step size of 0.01. In [B] (200 pps) and [C] (600 pps) the circles represent animal recordings, the lines represent previous models.

3.2 Post-stimulus time histograms

The PSTHs obtained using the model for two different fibers in response to a 300 ms pulse train for different pulse rates and amplitudes are shown in figure 2.8A. These histograms replicate data published by Zhang et al. (2007), which is shown in figure 2.8B.

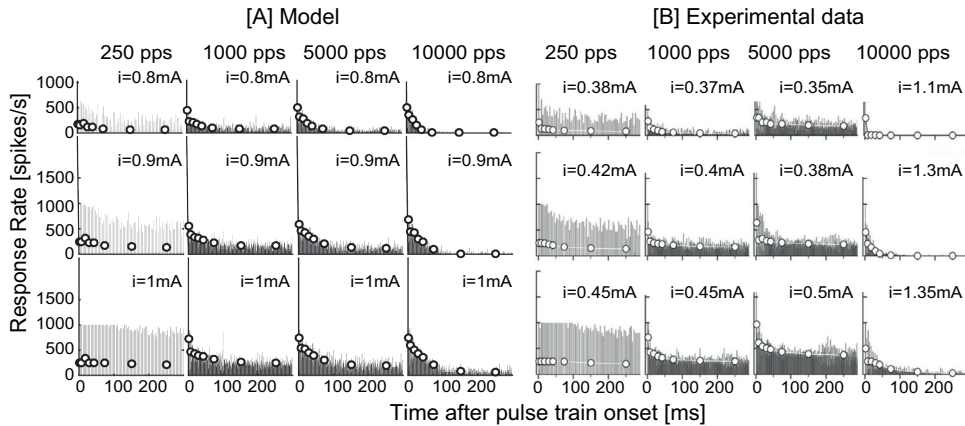


Figure 2.8. Post Stimulus Time Histograms. Examples of PSTHs obtained with simulations [A] and animal experiments [B] (Zhang et al., 2007, reprinted with permission) from the responses of an auditory nerve fiber (ANFs) at four different stimulus rates; 250, 1000, 5000 and 10,000 pps. Each column contains responses to stimulus trains of 3 different amplitudes. Amplitudes used for the simulations were 0.8, 0.9 and 1.0 mA. The vertical lines in the PSTH's are response rates during bins with a width of 1 ms. The open circles indicate the PSTH in binwidths with increasingly large bin-sizes: 0-4, 4-12, 12-24, 24-36, 36-48, 48-100, 100-200 and 200-300 ms.

All model parameters were set to the average values. When stimulated with the lowest pulse rate (250 pps, left column), the discharge rate in both the animal and simulation data decreased from around 800 pps initially to approximately 400 pps at the lowest amplitude, from 1000 pps to approximately 600 pps within the first 100 ms for the middle amplitude, and from 1000 to approximately 800 after 200 ms when stimulated with the highest amplitude. When stimulated with 1000 pulses/s, the discharge rates decrease much faster, within the first 50 ms for both animal experiments and simulations. The discharge rates in the animal and simulation data decreased from around 400 pps initially to approximately 100 pps at the lowest amplitude, from 500 pps to approximately 200 pps for the middle amplitude, and from 1000 to approximately 300 when stimulated with the highest amplitude. When stimulated with the 5000 pps pulse train, initial discharge rates were higher than when stimulated with the 1000 pps pulse train, and the decrease in discharge rate occurred later (around 50 ms) in both the animal data and simulations. However, the decrease in discharge rate was larger in the simulation than in the animal data. When stimulated with the highest rate pulse train (10,000 pps) the strongest adaptation for all different amplitudes in both the simulations and animal experiments

were seen. In the animal experiments much larger stimulus amplitudes were used, and a different fiber was stimulated. The modeled fiber showed a smaller decrease in discharge rate at larger stimulus amplitudes. It was tested that by choosing a fiber with larger adaptation characteristics in the model, or a fiber more off-center of stimulation, a decrease in discharge rate similar to animal experiments is seen at these high amplitudes and rates.

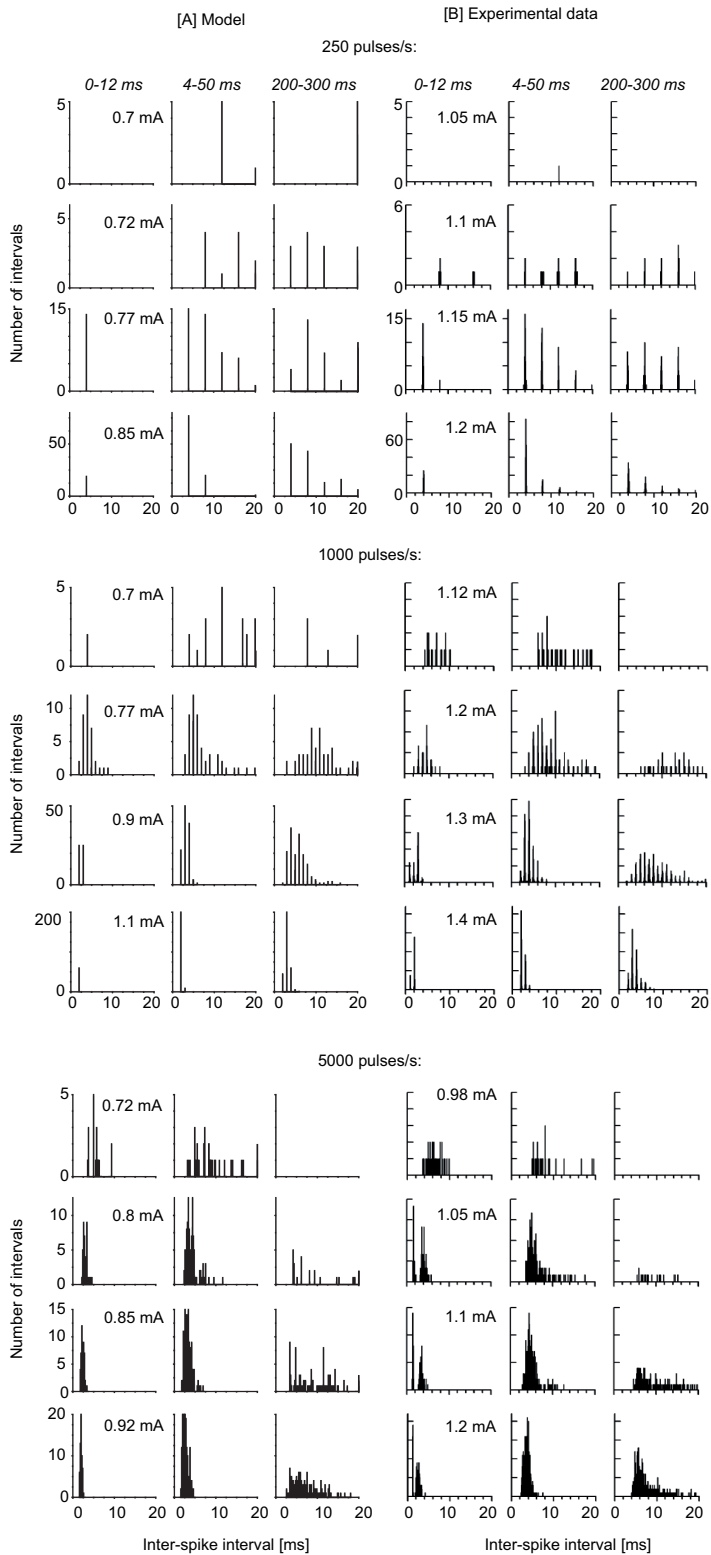
3.3 Interval histograms

The IHS were obtained to replicate the data from Miller et al. (2008) and are shown in figure 2.9. The IHS calculated from modeled responses are shown in the upper four rows, and those from experimental data are shown in the lower four rows. As in the PSTH simulations, for this IH simulation all model parameters were set to the average values (table 2.2). At all rates, the distributions were wider at later epochs; in the 0-12 epoch, especially at higher amplitudes, the intervals were mostly around 5 ms or shorter, whereas intervals of 10-20 ms were detected in both the animal and experimental data in the 200-300 ms epoch. When stimulated with 1000 or 5000 pps, both animal and simulated data exhibited a widening of the IH distribution and lowering of the peak in the last epoch compared to the second epoch. When stimulated with the largest amplitude at a rate of 5000 pps, the peak doubled from 10 to 20 intervals from the first to the second epoch and decreased back to 10 in the last epoch. The peak shifted from approximately 2 ms to 5 ms from the first to the last epoch in both the experimental and simulated data. The double peak at onset observed in the animal data when stimulated with the 5000 pps pulse train was missing in the simulations.

3.4 Spike rate decrements: 1200 and 4800 pps

Spike rate decrement data for a group of fibers was calculated to replicate measurements of multiple fibers by Litvak et al. (2001). Figure 2.10 shows the modeled [A] and the experimental data [B] for the final discharge rate, defined as the discharge rate in the last bin, versus the initial discharge rate (the discharge rate in the first bin). Decrements of fibers stimulated with a pulse rate of 1200 pps are shown as grey diamonds and those stimulated with a pulse rate of 4800 pps are shown as black stars.

Figure 2.9 (opposite). Interval Histograms. Examples of IHS obtained by simulations [A] and animal experiments [B] (Miller et al., 2008) by stimulating a fiber 300 ms with three different pulse rates (groups of columns) and four different amplitudes (rows). Stimulus levels are indicated at the left panel per rate and amplitude. For each different rate and level the IH at three different time windows are obtained, 0-12 ms, 4-50ms and 200-300 ms, labeled at the top in italic. Bin-width was set to 50 μ s.



When stimulated with 24,000 pps all modeled fibers showed complete adaptation. For the simulations, different fibers were used and their parameters were randomly drawn from the distributions. The results were visualized by plotting the final spike rate (average rate over 140-150 ms after onset) on the ordinate vs. the initial spike rate (in the epoch 10-20 ms after onset) on the abscissa. The two dotted lines in the left graph show the linear fit through the origin and the 1200 pps data (upper line) and 4800 pps modeled data (lower line). As shown by the linear regression lines, the highest stimulus rate (4800 pps) caused a lower final discharge rate than the 1200 pps stimulus rate pulse train. This difference in the decrease in discharge rate was visible in both experiments and simulations. There was a broad distribution of final vs. initial discharge rates in both the animal data and simulations.

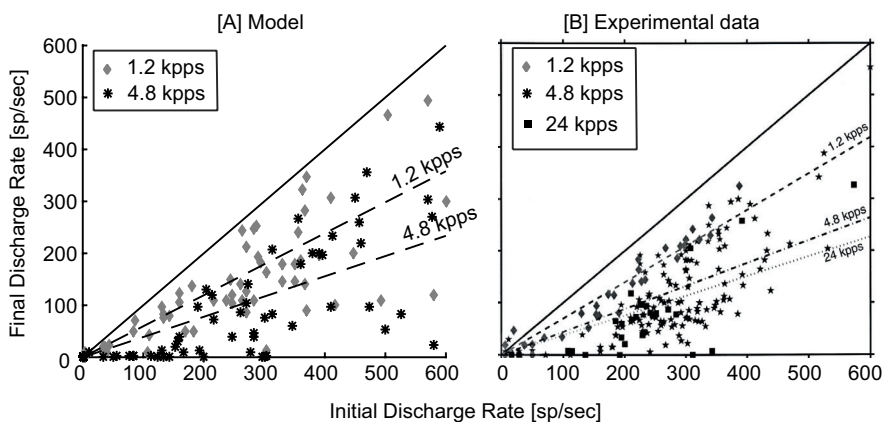


Figure 2.10. Final discharge rates. Modeled [A] and experimental data [B] (Litvak et al., 2001, reprinted with permission) showing the final discharge rate versus the initial discharge rate of different fibers in response to stimulus trains with a pulse rate of 1200 pps (grey diamonds) and 4800 pps (black stars). The 24,000 pps stimulus train was not modeled. For the simulations different fibers were used, their parameters randomly drawn from the distributions. Results are visualized by plotting the final spike rate (average rate over 140-150 ms after onset) on the ordinate vs the initial spike rate (in the epoch 10-20 ms after onset) on the abscissa. The two dotted lines in the left graph show the linear fit through the origin and the 1200 pps data (upper line) and the 4800 pps modeled data (lower line). Each point in the modeled data is based on 30 averages per fiber, 10 different fibers (every 10th fiber from 12000 to 12100) were stimulated at amplitudes of 0.85, 0.86, 0.87 and 0.88 mA.

3.5 Spike rate decrements: 250 to 10,000 pps

Discharge rate decreases were simulated and compared to recordings by Zhang et al. (2007) (figure 2.11). The spike rate decrements are plotted on the ordinate and the onset rate on the abscissa.

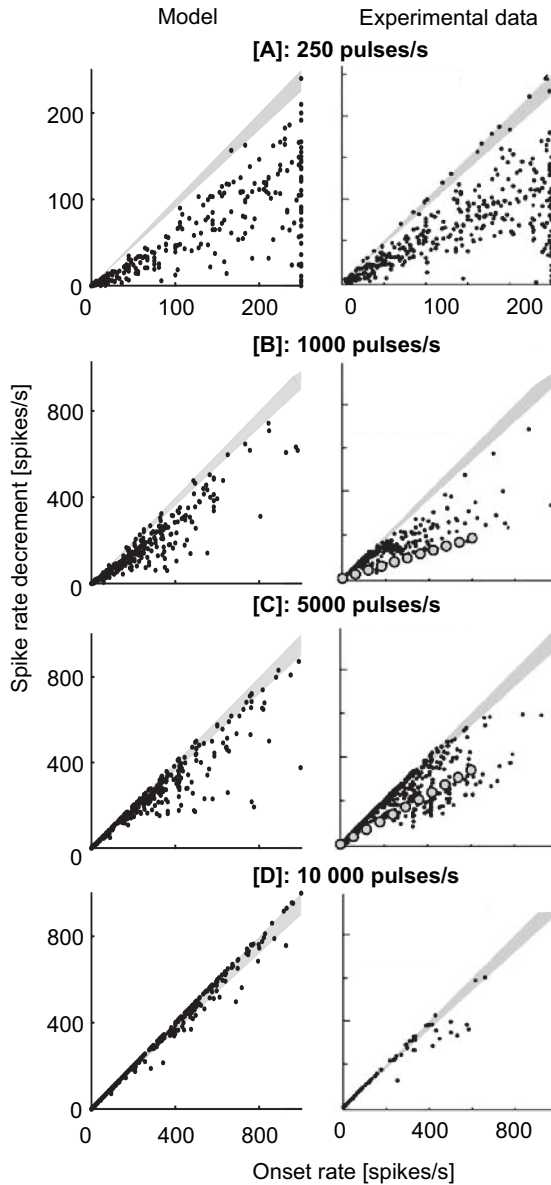


Figure 2.11. Discharge rate decreases. Modeled [A] and measured [B] (Zhang et al., 2007, reprinted with permission) rate decrements for 300 ms pulse trains with rates of 250 pps [A], 1000 pps [B], 5000 pps [C] and 10000 pps [D]. Results are visualized by plotting the final spike rate (average rate over 200-300 ms after onset) on the ordinate vs the initial spike rate (in the epoch 0-12 ms after onset) on the abscissa. The gray areas indicate a rate decrement of 90% or more of the initial discharge rate, thus very strong adapters. The gray circles in the animal data plotted at 1000 and 5000 Hz are the average rate decrements for the fiber evaluated by Litvak et al (Litvak et al., 2001) at 1200 and 4800 Hz respectively. For the simulations 30 trials were done for forty different fibers (every 10th fiber from 12000 to 12400) of which the parameters were drawn randomly from the normal distributions. Amplitudes used were 0.3 to 0.9 with a step size of 0.02 mA.

With increasing pulse rate there was an increase in adaptation and the spike rate decrements got closer to the initial spike rate. This was seen in both the simulations and the experiments. The average spike rate decrements for pulse trains with a rate of 250 pps were approximately half of the initial discharge rate. At a stimulus rate of 1000 pps, the average discharge rate decrements were higher, especially when the initial discharge rates were low. With a stimulus pulse train of 5000 pps, the rate decrement for trains with an initial discharge rate of up to about 250 pps was equal to the initial discharge rate. With stimulation of 10,000 pps there was almost complete adaptation for nearly all initial discharge rates. At all rates there was a deviation from the mean due to the variability of the model parameters. This variability in rate decrements was similar in the model and the animal experiments.

3.6 Whole nerve simulations

In figure 2.12, both the deterministic single pulse thresholds and the final discharge rates are plotted. In light grey (left y-axis) the average discharge rate per nerve fiber is shown, and the dark lines (right y-axis) indicate the deterministic single pulse thresholds. The discharge rates are averaged over the response to 200 ms stimulation. Every ten neighboring fibers have the same deterministic single pulse thresholds but different stochastic and temporal properties. Fibers with low thresholds had high firing rates and those with high thresholds had low firing rates. There was a large variability in discharge rates at fibers with the same deterministic single pulse thresholds due to their different properties. The deterministic single pulse threshold distribution had a strong effect on the final firing patterns.

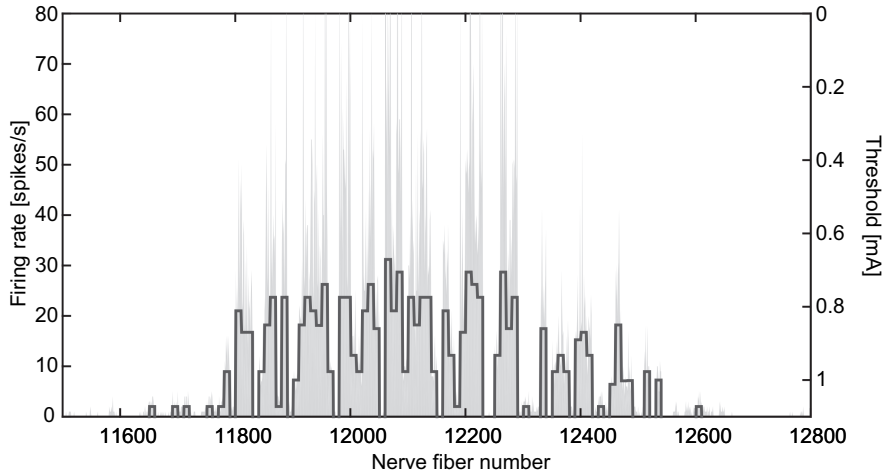


Figure 2.12. Whole nerve stimulation. 200 ms stimulation at electrode 8 with a rate of 2000 pps and an amplitude of 0.85 mA. Light gray (left y-axis) shows the average discharge rate per nerve fiber. Some fibers fire with very high pulse rates, up to 200 pps, not shown in this figure. The dark lines (right y-axis) indicate the deterministic single pulse thresholds as obtained from the 3D active nerve fiber model. Only the stimulated fibers, fiber 11500 to 12800, are shown.

Figure 2.13A shows the spike pattern of the stimulated region of the nerve in response to a pulse train with large stimulation amplitude. Figure 2.13B shows a color-coded plot of the number of spikes in bins of 25 fibers and 7 ms. Figure 2.13C shows the number of spikes in similar bins divided by the number of spikes in the first bin for every fiber. The figure shows that the fibers at the edges of the stimulated region adapted more strongly than the fibers in the center of the stimulated region.

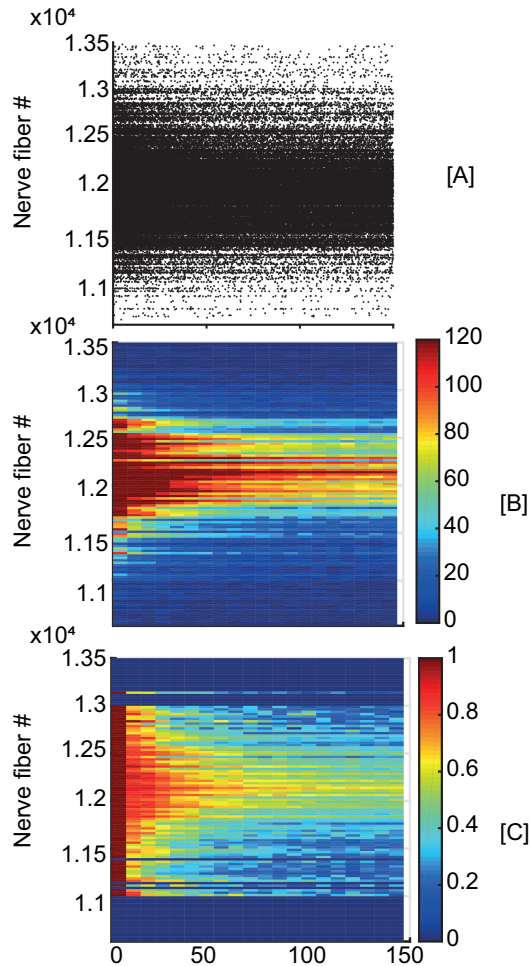


Figure 2.13. Location dependent adaptation. Nerve firing in response to a loud (1.4 mA) 150 ms pulse train with a rate of 5000 pps presented to electrode 8. Nerve fibers shown are 10500 to 13500, the center of nerve fibers stimulated by this pulse train. [A] spike raster plot showing a black dot every time a nerve fiber fires. [B] integrated nerve firing over windows of 25 fibers and 7 ms. Red indicates largest amount of firing per integration window, blue indicates no firing. The colors in the colorbar indicate the number of spikes in each bin. [C] The normalized firing in the integration window. In every window the firing is divided by the numbers of fibers firing in the window immediately after pulse train onset for those 25 fibers. For the normalization only fibers were taken that had more than 15 spikes in the initial bin. Where the initial numbers of firings in that bin were larger than 15, the normalized onset firing is equal to 1, here indicated in red. The colors in the colorbar indicate the normalized number of spikes in each bin.

4 Discussion

The model described in this paper is the first to combine a detailed geometric distribution of nerve fibers with stochasticity, refractoriness, adaptation and accommodation. It accurately simulates spike timings in response to long duration pulse trains as observed in a variety of animal experiments. Most models predicting auditory nerve responses to electrical pulse trains are single node models or include a homogeneous spread of the current. The model presented here includes a realistic 3D volume conduction model and thresholds of 32000 nerve fibers calculated with an active nerve cable model. To accurately predict temporal behavior in response to long duration pulse trains the model includes long term temporal parameters. Whilst most temporal models of auditory nerve responses to electrical stimulation include refractoriness, the inclusion of adaptation is less frequently reported (Negm and Bruce, 2008; Woo et al., 2009), and we are the first to publish a model that also includes an accommodation component. The presented model is shown to predict the auditory nerve responses to constant amplitude, long duration, and high-rate pulse trains. The ranges of discharge rate I/O curves, PSTHs, IHS, and rate decrements measured in animal experiments were all very similar to predictions done using the proposed model. Because of the extensiveness of the presented model in as well the spatial as the temporal domain, it can be used to evaluate whole nerve responses to pulse trains. Initial results show remarkable effects of cochlear position on temporal behavior. Because of the efficient implementation of temporal behavior, whole auditory nerve responses to long duration pulse trains, and thus different CI sound coding strategies, can be obtained.

4.1 Model parameters

The exemplary single fiber data could all be replicated by choosing the average model parameters. Replication of these fibers' responses could be improved by searching for a specific parameter set within the distribution of model parameters for the unique fibers. Group data was simulated by randomly choosing fibers from the whole nerve, which yielded similar distributions of fiber responses as seen in animal data. The model is validated by comparison with data obtained from experiments in cats. SFAP measurements are the most suitable measurement to compare predicted spike timings because SFAP is a direct measure of neural activity. A difficulty in the interpretation of SFAP measurements is that the exact measurement position relative to the nerve and stimulating electrode is unknown. As different CIs are used in the animal experiments and some details about the stimulation, such as voltage compliance and distance of the fiber from the electrode, are unknown, the absolute amplitude values are not comparable to the amplitudes used in the simulations. In addition, sometimes only the unexpected recordings of single fibers are presented in papers, making it difficult to derive model parameters for a model of the whole nerve. In the model presented here the distribution of fiber characteristics is assumed to be independent of the location of the nerve fiber along the basilar membrane. However, it is known that the fiber diameter varies with position along the basilar membrane and is related to some of the fiber properties

described by parameters in our model (Liberman and Oliver, 1984; Verveen, 1962). As suggested by Woo et al. (2010), greater rate adaptation may be associated with smaller auditory nerve fiber diameter. This suggestion is based on the observation by Zhang et al. (2007) that strong adapters have higher thresholds. As fibers with larger diameters are mainly located towards the cochlear apex, this could be approximated by implementing a cochlear location-dependent adaptation in the model. Dependency of nerve fiber parameters on cochlear position could be implemented in a further refinement of the model. Other difficulties in the interpretation of animal data arise since averaged data is obtained using a variable, and not always exactly reported, number of trials; Litvak used 20-40 trials per data point (Litvak et al., 2001), and Miller and Zhang used 30 to 100 of trials per point (Miller et al., 2008; Zhang et al., 2007). Due to the complexity of obtaining SFAP measurements, statistical sampling is limited (Woo et al., 2010). The SFAP measurements are all obtained from cat auditory nerve fibers, which are morphologically and physiologically different from human auditory nerve fibers, for instance in diameters and myelination (Liu et al., 2015; Paintal, 1966; Spoenclin and Schrott, 1989). It would be preferable to relate model output to human data, as for instance human ECAPs. Because the model presented in this paper encompasses the whole nerve, ECAP measurements can theoretically be simulated. The pattern of the ECAP depends on the interplay of the spatial distribution and the different temporal and stochastic components in the model. In a follow-up study the model parameters could be optimized for the human auditory nerve by simulating the ECAP in response to pulse trains. The SFAP data in the animal experiments used for the validation was obtained in acutely deafened animals, whereas duration of deafness affects the neural responses (L. F. Heffer et al., 2010; Ramekers et al., 2015). It would be interesting to use the proposed model to simulate full nerve ECAP responses as well as partial nerve ECAP responses to test the theoretical effect of neural degeneration on ECAP measurements.

Stochasticity

Stochasticity is implemented in various parts of the model; by using a stochastic distribution of thresholds over all nerve fibers, a threshold variability, an internal variability of the refractoriness and a distribution of model parameters over the fibers. Figure 2.12 shows that initial thresholds have a strong effect on overall discharge rates in responses to long duration pulse trains. The stochastic distribution of thresholds thus causes a nonhomogeneous distribution of firing rates over nerve fibers in response to continuous pulse trains. As previously shown by Bruce et al. (1999a, 1999b), RS is an essential model parameter to obtain I/O curves similar to animal data in response to electrical pulse trains. Bruce's model predicts smooth I/O curves, whereas animal data show rather rocky increases of discharge rates with stimulus intensity. We hypothesized that this rocky slope is a consequence of internal stochasticity. Our model used a similar approach as Bruce et al, but also implemented internal variations of refractoriness, and as expected produced rocky I/O curves. It is known from the literature that the RS depends on time since the last action potential (Imennov and Rubinstein, 2009; Matsuoka et al., 2001). The effect of such a dependency could be investigated by inclusion in a future version of the model. We

expect that this would lead to larger discharge rate variability at higher stimulation rates, and perhaps lead to a lower predicted detection thresholds as was shown by Badenhorst et al. (2015). In neurons there is also a stochasticity in the arrival times of the spikes, referred to as jitter. The proposed model is specified at fiber level and conduction times are neglected. Latencies and jitter can be implemented using a phenomenological approach for a complete fiber, similar to proposed by Hamacher et al., chapter 3.5.3 (Hamacher, 2004). The lowest latencies and jitter occur with the highest stimulation amplitudes. The model could be refined by introducing a stochastic delay (latency with jitter), depending on amplitude of stimulation. Alternatively, jitter in the nodes of Ranvier could be picked up in a future refinement of the biophysical model.

Refractoriness

The effects of refractoriness interplay with the effects of accommodation and adaptation. The effects of refractoriness are mostly visible at short time scales, for instance in onset rates and initial rate decrements. Miller et al. (2008) suggested that the shape of the IHS are determined mostly by refractory properties. Larger refractory parameters in the model lead to larger inter-spike intervals in the IH. Our model shows very similar peak heights and timing in the IHS as the experimental data, supporting that the choice of refractoriness are realistic values. In the interval histograms it was observed that the double peak at onset, which is present in the animal data when stimulated with the 5000 pps pulse train, was missing in the simulations. Zhang et al saw these responses in 27% of the fibers stimulated with these rates and amplitudes. They hypothesize is that it is related to the combined effects of refractoriness and rapid adaptation. Our model does not predict these double peaks, it is thus an unexpected artefact of the model; parameters as included in the proposed model do not explain this variable.

Adaptation and accommodation

The steepness of the slopes in figure 2.5 predicted by the model were more similar to the animal data published by Dynes et al. (1996) than predictions previously modeled by Bruce et al. A difference between this model and the model presented here is the inclusion of adaptation in our model, which results in a shallower slope. The accommodation effect is not prominent in the discharge rate I/O curves in figure 2.5, probably because only low rates, up to 800 Hz were used. The rate decreases in the calculated PSTHs in figure 2.8 were very similar to those obtained in animals by Zhang et al. (2007) for the different rates and amplitudes. These rate decreases occur both initially, mostly due to refractoriness, and at later time scales (up to 100 ms) mostly due to adaptation and accommodation. The accommodation effect is visible in the PSTHs in figure 2.8, where adaptation is stronger with increasing stimulus rate. The PSTHs published by Zhang et al. (2007) were modeled previously by Woo et al. (2010), who also demonstrated an effect of electrode position on rate adaptation. In the simulations the same fiber was used for all four different rates. In the experiments, the fiber stimulated with the highest pulse rate was another fiber. Despite of a larger stimulus amplitude used here, this fiber still shows a stronger adaptation than at lower rates. This can be easily simulated by modeling the fiber stimulated with 10,000

pps off-center of stimulation. The difference between the middle and last epoch in the IHS in figure 2.9 is due to adaptation. The IHS showed rate-dependent adaptation, as the rate decrease from the second to the last epoch was largest when stimulated with the highest rate pulse trains.

The range of spike rate decrements for nerve fibers in response to different rate pulse trains predicted by the model's parameters are similar to ranges of measured decrements as can be seen in figures 2.10 and 2.11. The rate decrement data in figures 2.10 and 2.11 for different fibers exhibited a very similar dependency on pulse rate in the model and in animal experiments. The rate decrements for both pulse rates shown in figure 2.10 were somewhat stronger in our model than in Litvak's data, matching the study published by Miller et al. (2008) in which the group data showed slightly stronger adaptation (figure 2.11). The spread in rate decrements observed by Litvak and Miller et al. was similar to the spread in rate decrements predicted by our model. The spread in decrements in the model is a consequence of the implemented distribution of refractory and adaptation parameters over nerve fibers. The simulations of rate decrements fairly closely matched the animal data up to 10000 Hz. However, at the 24.000 pps stimulation rate our model predicted complete adaptation, which was not observed in animal experiments, as seen in figure 2.10B. Maximal adaptation could be a consequence of saturation of the underlying physiological system, for instance an external Potassium concentration decaying over time (Woo et al., 2009). The animal data show that saturation of the adaptation occurs over time with rates as high as 24 kpps. There would be several options to modify the parameters in order to have the adaptation at 24kpps fit with the physiological data. A simple option would be to include a maximum value for adaptation. However it would also be likely that there is a gradual decrease in the increase of adaptation with rate. We have chosen not to implement a saturation as to our knowledge this is the only experiment available at this rate. To investigate which one is more closely related to the biological situation more data at high rate electrical stimulation is needed.

The time constant in the current model is assumed to be similar for both accommodation and adaptation. However, from a biological perspective it would be reasonable to assume that these different processes decay with different time constants. Accommodation depends mostly on the stimulus itself and could be affected by stimulus shape, but no data has been published yet regarding the effect of stimulus shape on accommodation in auditory nerves. To find the correct dependencies of accommodation parameters on pulse shapes and to validate models, more animal experiments data including longer stimulus durations and a larger variance of stimulus rates and amplitudes are required. In modern neuroscience the origin and relevance of accommodation, sometimes referred to as sub-threshold adaptation or stimulus-specific adaptation, is subject of discussion. A proposed model relates voltage activated K^+ -current to input-dependent adaptation, whereas calcium activated K^+ -currents were related to spiking dependent adaptation (Prescott and Sejnowski, 2008). It has been proposed in a model study by Negm and Bruce that stimulus dependent adaptation is caused by hyperpolarization-activated cation

channels (Negm and Bruce, 2014). Woo et al show that the implementation of a changing external potassium concentration based on K⁺ activity in a biophysical model leads to rate-adaptation as seen in the animal data (Woo et al., 2009).

Facilitation

The experimental PSTHs in figure 2.8B show an overall increase in discharge rate at 5000 pps relative to lower stimulation rates. There is evidence in the literature that, in chronic deafened animals, this facilitation plays a role when the fiber is stimulated by pulse trains with rates of approximately 2000 Hz and low amplitudes, when it evokes low onset spike probabilities (L. F. Heffer et al., 2010). There is a large spread in the effect, and its exact dependency on pulse train characteristics such as rate and amplitude level is yet to be investigated more thoroughly in animal experiments. Because the effect is seemingly only related to a narrow distribution of pulse rates and amplitudes and is not yet very well understood, we have chosen not to include facilitation in the model, consequently the model's predictions deviate from the animal SFAP data where the effect of facilitation is seen.

Whole nerve simulation

Since the deterministic single pulse threshold distribution has a large effect on final firing patterns, as shown in figure 2.12, it is of importance to include an accurate and realistic 3D volume conduction model. The 3D volume conduction model that we have incorporated includes a cochlear anatomy derived from μ CT data and contains a realistic spatial distribution of spiral ganglion cells throughout Rosenthal's canal (Kalkman et al., 2015). The electrical conductivities of the model structures were mainly obtained from literature (Briaire and Frijns, 2000); the conductivity values of temporal bone and the cochlear modiolus were obtained by an optimization process that was based on comparing intracochlear potential recordings from CI subjects to simulated values in subject-specific models (Kalkman et al., 2014). The model has been shown to accurately predict or describe loudness balancing curves in current steering (Frijns et al., 2009; Snel-Bongers et al., 2013) as well as loudness growth curves for different types of multipolar stimulation (Kalkman et al., 2015). This paper demonstrates that spike rate adaptation is dependent on spatial location relative to the current source. Relative rate decreases, and thus the amount of adaptation, is largest at the borders of the stimulated area. Adaptation is expected to be related to phase-locking of amplitude modulated input. Increased adaptation at the borders of the stimulated area could thus lead to stronger perception of pitch at borders of the stimulated region. It was suggested by Laneau et al. (2004) that the center of the activated region are most important for pitch perception. A previous modeling study showed that cochlear location of nerve fibers influences initial activation site on the fiber (Westen et al., 2011). The fibers located in the center of stimulation receive larger stimulus amplitudes, which has an effect on the initial location of firing. To test relative contributions of center and off-center fibers to place and rate-pitch perception the modeled auditory nerve response to amplitude modulated pulse trains should be evaluated in a follow-up study. The temporal behavior of the nerve is co-influenced by

the amplitude of stimulation, and thus by electrode position, as shown in a modeling study by Mino et al. (2004). Nerve morphology will affect the outcome of cochlear implant stimulation and has an important role in the interplay of spatial and temporal effects. To take the effects of the nerve's geometry in account and considering the strong effect of initial thresholds on long term nerve activation it is important to include both realistic spatial and temporal effects in a comprehensive model.

Future directions

Since the model incorporates detailed effects in both the temporal and the spatial domain it can be used to predict auditory nerve responses to CI stimulation. Contemporary cochlear implants use amplitude modulated input to convey important speech information in cochlear implants. Validation for amplitude modulated pulse trains as inputs has also been done and will be presented in a follow-up paper. Another interesting aspect is the neural behavior at much longer time scales, such as minutes. Modelling the adaptation as a power-law gives, as shown for the acoustically stimulated auditory nerve by work of Zilany et al. (Zilany et al., 2009; Zilany and Carney, 2010), a more realistic prediction of the neural behavior after longer durations of stimulation. An interesting future direction is to investigate power-law functions for prediction of auditory neural responses to electrical stimulation. As stated above, the model can be used to predict ECAP responses to pulse trains and compare those to data obtained directly from measurements in human. This output can be related to the stochastic, refractory, and adapting effects included in the model, and their interplay with the auditory nerve's morphology. Because this model is precise in the geometrical definition, and contrarily to most other models includes as well accommodation as adaptation, it is applicable to predict whole nerve responses. Ultimately the model can be used to predict complete neural spiking patterns in response to CI stimulation using different stimulation strategies. The conservation of temporal and spatial information present in the pulse train at the stage of neural activation can be evaluated. Because of the efficient implementation of spatial and temporal components, the model can easily be used to evaluate whole nerve responses to long duration sound segments. This can facilitate comparison of whole nerve responses to many different input signals, such as varying in amplitude, amplitude modulation, pre-processing, and coding strategies.

Inputs as used in perceptual patient testing such as minimal detection and identification tests can be used in the model. Comparison of simulated auditory nerve responses to perceptual data obtained from cochlear implant users will aid in the interpretation of the produced spiking patterns. As a next step an interpretation model of the spiking patterns in relation to the psychophysical perception of CI users will be built. Such an interpretation model could be used to evaluate complete auditory nerve responses to different sound coding strategies.

Conclusion

A model was developed that accurately predicts auditory nerve responses to long duration CI stimulation with a wide range of stimulus rates and amplitudes. The model is very well defined in the spatial domain and is temporally and stochastically extended. The model's responses were in good agreement with animal data for continuous long duration pulse trains. The model accurately predicts discharge rate I/O curves, PSTHs, IHS, spike rate decrements, and their variances for realistically located auditory nerves stimulated with a wide range of amplitudes and rates. The broad implementation of stochastic behavior results in predictions of variances of measures comparable to those seen in animal data. By combining spatial details with long-term temporal components and a broad implementation of stochasticity, a comprehensive model is developed. It is validated for long duration electric stimulation of a wide range of input parameters and that can be used to evaluate auditory nerve responses to cochlear implant sound coding strategies.

CHAPTER 3

Modeled auditory nerve responses to amplitude modulated cochlear implant stimulation

Margriet J. van Gendt

Jeroen J. Briaire

Randy K. Kalkman

Johan H.M. Frijns

Abstract

Cochlear implants encode speech information by stimulating the auditory nerve with amplitude-modulated pulse trains. A computer model of the auditory nerve's response to electrical stimulation can be used to evaluate different approaches to improving CI patients' perception. In this paper a computationally efficient stochastic and adaptive auditory nerve model was used to investigate full nerve responses to amplitude-modulated electrical pulse trains. The model was validated for nerve responses to AM pulse trains via comparison with animal data. The influence of different parameters, such as adaptation and stochasticity, on long-term adaptation and modulation-following behavior was investigated. Responses to pulse trains with different pulse amplitudes, amplitude modulation frequencies, and modulation depths were modeled. Rate responses as well as period histograms, Vector Strength and the fundamental frequency were characterized in different time bins. The response alterations, including frequency following behavior, observed over the stimulus duration were similar to those seen in animal experiments. The tested model can be used to predict complete nerve responses to arbitrary input, and thus to different sound coding strategies.

1 Introduction

To optimally encode speech and music, cochlear implants (CIs) must transfer cues including pitch, loudness, and fine-structure. A person's ability to perceive temporal fine structure correlates with music appreciation and speech understanding, especially in noisy environments (Lorenzi et al., 2006). In patients with CIs, modulation detection thresholds (MDTs) and temporal modulation transfer function (TMTF) are related to the attained temporal resolution, and thus to speech understanding and sound quality (Fu, 2002; Shannon, 1992; Won et al., 2011). Sound coding strategies should aim for maximal transfer of temporal information from amplitude-modulated input. In addition to testing in animals and human subjects such coding strategies can be evaluated using computational models.

A comprehensive computational model of auditory nerve responses to electrical pulse trains has been developed in our group (van Gendt et al., 2016). It can correctly predict the distribution of single-fiber responses to constant-amplitude pulse trains. This model incorporates spatial and pulse shape effects, as well as temporal and stochastic effects. Pulse shape effects are incorporated in the model by the use of a conductance-based 3D model, which is coupled to a biophysical neural model to calculate the deterministic threshold. Temporal effects are influenced through the threshold, but no direct relationship between pulse shape and temporal effects is incorporated in the model. Temporal effects include short-term refractoriness, and the long-term history effects of adaptation and accommodation. The model is computationally efficient and can predict full nerve responses to long-duration pulse trains. Validation of this model was based on experimental measurement of single-fiber action potential (SFAP) responses to constant-amplitude high-rate pulse trains published in the literature by qualitative comparison with modeled responses. As a follow-up to the previous validation of responses to constant-amplitude pulse trains, in the current study, we investigate the model's response to amplitude-modulated input. We compare the nerve's predicted responses to amplitude-modulated input to experimental animal single-fiber data.

Modern CI sound processing strategies, such as CIS, encode sounds' temporal envelope through amplitude modulation (AM) of the stimulating pulse train. In this process, most information necessary for pitch perception from firing rate is lost due to envelope extraction. In normal hearing, loudness is encoded by the number of fibers firing and their firing rates. Such loudness cues are important in sound perception (Fletcher and Munson, 1933). In electrical hearing, the dynamic range is severely degraded. The smaller dynamic range necessitates compression of temporal amplitude modulations, which are required for speech understanding and for appreciation of musical loudness variations.

The proposed model was validated by comparison with previously published SFAP measures obtained in animal experiments in response to amplitude modulated pulse trains. SFAP measurements are a precise tool for investigating different nerve fiber

responses and their variances. A properly validated neural model of long-term CI stimulation should adequately predict SFAP responses to continuous amplitude pulse trains. To predict effects of sound coding strategies relevant for CI processing, the model should also correctly simulate temporal envelope variations. Such a model should be further validated by comparison of the model's responses to amplitude-modulated pulse trains with physiological data. Several experimental studies have directly recorded animal auditory nerve responses to amplitude-modulated pulse trains (Hu et al., 2010; Litvak et al., 2001, 2003a). Hu et al. (2010) used 5000-pps pulse trains of 400-ms duration, modulated with a frequency of 100 Hz and a 10% modulation depth. They used the post stimulus time histograms (PSTHs) and interval histograms (IHs) obtained from SFAP measurements to relate the SFAP responses to the input. Litvak et al. (2001) stimulated the auditory nerve using pulse trains with a 4800-Hz rate and different amplitudes. The pulse trains were modulated only in the last part of the signal, with a modulation frequency of 400 Hz and modulation depths of 1% and 10%. Litvak et al. (2003b) stimulated cat auditory nerve fibers with 5000-pps pulse trains of up to 10 minutes in duration, which were amplitude modulated with different depths (0.5–10%) and frequencies (104–833 Hz) over the pulse train duration. They demonstrated that the use of high-rate pulse trains improved the temporal representation of sinusoidal modulation. Rubinstein et al. (1999) previously showed that a high-rate pulse train would cause de-synchronization of auditory nerve firing in a biophysical population model, thereby increasing the dynamic range and improving AM representation. If loudness is encoded by synchronization of firing of a group of fibers, a desynchronized fiber bundle would be able to slowly increase its synchrony and thus the loudness with stimulus level. Fibers showed varying responses to high-rate amplitude-modulated pulse trains. The sensitivity to modulations varied among fibers and modulation frequencies.

Different types of models are available to predict nerve responses to electrical stimulation. A major distinction can be made between the biophysical and phenomenological type of models. Biophysical models quantitatively describe nerve membrane behavior in response to an induced membrane current and have been shown to correctly predict membrane responses to single pulses and reasonably predict latencies, refraction, and facilitation effects (Frijns et al., 1994; Frijns and ten Kate, 1994; Reilly et al., 1985; Schwarz and Eikhof, 1987). These models can be combined with 3D volume conduction models of the cochlea to predict auditory nerve responses to electrical pulses as reported by Kalkman et al. (2015). Phenomenological models directly relate empirical observations to expected neural output. Such models have been used to efficiently predict responses to sustained stimulation by direct implementation of stochastic and temporal behavior (Bruce et al., 1999a, 1999b; Chen and Zhang, 2007; Goldwyn et al., 2010b; Litvak et al., 2003a; Macherey et al., 2007; Stocks et al., 2002; Xu and Collins, 2007). An overview of phenomenological auditory nerve models and their responses to constant amplitude pulse trains is given by Takanen et al. (2016).

A biophysical neural model study by Yang and Woo (2015) investigated the effect of different parameters on the amplitude modulation following behavior and reported that with increased axon diameter the Vector Strength (VS) and fundamental frequency (F_0), or transfer of fine temporal information, improves. Another biophysical model of a population of auditory nerve fibers has been used to simulate modulation detection discrimination in patients (O'Brien et al., 2016). It can predict modulation detection thresholds (MDTs) in CI users, and how they are related to stimulus intensity and carrier rate. For the population measures several hundreds of fibers are simulated. The human auditory nerve consists of around 30.000 fibers, therefore modeling the complete nerve's response using a biophysical population model requires a tremendous amount of computational power. Phenomenological models have also been used to calculate responses to amplitude modulated electrical input (Campbell et al., 2012; Chen and Zhang, 2007; Goldwyn et al., 2010b; Xu and Collins, 2007). Goldwyn et al. used a phenomenological approach to a single fiber, a point process analysis, to characterize neural responses to constant amplitude and amplitude modulated pulse trains (Goldwyn et al., 2012, 2010b). Their model included a variety of phenomena, including facilitation and jitter. They showed interval distributions of spikes and VS in response to amplitude modulated pulse trains with varying modulation depths and carrier rates qualitatively similar to experimental data. Campbell et al. (2012) used a phenomenological approach, and included longer temporal components to model responses to modulated input. In the current study a combined biophysical and phenomenological approach is used (van Gendt et al., 2016) to simulate complete auditory nerve responses to modulated inputs in a computationally efficient manner. The model presented in this paper builds on the previously published 3D volume conduction model of the cochlea and deterministic cable model of the human auditory nerve with active GSEF nerve fibers (Briaire and Frijns, 2005; Frijns et al., 2000; Kalkman et al., 2015). The deterministic thresholds obtained with that model are extended with stochastic behavior and history effects.

We investigated phase-locking and frequency-following behavior using post-stimulus time histograms (PSTH), period histograms (PH), inter-spike interval distributions (ISI), vector strength (VS), and amplitudes of the fundamental frequency (F_0). We will present the comparison between model simulations and experimental data in the results section, followed by our interpretation and analysis of the similarities and differences between simulations and data in terms of model parameters in the discussion section.

2 Materials and methods

2.1 Model

To calculate the deterministic nerve fiber thresholds at 3200 individual nerve fiber trajectories, we used the 3D volume conduction model and active nerve fiber model developed in the LUMC (Kalkman et al., 2015, 2014). This model was then extended with stochasticity, adaptation, and accommodation, and 10 different nerve fibers were introduced at each of the spatially different trajectories. Thus, the model effectively incorporated a total of 32,000 different auditory nerve fibers. Each nerve fiber's deterministic threshold was manipulated with stochasticity, and every nerve fiber was modeled with temporal characteristics. I_{det} was calculated using 3D volume conduction simulations and deterministic nerve model. Using the RS, the spiking probability can be calculated using a phenomenological approach, similar to Bruce et al. (1999b). After each pulse, the stochastic threshold was obtained from the normal distribution, $N(I_{det,SD})$. For each nerve fiber, stochasticity was induced by adding a standard deviation to the deterministic thresholds, which is obtained with the relative spread (RS) as in equation 3.1;

$$\text{Relative spread: } \sigma = I_{det} \cdot RS \quad (\text{Eq. 3.1})$$

To account for refractoriness these stochastic thresholds were elevated depending on the time since the last spike relative to refractory period as in equation 3.2;

$$\text{Refractoriness: } R = \frac{1}{1 - e^{-\frac{(t - \tau_{ARP})}{\tau_{RRP}}}} \quad (\text{Eq. 3.2}),$$

where τ_{ARP} and τ_{RRP} are the time constants for the absolute and relative refractory period, and t is the time since the last action potential. The model includes both firing-dependent adaptation and stimulus-dependent adaptation, with the latter referred to as accommodation. Spike adaptation (SA) was included by increasing the threshold after each spike (eq 3.3) and accommodation by increasing the threshold after each pulse (eq 3.4).

$$\text{Spike Adaptation: } SA = \sum_i \text{ampl}_{adap} \cdot e^{\frac{t - t_i}{\tau_{adap}}} \quad (\text{Eq. 3.3})$$

$$\text{Accommodation: } Acco = \sum_p 0.03\% \cdot I \cdot \frac{I_{\min}(\text{electrode})}{I(\text{electrode, fiber})} \cdot e^{\frac{t - t_p}{\tau_{adap}}} \quad (\text{Eq. 3.4})$$

$$\text{Total model: } I_{adj} = N(I_{det}, \sigma) \cdot R + SA + Acco \quad (\text{Eq. 3.5})$$

A spike was assumed to occur when: $I_{given} > I_{adj}$, where I_{given} is the stimulus current.

For each fiber, the stochastic and temporal parameters were randomly chosen from a pre-defined normal distribution, ensuring a random distribution of neural properties over the different trajectories. The parameters were obtained from measurements of the SFAP (Bruce et al., 1999b; Javel et al., 1987; Miller et al., 1999a) and by model fitting as described

in the previous paper (van Gendt et al., 2016). An overview of the parameters is given in table 3.1;

Table 3.1. Overview of parameters in the model

Parameter	Value (\pm SD)
RS	0.06 (\pm 0.04)
τ_{ARP}	0.4 (\pm 0.1) ms
τ_{RRP}	0.8 (\pm 0.5) ms
Within refractoriness stochasticity	5% of τ_{ARP} / τ_{RRP}
Adaptation amplitude	1.0% (\pm 0.6%) of threshold
Accommodation amplitude	0.03% of stimulus current · spatial factor
τ_{adap}	100 ms

Deterministic thresholds were obtained for specific pulse shapes and pulse widths. In the current paper biphasic pulses with pulse widths per phase of 18 μ s were used. Details of the model are described in a previous publication (van Gendt et al., 2016). The extended temporal and stochastic model was developed in Matlab (Mathworks, Inc.), the code is available from the authors upon request.

2.2 Experiments

To validate the model, we compared its predicted responses to amplitude-modulated pulse trains to the neural responses from similar pulse trains in experiments performed in cats by Litvak et al. (2001, 2003a) and Hu et al. (2010). We selected the durations, pulse rates, modulation frequencies and depths, and relative amplitudes according to the set-ups in the published animal experiments. Here we report the following output measures: post-stimulus time histograms (PSTH), period histograms (PH), vector strengths (VS), fundamental frequency (F_0) amplitudes, and inter-spike interval histograms (IH). All simulations were done by stimulating the electrode located at roughly 175 degrees from the round window. For the simulations of a single fiber, the neuron with the index 12000 was used; fibers are counted from base to apex. This fiber is located roughly at the same angle, close to the center of the stimulated electrode. For the group simulations, 80 different fibers evenly distributed over different spatial locations within the area stimulated by electrode 8 were simulated. In the complete model, the exact fiber thresholds were influenced by the pulse width of the stimulus train, because the exact stimulus shapes were used as inputs to the 3D conduction and biophysical model. The thus calculated deterministic thresholds were used in the temporal and stochastic part of the model. It was assumed that the temporal and stochastic properties of the model's threshold value were independent of the pulse width, which was set at 18 μ s for all simulations. Biphasic pulses with no inter-phase gap were used. The pulse width affects threshold; the absolute threshold value is therefore not directly comparable to animal data. The exact distance from stimulating electrode to the measured fiber is also not known in animal data, therefore exact amplitude levels are also not comparable. Furthermore, the parameters for

the temporal effects in the presented model are independent of pulse width; a different pulse width would change the threshold, but not the relative amplitude difference related to the temporal effects. The difference in pulse width between animal experiments and modeled responses is therefore not relevant. For the presented multiple-fiber data, the model parameters were set to the values shown in table 3.1. For the comparison with experimental single-fiber data, the simulations were obtained using average model parameters, unless otherwise noted. When statistical analysis was performed simulated results were compared with experimental data obtained by visual inspection of high-resolution graphs, as were received upon request from the authors.

2.2.1 Effect of stimulus amplitude

To mimic the experiments performed by Hu et al. (2010), we utilized AM pulse trains of 400-ms duration, with a rate of 5000 pps. The modulated amplitude was calculated as shown in equation 3.5, where A_u is the unmodulated amplitude, $m_{\%}$ is the modulation depth in percentage and f_m is the modulation frequency.

$$A(t) = A_u + m_{\%} \cdot A_u \cdot \sin(2\pi f_m t) \quad (\text{Eq. 3.5})$$

In the experiments of Hu et al f_m was 100 Hz, and $m_{\%}$ was 10%. Most responses were evaluated in bin-widths of 50 ms. The first experiment entailed stimulation of a single fiber with two different amplitudes. To mimic this in the model, we stimulated cochlear neuron 12000 with stimulus amplitudes of 0.9 mA (supra-threshold level, causing an average spike rate of 152 spikes/sec over the duration of 400 ms) and 0.75 mA (near the single-pulse threshold level, causing an average spike rate of 44 spikes/sec over the duration of 400 ms). We performed thirty repetitions per stimulus type, and PSTHs and PHs were obtained using a 0.1-ms bin-width. Interval histograms were evaluated in 50-ms bins, resulting in the plotting of five different epochs: 0–50 ms, 50–100 ms, 150–200 ms, 250–300 ms, and 350–400 ms.

The second experiment involved simulating a fiber (again cochlear neuron 12000) with parameters set to average values (table 3.1) at stimulation amplitudes yielding initial discharge rates similar to those in the published animal experiments. Three different fibers were stimulated to obtain the animal data. The rates were based on 100 different trials, response rates were averaged over these trials. For the three different fibers to which the simulations were matched, the initial spike rates were 50, 100, 200, 250, and 350 spikes/s for one fiber; 50, 125, 325, and 400 spikes/s for the second fiber; and 160, 225, 300, 425, and 550 spikes/s for the last fiber. In the simulations, all these three fibers were modeled with average parameter settings. Output measures included discharge rates, discharge rate decreases per bin relative to the onset discharge rate, vector strength, and F_0 amplitude, which were all calculated for each of the eight bins over a duration of 400 ms. The discharge rate was calculated from the number of spikes per fiber in each bin. The degree of adaptation was determined as one minus the discharge rate relative to the rate

in the first bin. Vector strength is a measure of modulation following behavior (Goldberg and Brown, 1969), and calculated here as shown in equation 3.6:

$$VS = \frac{1}{n} \sqrt{\left[\sum \sin(\theta_i) \right]^2 + \left[\sum \cos(\theta_i) \right]^2} \quad (\text{Eq. 3.6})$$

In this equation, n is the number of spikes per analysis window, and θ_i are the spike latencies within the bin relative to the stimulus period (between 0 and 2π).

F_0 amplitude, taken as the amplitude at the modulation frequency, refers to the fundamental component of the Fourier transform. For each epoch, the response was filtered with a periodic Hann window, using the Hann function in Matlab. This was multiplied with the response (spike rate). The Fourier transform was then obtained using the `fft` function. For the Fourier transform a sampling frequency of 55540 Hz was used, matching the step-size of the model. The amplitude of the power spectrum at the modulation frequency, at Hu 100 Hz, was extracted as F_0 . For all three output measures a regression analysis was performed.

The third experiment investigated the effects of refractoriness, relative spread, and adaptation. The performed simulation was similar to the previous experiment, but with variation of the model parameters under investigation. This was done to investigate the importance of using a stochastic distribution of model parameters and to evaluate the effect of the different parameters as well as to qualitatively get an indication of sensitivity of the responses to changes in these parameter settings. To match the initial discharge rates, we applied five different stimulus amplitudes to induce 160, 225, 300, 425, and 550 spikes/s respectively. Here again cochlear fiber with index 12000 was used for the simulations. To investigate the effect of refractoriness, we repeated the calculations for one set of amplitudes with the absolute refractory period (ARP) set to 0.3 ms, and relative refractory period (RRP) set to 0.5 ms. The simulations were also performed using a relative spread value of 0.02 instead of 0.06. To investigate the effect of a lower adaptation, we decreased the adaptation amplitude from 1 to 0.6. These variations were all within one standard deviation of the model parameter's values, as shown in table 3.1.

In both the second and third experiment statistical analyses were performed on all three different measures and fibers. Normalized Root Mean Squared Error (NRMSE) was determined by calculating the RMS of the difference between modeled and experimental data and normalizing it by division with the average experimental value. Generally, a low NRMSE belongs to a relatively good fit of that dataset. To calculate R-squared (R^2) modeled data was plotted versus experimental data and a linear regression line was fitted; the regression line was forced to pass the origin. The correlation coefficient, or R , was calculated, with R^2 indicating the amount of explained variance in the predictions. R^2 of zero means no predictive value, and R^2 of one means all variance in data is explained. A repeated measure ANOVA was performed on the response rates of 2 different fibers to

five different amplitudes in 8 temporal bins. The within-subject factors in the repeated measure ANOVA are model versus measurements and the bin. The between subject factors are the stimulus amplitude and the fiber. The dependent variable is the spike rate. The RM ANOVA calculates whether there is an effect of model versus measurement and of the bin. No significant effect of model vs bin was found ($F_{9,1}=1.37$, $p=0.272$). As expected, there was a significant effect of bin ($F_{1,07,9}=47.149$, $p=0.000$). Analysis was run in SPSS.

2.2.2 Sensitivity analysis

Two different fibers were modeled with varying parameters for adaptation amplitude, accommodation amplitude and adaptation time constant. The spike rates in response to the different amplitudes and at several epochs were compared to experimental data. Adaptation amplitudes were varied from 0.0 up to 2.0 with a step size of 0.25, accommodation amplitudes from 0 to 0.06 with a step-size of 0.01, and time constants of 80, 100 and 120 ms were used.

Group data and parameter distribution

We next determined the responses of groups of fibers. Different actual fibers showed differences in discharge rates, VS, and F_0 (Hu et al., 2010; Litvak et al., 2001, 2003a); thus, it was important that the model fibers also represented these differences. The experimental data defined four different sub-groups based on the discharge rate within the first 50-ms epoch: R1 (5–150 spikes/s), R2 (150.1–270 spikes/s), R3 (270.1–400 spikes/s), and R4 (400.1–972 spikes/s). For the group simulations, 80 different fibers evenly distributed over different spatial locations within the area stimulated by electrode 8 (located 163° to 180°) from the round window) were simulated, which is of importance because of the incorporation of the detailed 3D conduction model. Simulations were repeated 30 times, and plotted results are averaged data over these trials. The parameters of each fiber were drawn randomly from the normal distribution presented in table 3.1. For each fiber in each different epoch, we calculated the discharge rate over time, vector strength, and F_0 amplitude. We also calculated the group average for each of these output measures, as was done in the paper describing the experimental results. The 80 stimulated fibers were classified in rate groups R1 to R4 according to the spike rate in the initial epoch. As above, the NRMSE and the correlation coefficient R^2 were calculated over the average results in the groups per output measure.

Effects of modulation frequency and depth

Firing rates and vector strengths in response to different modulation depths were calculated, similar to Goldwyn et al (2012). Modulation depths were, similar as in Goldwyn's simulations, set to 0, 1, 2, 5, 10 and 15%. Modulation frequency was 417 Hz, stimulation rate was 5000pps. Rate and vector strength were determined over the average of 10 trials, each with a stimulus duration of 0.4 second. VS was not calculated for non-responders, which were classified by Litvak et al as fibers in which rate increased to maximally 100 spikes/sec. Both average model parameters and a manually optimized parameter set were used.

The AM experiments performed by Litvak et al. (2003) were replicated by stimulating a nerve fiber with a 5000-pps pulse train for 1 second, with amplitude modulation over the last 400 ms. For each simulation, 100 trials were performed. The utilized modulation amplitudes were 0.5, 1, 2.5, 5, and 10%, and the modulation frequencies were 104, 417, and 833 Hz. Interval histograms were obtained over the response to the modulated period of the input. For the interval histograms and period histograms, the bin-width was 0.2 ms. The model was used to replicate the experimental PHs and IHs of one fiber. These simulations were performed with all model parameters set to average. The simulations were repeated with varying values for RS and adaptation amplitude, within one standard deviation of the model, to determine whether a fiber yielding results more similar to the animal experiments existed within this distribution.

Modulation onset responses

The effect of modulation onset was simulated with a fiber with all model parameters set to average. After 50 ms of stimulation, modulation was started with a modulation frequency of 400 Hz, similar to Litvak et al. (2001). The amplitude was down-modulated, as shown in equation 3.7.

$$A(t) = A_u - 2 \cdot m_{\%} \cdot A_u \cdot \sin(2\pi f_m t) \quad (\text{Eq. 3.7})$$

such that the peak amplitude was equal in the modulated and the unmodulated portion of the stimulus. The fiber was stimulated in 30 trials over which average rates were calculated. The results are plotted in the PSTHs with a 5-ms bin-width. The first bin is not shown in the experimental results due to stimulation artefacts, and thus the first bin was also discarded in the simulated results.

Modulation Detection Thresholds

Similar to Goldwyn et al (2010) modulation detection thresholds were predicted using the Vector Strength measure. Stimuli of 400 ms were used, with a modulation frequency of 20 Hz and carrier pulse rate of 1000 Hz. VS was calculated in response to pulse trains with different stimulus levels. It was assumed the perception would be correct when VS was larger in response to the modulated than in response to the unmodulated stimulus in at least 78% of 10 trials. Spike trains with less than 3 spikes were discarded from the calculation.

3 Results

3.1 Effect of stimulus amplitude

Figure 3.1 shows the auditory nerve fiber response to modulated pulse trains of 400-ms duration and two different amplitudes, with data from animal experiments by Hu et al. (2010) shown presented side-by-side with the simulation results.

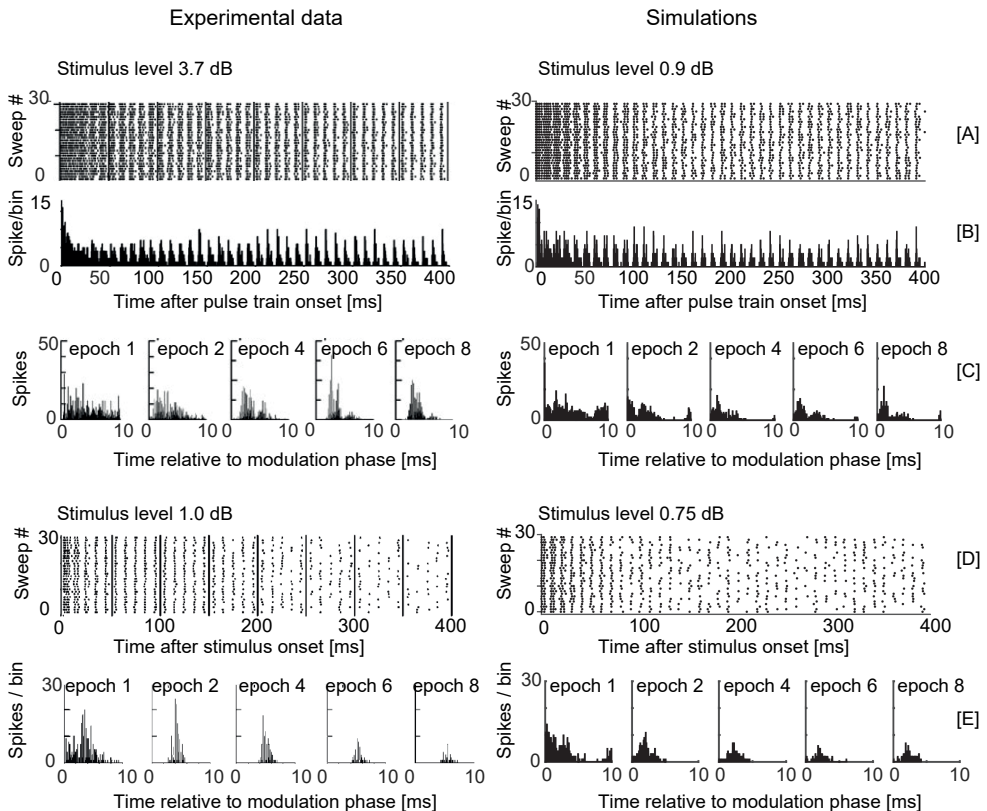


Figure 3.1. Single-fiber responses to a 400-ms 5000-pps pulse train modulated with a frequency of 100 Hz and a 10% modulation depth. The left column shows the experimental data (Hu et al., 2010) for a large stimulus amplitude (0.9 mA; [A, B, and C]) and a smaller stimulus amplitude (0.75 mA; [D and E]). The right column shows the model predictions using average model parameters. [A] spike patterns for 30 trials when stimulated with the louder pulse train. [B] corresponding post-stimulus time histograms (PSTHs) obtained in bins of 0.1 ms, averaged over 30 repetitions. [C] corresponding period histograms (PHs) in five different temporal epochs (0–50 ms, 50–100 ms, 150–200 ms, 250–300 ms, and 350–400 ms), calculated as the number of spikes per 0.1-ms bin relative to the modulation phase, averaged over 30 repetitions. [D] spike patterns for 30 trials when stimulated with the lower-amplitude pulse train. [E] corresponding PHs in the five different temporal epochs, averaged over 30 repetitions. The graphs with experimental data are adopted from the original work by Hu et al (2010), and are reprinted with permission.

For the large amplitude (0.9 mA in the simulations), spike patterns are shown for 30 repetitions (figure 3.1, row A), revealing decreased firing efficiency and increased phase-locking over time in both the animal data and model simulations. Figure 3.1 (row B) depicts the PSTH obtained from this data, showing similar decreases in spike rates and increased phase-locking, and thus increased synchrony, over time in both the animal and predicted data. Figure 3.1 (row C) shows the stimulus time histogram relative to the phase of amplitude modulation for the five different epochs. The onset of stimulation is taken as a phase zero. The amplitude modulation as calculated with equation 3.1 determines the period. The next period thus starts one modulation phase hereafter (dependent on the modulation frequency). For each spike the timing between the start of the last modulation onset phase is taken as the value that is counted in the PH. Double peaks are seen at the largest amplitudes in epochs 4 and 6 and somewhat in epoch 8 in both the experimental results and model simulations. Over the duration of stimulation, the peaks sharpen in both the simulations and animal experiments, but the peaks at later epochs are larger in the experimental data than in the simulations. In figure 3.1, rows D and E show the spike patterns for 30 repetitions obtained with the lower stimulus amplitude, near the single pulse threshold (0.75 mA in the simulations). The simulations and experimental data show spiking patterns that are similar in decrease, phase-locking, and jitter (figure 3.1, row D). Figure 3.1, row E, depicts narrowing of the phase distributions over time, as was also observed with the higher stimulus amplitude. The peak is higher in the second epoch than in the later epochs in both the experimental and animal data. Overall, however, the IHS obtained in animal experiments are more narrowly distributed and have higher peaks compared to the predicted IHS, thus showing a stronger phase-locking. The distributions are shifted towards shorter spike-timing because no spiking latency is included in the model.

Figure 3.2 shows the responses to 400-ms high-rate (5000-pps) pulse trains at different amplitudes, modulated with 100 Hz and a 10% modulation depth. Experimental results (Hu et al., 2010), and corresponding modeled data, of three different fibers in response to four or five different stimulus amplitudes are shown. For the simulations, the model parameters for each of the three fibers were set to average values, and stimulus amplitudes were chosen such that the rates in the initial bins matched the experimental data.

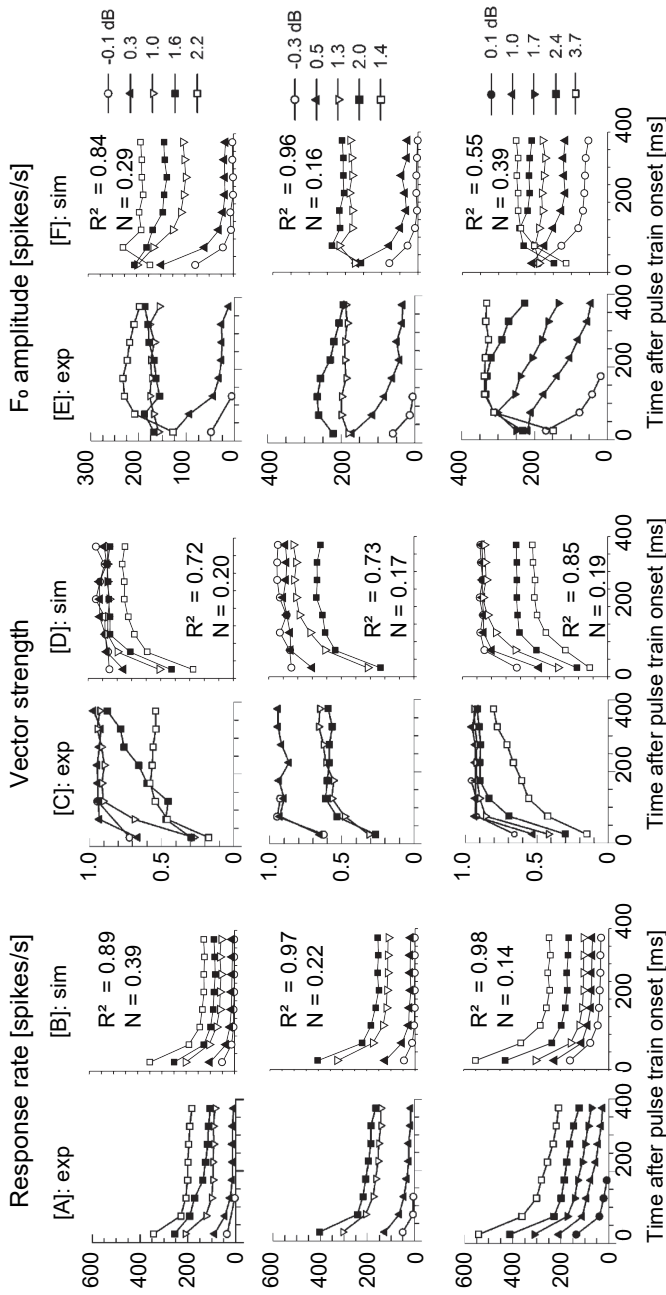


Figure 3.2. Three different fibers were stimulated at different amplitudes. [A, C and E] show results from animal experiments published by Hu et al. (2010). [B, D and F] show corresponding simulated results, with all model parameters set to average, all three fibers are modeled with the same parameters. The difference between the three simulations is thus the input amplitude. Amplitudes were chosen such that initial discharge rates corresponded with the initial discharge rates in the animal data: 50, 100, 200, 250, and 350 spikes/s in the first row; 50, 125, 325, and 400 spikes/s in the second row; and 140, 225, 300, 425, and 550 spikes/s in the last row. Results were obtained by averaging the response to 100 repetitions and calculated in bins of 50 ms. Regression analysis between each fiber and output measure prediction and model is run, R² values and NRMSE values (N) are shown in the model-plots. The graphs in [A, C and E] are adopted from the original work by Hu et al (2010), and are reprinted with permission.

The first two columns of figure 3.2 show the discharge rate in spikes/s, indicating similar decreases in discharge rate over time between the animal and predicted data. Across all epochs, the adaptation was stronger at smaller amplitudes in both the simulations and recordings. In the lowest row of column 3.2A, the fiber shows complete adaptation after 200 ms upon stimulation with the smallest amplitude in the experimental data, which was not replicated by the model. In the model (column 3.2B), the discharge rate plateaued after 200 ms, while the experimental data showed a continuous decrease. R^2 for the rates is relatively high, ranging from 0.89 to 0.98, and different for each fiber. Reported NRMSE values range from 0.14 to 0.39. RM ANOVA on the rates in fiber one and three yielded a p-value of 0.272, thus no significant difference was found between model and experimental data.

Vector strengths, seen in the middle two columns, initially ranged from 0.15 to 0.85 in both the measured [C] and simulated [D] data. For most fibers in both the measurements and simulations, vector strength increased during the first three epochs, and then reached a plateau. However, in the animal data, the VS continued to increase in two cases (column 3.2C, the second largest amplitude in the upper row, and the largest amplitude in the lower row). For both the simulations and the measurements, the increase in VS over the complete duration was in the same range: from 0.5 for the larger amplitudes to over 0.9 for lower amplitudes. In the second row of column 3.2C, the fiber shows variability of VS over time when stimulated with the smallest amplitudes. While this pattern was also seen in the model simulations, the variability was larger in the simulated data. In the first row of column 3.2C, the fiber shows a very steady VS at small amplitudes, whereas the model simulations are more dynamic. R^2 values for the simulated VS ranges from 0.72 to 0.85, thus somewhat lower than the rate predictions, yet again dependent on the fiber modeled. NRMSE values range from 0.17 to 0.20.

In both the animal data and the model, the last two columns in figure 3.2, the F_0 amplitude initially increased and then decreased when stimulated with the largest stimulus amplitudes—specifically, when stimulated with amplitudes evoking discharge rates in the first epoch of 350 spikes/s or greater. When stimulated with lower amplitudes, the F_0 amplitude decreased immediately after the initial bin, potentially reaching as low as zero in both the animal experiments and model simulations. The lowest row of columns 2E and F shows that the maximal F_0 amplitude for the largest amplitudes at the fiber was larger in the animal data than in the predicted responses. R^2 values for the simulated F_0 ranges from 0.55 to 0.96. NRMSE values were between 0.16 and 0.39.

Figure 3.3 shows that decreased refractoriness in the model led to a steeper decline in discharge rate, stronger degrees of adaptation, larger vector strengths, and larger F_0 amplitudes upon stimulation with pulse trains of the largest amplitude. With a lower RS, the discharge rates and degrees of adaptation were similar to when the fiber was modeled using average model parameters, but VS and F_0 values generally increased. At low amplitudes, VS grew steadier over time in both the model and the experimental data. Although F_0 amplitudes increased, they remained smaller than in the matched fiber. With a lower

adaptation value, V_S and F_0 values were lower, and discharge rates showed a less substantial decrease, which was reflected in the lower degree of adaptation. For this particular fiber, judging from the calculated NRMSE and R^2 values, the average model parameters seem to do the best job for rate and V_S prediction, whereas the lower RS seems to better predict F_0 ,

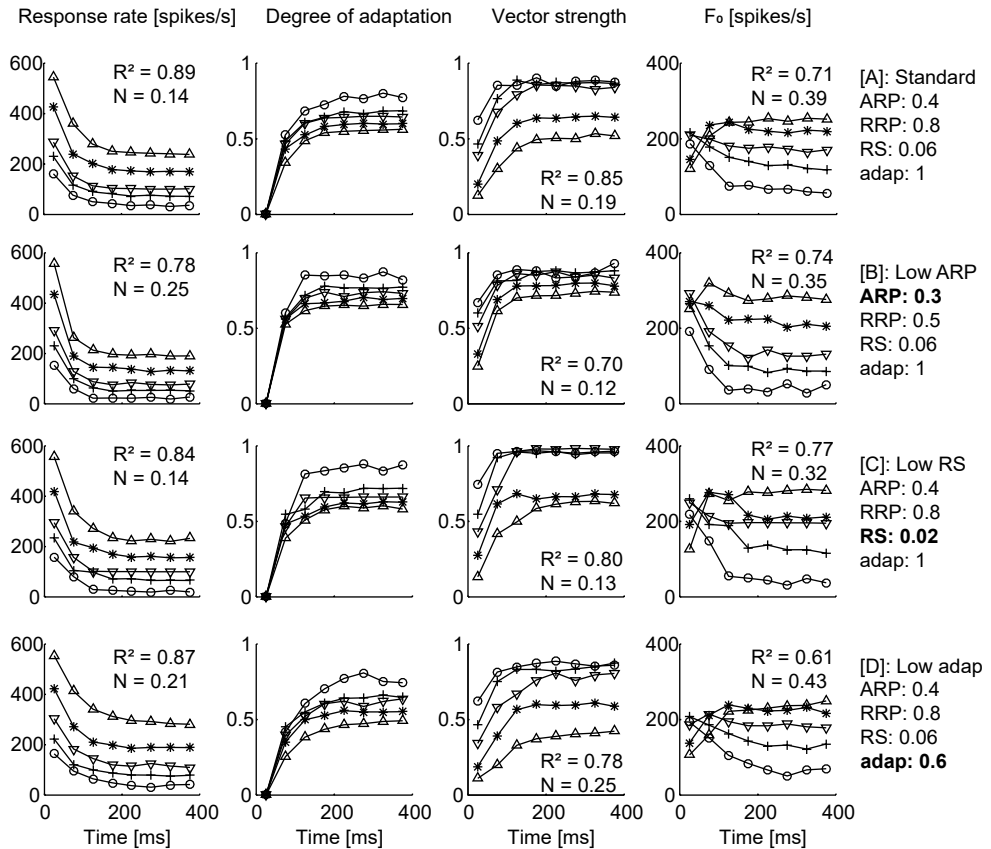


Figure 3.3. Effects on model predictions of the following model parameters: refractory periods, relative spread, and adaptation amplitude. Amplitudes matching the initial discharge rates equal to the lowest row in figure 3.2 were used: 160, 225, 300, 425, and 550 spikes/s. All model parameters were set to average in [A], refractory periods were lowered in [B], the RS in [C], and the adaptation amplitude in [D]. Regression analysis between each fiber and output measure prediction and model is run, R^2 values and NRMSE values (N) are shown in the model-plots. Graphs are adopted from the original work by Hu et al (2010), and are reprinted with permission.

3.2 Sensitivity analysis

Figure 3.4 shows that the optimal parameter set is different for both fibers. Also, there is a relatively wide range of adaptation and accommodation values for which the average difference is relatively low. The average chosen parameters of an adaptation amplitude of 1.0 and an accommodation amplitude of 0.03 is close to optimal for the fiber plotted in

[B]. The results plotted for the fiber in [A] show a minimum with an adaptation amplitude of 0.4% and accommodation amplitude of 0.02. Generally, it was seen that with the largest time constant the optimal values for adaptation and accommodation decreased, and the sensitivity to changes in these parameters increased. On the contrary, with a lower adaptation parameter, the most optimal accommodation parameter ought to be higher. Exclusion of adaptation and accommodation (the origins) causes a relatively large error for both fibers. Moreover, accommodation and adaptation parameters are interdependent.

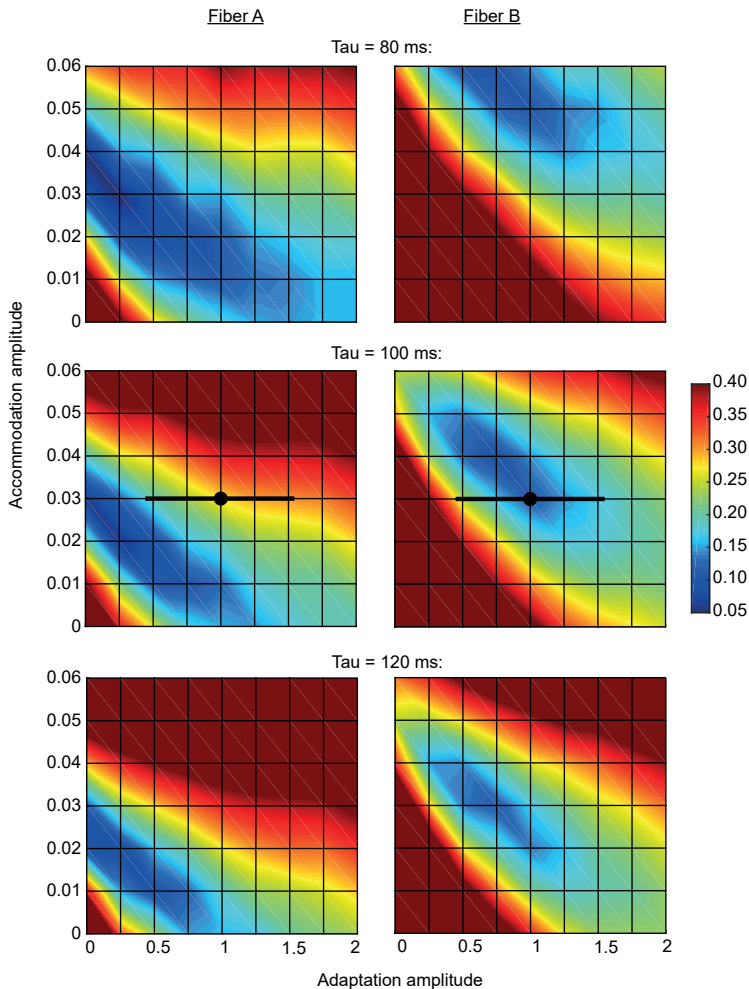


Figure 3.4. Sensitivity analysis. Normalized RMSE of spike rates (averaged over all bins and amplitudes) between modelled and experimental results in two different fibers. Adaptation amplitudes used were 0.0 up to 2.0 with a step size of 0.25, and accommodation amplitudes used were 0 to 0.06 with a step-size of 0.01. The black dots indicate the adaptation / accommodation values used in the current model, the solid black line indicates the standard deviation value as included on the adaptation parameter. Fiber A: fiber shown in the upper row of figure 3.2. Fiber B: fiber shown in the lowest row of figure 3.2.

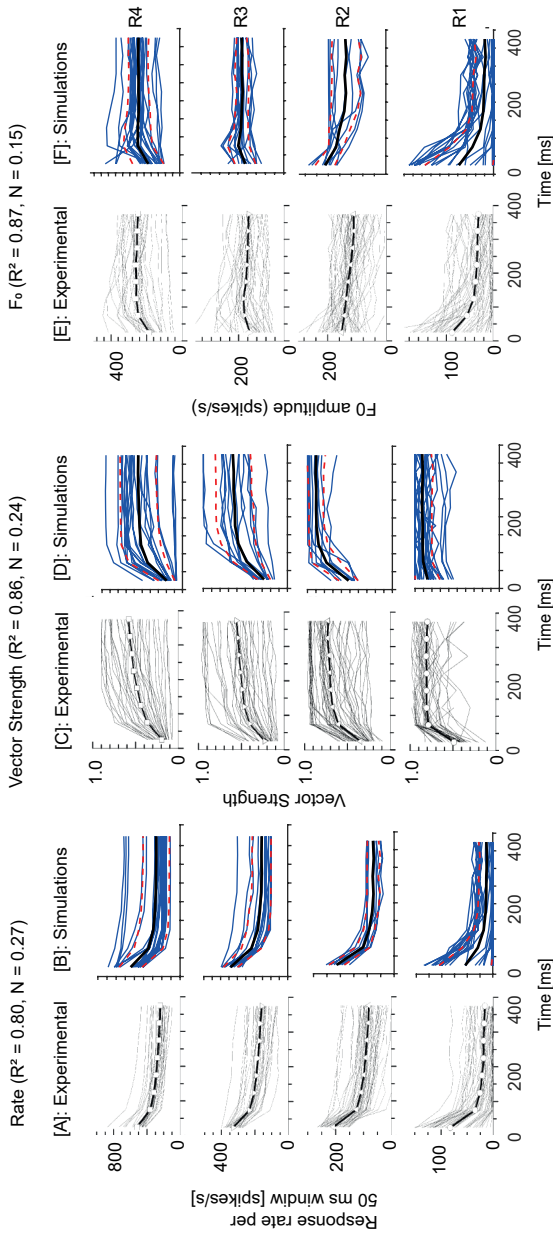


Figure 3.5. Group variability: A total of 80 fibers (1160 to 1240) were stimulated at an amplitude of 1 mA, and all model parameters were set within the normal distributions, as given in table 3.1. Results are presented as the average over 30 stimulations (trials). Modulation depth was 10%, modulation frequency 100 Hz. Columns [A, C and E] show experimental data (Hu et al., 2010), and columns [B, D and F] show model predictions. Thin lines indicate single fibers, while thick lines indicate the average of all fibers. The red dotted lines indicate standard deviations from the means. Fibers are ordered in four different sub-groups based on the response rate within the first 50-ms epoch: R1 (5–150 spikes/s), R2 (150.1–270 spikes/s), R3 (270.1–400 spikes/s), and R4 (400.1–972 spikes/s). The graphs in columns [A, C and E] are adopted from the original work by Hu et al (2010), and are reprinted with permission.

Group data; parameter distribution

Since all model parameters affected the discharge rates, VS, and F_0 , it was important that the complete model covered a realistic range of model parameters. Figure 3.5 shows the experimental data, and the model simulations for 80 different fibers stimulated at 1 mA, with the data ordered in four initial rate groups (R1–R4).

The 80 different fibers were all spatially distributed over the region expected to be excited by the stimulated electrode in the simulations. Spread of excitation over this region was included, which largely contributes to the differences in (initial) firing rates. As the responses were ordered according to the initial rates, the onset responses (figure 3.5, first column) were similar for the experimental and modeled results. The degrees of adaptation observed over the stimulus duration were also similar for experimental and modeled data.

With regards to the VS, the onset VS ranges were similar between the model and the experimental results. For all fibers, VS increased over time, similar to the animal data. Both experimental and predicted data showed a fluctuating VS in some fibers in R1. The greatest difference between the predicted and measured responses was that the VS in some modeled fibers in category R4 increased to 1 more rapidly than was observed in the animal data. Experimental and model data also showed similar ranges and behaviors of F_0 values over time in the different rate groups. In R1, fibers that started with a low F_0 showed a less substantial decrease in F_0 over time compared to fibers with an initially larger F_0 . In groups R3 and R4, this decrease was not seen. R3 showed an increase of F_0 in both the animal and model data. In R4, some modeled fibers started with F_0 values larger than the values observed in animal data. F_0 amplitude increased with rate group in both the experimental and modeled data. Statistical analysis yielded average R^2 -values when comparing rates VS and F_0 on group level between 0.80 and 0.87, and NRMSE values between 0.15 and 0.27. Overall, the stimulated ranges, variability, and averages in all three output measures were in good agreement with the measured responses.

Effects of modulation frequency and depth

Figure 3.6 shows rates and Vector Strengths in response to different modulation depths. figure 3.6A shows the experimental data, B and C are results obtained by our model, D is the modeled results obtained by Goldwyn et al. About half of the randomly selected fibers in our model were non-responders, which is similar to Litvak et al. Modeled discharge rates increase with modulation depth [B], this effect is seen similarly by Goldwyn et al [D]. In experimental data a steeper increase in rate is seen around 2-5% modulation depth. Using a sensitivity analysis [C] it was found that a fiber (Δ) with very low refractoriness, RS and adaptation/accommodation displays this steeper increase. Our model predicts a quicker increase of VS with modulation depth than the model of Goldwyn et al., but the experimental data exhibits the quickest increase. To investigate the effect of pulse width the model was separately run with a pulse width of 32 μ s. This yielded, at lower stimulus amplitudes, similar increases in Vector Strength and firing rate.

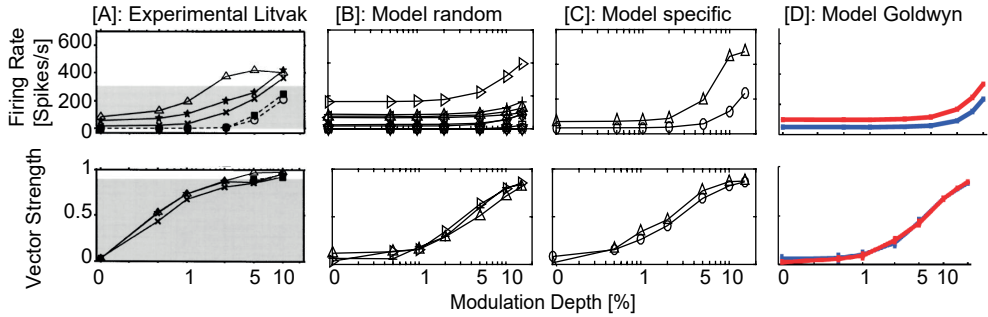


Figure 3.6. Dependency of rate and VS of a 0.4 second stimulus modulated with a frequency of 417 Hz. [A] Experimental data, Litvak et al. (2003). [B] Modeled responses of 10 fibers, with parameters from the normal distribution as given in table 3.1 and locations close to the stimulated electrode. Stimulus amplitude is 0.75 mA, close to the average fiber threshold in that region, and the fiber is stimulated 10 trials over which the average rates and VS are determined. VS is only calculated for those fibers that elicited a rate of minimally 100 pps, in replica of the experiments performed by (Litvak et al., 2003a). [C] Modeled fiber responses where the model parameter set was either adjusted to most accurately simulate data published by Litvak et al. (Litvak et al., 2003a) (marked with Δ) or set to one standard deviation below all average model parameters (marked with O). The model parameters for Δ were as follows; ARP = 0.2 ms, RRP = 0.2 ms, RS = 0.01, adaptation amplitude = 0.1, accommodation amplitude = 0.02. For these two simulations stimulus amplitude was set to 0.8 mA, and fiber location was close to the stimulating electrode. [D] Modeled results by Goldwyn et al. (2012). The graphs in column D are adopted from the original work by Goldwyn et al. (2012), and are reprinted with permission.

We also replicated the long-duration stimulation and modulation experiments by Litvak et al (2003a). In our simulations, 600 ms of unmodulated stimulation was followed by a modulated pulse train of 400 ms. Figure 3.7 shows the period histograms for the responses to the modulated portions of the pulse trains, while figure 3.8 shows the corresponding interval histograms.

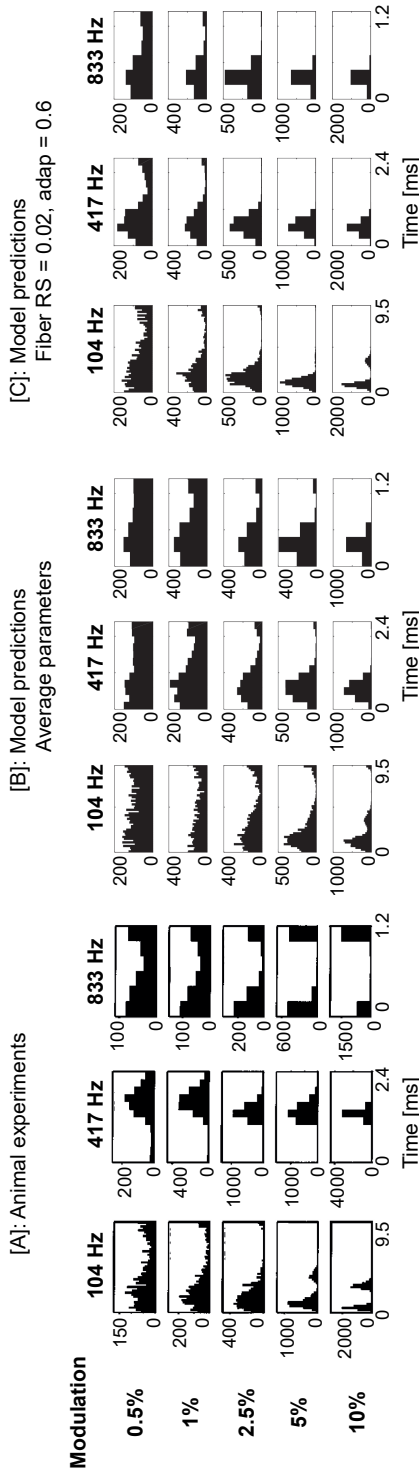


Figure 3.7. Period histograms showing the spikes per bin in response to AM pulse trains in animal experiments [A], (Litvak et al., 2003) and model outcomes [B and C]. Model parameters in [B] were set to average values: Absolute Refractory Period, 0.4; Relative Refractory Period, 0.8; Relative Spread, 0.06; alle sigma, 0; tau adap, 100; adap, 1; acco, 0.03; fiber, 1200; amplitude of 0.9 mA and stimulation rate of 5 kpps. The right plots [C] shows an improved match, with an RS down to 0.02 and adaptation to 0.6, amplitude is 0.9. Each plot was obtained by averaging the results over 100 trials. Graphs in [A] are adopted from the original work by Litvak et al. (2003) and are reprinted with permission.

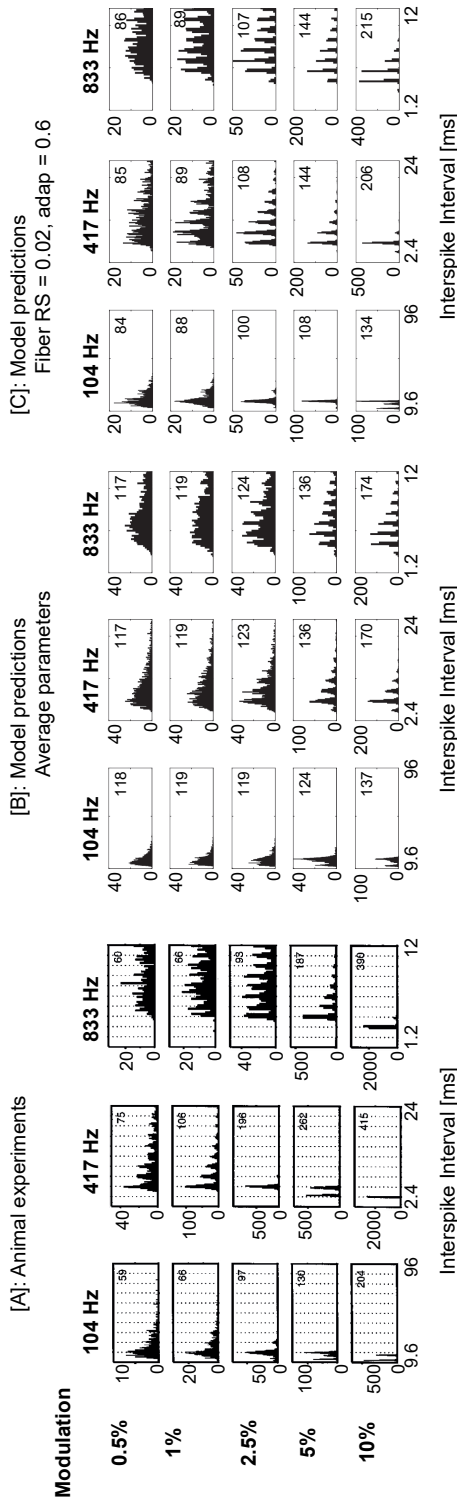


Figure 3.8. Interspike intervals [spikes/bin] in response to AM pulse trains with different modulation depths and frequencies. Plots on the left [A] show animal data as published by (Litvak et al., 2003a). Plots in the middle show simulation results with average fiber parameters [B]. Plots on the right show simulation results with adjusted model parameters [C]. Average model parameters were used: ARP, 0.4; RRP, 0.8; RS, 0.06; alle sigma, 0; tau adap, 100; adap, 1; acco, 0.03; fiber, 1200; and ampl, 0.9. Each plot was obtained by averaging the results over 100 trials. The number in the upper right corner of the ISI shows the number of spikes during the modulated portion of the signal. Graphs in [A] are adopted from the original work by Litvak et al. (2003) and are reprinted with permission.

Both figures 3.7 and 3.8 show the animal data, the simulated results with an average fiber, and the results for a fiber that better resembled the animal data for which the parameters were found in the manual search (adjusted fiber). The distributions of the interspike intervals and the relative periods showed similar patterns and changes with modulation amplitudes and frequencies. At all frequencies, larger amplitudes led the histograms to become more peaked and to shift to shorter interspike intervals. Particularly at the middle and high modulation frequencies, the higher harmonics disappeared in the responses in the simulated data, as was observed in the animal data. The period histograms of the responses to 104-Hz modulated pulse trains showed a double peak, especially at large modulation amplitudes, in both the experiments and simulations.

The second peak seen with the adjusted fiber was more similar to the animal data. The average fiber showed less phase-locking with 104 Hz and 0.5% modulation depth compared to in the animal data. Lowering the RS and adaptation parameter expectedly yielded better phase-locking. At 417 Hz, both the interval and the period histograms obtained with the simulations were wider than the histograms for the measured data. In the animal data, the responses turned out to be more strongly locked to the modulation phase. Decreasing the RS and adaptation value, decreased widths of the period histogram, such that they were more similar to the animal data. The corresponding interval histograms showed more pronounced peaks at the higher harmonics of the modulation frequency. The shift towards shorter ISIs seen in animal data was less strongly apparent in the adjusted fiber data, although some shortening was visible. The animal fiber appeared to show a stronger response to increases in modulation depth. At 833 Hz, both the average fiber and the adjusted fiber were similarly locked to modulation; however, the interval histograms for the adjusted fiber more closely resembled the animal experiments. In figure 3.8, the numbers in the upper right corner of the ISIs show the number of spikes during the modulated portion of the signal. The number of spikes increased with modulation depth, both in the simulated data and in the animal data. Compared to the average fiber, the adjusted fiber showed a stronger increase in rate that was more comparable with the animal data.

Modulation onset responses

In figure 3.9 the animal data showed an increased firing rate immediately following onset of modulation, which was not seen in the model simulations with the average fiber. Adjusting the parameters RS and adaptation amplitude also did not yield an immediate increase after modulation onset in the model simulations.

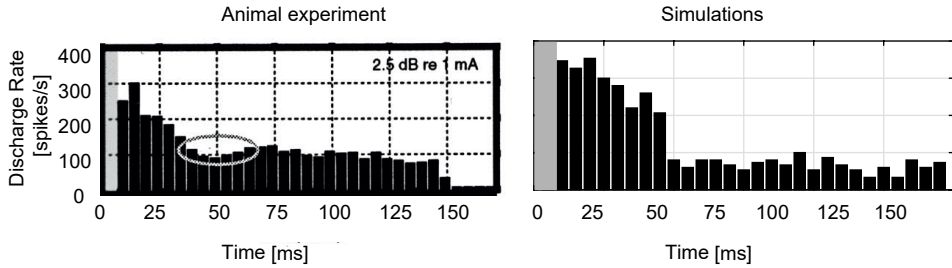


Figure 3.9. Post Stimulus Time Histograms of a fiber stimulated with a 4800-pps pulse train. The first 50 ms are unmodulated. After 50 ms, the input is down-modulated with a modulation frequency of 400 Hz and a modulation depth of 10%. The left graph shows animal experimental results (Litvak et al., 2001). The right graph shows model predictions using average model parameters. For the simulation stimulus, amplitude was set to 0.85 mA. Fiber 12,000 was simulated, and the results were averaged over 30 trials. The left graph is adopted from the original work by Litvak et al (2001) and is reprinted with permission.

Modulation Detection Thresholds

The predicted MDT's (figure 3.10) as a function of stimulus level are very comparable with the predictions of Goldwyn et al. The minimal MDT, at the center of the shape, is somewhat lower in our model predictions. The difference in levels on the abscissa is due to a general difference in fiber threshold.

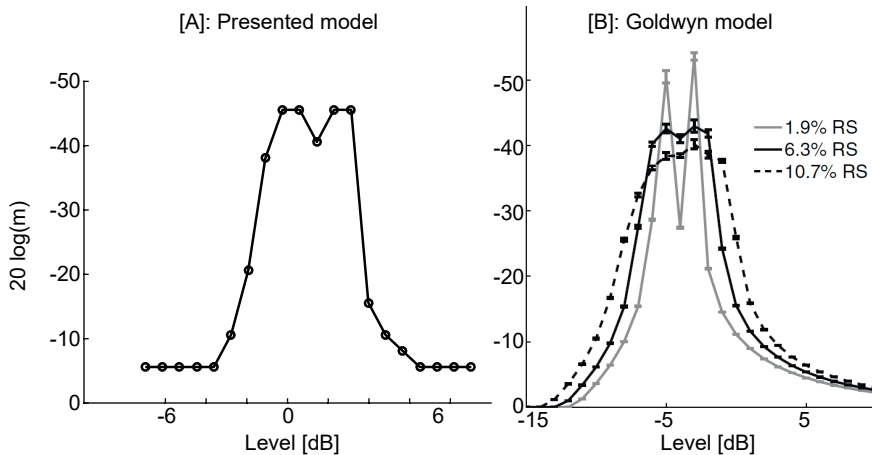


Figure 3.10. Modulation Detection Thresholds (MDTs) for different (average) stimulus levels, dB re 1 mA. [A] shows the prediction produced by our model with average parameter settings, [B] shows the results of another model, by Goldwyn et al. The ordinate represents the logarithmic equivalent of m , which is the minimal detectable modulation in percentage. Modulation frequency = 20 Hz, carrier pulse rate 1000 Hz. All model parameters were set to average values. Duration of the stimuli was 400 ms. The right graph is adopted from the original work by Goldwyn et al (2010) and is reprinted with permission.

4 Discussion

The results of our single-fiber model simulations generally were in good agreement with the data available from published animal experiments. The model is shown to predict responses to pulse trains with rates up to 5000 Hz and durations up to 400 ms. The simulations showed similar spiking patterns in response to high-rate amplitude-modulated pulse trains, for both near- and supra-threshold stimuli, and with different modulation depths and modulation frequencies. Group simulations showed that distribution of neural behavior is very similar to that in animal data. Interval histograms for the simulations showed distributions similar to those from animal experiments, with shapes and amplitudes that varied in accordance with stimulus duration and modulation characteristics. Period histograms in response to amplitude modulated input were previously modeled by Goldwyn et al (2012, fig 3.12). Similar to their model predictions, our results show increased locking to the modulation phase with increased modulation amplitude. In contrast to their predictions our model shows a stronger phase-locking, strongest visible at the 1% modulation depth. The period histograms revealed that both the computer model and animal studies exhibited similar amounts of phase-locking in the responses to the amplitude-modulated high-rate pulse train. The discrepancy in exact timing seen in the PHs in figures 3.1 and 3.7 is probably due to the exact location along the auditory nerve where recordings are taken in animal experiments. Overall, there is a slightly stronger effect of small modulation depths in animal data than seen in the simulations. The model is limited in its ability to handle sudden large changes in input, such as the sudden off-set of amplitude modulation in figure 3.9. This may be explained by the fact that very fast temporal components are not yet included in the current version of the model. Moreover, the model still has to be validated for inputs of much longer durations than half a second.

Validation challenges

In animal experiments, it is generally not known which fiber is stimulated, nor is the distance between the electrode contact and the stimulated fiber. Moreover, each study uses different electrode contacts. Thus, the amplitude given in the experimental data cannot be directly compared to the amplitude given for the simulations. Single-fiber data (as shown in figures 3.1, 3.2, 3.5, 3.6, and 3.7) are acquired from random fibers of the auditory nerve. These data are replicated by the present model using average parameter values, which is most likely not the closest match to individual fibers studied experimentally. Group data can provide a reliable sense of how the different parameters are distributed over a randomly chosen group of fibers. As seen in figure 3.5, the randomly chosen range of fibers in the model showed a good agreement with the range of fibers in the experimental data. Notably, the experimental data was all obtained in cats. To evaluate whether the simulations are also applicable in the context of humans, the model's output must be validated with human measurements. This could be performed by predicting ECAP data in response to pulse trains, and comparing these simulations to data from similar experiments in human CI recipients. Validation for arbitrary pulse shapes for single

pulses is done with the 3D geometric and active nerve model (Kalkman et al., 2014). The influence of pulse shape on stochasticity and temporal behavior is not evaluated in the presented paper. These effects could be implemented and should be validated by comparing the output of such a more extended version of the model with animal pulse train data where different pulse shapes are used. Validation against animal data with arbitrary pulse timing would be very relevant in order to verify the model's ability to study strategies using these types of stimulation. However, animal studies on this kind of stimulation which are suitable to be used as verification are scarce. We therefore think that animal responses to pulse trains in which pulse timings are not evenly spaced would be of great added value for future development and validation of models.

Refractory behavior

Our results showed that decreasing refractoriness leads to less firing and better frequency following behavior (figure 3.3). The faster variations in time are easier to follow, perhaps due to the quicker release of refractoriness. Overall, the average model parameter setting gives a better appraisal of this nerve's behavior. As refractory behavior can be studied with two-pulsed experiments our model uses values obtained from previous research.

Relative spread

We found that the RS parameter did not strongly affect discharge rates or the degree of adaptation, but may influence the modulation following behavior (figure 3.3). A lower RS resulted in slightly larger VS and F_0 values over time with low stimulus amplitudes. Running the model with larger RS values led to the opposite effect (results not presented). Modulation frequency following behavior, as assessed based on VS and F_0 values, increased with a lower RS. This is logical since amplitude modulations may or may not cause a spike, which will be more obvious with more deterministic fiber behavior, i.e., when spiking is more strongly related to the exact stimulus amplitude. For the particular fiber shown in figure 3.3, the NRMSE and R^2 for rate, VS and F_0 are comparable with the middle and the lower values of RS. Variation of RS affected the width of the peaks in the interval histograms. Interval histograms and period histograms (figures 3.7 and 3.8) also revealed that a lower RS value was associated with stronger phase-locking.

Adaptation parameter

Lower adaptation resulted in a reduced decrease in discharge rate, as well as in smaller VS and F_0 values (figure 3.3). As calculated with the NRMSE and R^2 -values, the lower adaptation parameters yield lower values for VS and F_0 . Thus, modulation following behavior was improved by adaptation in the nerve. Litvak et al. (2003a) grouped fibers showing a sustained response to high-rate amplitude-modulated stimulation, and fibers showing a transient response. It can be expected that the adaptation behavior differed between these two groups of fibers. The variance in model parameters is based on animal experiments (van Gendt et al., 2016). Similar to the refractory properties and RS, adaptation properties are assumed to vary among different nerve fibers. The sensitivity analysis visualizes the regions that produce optimal results. The optimal choices for adaptation

and accommodation amplitudes and the adaptation time constant are interdependent, and different per fiber. Because of the inter-fiber-differences, each fiber is modeled with its own set of parameters. Our model shows a stronger locking to the modulation frequency than shown by models without adaptation.

Smaller temporal components

Litvak et al. (2001) reported that 80% of the fiber responses showed a dip in the PSTH directly after the onset of the modulation at 50 ms (figure 3.9). Our simulations, however, do not show this effect. In the experimental study, fibers were clustered as stronger and lesser adapters, according to their response to stimulation. The fiber used for the simulation had average model parameters. However, most variations of the model parameters did not substantially increase the resemblance. Only adjustment of the adaptation time constant led to alteration of the recovery timing. The adaptation time constant turned out to be related to the time of recovery after modulation onset. Therefore, it could be argued that a faster adaptation component should be included, as was suggested by Zhang et al. (2007).

Longer temporal components

In the study by Litvak et al. (2003a), all measurements with different stimulus settings were done subsequently, yielding a total stimulus duration of about 10 seconds. This sequence was repeated until contact with the fiber was lost, yielding stimulation durations of up to 10 minutes. In the simulations each measurement was done independently, the fiber was stimulated each time for about 1 second. To test whether the longer duration of stimulation in the animal experiments would affect the outcomes, we performed a few simulations in which the fiber was stimulated for up to 10 seconds prior to stimulation with the modulated pulse train. This did not alter the outcomes of the present model. Since the outcomes of the model were very similar to the animal data, it can be argued that the desynchronization required for optimal amplitude modulation following behavior can be obtained after just a short onset period of adaptation. For the proposed use of a high-frequency desynchronizing pulse train, this finding implies that 600 ms of desynchronization would be sufficient to result in a better representation of modulation frequency (Hong and Rubinstein, 2003; Imennov and Rubinstein, 2009). Figure 3.2 shows a constantly increasing degree of adaptation and vector strength for the loudest amplitude during the stimulus duration, while the model predicts a plateau after 200 ms. By adjusting the different parameters, it was found that this is due to the exponential time constant of adaptation. With an exponential adaptation of longer than 100 ms, e.g. 200 ms, the VS and degree of adaptation increase after longer time periods. We therefore argue that the observation of longer lasting effects is likely due to longer time scale effects.

Spike timing

As seen in the PH's in figures 3.1 and 3.7, in the animal experiments the spike timings are later than in the model predictions; around 1.5 ms for the fiber in figure 3.1 (row [C] and [E]) and around 0.5 ms in figure 3.7. This relative temporal delay seen in the animal recordings can be due to either travel duration (runtime) of the action potential (AP)

through the nerve or rise time of the AP before it is detected in the electrophysiological recordings. Latencies in detection of AP's in electric stimulation of auditory fibers in cat were found between 0.2 and 1.3 ms, dependent on stimulus shape and amplitude (Miller et al., 1999a). As the temporal differences between the experimental data and results of about 0.5-1.5 ms are within a similar range, they are very likely due to the latency at the recording site which is due to runtimes and of the AP through the fiber and risetime of the AP. Furthermore, latency and jitter are related to spiking probability. Including latency and jitter, and their dependency on spiking probability might therefore improve the resemblance of the exact spike timings.

Pulse shapes

As explained in the introduction, in the present model the pulse shape directly influences the initial thresholds. The amplitude of the pulse hereafter determines all temporal and stochastic properties. They are however not influenced by the pulse width of pulse shape. It could be argued that the pulse shape affects the temporal and stochastic behavior. Especially accommodation, which is directly related to the stimulus. Increased pulse width would lead to larger charge build-ups and thus to larger accommodation. Animal experiments using similar pulse rates and amplitudes, but with different pulse widths, measured on the same fiber, could inform us about the effect of pulse width on accommodation and accommodation. For stochastics we also have chosen not to include an effect of pulse width, even though pulse direction and pulse width are shown to affect the RS (Miller et al., 1999a). In our model, the ranges of RS are wider than the differences seen in here, however a further development could include this to make the model more precise in evaluating pulse trains where different pulse shapes are used.

Implications

Sensorineural hearing loss often results in spiral ganglion cell degeneration, and thus to decreasing numbers of functional auditory nerve fibers (Ramekers et al., 2014). This decrement reduces the auditory nerve's effectiveness at using place coding to transfer pitch-related information. Furthermore, spatial spread of current in cochlear implantation diminishes the frequency specificity of the CI. Higher pulse rates can increase pitch perception among CI users, but typically only up to 300 Hz (Drennan and Rubinstein, 2008; Zeng, 2004). Amplitude modulation of the pulse train can also induce perception of amplitude modulation frequency, especially in the low frequency range and with large modulation amplitudes (Drennan and Rubinstein, 2008).

State of the field and future work

The proposed model showed good agreement with the presently available animal data. The model's performance compared to Bruce's model in response to continuous amplitude pulse trains is given in the previous paper (van Gendt et al., 2016). The model was shown to correctly predict rates and interspike intervals in response to up to 400 ms constant amplitude pulse trains of different rates and amplitudes. The current paper investigates response rates, VS and F_0 in response to amplitude modulated pulse trains. Results show

that average model parameters predicts behavior in the same ranges as in response to animal data. All output measures however depend differently on choice of parameters for refractoriness, relative spread and adaptation. For instance, decreasing the refractory periods, as seen in row [A] of figure 3.3, increases VS for low stimulus amplitudes. Lowering of the RS, as seen in figure 3.3 row [B], increases VS in response to the larger amplitude-pulse trains. Decreasing the adaptation parameter causes a lower VS for all amplitudes, but the effect is strongest at lowest amplitudes.

Prediction of rate and VS in response to different modulation depths presented in figure 3.6 was previously shown by Goldwyn et al. The average picture seen in their predictions is similar to ours. However, our model shows that within the fiber population, due to the distribution of parameters, better resembling data can be simulated. One difference between both models on the one hand and the experimental data on the other is a weaker effect of modulation depth. Therefore perhaps a shorter time constant is also involved, as would be the case in power-law adaptation, which might cause immediate release of adaptation in response to a slightly modulated input signal.

Prediction of dependency of the MDT on stimulus amplitudes by the proposed model is similar as that predicted by Goldwyn et al. (2010). However, a lower minimal detectable depth is seen at the levels yielding minimal MDTs, which might very well be an effect of adaptation. Adaptation brings the nerve in a state more responsive to changes, thereby logically decreasing the MDT. Goldwyn et al. (2010) and O'Brien et al. (2016) investigated the effect of temporal integration windows and the number of fibers on MDT prediction. Shannon et al (1992) show psychophysically that with increase of modulation frequency MDT's increase. As was shown by Goldwyn et al. and O'Brien et al (Goldwyn et al., 2010b; O'Brien et al., 2016) this can be due to jitter as large as 1-2 ms which is similar to temporal time constants for neural integration at interpretation level. The current paper demonstrates how a large distribution of model parameters is required to model the wide range of physiological behavior at a neural level. The distribution of behavior might affect the perceptual interpretation at neural level, which should preferably be evaluated with an interpretation model. In future research we would like to use whole nerve predictions to further study MDTs and other psychophysical measures.

First stage phenomenological models of auditory nerve responses to electrical stimulation included threshold, RS and refractoriness (Bruce et al., 1999a; Chen and Zhang, 2007; Xu and Collins, 2007). In addition phenomenological models have experimented with the inclusion of latency, jitter, RS dependency on time since pulse (related to channel noise) and summation (Goldwyn et al., 2012; Hamacher, 2004) or accommodation and adaptation (van Gendt et al., 2016). In an overview paper the temporal considerations of refractoriness, summation, accommodation and adaptation are theoretically entangled (Boulet et al., 2016). The current and previous paper (van Gendt et al., 2016) show that adaptation is important to model the effects of high rate pulse trains. None of the currently

existing models investigated responses to long duration stimulation (over 1 second), or recovery statistics after offset of amplitude modulation.

For prediction of responses to cochlear implants stimulation a complete nerve model, consisting of a realistic number of nerve fibers and a realistic current spread has to be included. Future studies should test this model for evaluating complete auditory nerve responses to different sound coding strategies. Before design of new CI strategies can be evaluated using a computational model, a validated interpretation model for neural response patterns has to be developed. The next step in modeling research must make the connection between physiological outcomes (such as those obtained in animal experiments) and psychophysical data obtained from CI users. The presently described auditory nerve model can be used to compare stimulus parameters and related neural outcomes to detection thresholds from different discrimination tests performed in CI users. Such comparisons could provide insight into the relationship between neural output and human auditory perception. These investigations will require the development of a neural interpretation model as the next step in the model's evolution. Using the comprehensive geometrical cochlear and auditory nerve model, including stochasticity and long-duration stimulation effects, in combination with such an interpretation model will provide a tool for evaluating developments in speech coding research.

Conclusion

The developed model can be used to predict full auditory nerve responses to amplitude-modulated long-duration high-rate cochlear implant stimulation. The model can show differences between different stimulations in a manner that reflects differences observed in neurophysiological measurements. Therefore, the model can be used to predict firing patterns in response to varying electrical stimulus patterns.

CHAPTER 4

Short and long-term adaptation in the auditory nerve stimulated with high-rate electrical pulse trains are better described by a power law

Margriet J. van Gendt

Michael Siebrecht

Jeroen J. Briaire

Sander M. Bohte

Johan H.M. Frijns

Abstract

Despite the introduction of many new sound-coding strategies speech perception outcomes in cochlear implant listeners have levelled off. Computer models may help speed up the evaluation of new sound-coding strategies, but most existing models of auditory nerve responses to electrical stimulation include limited temporal detail, as the effects of longer stimulation, such as adaptation, are not well-studied. Measured neural responses to stimulation with both short (400 ms) and long (10 minutes) duration high-rate (5kpps) pulse trains were compared in terms of spike rate and vector strength (VS) with model outcomes obtained with different forms of adaptation. A previously published model combining biophysical and phenomenological approaches was adjusted with adaptation modeled as a single decaying exponent, multiple exponents and a power law. For long duration data, power law adaptation by far outperforms the single exponent model, especially when it is optimized per fiber. For short duration data, all tested models performed comparably well, with slightly better performance of the single exponent model for VS and of the power law model for the spike rates. The power law parameter sets obtained when fitted to the long duration data also yielded adequate predictions for short duration stimulation, and vice versa. The power law function can be approximated with multiple exponents, which is physiologically more viable. The number of required exponents depends on the duration of simulation; the 400 ms data was well-replicated by two exponents (23 and 212 ms), whereas the 10-minute data required at least seven exponents (ranging from 4 ms to 600 s). Adaptation of the auditory nerve to high-rate electrical stimulation can best be described by a power-law or a sum of exponents. This gives an adequate fit for both short and long duration stimuli, such as CI speech segments.

1. Introduction

Cochlear implants (CIs) are implantable hearing devices for people with severe to profound hearing loss. CIs generally allow good speech understanding, but outcomes are highly variable and speech perception remains challenging in more complex listening situations. Many different sound-coding strategies have been introduced in the last decade to improve sound coding, but performance on perception tests has not improved significantly (Zeng, 2017). New stimulation strategies are commonly investigated in psychophysical experiments and clinical trials, which is time-consuming for both the patient and researcher and does not provide insight into physiological characteristics underlying the large variability in perception scores. Alternatively, strategies could be evaluated using computational models. A variety of models are currently available that can simulate responses of the auditory nerve to electrical stimulation.

Models that simulate responses of the auditory nerve to electrical stimulation can be classified as phenomenological or biophysical. Biophysical models, which describe physiological elements of the neuron in detail, have been shown to reproduce deterministic threshold characteristics and refractory behavior in response to a stimulation of several milliseconds, with arbitrary pulse shapes (Dekker et al., 2014; Frijns et al., 2001; Frijns and ten Kate, 1994; Kalkman et al., 2015; O'Brien and Rubinstein, 2016). Methods to biophysically model more complex neural behavior, such as stochasticity and the effects of long temporal spiking history, have also been suggested. These methods provide insight into the physiological processes, but have the disadvantage of requiring many parameters to be fitted and consume great computational power (Negm and Bruce, 2014; O'Brien and Rubinstein, 2016; Woo et al., 2010, 2009). Efficient computation of the neural responses of all ~30,000 auditory nerve fibers is fundamental to predicting perception outcomes. Alternative to biophysical models, phenomenological models, that describe the behavior of the neuron empirically, can be used efficiently for these purposes. Stochasticity is such a phenomenon that can be included (Bruce et al., 1999b, 1999a), and more recently adaptation has been included in phenomenological models (Boulet et al., 2016; van Gendt et al., 2019, 2016). The effect of adaptation increases with stimulus duration and rate (van Gendt et al., 2017, 2016). Therefore, in simulations of neural responses to segments of speech, which are of long durations, adaptation becomes relevant. Contemporary CIs use pulse rates of 800-2000 pps, but depending on the spatial spread single neurons may be stimulated by higher rates.

Single fiber auditory neuron recordings in response to long duration electrical stimulation, which can be used for verification, is available only for high pulse rates (5 kpps). For lower stimulus rates adaptation is expected to have a smaller effect. It has been suggested that high rate pulse trains can be used as desynchronizing pulse trains (Rubinstein et al., 1999). In the healthy auditory nerve there is spontaneous activity, which yields linear behaviour also for low stimulus levels. Electrically stimulated auditory nerve fibers, however, respond highly synchronized, diminishing the dynamic range. To overcome this, it has been

suggested to first stimulate the auditory nerve with a high-rate (e.g., 5kpps) pulse train, bringing all fibers in a refractory or adapted state, after which spiking will be less coherent.

Adaptation is a well-known phenomenon in general neuroscience that is particularly well-studied in the visual system. Adaptation has been shown to maximize information transmission (Barlow, 1961; Wark et al., 2007). Neural adaptation dynamics depend on the stimulus history (de Ruyter van Steveninck et al., 1986). Neurons not only adapt to stimulus gain, but to a range of stimulus statistics, so that stimuli in a dynamic environment are represented most efficiently (Brenner et al., 2000). Such statistics may be very different over different durations of stimulation. After long durations of stimulation, the dynamics of adaptation in neural systems in general are often better described by a power law than an exponent (Toib et al., 1998). In the fly's visual system, adaptation was demonstrated to occur at different time scales; short time scales are necessary for optimal information encoding of rapid stimulus variations within an ensemble, whereas long time scales adjust the rate and statistics of the firing pattern to provide information about the ensemble of the stimulus (Fairhall et al., 2001). A power law function can be approximated by a combination of a large number of exponential processes with a range of time constants (Drew and Abbott, 2006). Many natural processes decay and grow exponentially. Although neurons behave according to a power law, no individual biological processes that can be described by a power law have been detected in neurons (Drew and Abbott, 2006), and the dynamics probably arise physiologically from different exponential processes. Because of the power law dynamics, neurons are capable of adapting their responses to stimulus statistics over a wide range of time scales, from tens of milliseconds to minutes. Thus, adaptation has been shown to play a role in efficient coding of the continuously (rapidly or slowly), changing sensory world.

In the auditory system, adaptation is also a supposed mechanism for optimized information transmission (Clague et al., 1997; Epping, 1990). Neurons can adapt to stimulus statistics, such as sound level and variance (Dean et al., 2005; Wen et al., 2009). The dynamic range is adjusted to the range of presented sound levels, leading to high accuracy of the perception of differences in loudness, regardless of the large dynamic range spanned by the input levels. Auditory nerve responses to statistically varying acoustic input were well-replicated by a model that included power law adaptation (Zilany et al., 2009; Zilany and Bruce, 2006). This model showed that power law adaptation increases the dynamic range of the auditory neuron (Zilany and Carney, 2010). Auditory neurons also adapt in response to electrical stimulation (Heffer et al., 2010; Litvak et al., 2003; Zhang et al., 2007). This becomes especially apparent with stimulus durations >100 milliseconds, as is the case in pulse trains encoding speech segments. Thus, a model of the auditory nerve that simulates responses to electrical CI stimulation representative of speech should account for adaptation. Previously, a model combining the biophysical and phenomenological approaches was shown to accurately simulate spiking of the auditory nerve in response to electrical pulse trains of durations up to a few hundred milliseconds (van Gendt et al., 2019, 2017, 2016). In these studies, adaptation was modeled by increasing the threshold

following each spike or pulse with a certain amplitude that exponentially decayed over time. Exponential spike adaptation and accommodation with a time constant of 100 ms was found to explain spiking behavior in response to both amplitude modulated and continuous amplitude pulse trains with duration up to 400 ms. This model, with a single exponent, successfully replicated responses, but its success was restricted to the limited stimulus ranges for which its parameters were optimized. The model has not been validated for longer duration stimulation. In addition, no studies have evaluated whether a power law, a single exponent, or a sum of exponents best describes the response of the auditory nerve to electrical stimulation.

As speech segments have durations of up to several seconds and a large dynamic range, it is important that the adaptation be correctly implemented in a model of neural responses to speech coding in CIs. The present study evaluated which model of adaptation best describes the responses of the auditory nerve to long duration stimulation. For this, recordings of the auditory neuron's responses to pulse trains with short and long durations were simulated with different models of adaptation. The used model builds on a previously developed computationally efficient model (van Gendt et al., 2017).

It is plausible to expect that more than one time-component is required to model long duration responses. This could be modeled as multiple exponentials, or, with less parameters, with a power law. This study investigates how both short- and long-term adaptation of auditory neurons to electrical stimulation can most adequately, physiologically realistic and computationally efficient be described and fitted.

2. Methods

Responses of the electrically stimulated auditory nerve were modeled using a combined biophysical and phenomenological model.

2.1. Deterministic thresholds

First, deterministic fiber thresholds (I_{det}) were calculated with a 3D volume conduction model and active nerve fiber model developed in the LUMC (Kalkman et al., 2015, 2014). The cochlear geometry is based on micro-CT data, the electrode array geometry is based on the HiFocus1J array (Advanced Bionics, Valencia, CA, USA) in lateral position. Deterministic thresholds were obtained for specific pulse shapes and pulse widths. In the current paper biphasic pulses with pulse-widths per phase of 18 μ s were used.

2.2 Phenomenological threshold adjustments

These deterministic thresholds were adjusted with stochasticity, adaptation, and accommodation using a phenomenological approach (van Gendt et al., 2017, 2016). For each nerve fiber, the stochastic threshold was taken from the normal distribution,

$N(I_{det}, SD)$, with SD calculated with a relative spread (RS) as $SD = I_{det} \cdot RS$. Subsequently, refractoriness (R), as calculated with equation 4.1, was added to the stochastic threshold.

$$R = \frac{1}{1 - e^{-\frac{(t - \tau_{ARP})}{\tau_{RRP}}}} \quad (\text{Eq. 4.1})$$

where τ_{ARP} and τ_{RRP} are the time constants for the absolute and relative refractory period, and t is the time since the last action potential. It was shown previously (van Gendt et al., 2017, 2016) that the adaptation behavior of the auditory nerve in response to electrical stimulation is a consequence of both sustained firing, referred to as spike adaptation (SA), and sustained stimulation, referred to as accommodation ($Acco$). Different models to describe SA and $Acco$ are described below. The final threshold was calculated as follows;

$$I_{adj} = N(I_{det}, \sigma) \cdot R + SA + Acco \quad (\text{Eq. 4.2})$$

A spike was assumed to occur when: $I_{given} > I_{adj}$, where I_{given} is the stimulus current. The parameters for stochasticity, refractoriness, and single exponential adaptation were previously fitted (van Gendt et al., 2017, 2016). An overview of the parameters is given in table 4.1 in the appendix. The present paper determined parameters for power law adaptation and multiple exponentials.

Single exponent adaptation

Adaptation was previously modeled with an exponential decay as in equation 4.3:

$$A = \alpha \cdot \sum_i SP \cdot e^{-\frac{t-t_i}{\tau_a}} \quad (\text{Eq. 4.3})$$

α is the adaptation amplitude or the accommodation amplitude. SP , a spatial factor, is 1 for spike adaptation, and $0.03\% \cdot I \cdot \frac{I_{min}(electrode)}{I(electrode, fiber)}$ for accommodation, $I_{min}(electrode)$ is the threshold for the fiber most sensitive to the used electrode, and $I_{min}(electrode, fiber)$ is the threshold for a particular fiber to that electrode. For spike adaptation i refers to the last spike, for accommodation i refers to the last stimulus pulse given.

Power law adaptation

The power law function was implemented in the neural model as in equation 4.4:

$$PLA(t) = \alpha \cdot \sum_i SP \cdot (t - t_i + offset)^\beta \quad (\text{Eq. 4.4})$$

where i , α and SP are the same as above, $offset$ represents a shift in the power law function, and β is the power component for the power law. $offset$ and β were assumed equal in both spike adaptation and accommodation.

Power law approximation with multiple exponents

Power law adaptation can be approximated by multiple exponents (Drew and Abbott, 2006). This was implemented here as in equation 4.5 for one exponent and equation 4.6 for multiple (k) exponents:

$$ExpA(t)_k = \alpha \cdot \sum_i SP \cdot e^{\frac{t-t_i}{\tau\alpha}} \quad (\text{Eq. 4.5})$$

$$ExpA(t) = \sum_k ExpA(t)_k \quad (\text{Eq. 4.6})$$

where i , α and SP are the same as above, and τ refers to the time constant for the exponential adaptation.

2.3 Model optimization

The parameters for the single exponent adaptation model were previously fitted (van Gendt et al., 2017, 2016), and the formulas and optimal parameters are given in Appendix A. The power law adaptation model was fitted to two different data sets. The first data set consisted of the responses of one fiber to short duration (400 ms) amplitude-modulated electrical pulse trains with five different stimulus amplitudes (Hu et al., 2010) (figure 4.2). For this short duration data, similar to the recordings, stimulation amplitudes were set to a certain relative amplitude compared to the threshold, which was defined as the stimulus amplitude that yielded a response of 100 spikes/s in the first bin. Similar to the recordings by Hu et al. (2010), the stimulus duration was 400 ms, bin-width 50 ms, pulse rate 5000 pps, modulation frequency 100 Hz, and modulation depth 10%. The second data set consisted of the responses of seven different fibers to long duration (600 s) continuous amplitude electrical pulse trains (Litvak et al., 2003). For this long duration data, the measurements of the seven different fibers (figure 4.1) were replicated. Stimulus levels that elicited the same simulated discharge rate in the initial bin as in the recordings were chosen. The duration was 600 seconds, the rate was 5000 pps, and bin-width was 1 second. Responses of fiber 1200 (located roughly 180° from the round window) to stimulation of the nearest electrode contact were simulated.

Parameter search

Simulations were performed for both data sets using a range of parameters (table 4.1). Combinations of different parameter settings in the range (i.e., 432 unique parameter sets) were used to simulate both datasets. Refractoriness and relative spread were set to the average values as published by van Gendt et al. (2017). See Appendix A for an overview of these parameters.

Table 4.1. Parameters for optimization

Parameter	Range
Accommodation amplitude (α_{acco}), %	0.004 – 0.014, step size: 0.002
Adaptation amplitude (α_{adap}), %	0.00 – 0.05, step size: 0.01
Offset, ms	1, 5, 20, 40
Exponent β	-1.2, -1.1, -1.0, -0.9

Minimal normalized RMS error

Values were visually extracted from the published data recordings for the measured discharge rates in all different bins. Differences between simulated and measured discharge rates were calculated using the normalized root mean square error (NRMSE), normalization was done by dividing by the range of the measured rates per stimulus amplitude. The NRMSE was calculated for each stimulus amplitude (a) as in equation 4.7:

$$NRMSE_a = \frac{\sqrt{\sum_{n=1}^N (\bar{r}_a - r_a)^2}}{r_{a,max} - r_{a,min}} \quad (\text{Eq. 4.7})$$

where for N bins, r is the measured rate and \bar{r} the simulated rate.

The NRMSE values for all stimulus levels were averaged. For both data sets, the parameter set with minimal error was defined. These parameter sets were used to simulate responses to the other data set for which it was not optimized. An optimal parameter set, defined as the set yielding minimal average NRMSE of both data sets. In addition, in the long duration data, seven different fibers were used, and the optimal parameter set was defined for each individual fiber. A sensitivity analysis was performed in which the effect of parameter variations on the NRMSE was investigated.

2.4 Approximating the power law fit with multiple exponents

The optimal power law parameter set was matched to a sum of exponents using least squares optimization. The number of exponents (n) for this fit was increased until 5 or, if no good fit was found with 5 exponents, until the NRMSE did not decrease more than 10% with an extra exponent. In order to limit the search space for the least squares-optimization of the parameters for the set of exponents, the power law kernel was divided into n parts of equal log-length. The longest exponent was fitted first and only on the last part of the power law kernel. The second longest exponent was fitted on the last two parts of the power law kernel taking the contribution of the longest exponent into account. Following this pattern, the shortest exponent was fitted last on the entire duration of the power law kernel taking all other exponents into account. This method ensured that all exponents were properly normalized. The log spacing ensured that the exponents overlapped equally with each other.

3. Results

The optimal parameter set was defined as the combination of parameters that yielded the smallest NRMSE. Table 4.2 shows these parameter sets optimized for the short and long duration data and those combined (columns Short, Long and Both respectively), and for each of the individual fibers of the long duration data (F1 – F7).

Table 4.2. Optimal parameter sets yielding the smallest NRMSE averaged for the different stimulus amplitudes on the short duration data (Short), the seven different fibers used in the long duration data (Long), for both errors averaged (Both) and per fiber (F) in the long duration data.

	Short	Long	Both	F1	F2	F3	F4	F5	F6	F7
Offset [ms]	20	5	20	5	5	5	5	40	20	40
Exponent β	-1	-1	-1.1	-0.9	-0.9	-1.1	-1	-1.2	-1	-0.9
α accommodation [x 10 ⁻⁴ % of stimulus]	10	6	8	6	4	4	4	12	6	4
α adaptation [% of threshold]	0.03	0.02	0.02	0.02	0.01	0.00	0.01	0.05	0.02	0.01

3.1 Comparison of model simulations to recordings

Long duration simulations

For the long duration simulations, measured and simulated spike rates over the course of the stimulus are plotted in figure 4.1. Data were recorded from seven different fibers from one animal (Litvak et al., 2003). The two units with the lowest response amplitudes stopped discharging after 1-2 minutes, the other five units exhibited adaptation over the first 100 seconds followed by either slow adaptation or a steady response. For comparison, the simulations for the previously published model with an exponent of 100 ms is shown in figure 4.1A. The power law adaptation simulations with the optimal parameter set (table 2) for the short and long duration data are shown in figure 4.1B and 4.1C respectively, 4.1D shows the simulations with the parameter set that yielded the minimal combined error. Figure 4.1E shows the power law fit when the optimal parameter set is chosen per fiber.

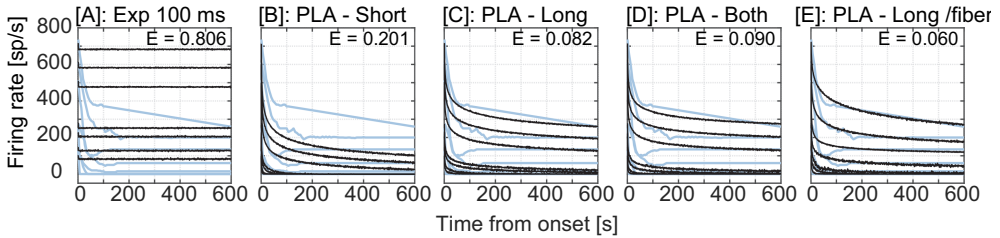


Figure 4.1. Discharge rates in response to long duration stimulation (600 s). The simulations are plotted in black. The visually extracted data from Litvak et al. (2003) is plotted in blue in each graph. The E in the upper right corner refers to the mean NRMSE for all fibers. Simulated discharge rates are calculated with the 100 ms exponential model [A], with the power law model optimized for the short duration data [B], with the power law model optimized for the long duration data [C], with the power law model optimized for both the short and long duration data [D] and with the power law model optimized per fiber for the long duration data [E].

The simulations with exponential adaptation only showed an initial, small decrease in spike rate, whereas all power law adaptation models demonstrated a continuous spike rate decrease over the course of stimulation (figure 4.1). Quantitatively, the power law outperformed the model with exponential adaptation, as reflected in the NRMSE value of 0.806 for exponential adaptation, 0.201 for power law adaptation with the parameter set optimized for the short duration data, 0.082 optimized for the long duration data set, 0.090 for both data sets and 0.060 optimized per fiber. Both the parameter set optimized for this particular data and the parameter set optimized for the short duration data yielded a substantial improvement in predicting the discharge rate relative to the single exponent. The best replication was obtained when optimized per fiber. The only difference between the recordings and these per-fiber-simulations was that the dip in the spike rate at approximately 50 to 150 seconds was not replicated by the model.

Short duration, amplitude-modulated simulations

To investigate which model best described the discharge rates and modulation following behavior in response to short duration amplitude-modulated pulse trains, the recordings from Hu et al. (2010) were simulated. The single exponent model and the power law models optimized for the short duration data and for the long duration data were used. For ease of comparison, recordings and simulations are plotted together in figure 4.2.

For the spike rates, the exponential adaptation yielded an NRMSE of 0.094. The power law model with the parameters optimized for this data and the combined data sets had NRMSE's of 0.065 and 0.068 respectively, outperforming exponential adaptation, whereas the parameters optimized for the long duration data only performed quantitatively worse, with an NRMSE of 0.134. For the VS, the single exponent model performed better than any of the power law models. Vector Strength measures periodicity in the neural response to a periodic input. The vector strength in the models is above zero but lower than the

recordings. This means that some periodicity is maintained in the modeled responses, but not as much as in the recordings.

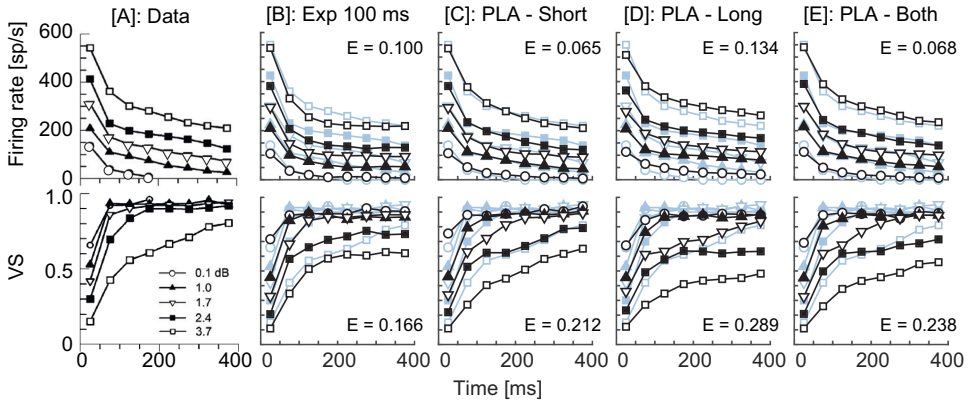


Figure 4.2. Simulation of responses to short duration, amplitude-modulated pulse trains. Upper row shows spike rates determined in bins of 50 ms in response to five different stimulus amplitudes. The lower row shows vector strengths obtained from the same bins. For clarity, the recorded data are plotted separately in [A], and in [B-E] in grey-blue in the background (data from Hu et al., 2010, reprinted with permission). The numbers in the lower right corner in [A] indicate amplitudes relative to the threshold. In [B]-[E] simulations are plotted in black. Simulations were modeled with exponential adaptation, single exponent (100 ms) in [B], with the parameter set optimized for the short data in [C], with the parameter set optimized for the long duration data in [D], and with the parameter set optimized for both data sets in [E]. The optimal parameter sets are given in table 4.2.

3.2 Sensitivity analysis

To find the parameter sets yielding the minimal NRMSE, simulations were performed with a range of stimulus parameters. To investigate how the error was affected by the variation in the parameters, a sensitivity analysis was performed. The sensitivity to the adaptation and accommodation parameters was investigated by plotting them for each exponent and offset combination, and the sensitivity of the exponent and offset parameters was investigated by plotting them for each adaptation and accommodation combination. The resulting graphs including the optimal parameters are shown in figure 4.3.

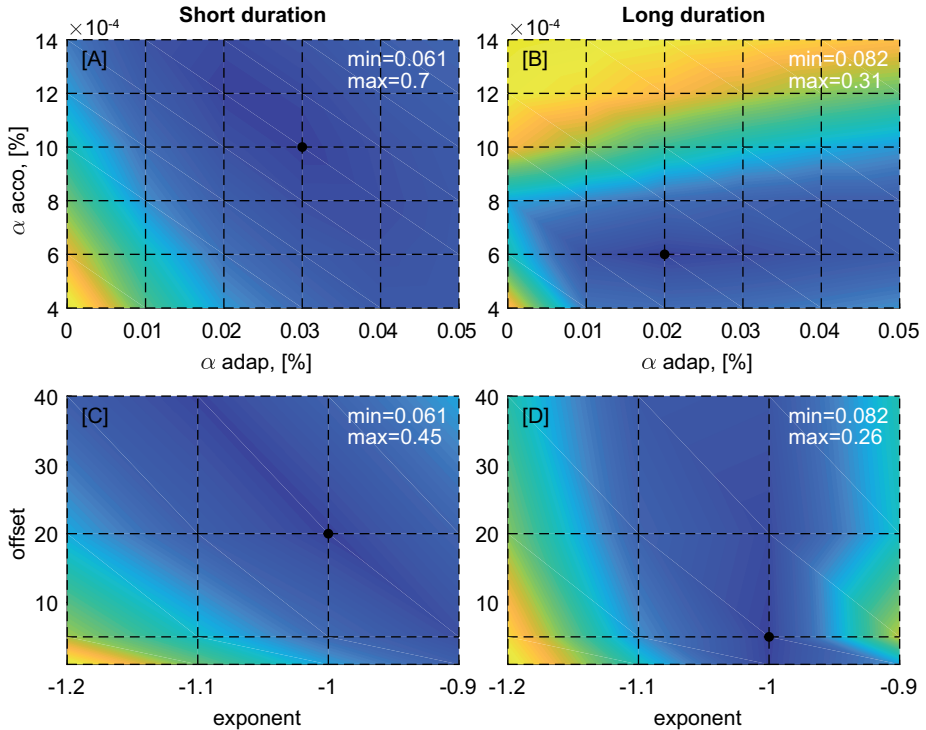


Figure 4.3. NRMSEs for the short duration data (left) and long duration data (right). Color coding ranges from the minimal error in blue to the maximal error in yellow. The minimal and maximal values are included in each sub-figure. At all intersections of the dotted lines, responses were calculated, and between those points is interpolated. The following parameters were set so that the optimal value was included in each sub-figure: [A] offset = 20 ms, exponent = -1; [B] offset = 5 ms, exponent = -1; [C] adaptation = 0.03%, accommodation = $10 \times 10^{-4}\%$; and [D] adaptation = 0.02%, accommodation = $6 \times 10^{-4}\%$.

The patterns in figure 4.3 are different for the short and long duration data. For long duration data, larger accommodation values led to strong errors, which was not seen in the short duration data. The short duration data exhibited a combined effect of adaptation and accommodation amplitudes; larger adaptation amplitudes required smaller accommodation amplitudes for similar errors. Furthermore, we identified an entangled effect of offset and β in the short duration simulations that was not seen in the long duration simulations. In the long duration data, the exponent influenced the error much more than the offset.

3.3 Fitting the power law with multiple exponents

Short duration fits with multiple exponents

The actual physiological processes underlying adaptation likely have exponential dynamics, but together behave in line with power law dynamics. Therefore, we investigated how many exponential processes would be required to explain the data. Each added exponent adds two new parameters to the parameter space that needs to be fitted. Fitting with several parameters can lead to overfitting or lack of convergence. Moreover, running simulations of the history-dependent neural responses with multiple exponents requires tremendous computational power. Alternatively, the exponential parameters can be fitted on the power law function that, in turn, was fitted on the data. Here, the minimum number of exponents needed to reliably simulate the recordings was tested. The time constants and weights for each number of exponents are given in Appendix B. The simulations of the short duration data with multiple exponents are shown in figure 4.4.

Going from the fit with 1 exponent ($\tau=77$ ms) to two exponents ($\tau_1=23$ and $\tau_2=212$ ms) induced the largest improvement. The NRMSE decreased from 0.100 to 0.066, and a continuous decrease in the spike rate was seen, similar to the animal data. The VS also improved with the addition of a second exponent; the NRMSE decreased from 0.25 to 0.219. When the number of exponents increased further, no additional substantial improvement in replication of the data was seen.

Long duration fits with multiple exponents

In a similar approach as with the short duration data, the long duration data were fitted with exponents. The simulations with 1, 5 and 7 exponentials are shown in figures 4.5A-C. The NRMSE values for up to 10 exponentials are shown in figure 4.5D.

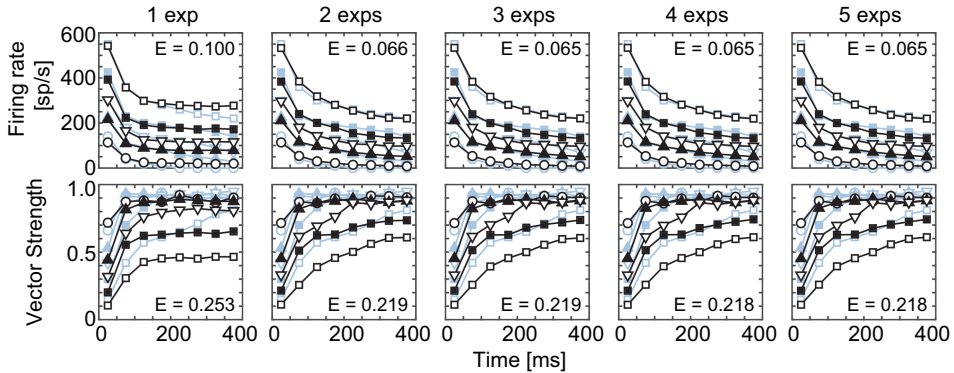


Figure 4.4. Simulations with adaptation as sums of exponential functions, compared to the short duration data (Hu et al., 2010). Results of the simulations are shown in black, and the experimental counterparts as published by Hu et al. in grey-blue. The number of exponents to model the adaptation varied from 1 to 5. The exponential components were fitted to a power law function with the optimal parameters to fit the short duration data itself; $\beta = -1$ and offset = 20 ms.

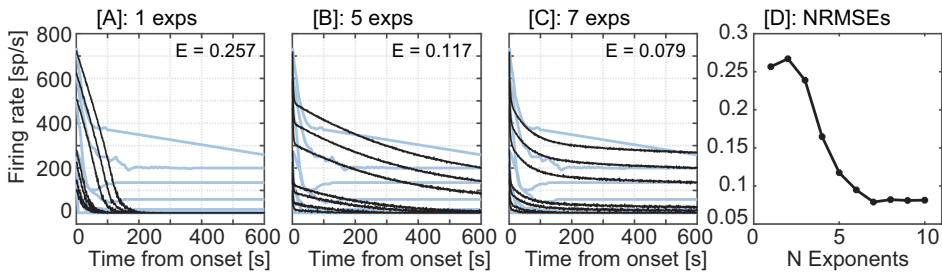


Figure 4.5. Power law adaptation fitted with 1, 5 and 7 exponents in [A-C], the NRMSE compared to the long duration data (Litvak et al., 2003) for 1 up to 10 exponents is plotted in [D]. The results of the simulations are shown in black, and the experimental counterparts as published by Litvak et al. in grey-blue. Exponential functions were fitted to a power law function with $\beta = -1$ and offset = 5 ms.

As can be seen in figure 4.5D, with up to seven exponents the fit improved; NRMSE decreased from 0.257 with the one fitted exponent to 0.079 with seven exponential functions. With seven exponents the taus ranged from 4 ms to 600 s, with approximately one order size difference between each tau. The NRMSE of 0.079 as found with seven exponents is similar to the NRMSE found with the power law fitted on the long duration (0.082, figure 4.1C).

4. Discussion

Power law and exponential models of adaptation were evaluated for their performance in simulating the responses of the auditory nerve to electrical pulse trains of different durations. Firing rates were better simulated with power law adaptation optimized on both data sets combined than with exponential adaptation. For both data sets, when optimized for the data set itself the best results were obtained. The power law parameters optimized for short duration data also predicted the long duration data reasonably well, but short duration data simulated with the parameters for long duration data yielded a fit worse than the exponential. Vector strength was best simulated with exponential adaptation, but was in all simulations smaller than in the recordings. For individual fibers, slightly different parameter sets were found. The power law could be fitted with multiple exponents, which is physiologically more realistic. When enough exponents were included, this yielded similar responses as with the power law. The number of required exponents depended on the duration of stimulation. The effect of long duration stimulation is important because relevant temporal segments, such as sentences, are in the order of seconds rather than milliseconds, and regular CI usage will last a day. With improved models of adaptation as suggested here, extended with an interpretation model, the effect of sound-coding strategies for speech segments and longer duration stimulation can be evaluated. It will be particularly interesting to evaluate how the adaptation in the auditory nerve alters loudness perception and dynamic range. In the future, this improved understanding of neural adaptation could be used to test the performance of sound-coding strategies in long duration stimulation and provide suggestions on how to integrate adaptation in sound-coding strategies to optimally encode the acoustic environment.

Optimal power law parameters

Here, two different data sets were used to find the optimal parameter set, and an overall optimum parameter set was determined. The separate data sets were best described by a power law with an exponent of -1, the combined optimum was obtained with an exponent of -1.1. These values are in line with earlier studies of adaptation mechanisms in general computational neurosciences, and with specific studies on adaptation of the auditory nerve in response to acoustic stimulation (Zilany and Carney, 2010), where the exponent was found to be around -1. The parameter set found by minimizing the combined error outperforms the single exponential model for both the short and long duration data.

Power law adaptation has been argued to result in whitening of the neural responses, with the power law exponent optimizing information transmission by removing both short-range and long-range temporal correlations in spike trains (Pozzorini et al., 2013). For the individual fits, the exponents varied between -0.9 and -1.2 (table 4.2). This spread in individual power law components suggests that the characteristic exponent depends on the frequency sensitivity of the neuron and the corresponding temporal correlations, thereby optimizing information transmission in the population of fibers. As seen in the sensitivity analysis for the short duration data (figure 4.3), there is a relationship between

offset and exponent; with a smaller exponent, a smaller offset was required to yield minimal error. For the long duration data, such a relationship was not as clear. When the optimized power law was fitted to a single exponent, the resulting time constant (77 ms for the short duration data, and 60 s for the long duration data) was different from the time constant found in previous studies (100 ms) (van Gendt et al., 2017, 2016). A possible explanation for this is that, in previous studies, the exponent was found by directly optimizing on the data, whereas in the present study the exponent was found by fitting on the optimal power law. Moreover, previously, the time constant of 100 ms was based on a larger number of data sets. Previous studies combined the power law with exponential adaptation to ensure that adaptation on the shortest time scales was properly modeled (Zilany and Carney, 2010). In the model presented here, temporal neural behavior was described by both power law adaptation and refractory behavior, which is exponential with a time constant of approximately 1 ms. Parameters of the approximation with multiple exponents were obtained by a direct fit to the power law and minimizing the error. Alternatively, the error between expected output and simulated neural responses can be minimized directly, but requires much more computational effort. The computational effort depended mostly on stimulus duration and level, and was comparable for power law and exponential adaptation.

Biophysical origins of adaptation

The dynamics of adaptation in the auditory nerve in response to electrical stimulation, and more specifically the dynamics of power law adaptation, can be attributed to underlying phenomena with exponential dynamics. Generally, many biological processes cannot be described by a single exponential time constant, but rather by a sum of exponents with a wide range of time constants. Such a sum yields a single power law, which has been applied to model adaptation in neural systems (Anderson, 2001; Thorson and Biderman-Thorson, 1974). Up to this date it is unclear which biophysical processes cause power law adaptation and whether this is a single process or multiple processes operating on different time scales (Pozzorini, 2014). It has been suggested to be related to ion channel- (Teka et al., 2016; Toib et al., 1998), synaptic- (Fusi et al., 2005), and psychophysical dynamics (Fairhall et al., 2001; Zilany et al., 2009). The synaptic mechanism can be caused either by depletion of presynaptic neurotransmitters, or desensitization of post-synaptic receptors (Zilany et al., 2009). With electrical stimulation of the auditory nerve and recorded peripherally, as in this study, no synapse mechanisms or complex neural networks have been in place. Rather, the power law response in the recordings replicated here is an effect of adaptation in the behavior of the ion channels in the membranes of the auditory neurons.

Ion channels can show power-law dynamics under the assumption of a large number of hidden states (Ben-Avraham and Havlin, 1991; Teka et al., 2016), producing anomalous diffusion with power-law behavior. Such behavior has been shown to accurately capture single channel dynamics (Goychuk and Hänggi, 2004), with phenomenological power-law parameters relating to the transition probabilities between these hidden states. The

exact parameters to be implemented in the kinetics of ion channels to yield the power law dynamics could be evaluated using a biophysical model.

Specific adaptation currents have been suggested in the literature, and have been related to different ion channels and time constants. The most well-known are the voltage-gated potassium (M-) currents, may cause adaptation with time constants of a few milliseconds (Benda and Herz, 2003). Secondly, calcium-gated potassium currents have been shown to cause adaptation with time constants of around 50 milliseconds (Madison and Nicoll, 1984). A third, slower, mechanism is the slow recovery from inactivation of the sodium channels (Vilin and Ruben, 2001). The time constant of the slow inactivation process ranges from a few 100ms up to tens of seconds (Benda and Herz, 2003; Blair and Bean, 2003). Moreover, a model study showed that hyperpolarization-activated cation and low-threshold potassium ion channels may play a role in adaptation with a time scale around 100 ms (Negm and Bruce, 2014). An after hyperpolarization, adaptation current may be generated by a cascade of exponential processes (Drew and Abbott, 2006). The number of relevant processes, the time scales involved, and the parameters required to couple the different processes depend on the duration of stimulation to be simulated.

Implications of power law adaptation behavior

Power law adaptation provides an improved dynamic range and enhanced representation of stimulus dynamics (Fairhall et al., 2001; Mensi et al., 2016). The slow components of adaptation provide information about the context or stimulus statistics, whereas the fast components provide information about the rapid stimulus variations (Fairhall et al., 2001). Because of the slow variations, the human auditory system is sensitive to a wide range of stimulus levels, including levels of soft speech and loud shouting. With power law adaptation, auditory neurons that adapt to sound-level statistics (Zilany and Carney, 2010) are more sensitive to amplitude modulations in the presence of a steady background noise (Zilany et al., 2009) and to abrupt changes, such as those reflected in oddball paradigms (Antunes et al., 2010). When the neuron is adapted to a certain sound level, small variations are better detectable, i.e., just noticeable differences become smaller. A previous modeling study showed that weaker adaptation reduces the vector strength and vice versa, but vector strength is the results of a complex interplay of adaptation, stochasticity and refractoriness (van Gendt et al., 2017). Power law adaptation has been suggested to improve dynamic range, or precision coding in a dynamic environment. The question is whether long term adaptation components would come at the expense of short-term components, yielding the drop in vector strength. Models developed so far slightly underestimate vector strength of phase locking properties of the electrically stimulated auditory nerve (Goldwyn et al., 2010; van Gendt et al., 2017). It would be of great value to further investigate what neural behavior could underlie this strong phase locking. Future simulations with amplitude modulated pulse trains with means slowly varying over time could demonstrate how power law adaptation affects precision coding in a dynamically changing environment.

The modulation rate of the speech envelope is 2 to 50 Hz (Rosen, 1992), and peaks at 3-5 Hz. These slow modulations are important for speech perception. Frequency modulations, often referred to as fine-structure, occur on much shorter time scales. These faster modulations in speech (milliseconds or less) convey information about prosody, melody, intonation, timbre, and the quality of speech. One can expect that, because power law adaptation improves precision coding in a dynamic environment, it also improves the perception of both of these cues. This could be evaluated in a follow-up study including amplitude-modulated signals with different modulation rates and switching stimulus levels.

In CIs, loudness is generally coded by charge, i.e., the amplitude or width of the stimulus pulse, by which a larger number of fibers are stimulated. For normal hearing, loudness increases with a compressive function of sound pressure, whereas for electrical stimulation, loudness increases with an expansive function for increasing stimulation (Vellinga et al., 2017). Moreover, the dynamic range in CI listeners is much smaller than that of normal hearing listeners. Compression can be employed to compensate for the steep build-up in loudness. In addition, in contemporary CIs, matching the dynamic range of naturally occurring sounds to the perceptual dynamic range is improved through the automatic gain control (AGC). The AGC adjusts the loudness cue according to the history of stimulus levels averaged over a certain amount of time, thereby improving the comfortable audibility of a wide range of stimulus levels. These systems are generally slow- or fast-acting or dual. Fast-acting systems aim to evoke the loudness perception most true to nature, whereas slow-acting systems are designed to maintain the audibility of the amplitude differences for the modulation rates conveying speech information (Boyle et al., 2009). With an ideal AGC, neural activation would replicate the situation of natural hearing, and the optimal dynamic range would be achieved. To further optimize existing AGC designs in this direction, the difference in adaptation dynamics between the normal hearing situation and the electrically stimulated degenerated auditory nerve could be established and accounted for by sound processing. The present study shows that power law dynamics best describe the adaptation in the electrically stimulated auditory nerve. Ideally, the dynamics and strength of adaptation of the auditory nerve in an individual CI user would be determined. Subsequently, the adaptation mechanism in the sound-coding strategy could be adjusted so that the stimulation pattern effectively yields activation similar to the normal hearing situation.

In real-life, a CI listener will wear the CI continuously. Although there will be moments of relative quiescence, adaptation will occur continuously to a larger or smaller extent. Consequently, models of the auditory nerve in response to electrical stimulation will have to be tuned to this. Psychophysical experiments generally start in quiet. This may lead to inherent changes within the duration of the experiments. This should be considered while designing an experiment. When one wants to use a desynchronizing pulse train to activate the neurons from an adapted situation (Rubinstein et al., 1999), the duration of stimulation must be evaluated. As can be seen from the recordings (Litvak et al., 2003),

most fibers fire at a constant rate after a stimulus duration of around 200 seconds. This suggests that here the maximum adaptation is reached.

The pulse trains simulated in the current study had pulse rates of 5 kpps. Stimulus rates used in contemporary cochlear implants vary from 800 to 2000 pps, with new developments in the lower frequency range. Because of cross-over stimulation between electrodes, neurons are likely to be affected by much higher rates than the stimulus rates on single electrodes, notwithstanding the fact that there will be a large variability of stimulus rates at the site of the neurons. It has been shown that the stimulus rate has an effect on the spike rate over time for short duration responses (Heffer et al., 2010; Zhang et al., 2007). Previous modelling work showed that such differences over time can be replicated with a single model with the same parameters (van Gendt et al., 2016). For long duration electrical stimulation, unfortunately, such experimental data of neural responses to a variety of stimulus rates is not available. Such data would enable validation of, or optimization of the power law parameters (alpha, beta and offset) for low rate pulse trains. To investigate the theoretical effect of power law adaptation on clinically used, lower rate pulse trains, responses to long duration stimulation with 800 and 1800 pps were simulated, results are shown in figure 4.6.

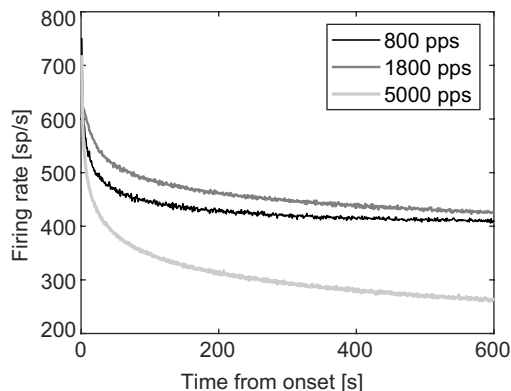


Figure 4.6. Response rates simulated with power law adaptation (offset = 5 ms, exponent = -1, accommodation = 6×10^{-4} % of stimulus, adaptation = 0.02% of threshold) for long duration pulse trains (600 seconds) with different stimulus rates; 800 pps (black), 1800 pps (middle grey) and 5000 pps (light grey). For all pulse trains the stimulus level was used that elicited the 720 spikes in the first second in response to the 5kpps pulse train.

Figure 4.6 shows that also with lower rates the induced firing rates are expected to decrease over a long period of stimulation. The lower stimulation rates (800 and 1800 pps) had higher sustained firing rates than the response to 5000 pps, in which the neuron was supposedly less affected by adaptation and refractoriness. The sustained firing

rates in response to 800 and 1800 pps are very similar. The exact response is the result of a complex interplay between refractory properties, accommodation, adaptation, and stimulus rate, and therefore dependent on stimulus rate in a nonlinear manner.

Limitations and suggestions for further research

The optimal parameter set was found via direct comparison of the simulated and recorded spike rates. However, especially for the long duration simulations, the model did not replicate some anomalous behavior of the recorded spike rates. Examples of this behavior were the dip in response rates around 50 ms and the continuous decrease in the strongest responding neuron. This latter observation may have been a result of continuing damage being done to the neuron due to the recording electrode, or displacement of the recording electrode. A larger number of these kinds of recordings from neural fibers would be required to determine whether this is an intrinsic neural behavior that should be modeled, or whether it is merely an effect of the recording method.

The short duration data fitted in this paper were all obtained from a single neuron. The other two fibers presented in Zhang et al. (2007) did not show the continuous decrease and were already reliably simulated by the model with a single exponent. Such inter-fiber differences indicate great variability between fibers in adaptation behavior. The improved fit on long duration data when optimized per fiber indicates that different fibers require a different parameter set and exhibit different neural behaviors. More experimental data is needed to obtain ranges for the parameters in auditory neurons. A previous study showed that the strength of adaptation may be related to the health of the auditory nerve (van Gendt et al., 2019). How the characteristics of the power law adaptation relate to neural health is unknown, but could be evaluated in a physiological study.

In a follow-up study, the effect of the amount of adaptation on long duration stimulation, especially speech segments, should be evaluated. An interpretation model that can relate the neural spiking to perceptual outcomes will be required. Hypotheses relating neural adaptation to increased dynamic range and loudness discrimination could be tested. In addition, the effect of diminished adaptation, in amplitude or temporal length, as may occur in a degenerated auditory nerve, on perceptual outcomes could be tested. Besides evaluating how the neural behavior can be expected to be related to perceptual outcomes, the model can also be used to compare different sound-coding strategies. After validation, new approaches to sound coding can be tested efficiently. With the model presented here, the performance of new designs and strategies in the perception of long duration speech segments can be evaluated.

Appendices

A. Exponential model formula and parameters

- Relative spread: $\sigma = I_{th} \cdot RS$
- Refractoriness: $R = 1 - e^{-\frac{t-\tau_{ARP}}{\tau_{RRP}}}$
- Adaptation: $AF = \sum_i ampl_{adap} \cdot e^{-\frac{t-t_i}{\tau_{adap}}}$
 - Every pulse: adaptation amplitude is increased:
Adaptation parameter:
 $ampl_{adap} = ampl_{adap}(oud) + \text{Adaptation amplitude} \cdot \text{threshold (initial)}$
 - Every spike: adaptation amplitude is increased (accommodation):
Adaptation parameter (accommodation):
 $ampl_{adap} = ampl_{adap}(oud) + \text{Accommodation amplitude} \cdot \text{stimulus current} \cdot \text{spatial factor}$
 - $\text{spatial factor} = \frac{I_{\min}(\text{electrode})}{I(\text{electrode, fiber})}$
- Total model: $I_{final,th} = N(I_{th}, \sigma) \cdot R + AF$

Table A.1: Model parameters

Parameter	Value
RS	0.06
τ_{ARP}	0.4 ms
τ_{RRP}	0.8 ms
Within refractoriness stochasticity	5% of τ_{ARP}/τ_{RRP}
Adaptation amplitude	1% of threshold
Accommodation amplitude	0.03% of stimulus current spatial factor

B. Power law approximation with exponents

Table B.1: Fitted exponents and their weights to approximate the power law for short duration data. Exponential time constants and weights for the fit to power law with $\beta = -1$ and offset = 20 ms.

1 exp in ms weight	77				
2 exps in ms weights	23 0.72	212 0.26			
3 exps in ms weights	17 0.61	80 0.28	376 0.13		
4 exps in ms weights	15 0.52	50 0.28	159 0.14	512 0.07	
5 exps in ms weights	14 0.45	36 0.27	93 0.16	237 0.09	606 0.05

Table B.2: Fitted exponents and their weights to approximate the power law for long duration data. Exponential time constants and weights for the fit to power law with $\beta = -1$ and offset = 5 ms.

1 exp ms weights	6e5 2.5e-4									
2 exps ms weights	21 0.76	6e5 1.9e-4								
3 exps ms weights	10 0.86	150 0.13	6e5 1e-4							
4 exps ms weights	6.3 0.81	49 0.25	748 0.03	6e5 1.1e-4						
5 exps ms weights	5 0.71	26 0.35	197 0.067	2.8e4 7e-3	6e5 1e-4					
6 exps ms weights	3.8 0.61	17 0.41	88 0.11	628 0.021	7.8e3 2.3e-3	6e5 5.9e-5				
7 exps ms weights	4 0.56	14 0.43	68 0.13	407 0.028	3608 4.1e-3	6.5e4 2.9e-4	6e5 1.9e-5			
8 exps ms weights	3 .50	12 0.45	48 0.17	239 0.042	519 7.9e-3	134e2 1.0e-3	897e2 1.0e-4	6e5 2.8e-5		
9 Exps ms weights	2.8 0.43	9.4 0.47	35 0.20	140 0.061	710 0.014	4.1e3 2.6e-3	2.2e4 4.5e-4	1.1e5 8.6e-5	6e5 2.3e-5	
10 exps ms weights	2.4 0.35	7.3 0.47	23 0.25	82 0.089	320 0.026	1.4e3 6.6e-3	7.1e3 1.3e-3	3.1e4 2.7e-4	1.4e5 6.2e-5	6.0e5 2.2e-5

CHAPTER 5

Effect of neural adaptation and degeneration on pulse-train eCAPs: a model study

Margriet J. van Gendt

Jeroen J. Briaire

Johan H.M. Frijns

Abstract

Electrically evoked compound action potentials (eCAPs) are measurements of the auditory nerve's response to electrical stimulation. ECAP amplitudes during pulse trains can exhibit temporal alternations. The magnitude of this alternation tends to diminish over time during the stimulus. How this pattern relates to the temporal behavior of nerve fibers is not known. We hypothesized that the stochasticity, refractoriness, adaptation of the threshold and spike-times influence pulse-train eCAP responses. Thirty thousand auditory nerve fibers were modeled in a three-dimensional cochlear model incorporating pulse-shape effects, pulse-history effects, and stochasticity in the individual neural responses. ECAPs in response to pulse trains of different rates and amplitudes were modeled for fibers with different stochastic properties (by variation of the relative spread) and different temporal properties (by variation of the refractory periods, adaptation and latency). The model predicts alternation of peak amplitudes similar to available human data. In addition, the peak alternation was affected by changing the refractoriness, adaptation, and relative spread of auditory nerve fibers. As these parameters are related to factors such as the duration of deafness and neural survival, this study suggests that the eCAP pattern in response to pulse trains could be used to assess the underlying temporal and stochastic behavior of the auditory nerve. As these properties affect the nerve's response to pulse trains, they are of uttermost importance to sound perception with cochlear implants.

1 Introduction

Electrically evoked compound action potentials (eCAPs) arise from the auditory nerve's response to electrical stimulation. ECAPs are often measured in cochlear implant (CI) recipients, the clinical applicability is widely studied (e.g. Al Muhaimed et al., 2010; Hughes et al., 2000; Mittal and Panwar, 2009) and for a review see de Vos et al. (2017). In the most conventional eCAP measurements, a forward masking paradigm is used to obtain information about the neural response to a single pulse. The N1-P2 peak in that response provides insight into the number and location of fibers firing in response to the given stimulus. In a different approach (Wilson et al., 1994), the neural response to a train of pulses can be measured, an example of which is shown in figure 5.1 (Hughes et al., 2012). In the present study, this type of measurement is replicated using a comprehensive computational model.

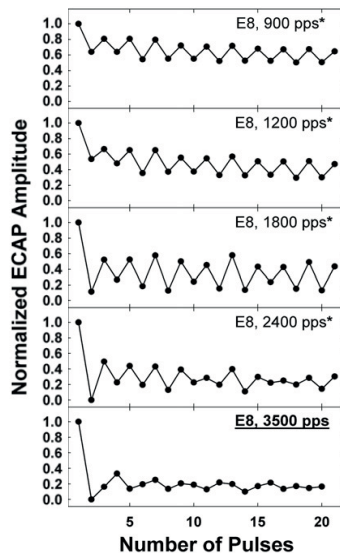


Figure 5.1. Human eCAP data in response to constant amplitude pulse trains (Hughes et al., 2012) Reprinted with permission.

eCAP measurements in response to pulse trains were first performed in humans by Wilson et al. (1994), who showed alternating eCAP amplitudes in response to certain stimulation rates. Such responses to pulse trains with rates up to 4000 pps were then studied in several groups of CI users (figure 5.1) (Hughes et al., 2014, 2012; Wilson et al., 1997, 1994). This alternation pattern is most clearly seen at rates of 1000-2000 pps and is thought to be an effect of refractoriness and membrane noise. At higher rates, the alternating pattern disappears, probably due to asynchronous firing. The rate at which the alternation disappears is sometimes referred to as the stochastic resonance frequency.

This was hypothesized to be a desirable state of the auditory nerve as the nerve then may be sensitive to small input fluctuations, and could be obtained by including a noise conditioner (Rubinstein et al., 1999). Overall eCAP amplitudes decrease at higher pulse rates, which is thought to be related to adaptation and accommodation (Cohen, 2009; Hay-McCutcheon et al., 2005; Schmidt, Clay, and Brown, 2007). Animal studies show similar behavior of the pulse-train eCAP (Abbas et al., 1999; Campbell et al., 2012; Haenggeli et al., 1998; Jeng et al., 2009; Loquet et al., 2004; Matsuoka et al., 2000; Ramekers et al., 2015).

Several researchers have attempted to correlate the pulse-train eCAP in response to psychophysical measures of temporal processing (e.g., gap detection, pitch perception, and loudness summation) or speech perception (Hay-McCutcheon et al., 2005; Huarte et al., 2014; Hughes et al., 2014; McKay et al., 2013; Zhang et al., 2013). Better pitch perception was shown to be related to lower alternations in responses (Carlyon and Deeks, 2015). There is however a large inter-patient variability in the eCAP alternation and correlations with psychophysical measures, which therefore up to this date remains a subject of debate.

As sensorineural hearing loss results in a reduction in the spiral ganglion cell population and demyelination of the peripheral dendrites up to the central axon (Leake and Hradek, 1988), differences in morphology and physiology of auditory neurons may be a major cause of the variable outcomes observed in CI users. Hearing loss and altered neural refractoriness have been shown to occur concomitantly. Ramekers et al. (2015) studied the effect of deafness on the eCAP response to pulse trains, comparing eCAP data to histology. Pulse-train eCAP responses in deafened animals showed an increase in normalized eCAP amplitude and eCAP alternation at specific rates at the end of 100-ms stimulation. The time course of SGN degeneration after deafness seems to be species-dependent (Kalkman et al., 2016). For instance, in cats, Leake and Hradek et al. (1988) showed continuous degeneration of spiral ganglion neurons, which could progress over up to several years, following administration of ototoxic drugs. On the contrary, in humans a gradual degeneration of the peripheral processes is suggested, where possibly after long duration deafness only the unmyelinated terminal disappears (Snel-Bongers et al., 2013).

Though most research on pulse-train eCAPs has focused on constant-amplitude pulse trains, some studies have measured responses to amplitude-modulated input, both in humans and animals (Abbas et al., 1999; Jeng et al., 2009; Tejani et al., 2017; Wilson et al., 1997, 1994). Such measurements are relevant to contemporary CIs, which encode speech by transferring the envelope and amplitude modulations in the speech signal. Tejani et al. (2017) found an increased modulated response amplitude (MRA) with increased modulation frequency, attributing this to neural adaptation. The MRA was defined as the average difference between the minimal and maximal eCAP response over one modulation cycle. Comparing the MRA to the modulation detection thresholds in the same patients revealed a trend of better modulation detection, with larger MRA in the lower frequencies, indicating a potential role for a central limiting factor. A comprehensive

neural model could be used to test and better understand the effect of these modulation depths, as well as the effects of other parameters, such as neural adaptation and stimulus amplitude, on MRA.

Biophysical models can reproduce the effect of stimulus parameters on auditory neurons (Dekker et al., 2014; Frijns and ten Kate, 1994; Mino et al., 2004; Reilly et al., 1985; Resnick et al., 2018; Woo et al., 2009). However, modeling the response of large numbers of auditory nerve fibers to pulse trains requires a lot of computational power. To reduce computational demands, phenomenological models have been developed to predict eCAP responses to sustained stimulation. These models have included stochastic and temporal behavior (I. C. Bruce et al., 1999; Chen and Zhang, 2007; Macherey et al., 2007; van Gendt et al., 2017, 2016; Xu and Collins, 2007). Previous modeling work has shown that the alternating pattern may be produced by interactions between refractoriness and stimulus rate. For short-duration stimuli, a model that includes latency, jitter, membrane stochasticity, and refractoriness predicts human responses very well (Hamacher, 2004; Matsuoka et al., 2000; Rubinstein, 1995; Wilson et al., 1994). Membrane stochasticity is described by the relative spread parameter (RS). RS is defined as the standard deviation of the Gaussian distribution of thresholds divided by its mean (Verveen and Derksen, 1968). Simulations showed, depending on the stimulus rate, a smaller alternation depth with larger RS. Campbell et al. (2012) found that inclusion of adaptation removed the overestimation of probability of firing after a longer duration of stimulation. Thus, patterns in the eCAP response to pulse trains provide insights into the temporal behavior of the auditory nerve. Our biophysical model is the first that combines pulse shape, geometry of current spread, a realistic number of auditory neurons, and phenomenological stochastic parameters of short-term and long-term behavior. By combining this with a unitary response, we were able to reproduce human whole-nerve responses to pulse trains.

The goal of this study was twofold; firstly to validate the previously published model (van Gendt et al., 2017, 2016) with human data, and secondly to investigate the effect of neural parameters on the pulse-train eCAP. The investigated neural parameters were adaptation and accommodation, refractoriness, relative spread, jitter, and the number of fibers, which are important for sound perception with a cochlear implant. By using a model of the auditory nerve's response to CI stimulation we try to understand the origin of the pulse-train eCAP response, inter-patient variability in those responses, their relationship with psychophysical measurements, and the effect of hearing loss on these responses. We hypothesize that neural degeneration may be related to abnormal refractoriness and adaptation, and that the effect of both refractoriness and adaptation are visible in the pulse-train eCAP responses.

2 Methods

2.1 Model

eCAP responses to constant-amplitude and amplitude-modulated pulse trains produced and detected with a CI were simulated. The modeled nerve consisted of 32,000 stochastically independent neural fibers at 3200 different spatial locations. Electric-field spread of the stimulus and its effect on neural thresholds was calculated using the three-dimensional volume conduction model and an active nerve fiber model (Frijns et al., 1995; Kalkman et al., 2015, 2014). This model was extended with empirical parameters for refractoriness, membrane stochasticity, adaptation, and accommodation based on single-fiber animal studies (van Gendt et al., 2017, 2016). For each fiber, all phenomenological parameters were chosen randomly from a pre-defined normal distribution as described by van Gendt et al. (2016, 2017). Deterministic thresholds were obtained for single pulses with specific pulse shapes and pulse widths. The accommodation parameter is dependent on the pulse width. Monopolar biphasic pulses with a pulse duration of 25 μs were used for the simulations. The 1J electrode array with 16 electrode contacts was placed in the model. The electrode contact located roughly 180° from the round window was stimulated. Figure 5.2 shows the threshold profile related to this electrode based on the thresholds from the deterministic model for each fiber. A description of the complete model and validation for single fiber responses to constant-amplitude and amplitude-modulated pulse trains can be found in previously published papers (van Gendt et al., 2017, 2016). In addition to the previously used parameters, a spike time latency was implemented, with the mean latency value referring to the delay between stimulus and spike, and with the jitter value referring to the standard deviation of the latency.

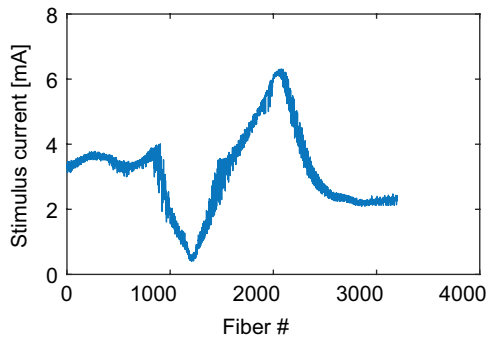


Figure 5.2. Threshold profile for electrode 8 (located 180° from the round window). The line shows the threshold for each individual fiber. Pulse-width used is 25 μs . The fibers have equidistant locations along the basilar membrane. Location #1 refers to the fiber closest to the round window, #3200 is the most apically located fiber.

The model is validated to predict spike timings of neurons in response to pulse trains (van Gendt et al., 2017, 2016). To calculate the eCAP responses, these predicted pulse timings were convolved with an estimation of the unitary response (Miller et al., 1999b). This unitary response was derived using the method proposed by Goldstein and Kiang (1958), who assumed that the eCAP(t) is a convolution of the compound PST histogram, $P(t)$, and the unitary response $U(t)$ as described in equation 5.1;

$$eCAP(t) = \int_{-\infty}^t P(\tau) \cdot U(t - \tau) d\tau \quad (\text{Eq. 5.1})$$

The unitary response was obtained by deconvolving a typical eCAP waveform with a modeled post-stimulus time (PST) histogram, assuming an equal contribution of all fibers to the neural eCAP (Miller et al., 1999b). The current paper uses Miller et al.'s unitary response based on a cat's eCAP response to a monophasic anodic pulse of 39 μs and based on the assumption that all fibers contribute equally to the response. This latter assumption is validated by studies showing that fiber diameters of different regions of cochlear innervation are comparable (Arnesen and Osen, 1978; Liberman and Oliver, 1984). Figure 5.3 shows the predicted unitary response as included in the current model (Miller et al., 1999b). The shape of the unitary response is a scaled version of the eCAP waveform.

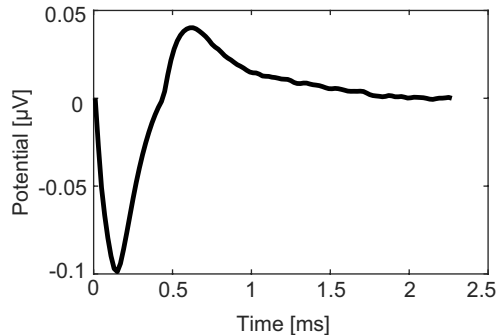


Figure 5.3. Unitary response used in the simulations (after Miller et al., 1999). Since a unitary response is assumed, the y-axis is directly proportional to the eCAP amplitude.

This unitary response is subsequently convolved with all our predicted spike timings per fiber $R(t)$ and the resulting response in time is summed over all fibers (f), as described in equation 5.2;

$$eCAP(t) = \sum_{f=1}^{32000} \sum_{\tau=-\infty}^t R(t) U(t - \tau) d\tau df \quad (\text{Eq. 5.2})$$

2.2 Stimulus levels

To investigate the effect of stimulus level on the eCAP response the stimulus levels were varied; levels of 1.2, 1.5 and 1.8 mA were used. Figure 5.4 shows the growth in neural recruitment with stimulus level for different rates. The initial (deterministic) thresholds are determined by the 3D volume conduction and the cable model (Kalkman et al., 2014). In the deterministic model, threshold and most comfortable loudness levels are defined by the number of excited neurons, based on observations in current steering experiments (Snel-Bongers et al., 2013). This corresponds to 1- and 4-mm excitation along the basilar membrane in the 3D cochlear model, which in our current model corresponds to 1000 and 4000 excited neurons.

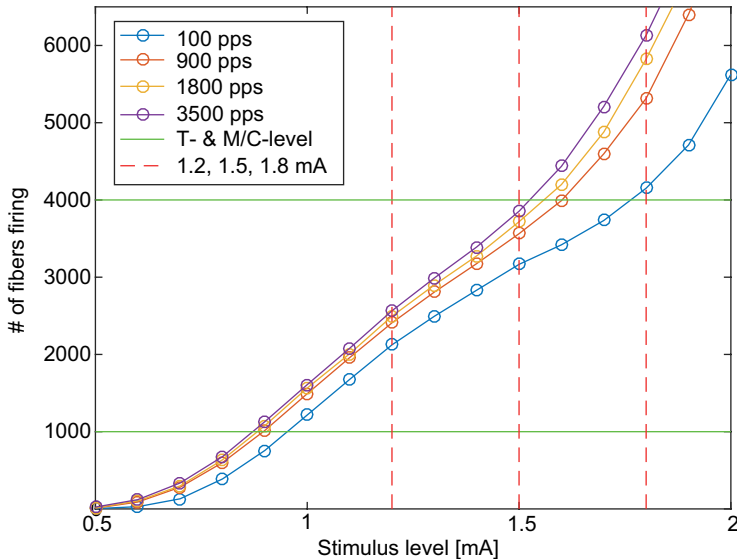


Figure 5.4. total number of fibers firing in response to a 150-ms pulse train for pulse rates from 100 to 3500 pps. The green solid lines show where the T- (1000 fibers, 1mm, see explanation in section 2.2) and M/C (4000 fibers, 4mm, see explanation in section 2.2). The red dotted lines indicate stimulus levels used in the other stimulations.

Despite the fact that the parameters are chosen within physiological boundaries, the resulting predicted thresholds of the neural cable model are much higher than those seen in patients, which is a known issue in cable models (Kalkman et al., 2016). Thus, while single-fiber electrophysiological recordings are well predicted, there are discrepancies with whole nerve recordings, which are not yet understood. Absolute stimulus levels used in our model can therefore not be quantitatively related to those used in patient studies, but we can interpret the levels in terms of the dynamic range (the stimulus level relative to T- and M/C-levels).

2.3 Variation of model parameters

The model was validated by comparing its output in response to pulse trains with existing human data using the standard parameters shown in table 5.1. To investigate the effect of adaptation, refractoriness, relative spread, and the number of functional fibers on the eCAP responses to pulse trains, model parameters were varied as shown in table 5.1. The values for RS and refractory periods were based on literature. Animal experiments have shown that RS is dependent on pulse shape and ranged from 0.07 ± 0.07 for monophasic to 0.12 ± 0.06 for biphasic pulse shapes, all measured in cats (Bruce et al., 1999b; Javel et al., 1987; Miller et al., 1999a). To investigate both the average and very extreme cases, we have chosen to set the RS to 0.06 ± 0.04 in the standard parameter setting, and to 0.0 ± 0.0 and 0.12 ± 0.08 in the extreme ranges. For refractoriness, the absolute refractory period (ARP) and the relative refractory period (RRP), data are available from animal experiments combined with computational modeling (Dynes, 1996; Miller et al., 2001). Estimated ARP values ranged from 0.3 ± 0.1 (Miller et al., 2001) to 0.7 ms (Dynes, 1996) and RRP values from 0.4 ± 0.2 to 1.32. These extreme values were all characterized in cats. For humans, values were around 0.7 ms based on eCAPs by using an exponential fit (Cartee et al., 2000). To cover the whole range of experimental data, our average parameter settings for ARP and RRP were set to 0.4 ± 0.1 and 0.8 ± 0.5 respectively, whereas for the extremes these values were multiplied by 0.5 and 1.5, resulting in ARP and RRP values of 0.2 ± 0.05 and 0.4 ± 0.25 for the low refractory and 0.6 ± 0.15 and 1.2 ± 0.75 for the high refractory case.

The standard adaptation and accommodation values were all based on our previous modeling work (van Gendt et al., 2017, 2016), where these values were derived by comparison of the model output with published animal data (Litvak et al., 2001; Miller et al., 2008; Zhang et al., 2007). To investigate the necessity of including adaptation and accommodation in a model of cochlear implant stimulation, the model was also run without these effects. To test the sensitivity of the response to the chosen values, the parameters were varied to the extreme high adaptation/accommodation scenario. These extreme values are double the average values, chosen as such because of the large standard deviation on the adaptation parameter as determined in the previous modeling work.

The model has 32,000 fibers, which closely matches the number of type I auditory nerve fibers in the normal-hearing human situation. As an extreme case of neural degeneration a uniformly distributed neural survival of 10% was chosen. In some simulations jitter and latency were implemented using the parameters reported in cats (Miller et al., 1999a). For the simulations, both constant-amplitude and amplitude-modulated pulse trains were used.

Table 5.1. Model parameter variations. RS = relative spread, ARP = absolute refractory period, RRP = relative refractory period, Adap = adaptation, Acco = accommodation, # fbrs = number of fibers, Lat = latency, Jit = jitter

	RS	ARP, ms	RRP, ms	Adap	Acco	# fbrs	Lat, ms	Jit, ms
Standard	0.06 ± 0.04	0.4 ± 0.1	0.8 ± 0.5	1 ± 0.6	0.03	32,000	0	0
Low	0	0.2 ± 0.05	0.4 ± 0.25	0	0	3200	-	-
High	0.12 ± 0.08	0.6 ± 0.15	1.2 ± 0.75	2 ± 1.2	0.06	-	0.7	0.07

Experiment A: short-duration pulse trains

To validate the model with human data, human recordings as published by Hughes et al. (2012) were simulated with standard parameter settings as listed in row 1 of table 5.1. To evaluate the effect of neural parameters these simulations were replicated with the model parameters as indicated in rows 2 and 3 of table 5.1. In each of these simulations, one parameter was varied to either the low or high extreme value. To replicate the recordings by Hughes et al., constant-amplitude pulse trains with rates of 900, 1200, 1800, 2400, and 3500 pps were used. Stimulus amplitude was set to 1.5 mA. The effect of neural degeneration was tested by comparing 10% neural survival distributed evenly over the cochlea with the 100% neural survival situation (32,000 fibers). Responses to the first 20 pulses were simulated, the total stimulus duration was thus dependent on the rate. Results were normalized to the amplitude obtained in response to the first pulse. The alternation depth was calculated as the difference between the average normalized response to the odd and even pulses from pulse numbers 2 to 21.

Experiment B: short-duration, low-rate pulse trains

eCAPs in response to 100-ms, low-rate, pulse trains as measured in CI listeners by Carlyon and Deeks (2015) were simulated for comparison to human data and to investigate the effect of neural parameters and stimulus amplitude. Alternation depth was defined as the ratio between the responses to the odd and even pulse numbers. Responses to stimulation rates of 100, 130, 200, 270, 300, 400, and 500 pps were simulated, and stimulus levels of 1.2 and 1.5 mA were used. For the stimulus amplitude of 1.2 mA, varying model settings were evaluated. In the experiments done by Carlyon and Deeks (2015) stimulation rates up to 500 pps were used, whereas in the experiments by Hughes et al. (2012) rates of 900 pps and higher were used. To investigate whether the simulations of the two studies would have been the same when the same rates were used, the simulations were repeated with a stimulus rate of 900 pps.

Experiment C: long-duration pulse trains

Predicted eCAP responses to 100-ms pulse trains were compared to animal data published by Ramekers et al. (2015) in order to investigate the temporal and stochastic effects on responses to longer duration pulse trains. Stimulus rates were set to 125, 250, 500, 625, 1250, 1667, and 2500 pps. The stimulus amplitude was 1.2 mA. The responses were predicted with the standard parameter settings and the parameter variations listed in table 5.1. Uniformly distributed neural survival rates of 100% and 10% were tested.

Experiment D: amplitude-modulated pulse trains

Responses to 100-ms amplitude-modulated pulse trains were simulated and compared to previously published animal data (Jeng et al., 2009). The amplitude used was 1.5 mA, and different model parameter settings were evaluated. The modulation depth was set to 10% and modulation frequency to 25, 50, 100, 200, 300, and 400 Hz. The carrier rate was 1000 pps.

Experiment E: Short-duration amplitude-modulated pulse trains

Responses to 15-ms amplitude-modulated pulse trains were simulated and the resulting modulation response amplitudes compared to published human data (Tejani et al., 2017). Stimulus amplitudes of 1.5- and 1.8-mA were used to mimic patient measurements. At the lowest amplitude and 30% modulation depth, both complete and partial (10%) neural survival was simulated. Full nerve simulations were performed with all parameter settings as shown in table 5.1. The modulation depth was set to 10%, 20%, and 30% and modulation frequency varied to 125, 250, 500, and 1000 Hz. As in the experiments with humans, the carrier rate was 4000 pps. Tejani's detection of modulation as a function of MRA was used to evaluate the modulation following behavior, with a larger MRA implying increased modulation following behavior of the auditory nerve. These simulations were performed to investigate whether the modulation following behavior was determined mostly by stimulus parameters, or by the neural properties as suggested by Tejani et al.

3 Results**3.1 Experiment A: Short-duration pulse trains**

The responses to short-duration pulse trains are shown in figures 5.5 and 5.6, with summary data shown in table 5.2. Simulated eCAP responses obtained with four different model settings when stimulated with pulse trains of 1.5 mA are shown in figure 5.5. Removal of adaptation did not change the auditory nerve's response to this stimulation. With a shorter refractory period, the alternation pattern was stronger at higher stimulus rates, and the decrease in average response amplitude from the first to the last pulse was somewhat smaller for all rates than when standard parameter settings were used. Removal of RS, i.e., making the fibers deterministic, led to enhanced alternation and did not affect the preferred stimulation rate for alternation. With lower stimulus amplitudes (data not shown), similar behavior was observed, though a slightly larger relative decrease occurred quickly after the onset of stimulation at the lowest two rates. When only 10% of the fibers were modeled, the results were very similar to when 100% of the neurons were included in the model and are therefore not plotted.

Table 5.2. Summary of the effects of each model perturbation on both the eCAP alternation depth and the eCAP response amplitude, as shown in more detail in figure 5.6;

Model perturbation:	eCAP alternation depth:	eCAP response amplitude:
Short refractoriness	Decrease for low rates Increase for high rates	Increase
Long refractoriness	Minor decrease at rates 1200 & 1800 pps	Decrease
Deterministic	Increase	Minor decrease
High RS	Minor decrease at rate 900 pps	Minor increase

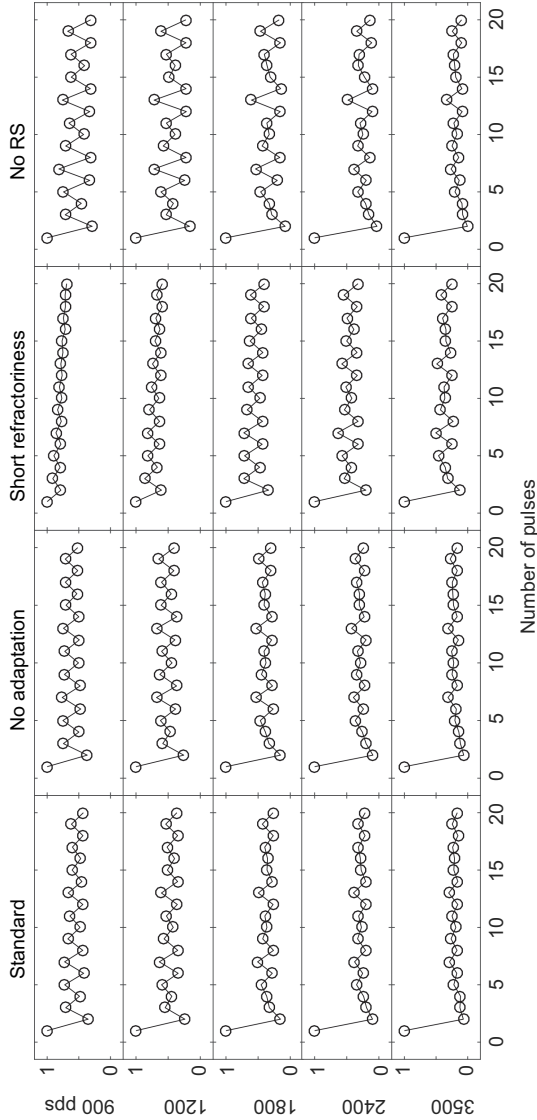


Figure 5.5. Simulations of eCAPs in response to different pulse rates. Responses to the first 20 pulses are plotted. The first column shows results obtained with the standard model parameters, the second column without adaptation, third column with short refractoriness and the fourth with deterministic parameter settings (without relative spread).

The average eCAP alternation depth and relative eCAP amplitude for each of the model parameter settings are shown in figure 5.6 for stimulation with 1.5-mA pulse trains. The results are plotted as lines overlaying the figure published by Hughes et al. (2012). By changing neural parameters, the predicted alternation depth and amplitude exhibit variability similar to that seen in the experimental data. As visible in figure 5.6A, the maximum alternation depth occurred from 900 to 1800 pps with the standard model parameters, which matches the human data. In both the human and simulated data, the alternation depth decreased when stimulated with rates of 2400 and 3500 pps. Removal of RS shifted the eCAP alternation depth at all stimulus rates tested. Both the standard parameter set and the sets with adjusted threshold stochasticity exhibited response amplitudes within the range of one standard deviation of the human data. Decreasing the refractory period increased the rate at which maximum alternation depth was visible from 900 pps in the standard model to 1800 pps, which matches the human data better. However, with this decrease the alternation depth was underestimated at 900 pps and overestimated at the highest two stimulation rates. Figure 5.6B shows that the normalized eCAP response amplitudes decreased with rates in all simulation modes, as well as in the human data. Increasing and decreasing the refractory periods caused a decrease and increase, respectively, in the normalized amplitude for all rates. Changing the adapting behavior of the neuron did not change the alternation depth or amplitude in these short duration experiments and was therefore not plotted in figure 5.6.

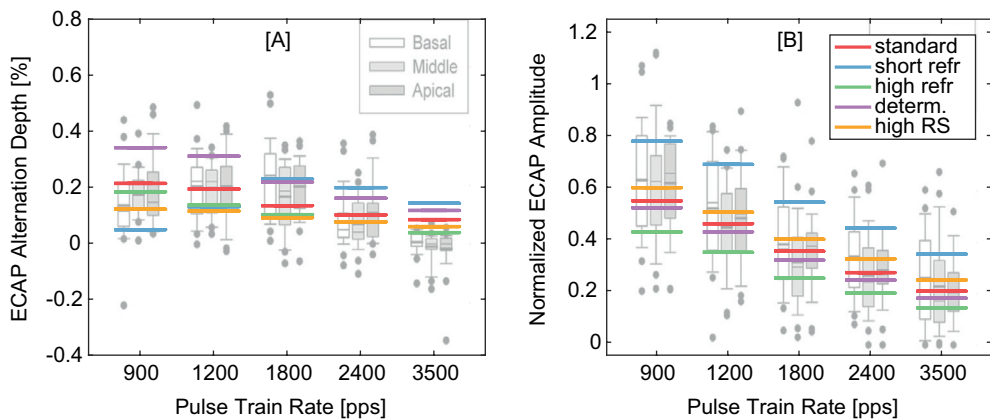


Figure 5.6. Average alternation depths [A] and eCAP amplitudes [B] for a stimulus amplitude of 1.5 mA. Normalization is achieved by dividing the eCAP amplitudes by the amplitude in response to the first pulse. Colors indicate the model setting used. Background image in grayscale shows the human data published by Hughes et al. (2012). Reprinted with permission

3.2 Experiment B: Short-duration, low-rate, pulse trains

In figure 5.7 the results obtained with the standard parameter settings and two different stimulus amplitudes (1.2 and 1.5 mA) are compared. Both amplitudes evoked eCAP modulations similar to the lower range of modulations seen in human data by Carlyon and Deeks (2015). Some patients' eCAP responses exhibited much larger alternations, up to 30% at 500 pps. This could be achieved in the model by increasing the refractory periods, or by using a deterministic model by omitting the threshold stochastics. The removal of threshold adaptation of the neuron did not change the predicted alternation amplitudes. The modulation amplitude increased with refractory period at low stimulus rates. It decreased at short refractory periods compared to the standard parameter setting, as similarly seen for the low rates in figures 5.5 and 5.6. The minor differences in alternation amplitude between the 900-pps simulations in figure 5.6 and 5.7 can be explained by the fact that stimulus levels and durations slightly differed. This was necessary because we intended to replicate the experiments performed in human subjects

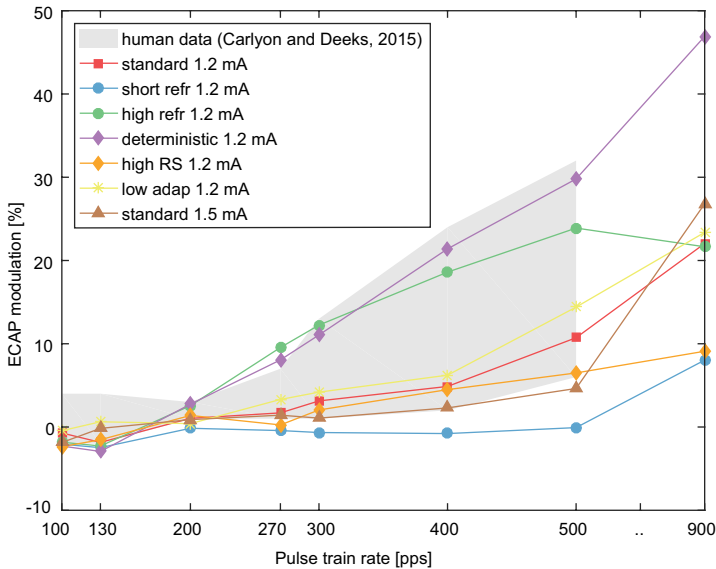


Figure 5.7. Percentage eCAP modulation in simulated responses to 100-ms pulse-trains. Responses predicted to 100, 130, 200, 270, 300, 400, and 500 pps for two different stimulus levels and varied parameter settings, which were compared to human data from Carlyon and Deeks (2015), which appears in grey as a reference. Also, stimulations with 900 pps are included to allow comparison with the data by Hughes et al (figure 5.6).

3.3 Experiment C: Long-duration pulse trains

Figure 5.8A-C show simulated normalized responses to 1.2-mA, constant-amplitude, pulse trains, at the last 10 pulses of stimulation. Results for the standard parameter setting and two model settings, namely one with longer refractory periods and one where the adaptation property was removed from the model, are shown in the respective figure 5.8A-C. Figure 5.8B shows that elongating the refractory periods by multiplication with a factor of 1.5 did change the eCAP response pattern by less than 10% compared to the standard parameter setting. The average eCAP amplitude at the end of the pulse train was slightly lower at longer refractory periods than in the standard parameter setting. Removal of adaptation (figure 5.8C) caused more alternation at the end of the pulse train for pulse rates of 500 to 1250 pps. The average response amplitude increased up to about 100% when adaptation was removed (e.g. 1667 pps, figure 5.8C). Both increased eCAP alternation and increased eCAP amplitude were also seen in the animal data after deafening (figures 5.8E and F). Figure 5.8D shows the predicted alternation amplitudes for the three different model settings, when stimulated with different IPIs. The largest alternation was seen when the adaptation property was removed (yellow line). Figure 5.8G shows the measured maximum alternation on a group level, where the largest alternations are visible after 6 weeks of deafening (black line).

Removal of RS also led to increased alternation amplitudes, but with average response amplitudes comparable to the situation with RS set as in the standard parameter setting. Unlike these predictions, data from deafened animals showed an increased normalized response amplitude at the end of the pulse train. Runtimes of the action potential, as investigated by inclusion of latency and jitter, as well as the number of fibers, did not affect the shape of the pulse-train eCAPs.

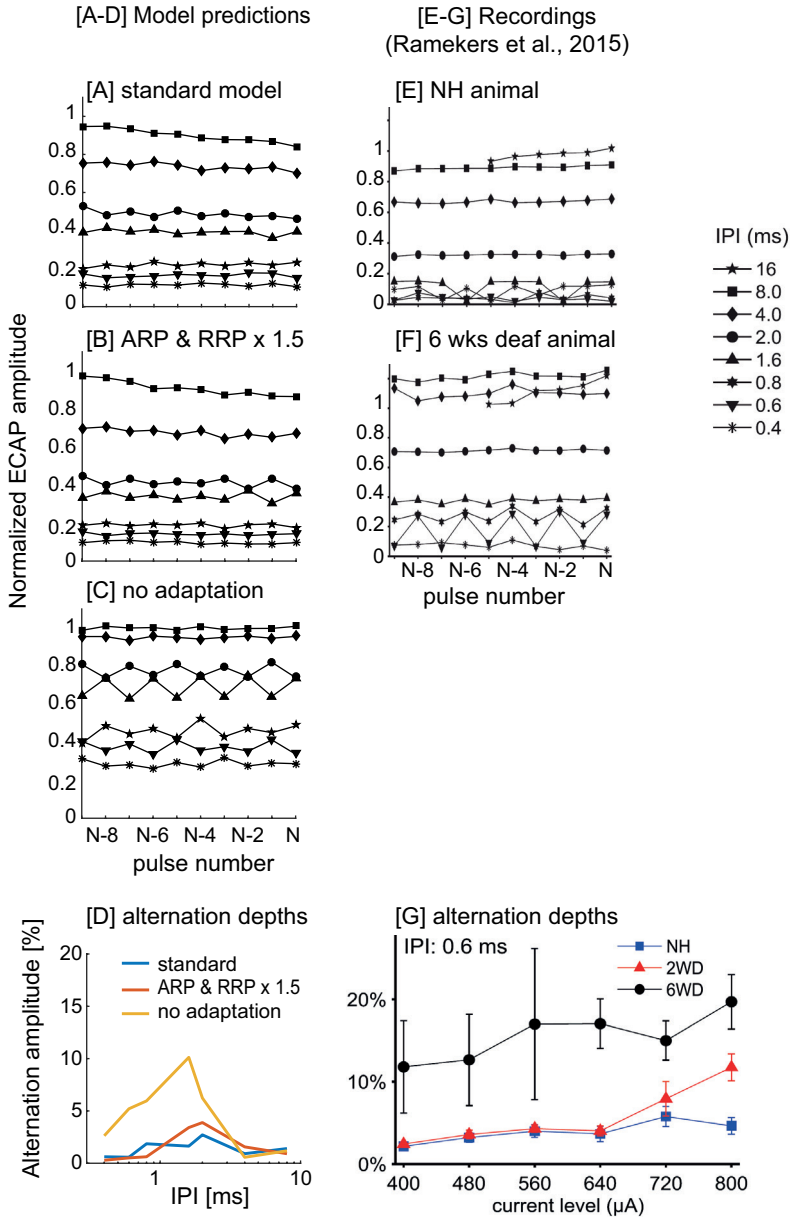


Figure 5.8. Effect of temporal properties on eCAPs in 100-ms pulse trains. [A-D] model predictions [A] Results obtained with the model with standard parameters. [B] Results obtained with elongated refractory periods or [C] without adaptation. Stimulus amplitude was 1.2 mA. [D] alternation amplitudes for the three different model perturbations at different IPI's [E-G] experimental data by Ramekers et al. (2015), reprinted with permission [E] experimental results obtained in a normal-hearing guinea pig [F] experimental results obtained in the same guinea pig, six weeks after deafening [G] group results of the average alternation in normal-hearing, 2 weeks deaf and 6 weeks deaf guinea pigs, observed at an IPI of 0.6 ms, plotted as a function of stimulus amplitude.

3.4 Experiment D: Long-duration amplitude-modulated pulse trains

The responses to amplitude-modulated pulse trains of long duration are shown in figure 5.9. Note that, in these responses, the absolute amplitudes are evaluated, whereas previous simulations looked at relative decreases in amplitude.

Modulation is followed correctly in both the experiments and the simulations. With the standard parameters, simulated responses exhibited similar behavior as in the animal experiments. However, using the standard parameter setting the eCAP amplitude never came as close to zero as the data, especially not when stimulated with the lower modulation rates. This stronger decrease in eCAP amplitude in experimental data was only replicated by the model when a strong adaptation was included, as visible in figure 5.9C. Increasing the refractoriness yielded slightly lower eCAP responses over the course of the stimulus, and a larger initial decrease in eCAP amplitude. Changing the RS had no visible effect on the eCAPs in response to amplitude-modulated pulse trains (data not shown).

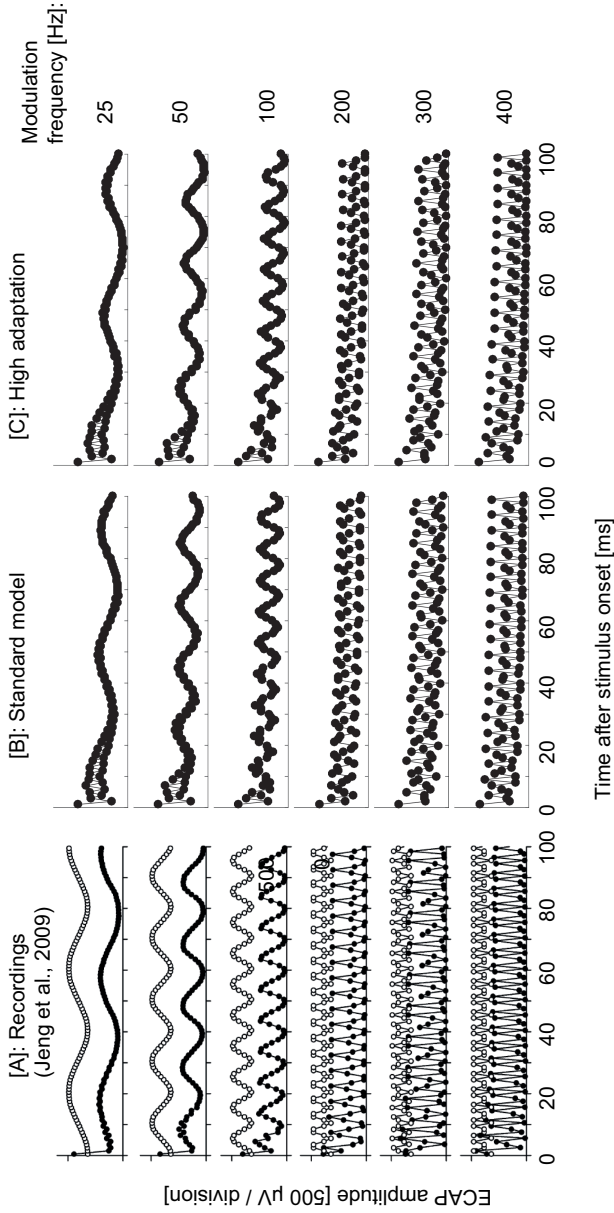


Figure 5.9. eCAP amplitudes in response to pulse trains with 10% modulation depth and modulation frequencies of 25, 50, 100, 200, 300, and 400 Hz. [A] Animal data published by Jeng et al. (2009). Reprinted with permission. The closed circles show the eCAP responses to stimuli in the amplitude-modulated pulse train. The open circles show the predicted eCAP responses based on a model without inter-pulse and stochastic effects. [B] Modeled predictions using the standard parameter settings (1.5 mA). [C] Modeled predictions with strong adaptation (1.5 mA).

3.5 Experiment E: Short-duration amplitude-modulated pulse trains

Simulated MRAs in response to pulse trains modulated with different frequencies and modulation depths are plotted in figure 5.10. The simulated responses show an increased MRA with modulation frequency and modulation depth, which was also observed in human data (Tejani et al., 2017). Stimulus level and the number of fibers modeled largely influenced the MRA, with more fibers and larger pulse amplitudes leading to larger MRAs. Variation of adaptation and RS parameters did not affect the responses. The only parameter that, though to a small extent, affected the response was the refractoriness, with a shorter refractoriness leading to larger MRAs, which was best seen at the lower modulation frequencies. All model settings are physiologically viable based on a comparison to human data from Tejani et al (2017).

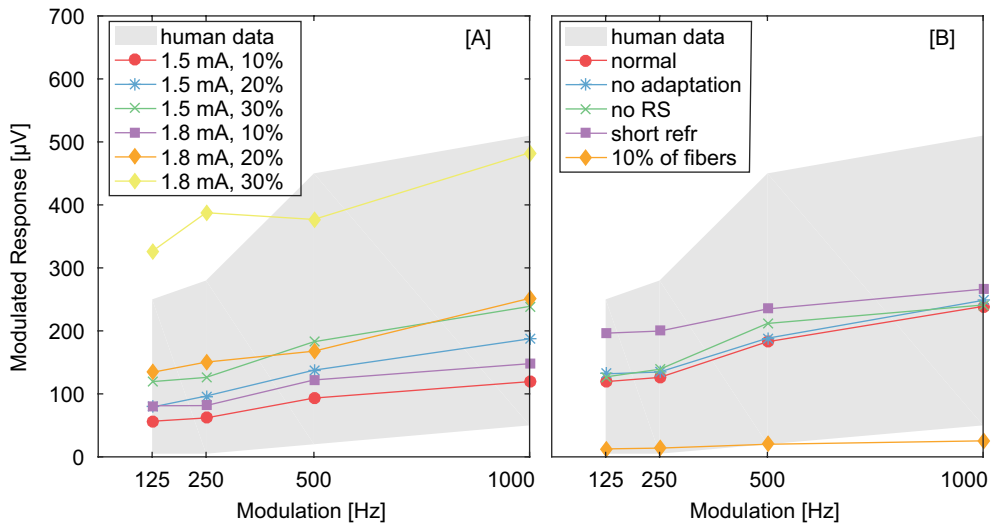


Figure 5.10. Modulated response amplitudes to modulated pulse trains with modulation frequencies of 125, 250, 500, and 1000 Hz. [A] Effect of stimulus amplitude and modulation depth. Modulation depths were varied from 10 to 20 and 30%, with mean amplitudes of 1.2 and 1.5 mA. [B] Effect of neural parameters. MRA responses obtained with standard and adjusted parameter settings are shown. Grey areas indicate the data as obtained from human experiments by Carlyon and Deeks (2015).

4 Discussion

Predicted pulse-train eCAP responses to both short- and long-duration stimuli and both animal and human studies were validated by comparison to different sets of measurement data (Carlyon and Deeks, 2015; Hughes et al., 2012; Jeng et al., 2009; Ramekers et al., 2015; Tejani et al., 2017). The model predictions were reproducible with variation of the temporal and stochastic behavior of the nerve within physiological ranges, explaining the large inter-patient variability in experimental studies (Hay-McCutcheon et al., 2005; Huarte et al., 2014; Hughes et al., 2014, 2012; McKay et al., 2013; Wilson et al., 1997, 1994; Zhang et al., 2013). Different aspects of eCAP responses to pulse trains were predicted. The main findings of the study are that, for constant-amplitude stimuli, refractoriness affects the frequency of maximum alternation, RS affects the maximum depth of the alternation, and adaptation affects the average response amplitude and alternation depth after long durations of stimulation. As we hypothesized, the eCAP responses to pulse trains were related to adaptation, as simulations with diminished adaptation explained data obtained from deafened animals. Thus, the model showed that patterns in the eCAP response to pulse trains provide insight into both the temporal and stochastic nature of the auditory nerve. The model, as a tool of interpretation, provides additional insights into the temporal and stochastic behavior of the nerve, which is expected to be related to auditory performance in patients with a CI, from pitch discrimination and amplitude modulation detection to speech perception.

Model validation with human data

Experiments A and B show that on a group level, all eCAP alternation depth predictions are within the range of physiological data for short duration stimulation with rates up to 2400 pps. For the highest rate simulations, the short refractory and deterministic setting predict a too large alternation depth. Our predictions of eCAP alternation depths were unaffected by the inclusion of latency and jitter. The latency merely caused a slightly delayed response. Spike jitter, or variability in spike timing, can theoretically cause smaller eCAP amplitudes, due to reduced synchronous fiber responses. However, the included mean jitter was approximately 70 μ s and the unitary response width approximately 1 ms, and hence the jitter effect was predicted to be too small to be visible in the predictions. Overall, we conclude that our standard parameter settings, or longer refractory periods combined with a larger stochasticity, would describe the group behavior of the alternation depth best.

In both short duration experiments (A and B), the eCAP amplitudes as predicted by the standard parameter settings are well within the standard variation of patient data. The final amplitude was lower when higher stimulus rates were used. This steeper decrease has been attributed to adaptation and accommodation (Hughes et al., 2012). Our model shows however that removal of adaptation did not affect the final amplitude in the short-duration, high-stimulation-rate, experiments, but was merely dependent on the refractoriness.

Our simulations show that the nerve's refractory period alters the rate at which the maximum alternation is seen; with larger refractory periods, the stimulus rate at which the alternation depth is largest decreases. Two-pulse-eCAP paradigms provide a measure of the mean refractory behavior of an auditory nerve (Miller et al., 2001). On the basis of the results presented here, we provide an alternative method for deducing the refractory behavior of the nerve. To apply this alternative method, the alternation depth has to be measured as a function of pulse rate per individual, and not averaged over the group as in the study by Hughes et al. (2012). By finding the stimulus rate at which the eCAP alternation is maximal, the average refractory period of the nerve can be estimated. After obtaining jitter, RS and refractory periods, by using long duration stimulations for the same fiber, also a value for adaptation can be estimated.

Neural behavior and short duration pulse-train eCAP responses

As mentioned, the implemented variations of parameters describing the neural behavior result in a variability in pulse-train eCAPs similar to that seen in human data. The underlying biophysical phenomena causing differences in eCAP responses could be related to size, myelination and the number of sodium channels in the auditory nerve. Neuronal degeneration that follows deafness leads to axonal shrinkage, demyelination and a progressive retraction of the peripheral axon (Leake and Hradek, 1988). Stochasticity, or the RS of the threshold, was shown in a model study to depend on the myelination of the nerve, with demyelination reducing RS (Resnick et al., 2018), though in another study no relation between deafness and dynamic range of the auditory neurons was found (Sly et al., 2007). Our model showed that decreased stochasticity (i.e. reduced RS) of the nerve can lead to increased alternation depths independent of stimulus rate. Several studies have shown that refractory periods are longer in animals with hearing loss than in control animals (Rubinstein, 1995; Shepherd et al., 2004; Shepherd and Javel, 1997; Sly et al., 2007; Walton et al., 1995; Waxman and Ritchie, 1993). Prolonged refractory time-constants have been observed in demyelinated neurons (Waxman and Ritchie, 1993), of which the chronically deafened auditory nerve is an example (Leake and Hradek, 1988). Demyelinated nerve fibers have relatively fewer potassium channels, which might result in a leakage of internodal potassium currents into the nodal regions and thus cause a prolongation of refractory time constants. Our simulations show that increased refractoriness and decreased stochasticity can cause this increase in eCAP modulation. Thus, measurement of the pulse-train eCAP alternation could provide a measure related to hearing loss. A psychophysical study by Carlyon and Deeks (2015) showed that patients with larger alternation depths in their eCAP responses performed worse on rate discrimination tasks. Our data suggests that patients with better rate discrimination have auditory neurons with short refractory periods and strong stochastic behavior.

Neural behavior and long duration pulse-train eCAP responses

Our model shows that a decrease in adaptation magnitude produced the increased alternation of eCAP amplitude and response amplitude as seen in deafened guinea pigs in the study of Ramekers et al (2015). In their study an increased alternation depth

of pulse-train eCAP in chronically deafened animals was hypothesized to be related to altered refractoriness or jitter in hearing impaired animals. Our study shows that the only parameter adjustment that can cause both the increased alternation depth and increased eCAP amplitude is removal of adaptation. Some earlier studies investigated the relationship between hearing loss and neural adaptation in both animals and humans, and attempted to investigate the relationship between adaptation and deafness on different neural levels (Abbas, 1984; Haenggeli et al., 1998; Kidd et al., 1984; Kotak, 2005; Scheidt et al., 2010; Walton et al., 1995; Wojtczak and Oxenham, 2010; Xu et al., 2007; Xu and Collins, 2007; Zhang et al., 2010). Apart from the study by Ramekers et al. (2015) there are to our knowledge no other studies that describe the relation between hearing loss and pulse-train eCAP alternation depth in response to long-duration pulse trains. Such data could be extracted from existing studies. For example, from the study by Hay-McCutcheon et al. (2005) the adaptation could be calculated as the final decrease versus the initial decrease in eCAP amplitude, and subsequently be related to deafness.

Neural behavior and MRA

The MRA was suggested by Tejani et al. (2017) to be related to neural adaptation. However, changing the adaptation parameter in our model did not affect the predicted MRAs, suggesting that the MRA in response to these stimuli is not a good measure of the nerve's adaptive behavior. The only neural parameter variation that, and only to a small extent, affected the MRA was the refractory period. Electrophysiological recordings of chicken auditory nerve fibers have shown that refractoriness in the auditory nerve potentially enhances entrainment in response to sound stimuli and, thus, is important for temporal coding (Avisar et al., 2013). Our simulations confirmed these conclusions, as the simulation with shorter refractory periods yielded larger MRAs, implying that longer refractoriness due to hearing loss causes lower modulation response amplitudes. As amplitude modulations are important aspects of speech, we hypothesize that the increased refractory periods lead to lower modulation response amplitudes and decrease the intelligibility of speech for CI users. However, as Tejani et al. showed, the MRA increases with modulation frequency, whereas the psychophysical measure of modulation detection deteriorates. This suggests that more central factors also play a role, possibly limiting the detection of amplitude modulations. The modeled MRA responses were unaffected by adaptation or RS. ECAP responses to amplitude-modulated stimulation slightly depend on the nerve's behavior (refractoriness), but are more strongly affected by the stimulus modulation-depth and frequency. No model perturbation reproduces the large modulation response amplitude at 500 and 1000 Hz modulation reported by Tejani et al. (2017). The patient showing the largest MRA was also stimulated with the largest modulation depth, 35%. An additional simulation, with this modulation depth, yielded an MRA of around 500 μ V for 1000 Hz modulation, very similar to the experimental results. Therefore, we conclude, in line with the observations by original authors, that there is a strong correlation between the MRA and modulation depth (Tejani et al., 2017), and that interpatient differences in MRA are mostly a consequence of modulation depth and stimulus amplitude used rather than the neuronal status.

Model improvements

In some experiments, increased eCAP amplitudes over the stimulus duration were observed (He et al., 2015). This is thought to be caused by integration effects, which were not included in our current model. Huarte et al. (2014) and Schmidt, Clay, and Brown (2007) recorded eCAPs in response to minute-long stimulations in humans and saw the eCAP amplitude decrease over longer periods of time. To reproduce such long-term effects, temporal adaptation components longer than 100 ms will have to be included in the model or be modeled using a power-law as shown previously for the response of auditory neurons to sound (Zilany and Carney, 2010).

The unitary response used is based on cat data (Miller et al., 1999b). We have repeated all our simulations with the unitary response published by Versnel et al. (1992). These altered simulations did not yield changes in the predicted normalized pulse-train eCAP responses. Some studies suggest that the unitary response is an oversimplification of the actual contribution to the eCAP for all different fibers, especially for high stimulation levels (Briaire and Frijns, 2005; Westen et al., 2011). Doucet and Relkin (1997) showed that when the total area of neural activation spans more than three octaves, location effects also become significant. A more elaborate version of our 3D model could be used to study this issue in more detail. Not only the exact site of activation can be predicted using the active cable model, but also the propagation of the action potentials along these fibers, and their contribution to the SFAP (Briaire and Frijns, 2005). Differences in fiber kinetics, neuron myelination, size, and morphology between the cochleae of different species influence the shape of the unitary response. An important factor is for instance that in humans the soma is unmyelinated, which effectively adds a large capacitance to the human auditory nerve, leading to altered spike propagation times along the nerve. For prediction of the human eCAP, a unitary response derived especially for the human situation would be desirable. Deconvolution of the human eCAP with modeled predictions of the spike responses, including latency distributions, can provide insight into the variations in the contributions of different human auditory nerve fibers (Schoonhoven, Stegeman, and van Oosterom, 1988). One could potentially use a deconvolution method as suggested by Strahl et al. (2016), to include the optimization of the shape of the human unitary response while fitting recorded human eCAP data (Dong et al., 2018). The active cable model used in the current paper contains a human morphology, described as the new human soma, combined with GSEF kinetics (Kalkman et al., 2015). Kinetics more based on the human situation as described by Schwarz and Reid (Schwarz et al., 1995) are being implemented in a newer double cable version of the model that we hope to use in future research.

CHAPTER 6

Simulating intracochlear electrocochleography with a combined model of acoustic hearing and electric current spread in the cochlea

Margriet J. van Gendt

Kanthaiah Koka

Randy K. Kalkman

H. Christiaan Stronks

Jeroen J. Briaire

Leonid Litvak

Johan H. M. Frijns

ABSTRACT

Intracochlear electrocochleography (ECoChG) is a potential tool for the assessment of residual hearing in cochlear implant users during implantation and of acoustical tuning post-operatively. It is, however, unclear how these ECoChG recordings from different locations in the cochlea depend on the stimulus parameters, cochlear morphology, implant design or hair cell degeneration. In this paper a model is presented that simulates intracochlear ECoChG recordings by combining two existing models, namely a peripheral one that simulates hair cell activation, and a three-dimensional (3D) volume-conduction model of the current spread in the cochlea. The outcomes were compared to actual ECoChG recordings from subjects with a cochlear implant (CI). The 3D volume conduction simulations showed that the intracochlear ECoChG is a local measure of activation. Simulations showed that increasing stimulus frequency resulted in a basal shift of the peak cochlear microphonic (CM) amplitude. Increasing the stimulus level resulted in wider tuning curves as recorded along the array. Simulations with hair cell degeneration resulted in ECoChG responses that resembled the recordings from the two subjects in terms of CM onset responses, higher harmonics and the width of the tuning curve. It was concluded that the model reproduced the patterns seen in intracochlear hair cell responses recorded from CI-subjects.

1 INTRODUCTION

Clinically, extracochlear electrocochleography (ECoChG) is an established tool in the objective diagnosis of hearing loss, Meniere's disease and retro-cochlear pathologies (Davis et al., 1958; Ferraro et al., 1985; Gibson, 1983; Gibson et al., 1977; Morrison et al., 1976; Schoonhoven et al., 1996). In ECoChG, electrical potentials generated by hair cell and neural activity in response to acoustic stimulation are recorded by an electrode, usually placed close to the round window. The ECoChG response is recorded in response to both condensation and rarefaction stimuli, which are then subtracted to obtain the difference response or added to obtain the summed response. The difference response reveals the cochlear microphonic (CM). The CM is defined as the amplitude in the difference response at stimulus frequency. The difference response consists mostly of hair cell, but also some neural activity. The latter is referred to as the auditory nerve neurophonic (ANN) (Fontenot et al., 2017; Forgues et al., 2014; Tasaki et al., 1954). The summed response contains the summing potential (SP) originating from hair cell activity, and the compound action potential (CAP) and ANN originating from neural activity (Dallos, 1986, 1985, 1984; Davis et al., 1958; Durrant et al., 1998; Forgues et al., 2014; Russell and Sellick, 1977; Tasaki et al., 1954).

Nowadays, ECoChG can readily be recorded intracochlearly through the use of the reverse telemetry functionality of cochlear implants. Intracochlear ECoChG recordings are different from the widely described extracochlear ECoChG recordings in the sense that they are recorded much closer to the source and can hence be higher in amplitude. Moreover, they can be recorded by electrodes along the length of the array. Intracochlear ECoChG can be used to detect hair cell damage during cochlear implantation surgery (Calloway et al., 2014; Campbell et al., 2017; Choudhury et al., 2012; Harris et al., 2017; Helmstaedter et al., 2018; Koka et al., 2017b), allowing for direct feedback to the surgeon (Campbell et al., 2015; Dalbert et al., 2015; Koka et al., 2017b; Mandalà et al., 2012). Sudden drops in CM amplitudes are hypothesized to be related to hair cell damage during insertion (Giardina et al., 2019; Koka et al., 2018). Feedback of the CM amplitude is believed to lead to more controlled insertions, which can reduce the risk of cochlear damage. This risk is particularly relevant for patients with ski-slope hearing losses, which can be treated with electric and acoustic stimulation (EAS) (Gantz and Turner, 2010). EAS allows the high-pitched sound perception induced by electrical stimulation to be complemented with low acoustic frequencies delivered by a hearing aid.

Intracochlear ECoChG can also be used postoperatively, to measure residual hearing objectively. This procedure is particularly relevant for recipients where acoustic thresholds are difficult to obtain subjectively (e.g., young children). Intracochlearly recorded CM amplitudes were shown to correlate to the frequency-specific audiometric thresholds (Koka et al., 2017b, 2017a). Additionally, the acoustic tuning of the electrodes can be determined postoperatively, allowing for the matching of acoustic and electrical frequencies in the EAS system (Campbell et al., 2017).

The number of studies reporting recordings of intracochlear ECochG responses from CI-subjects during surgery (Calloway et al., 2014; Dalbert et al., 2015; Giardina et al., 2019; Harris et al., 2017; Koka et al., 2018) or post-operatively (Tejani et al., 2019) is increasing. However, at present, it is unknown how the response depends on exact intracochlear recording position and how it is affected by stimulus- and patient-specific factors. Such knowledge is vital for the interpretation of intracochlear ECochG recordings during insertion or post-operatively along the array.

The potentials arising in the cochlea in response to sound depend on stimulus characteristics and cochlear health (Dallos and Cheatham, 1976; Davis et al., 1958). Sensitivity of the recording electrodes at different positions in the cochlea to these potentials depends on the distance, cochlear morphology, electrode design and electrical properties of the cochlear tissue. The exact location of the implanted electrode, and related the distance from current sources such as hair cells to the implanted electrode, depends on cochlear morphology and electrode design (van der Jagt et al., 2017). Electrical properties of the tissue also affect the sensitivity of the electrode to the different current sources. Previously, modeling studies have been used to estimate the electrical attenuation along the basilar membrane. However, these studies have yielded incongruent estimates, with reported values ranging from 2 to 30 dB/mm (Ayat et al., 2015; Charaziak et al., 2017; Davis et al., 1958; Dong and Olson, 2013; Fridberger et al., 2004; Mistrík et al., 2009; Tasaki and Fernández, 1952; Teal and Ni, 2016; v. Békésy, 1952, 1951; Whitfield and Ross, 1965).

A detailed 3D model of the cochlea, that is verified for its simulations of electrical conductivities for the implanted electrode, could provide accurate simulations. The combination of the electrical potentials arising in the cochlea in response to sound stimulus and how they are conducted in the cochlea determine the ECochG response at each different location.

The goal of the current study was to aid in the interpretation of intra- and postoperative ECochG recordings, by modeling these responses. In such a model, both the potentials arising in the cochlea in response to sound and the attenuation of potentials within the cochlea must be included. To accomplish this, a model of the auditory periphery predicting hair cell responses was combined with a 3D model of current spread. Effects of stimulus frequency and level, recording electrode, cochlear morphology, electrode design and hair cell damage were tested. The model was compared to intracochlear ECochG recordings from two CI-subjects.

2 METHODS

Intracochlear ECoChG hair cell responses were simulated with a combined model of inner hair cell (IHC) and outer hair cell (OHC) activation throughout the cochlea (Zilany et al., 2014; Zilany and Bruce, 2006) and of current spread in the cochlea (Kalkman et al., 2015, 2014). The following sections describe the model. Section A describes how hair cell potentials are simulated. Section B describes how electrical attenuation, for different cochlear morphologies and electrode designs, is modeled. Section C describes how both models were combined to calculate the intracochlear ECoChG response. Hearing loss was modeled by including different types of hair cell degeneration, the approach hereto is described in section D. Lastly, section E describes how subject recordings were performed.

2.1 Modeled hair cell responses

The voltages over the IHC and OHC membranes were calculated with a model of the auditory periphery developed by Zilany et al. (Bruce et al., 2018, 2003; Carney, 1993; Zhang et al., 2001; Zilany and Bruce, 2006). The model is freely available on the internet. A schematic diagram of the model is shown in Figure 6.1.

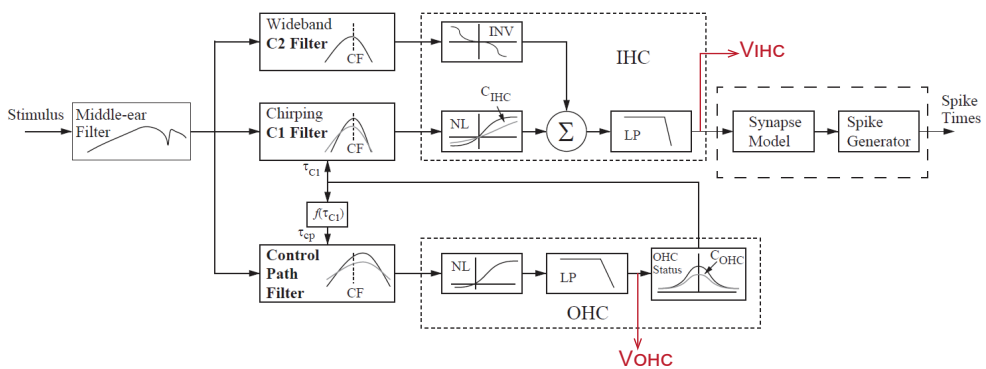


Figure 6.1. Schematic diagram of the auditory-periphery model used to calculate the intracellular voltages. The stimulus is the sound pressure waveform in Pa and the outputs used in the current paper are the intracellular voltages V_{IHC} and the V_{OHC} for the inner hair cell (IHC) and outer hair cell (OHC) respectively. These potentials are extracted immediately after the Non-Linearity (NL) and the Low-Pass Filter (LP), as indicated by the red arrows. The model includes a middle-ear filter, inner hair cell (C1 and C2) and outer hair cell (control) pathways, a synapse and spiking model. C_{OHC} and C_{IHC} are scaling constants that control OHC and IHC status. CF: characteristic frequency, INV: inverting nonlinearity. [from Zilany and Bruce, 2006, reprinted with permission]

The auditory periphery model included a middle ear filter, inner hair cell and outer hair cell pathways, a synapse model and a spike generator. Human cochlear tuning was used (Shera et al., 2002). Each hair cell had a scaling constant ('C-factor') that described its physiological health. The C-factor could be adjusted from 1 for healthy hair cells, to 0 for complete functional loss for IHCs and OHCs separately. The C_{OHC} had an effect on the bandwidth of the

inner hair cell pathway. The potentials over the hair cell membranes were extracted at the output of the cochlear pathways. This auditory peripheral model was previously validated by comparing spiking behavior in auditory nerve (AN) fibers generated by the model to physiological data from single fiber and membrane voltage recordings in cats (Bruce, 1997; Bruce et al., 2018; Zhang et al., 2001; Zilany et al., 2014, 2009; Zilany and Bruce, 2006). It was shown that level- and frequency-dependency of auditory nerve fiber responses were correctly simulated by the peripheral model.

There were two modifications included in the analysis of the hair cell output for the current implementation; 1) scaling of outer hair cell contributions and 2) converting from membrane voltages to extracellular currents. The OHC voltages in the auditory peripheral model were originally applied only as a qualitative measure. For the current study, however, both inner and outer hair cell responses were needed. In animal recordings the responses of IHCs to stimulation with a tone of 800 Hz and 15 dB were four times larger than the responses of OHCs (Dallos, 1986, 1985). In the current study, the simulated OHC responses were scaled, such that the IHC Alternating Current (IHC-AC) response was four times larger than the IHC-AC response to acoustic stimulation at 800 Hz and 15 dB. OHC responses at other CFs, and in response to other stimulus frequencies, were scaled with the same factor. Comparison of the scaled simulations to previously published recordings from animal data (Dallos, 1986, 1985) (appendix A) showed that relative dependency of IHC and OHC intracellular hair cell potentials on stimulus level and frequency was qualitatively described by the model.

The original hair cell model simulates potential differences across the hair cell membranes. However, to model the ECochG, extracellular currents corresponding to these hair cell voltages were needed, which depend on the capacitive and conductive behavior of the hair cell membranes. Resistances across the apical membrane of the hair cell are modulated by the opening and closing of voltage-gated channels (Housley G.D. and Ashmore, 1992; Mammano and Ashmore, 1996). These resistances depend on the voltage over the membrane. The voltage-dependent conductance (G) can be fitted with the Boltzmann equation (Johnson et al., 2011):

$$G(V) = \frac{G_{max}}{1 + e^{-(V - V_{0.5})/V_S}} \quad (\text{Eq. 6.1})$$

where $V_{0.5}$ is the voltage at the 50% point on the Boltzmann curve; G_{max} the maximum conductance; and V_S is the slope at the 50% point on the Boltzmann curve. For IHCs, the $G_{max} = 470$ nS, $V_{0.5} = -31$ mV, $V_S = 10$ mV, and a resting potential V_{rest} of -55 mV. For OHCs, the $V_{0.5}$ equals -60 mV and is independent of characteristic frequency (CF). All other parameters depend on the CF. A linear fit performed on the data presented by Johnson et al. (2011) yielded: $G_{max}(CF) = 0.02 \times CF + 40$, and $V_S(CF) = 8 \exp^{-4} \times CF + 8.5$. The same paper showed that the hair cell membrane capacitance induced first-order low-pass filtering, with an IHC time constant $\tau = 0.26$ mV ($F_0 = 610$ Hz). For OHCs, the cut-off frequencies were shown to be higher than estimated previously, and increased linearly with the cells' CF, with a slope of nearly 1; the $F_0 = CF$ and $\tau = 1/2\pi F_0$.

2.2 Volume conduction model

Intracochlear potentials resulting from hair cell currents were calculated using a volume conduction model of the implanted human cochlea (Kalkman et al., 2015, 2014). This volume conduction model, which uses the Boundary Element Method, was previously validated by comparison to clinically recorded intracochlear impedances (Kalkman et al., 2015, 2014). In the current study, electrical impedances from currents induced by hair cell activation to electrodes at different cochlear positions were calculated.

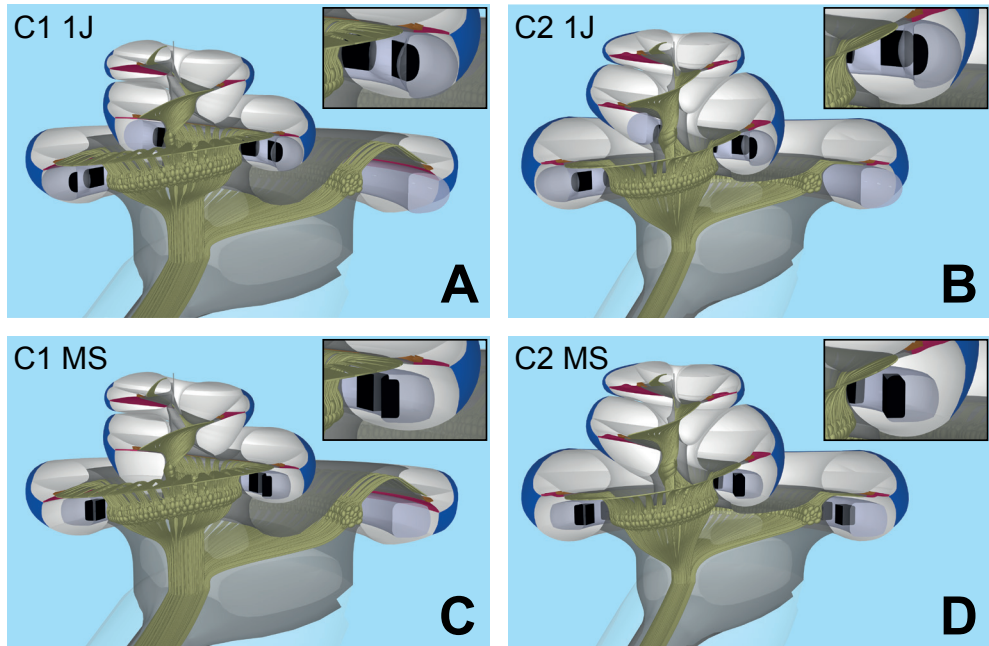


Figure 6.2. Cochlear morphologies C1 and C2 based on human histological sections implanted with 1J (straight, lateral wall) or MS (pre-curved, mid-scalar) electrodes in the scala tympani, which are plotted in grey with black electrode contacts. [A]: cochlea 1, electrode 1J; [B]: cochlea 2, electrode 1J; [C]: cochlea 1, electrode MS; [D]: cochlea 2, electrode MS.

To infer to which extent cochlear morphology and electrode placement caused inter-patient variability, two different cochlear morphologies and electrodes were implemented, figure 6.2. The cochlear morphologies and cross-sectional hair cell positions were based on individual histological sections of human cochleae, and differ for instance in their relative height and shapes of the different scalae. Two different electrode array designs were used for the simulations: a lateral wall, straight, HiFocus1J (Advanced Bionics) electrode (figure 6.2), and a pre-curved, HiFocusMS (Advanced Bionics) electrode, located in a mid-scalar position. The HiFocusMS electrode contacts were placed approximately equidistant from the basilar membrane, whereas the 1J electrode contacts were placed closer to the basilar membrane on the apical end and further from the membrane on the basal end.

3200 sets of hair cells were evenly distributed along the length of the basilar membrane, one row of IHCs and three rows of OHCs. Among these locations, 2840 sets of hair cells had CFs above 125 Hz. For those hair cells the auditory peripheral model could simulate voltage responses. Hair cells were considered dipoles, because of their anisotropic morphology and properties, and in line with a previous modeling study (Teal and Ni, 2016). The bottom pole of the current source of each hair cell was located in the basilar membrane, and the top pole of the current source was located in the scala media, as shown schematically in figure 6.3. The lengths of the dipoles varied throughout the geometries ranging from roughly 30 μm at the base of the cochlea to 70 μm at the apex (Pujol et al., 1992). In the cochlear geometries, the CF at a given position along the cochlea was determined by the Greenwood map (Kalkman et al., 2014). Simulated electrical potentials generated by the inner and outer hair cell dipoles and measured at the modeled recording contacts were divided by the dipole current amplitudes to obtain electrical impedance values for each dipole-contact pair.

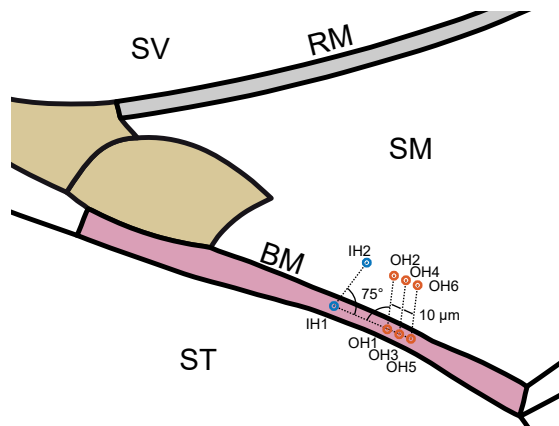


Figure 6.3. Mid-modiolar cross-section of the cochlea, centered around the scala media (SM), showing the hair cell positions of the three different rows of hair cells. SM = Scala Media, ST = Scala Tympani, SV = Scala Vestibuli, BM = Basilar membrane, RM = Reissner's membrane, IH1 = inner hair cell bottom, IH2, inner hair cell top, OH1, 3, 5 = outer hair cell bottoms in three different rows and OH 2, 4, 6 = outer hair cell tops in three different rows. A line drawn through the current dipoles was situated at an angle of 75° relative to the basilar membrane, with the IHCs and OHCs leaning towards each other. The three OHC dipoles were exactly parallel to each other and were positioned 10 μm apart, in the lateral direction along the basilar membrane.

The distances between individual dipoles were much smaller than the dimensions of the model's surface elements; therefore, some discretization/interpolation artifacts were present in the simulated electrical potentials. These artifacts were smoothed by applying a

spatial low-pass Butterworth filter to the potentials along the basilar membrane, induced by each row of 3200 dipoles.

2.3 Simulating intracochlear hair cell ECochG responses

The ECochG response for a recording electrode, e , was calculated as follows;

$$\text{ECochG} = \sum_{hc=1}^{hc=last} Z_{VC}(hc, e) \cdot I_{hc} \quad (\text{Eq. 6.2})$$

Where I_{hc} refers to all hair cell (hc) contributions, $Z_{VC}(hc, e)$ to the electrical impedance from hair cell to the recording electrode as calculated by the Volume Conduction (VC) model (Kalkman et al., 2015, 2014). For each stimulus, the total ECochG response is calculated as the sum of contributions from all hair cells in time. Simulated sound stimuli were tone bursts with frequencies of 250, 500, 1000, 1500, 2000 and 4000 Hz with stimulus levels of 20- to 110-dB sound pressure level (SPL) with increments of 10 dB. The tone bursts had stimulus durations of 50 ms and rise and fall times of 0.5 ms. For all simulations, the sampling frequency was 100 kHz. The summation and difference response were obtained from the simulations of responses to condensation and rarefaction stimuli. The CM amplitude was calculated as the amplitude at the stimulus frequency in the difference response, obtained from the Fourier transform, over the response between 25 and 50 ms, to remove the onset response from this analysis.

2.4 Modeling hearing loss

Sensorineural hearing loss was simulated by lowering the number of surviving hair cells and by decreasing the C-factor. Six hypothetical types and degrees of hair cell degeneration were tested, namely:

- Only IHCs) All C-factors to 1, only responses from IHCs are considered
- Only OHCs) All C-factors to 1, only responses from OHCs are considered
- Hearing Loss (HL)-A) Equally distributed hair cell degeneration: hair cell survival 10%, C-factor of 1;
- HL-B) Equally distributed hair cell degeneration: hair cell survival 10%, C-factor of 0.1;
- HL-C) Sloping hair cell degeneration: hair cell degeneration decreased with CF from 100% apically to 0% in the base. The C-factor was related to the hair cell degeneration. This resulted in 100% survival in the apex combined with a c factor of 1, 50% survival and C-factor of 0.5 in the middle, and 0% survival and C-factor of 0 in the base;
- HL-D) Dead basal region: No hair cell degeneration in the basal 1/3rd of the cochlea, and 10% survival elsewhere combined with a C-factor, of 0.1.

An overview of the parameters in the six types and degrees of hair cell degeneration is given in table 6.1.

Table 6.1. Overview of parameters in the six different hair cell degeneration

HL	Shape	Survival rate	c-factor
ihc	Flat	100%	1
ohc	Flat	100%	1
A	Flat	10%	1
B	Flat	10%	0.1
C	Sloping	100% apical to 0% basal	1 apical to 0 basal
D	Dead region	10% apical and mid, 0% basal	0.1 apical and mid, 0 basal

2.5 Subject recordings

Intracochlear ECoChG responses were recorded in two subjects with CIs with residual hearing in the implanted ear. Data on the hearing loss and implants of these subjects is given in table 6.2.

Table 6.2. Audiograms and subject information for the two subjects (ID-1 and ID-2). Audiogram values are the thresholds (dB_{HL}) at each frequency

Pt	Audiogram Frequency, Hz					Subject information				
	125	250	500	1000	2000	CI use	Ear	Age	Cause	Device
ID-1	25	40	50	55	50	3 yrs	R	57	SNHL	Advantage, HiFocus MS
ID-2	55	60	70	75	>100	3 yrs	R	85	SNHL	Advantage, HiFocus MS

Acoustic stimulations were done with 50 ms tone bursts, with 1 cycle each for the ramp up and the ramp down, with a Hanning window. In the recordings a bin-width of 36 Hz was achieved with a rate of 9280 Hz and 512 samples. The signal was defined as the amplitude of the Fourier transform at the stimulus frequency. The initial stimulus amplitude was 110 dB SPL and was decreased in 10-dB steps until the signal-to-noise ratio was below 18 dB. Noise amplitude was defined as the average amplitudes of 4 to 6 bins flanking the stimulus frequency. Alternatively, in the absence of a distinct peak at the stimulus frequency, up to 40 averages were registered.

3 RESULTS

Simulated attenuation of currents within the cochlea, or modeled current distributions, are shown in section A. Section B reports on recordings and simulations of intracochlear ECoChG potentials, both in the time- and frequency- domains. Section C investigates how the CM amplitude in response to different stimulus frequencies and amplitudes changes with exact recording position, and how it is affected by cochlear morphology, electrode design and hearing loss.

3.1 Electrical attenuation simulated by the volume conduction model

The simulated inner hair cell impedance curves are plotted in figure 6.4 for different cochlea-implant configurations.

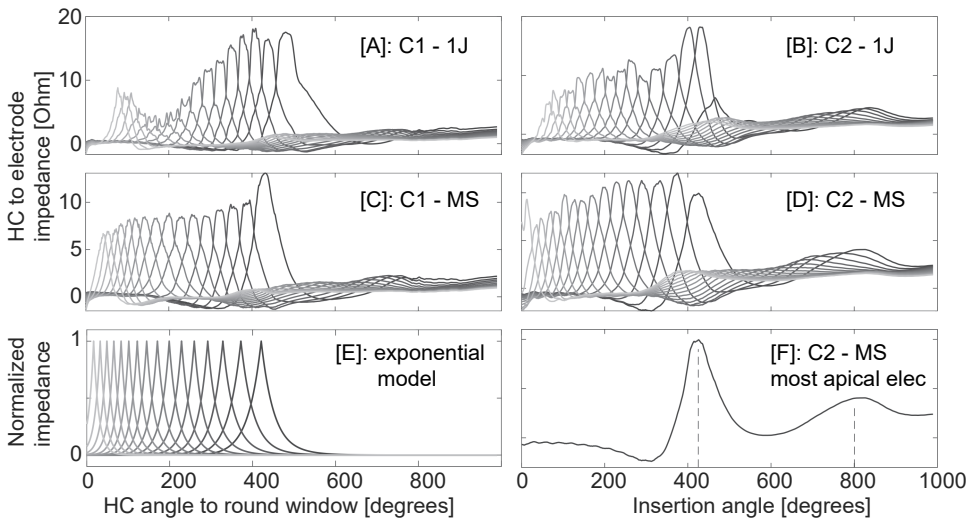


Figure 6.4. Electrode impedances in response to inner hair cell activities, modeled at 3200 different locations and 16 different electrode positions. Calculations were performed for the following configurations; [A] cochlea 1 - 1J; [B] cochlea 2 - 1J; [C] cochlea 1 - MS; [D] cochlea 2 -MS; [E] Exponential model; [F] impedance function for the most apical electrode contact from cochlea 2 - MS. Dotted lines in F indicate the sensitivity-peaks. Each curve corresponds to impedance values from all individual inner hair cells, measured at specific recording contact; hair cell locations are indicated along the x-axes as a function of insertion angle, measured from the round window.

Impedances between electrodes were more consistent in the MS array than in the 1J electrode. In the latter, impedances varied by as much as a factor of 3 between the least and most responsive electrode. In C2 the electrode contacts showed a moderately larger impedance to hair cells in the basal region. Figure 6.4F clearly demonstrates the double

peak in sensitivity to hair cell activation, in the exemplary impedance function for the most apical electrode in the C2-MS configuration. The regions of the peaks are almost 400 degrees apart, i.e., close to a complete turn (dotted lines), indicating cross-turn sensitivity.

3.2 Single electrode ECochG responses

This section describes ECochG responses simulated and recorded at the most apical electrode contact.

Single electrode recordings

ECochG summed and difference responses from two different subjects are shown in Figure 6.5. A temporal onset response was seen in the difference recording in subject ID-2, but not in the recording from subject ID-1. Higher odd harmonics in the spectral domain were also only seen in recordings from subject ID-2. In the summed responses recordings from subject ID-2 showed the first harmonic, whereas in subject ID-1 the even harmonics did not exceed the noise floor. There was no large direct current component in the recordings, probably due to high-pass-filtering of the recording set-up.

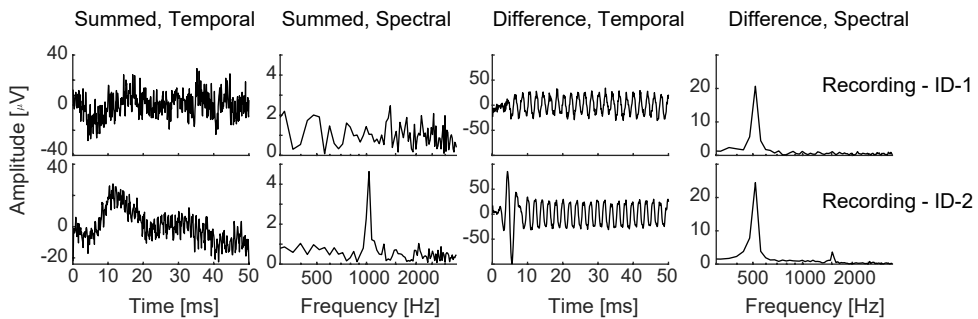


Figure 6.5. recorded ECochG responses to a 50-ms, 500-Hz, 100-dB SPL tone burst from subjects ID-1 and ID-2. The recordings were obtained from the most apical electrode contact.

Effect of hair cell damage on single electrode simulations

Figure 6.6 shows modeled ECochG summed and difference responses for different hair cell configurations. The amplitude of the AC component in the summed response varied among the different configurations of hair cell degeneration. The largest amplitude was seen in the healthy cochlea, and the smallest in hearing loss configuration B. The onset in the difference responses as observed in the recording of subject ID-2 was seen in some of the simulations; with the complete cochlea, with HL-A and with HL-C. The configurations used in these three simulations all included healthy inner and outer hair cells (in which C_{OHC} equals 1). The second harmonic was visible in almost all simulations, except for the simulation with only IHCs surviving, and was largest in again the complete cochlea, HL-A and HL-C. Difference responses from the simulations with only IHCs and only OHCs had nearly opposing phases, and the corresponding CM amplitudes were larger than from the

intact, complete cochlea. With any of the four HL simulations, amplitudes were around five times smaller than when all hair cells survived. Comparison to the subject recordings show that subject ID-1 best resembled the simulations without OHCs or HL-B or HL-D, since in these simulations no onset response was seen and higher harmonics were absent or small. Recordings from subject ID-2 closely matched the simulations with the complete cochlea, HL-A and HL-C, as these all showed a strong onset and higher harmonics.

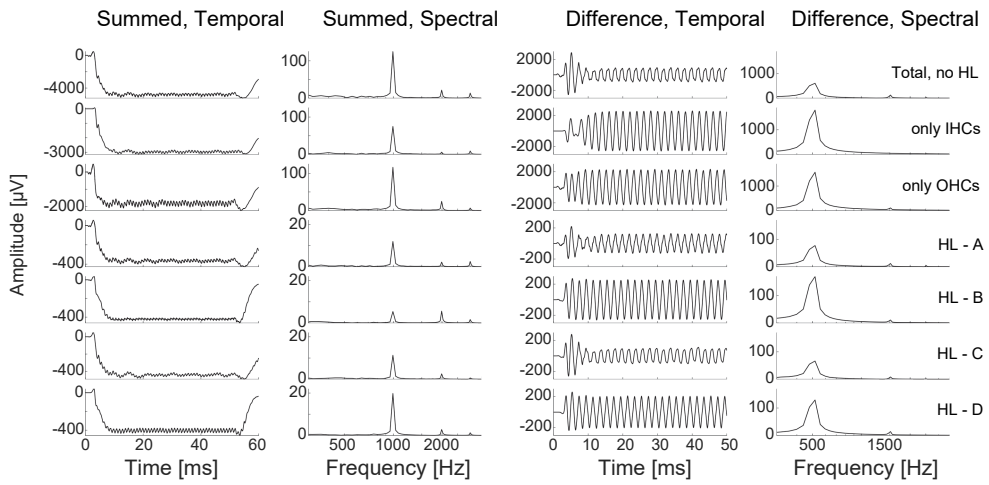


Figure 6.6. Simulated summed and difference responses for different hair cell configurations in both the temporal and the frequency domain. The top three rows show the responses from a cochlea when all hair cells, only the IHCs, or only the OHCs are taken into account, respectively. The other rows show responses for modeled hearing loss, namely 10% survival, $c=1$ (HL-A); 10% survival, $c=0.1$ (HL-B); sloping survival, sloping c (HL-C); no basal hair cells, other regions 10% survival and $c=0.1$ (HL-D).

3.3 CM along the array

This section explores the effects of stimulus configurations, cochlear morphology and electrode design, and hair cell survival on the CM amplitudes along the implanted array.

Effect of stimulus configuration

Figure 6.7 shows the recorded (two top rows) and simulated (two bottom rows) CM responses. The two bottom rows show CM simulations from the intact C1 cochlea with an MS array, stimulated with low (20 to 60 dB) and high (70 to 100 dB) stimulus levels respectively.

In both subjects as well as in the simulations, the response amplitudes increased as the stimulus intensity increased, and the peak-response shifted basally as the stimulus frequency increased. Subject ID-1 showed a narrow tuning. In subject ID-2, a second peak

appeared basally at most stimulus frequencies, when stimulated with 100- or 110-dB SPL. Simulated responses to low stimulus levels (figure 6.7, third row) showed narrow tuning, similar to the recordings from subject ID-1 (figure 6.7, first row). In response to higher stimulus levels, the simulated response amplitudes increased and the response became wider (figure 6.7, fourth row), which more closely resembled recordings from subject ID-2 (figure 6.7, second row).

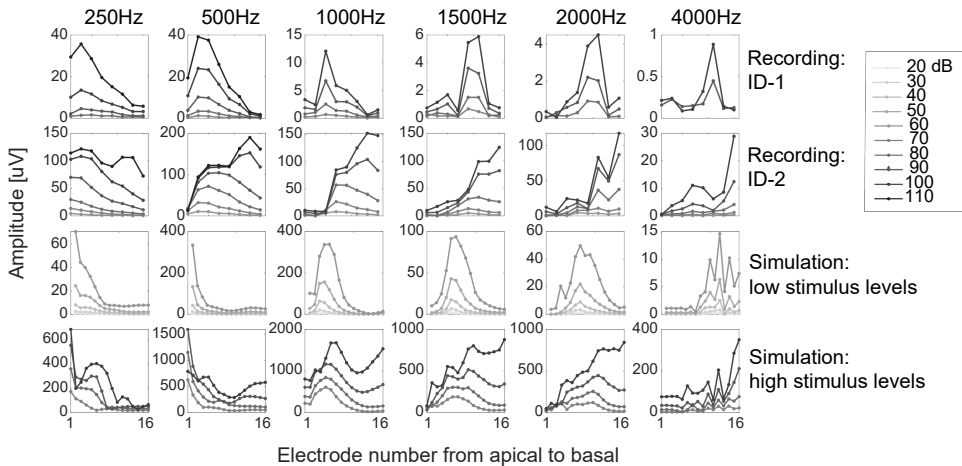


Figure 6.7. Intracochlear ECoChG along the array. Top rows: measurements in the two different subjects, first and second row representing subjects ID-1 and ID-2 respectively. The recording electrode number on the x-axis varies from 1 (the most apical) to 15 (the most basal). Recordings were done at the odd electrode contacts only. Lowest rows: modeled CM responses (in μV) at 16 electrode positions for the C1 - MS configuration in response to low stimulus levels (20 - 60 dB SPL, third row) and high stimulus levels (70 - 100 dB SPL, fourth row). Each column shows the response to a different stimulus frequency (250-4000 Hz). Grey scale indicates stimulus level, increasing from light to dark.

Effect of cochlea and implant on the response along the array

To investigate effects of cochlear morphology and implanted electrode design, CM responses to 90 dB SPL were modeled for each cochlea-implant configuration (figure 6.8). The electrode location where the maximum response was recorded was slightly different for each configuration. In response to 250 or 500 Hz stimuli, a second peak was recorded basally in all configurations. The exact location and size of this second peak however differed per configuration. In response to 1000 Hz only the response in the C2-1J configuration showed a double peak. The 4kHz CM amplitudes along the array exhibit a jagged response in configurations B, C and D.

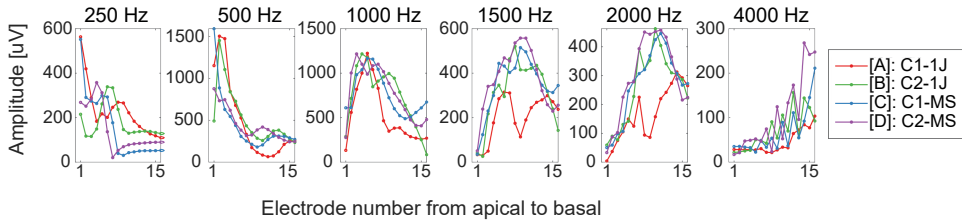


Figure 6.8. Modeled CM responses for the different cochlea-implant configurations, in response to a stimulus of 90 dB SPL. Each graph shows the response to a different stimulus frequency (250-4000 Hz). Each color shows a different configuration; [A]: cochlea 1, 1J in red; [B]: cochlea 2, 1J in green; [C]: cochlea 1, MS in blue; [D]: cochlea 2, MS in purple. X-axis denotes the electrode location.

Effect of hair cell type and degeneration on the response along the array

ECochG responses from IHCs and OHCs were simulated separately to evaluate how hair cell type affected the intracochlear pattern. Simulations of how different types of hair cells contributed to the intracochlear CM response are shown in figure 6.9. The peak of the response originating from IHCs was narrower than the response originating from OHCs. Response amplitudes increased faster with stimulus levels for IHCs than for OHCs. The OHC responses showed double peaks, especially in response to higher stimulus levels. This was also seen in the recordings from subject ID-1 in figure 6.7.

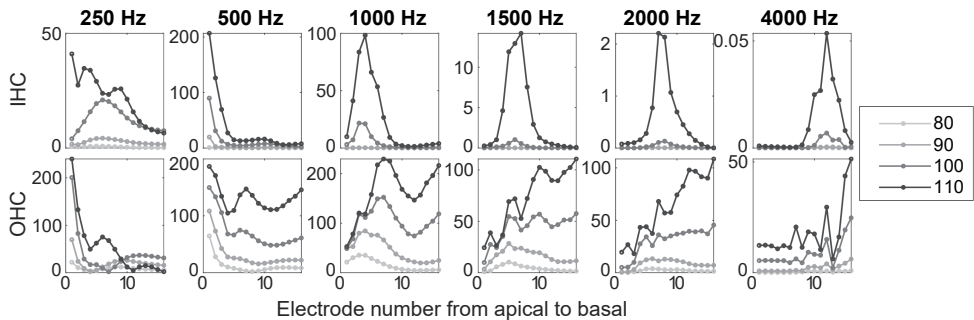


Figure 6.9. Effect of hair cell type; Simulated intracochlear CM responses along the electrode array originating solely from IHCs (top row) and originating solely from OHCs (lower row). Simulations were done with the intact cochlea. Hair cell survival rate was set at 100% and c-factors at 1. Simulations show responses to stimulus levels of 80- to 110- dB SPL and stimulus frequencies of 250- to 4000 Hz.

To investigate the effect of hair cell damage on the intracochlear CM, responses are simulated for four different degrees of hair cell degeneration. Results are shown in figure 6.10. CM responses were very similar when hair cell damage was equally distributed (hearing loss degrees HL-A and HL-B). Sloping hair cell damage, as in HL-C, resulted in

smaller response amplitudes to high stimulus frequencies on the basal electrodes, compared to HL-B. A basal dead region (HL-D), resulted in minimal activation at the 5 most basal electrode contacts (electrode number 11 – 15) in response to stimulus frequencies of 1 kHz and higher.

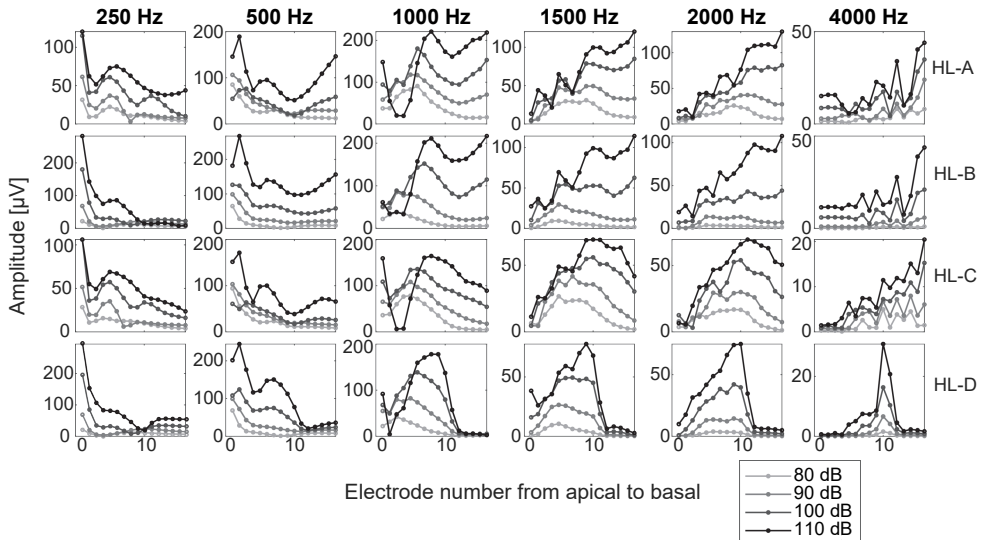


Figure 6.10. Effect of hair cell survival; Simulated intracochlear CM responses along the electrode array in cochleae with different configurations of hair cell survival. The different hair cell configurations are referred to as HL-A, HL-B, HL-C and HL-D. Simulations show responses to stimulus levels of 80- to 110- dB SPL and stimulus frequencies of 250- to 4000 Hz.

4 DISCUSSION

A model was developed that replicated characteristics seen in intracochlear ECoChG recordings in the temporal, spectral and spatial domain. Simulations with different degrees and size of hearing loss yielded similar results as recordings from two different subjects. 3D volume conduction simulations showed that the intracochlear ECoChG is a local measure of activation. This local sensitivity was reflected in the steep fall-off of impedances with distance along the basilar membrane (figure 6.4). In line with the theory of place-coding, and the level-dependency of hair cell activity, increasing stimulus level resulted in wider tuning curves. The peaks shifted basally with increasing stimulus frequency. The exact location on the array of the peak CM amplitude depended on cochlear morphology and implant type. Double peaks were seen in response to the highest stimulus levels. These double peaks could be either attributed to cross-turn sensitivity or wide tuning of the hair cells. The width of the tuning was different in both subjects. Simulations showed that different tuning width could result from different stimulus levels, morphologies and

degrees and types of hearing loss. Differences in hearing loss could explain differences between the recordings from the two subjects in terms of CM onset responses, higher harmonics, and the width of the tuning curve. Concluding, the model reproduced intracochlear hair cell responses recorded from CI-subjects and can be used to investigate effects of individual differences.

Cochlear morphology and electrode design

While the impedance curves in Figure 6.4 are primarily determined by the distance between the recording electrode contacts and the individual hair cells, they are also affected by other geometric factors such as the relative orientations of the recording contacts and hair cells, as well as the size and positioning of the electrode array's silicon carrier. In the models of the 1J array, the silicon carrier can be pressed up close to the basilar membrane at various points (e.g. see inset of figure 6.2A), which partially insulates the recording contacts from the current generated by the hair cells. This results in a more irregularly shaped set of impedance profiles for the 1J compared to the MS arrays (compare the peak impedance values in figures 6.4A&B to 6.4C&D), since the MS array's mid-scalar positioning offers a clearer and more consistent current pathway from hair cell to electrode through the scala tympani. Counter-intuitively, this also leads to lower peak values in the impedance curves for the 1J at certain insertion angles, despite the 1J being positioned closer to the basilar membrane than the MS (e.g. compare peak values between the 1J and MS at around 180° in figures 6.4A and 6.4C).

The jagged responses in the CM recordings along the array in response to 4 kHz originate from the OHC responses (figure 6.9), which had a much wider activation than IHCs. The OHC responses to 4 kHz showed a relatively quick change in phase along the basilar membrane, and as a consequence, the way these responses add to a CM-signal on an individual electrode is highly influenced by the exact phases of the OHC-responses in its neighborhood.

Hearing loss and the intracochlear ECoChG

Different degrees of hair cell degeneration yielded responses that mimicked characteristics of recorded responses, in the temporal and spectral domain (cf. figures 6.5 and 6.6) and in the spatial domain (cf. figures 6.7, 6.9 and 6.10). In the summed response recorded from subject ID-1 no AC component was above noise floor (figure 6.5). Simulations showed lower AC components in the summed response when only IHCs were modeled or in HL-B. Recorded difference responses in subject ID-1 (figure 6.5) showed a clear CM, but no onset response and no harmonics. In the simulations this is seen when only IHCs or only OHCs were modeled, or when low *c*-factors were applied (0.1 or less in the models HL-B and HL-D). Recordings from subject ID-1 showed narrow tuning curves, which was replicated in the model by removing OHCs, but retaining all the IHCs. The simulations therefore suggest that subject ID-1 suffered from (near-)complete OHC loss or large functional damage to the OHCs. In line with this observation, subject ID-1 had a flat audiogram and relatively good audiometric thresholds.

In subject ID-2 the second harmonic was present in the summed response, which was seen in most simulations except in the simulation HL-B. In the difference response the CM was large and a prominent onset response was observed. Higher harmonics were clearly visible in the spectral domain. Onset responses and higher harmonics were seen in the HL-A and HL-C simulations or in a healthy cochlea. These simulated conditions all had high c-factors, up to 1 in the apical regions. The onset response was not seen when only IHCs or OHCs were modeled. This suggests that it is an interaction effect caused by phase differences between the IHCs and the OHCs at onset. The width of the responses along the array in subject ID-2 is most similar to the widths in HL-A and HL-B, where hair cell degeneration was equally distributed along the basilar membrane. The simulations thus suggest that subject ID-2 has good functioning IHCs and OHCs, but that their numbers are reduced equally throughout the cochlea.

IHCs and OHCs contribute differently to the intracochlear ECoChG

Evaluating the separate IHC and OHC contributions (figure 6.9) showed that the intracochlear ECoChG CM response is dominated by OHCs, especially in response to high stimulus frequencies. OHC domination of the ECoChG response is consistent with animal experiments (Dallos, 1986, 1985, 1983; Dallos et al., 1972; Dallos and Cheatham, 1976; Davis et al., 1958; Russell et al., 1986). Modeled electrical impedances were similar between IHCs and OHCs, and hence impedance differences cannot explain the difference. OHC voltages as produced by the hair cell model are generally four times smaller than the IHC voltages. OHCs are about three times larger in number than IHCs. Both those facts combined would expect equal total contributions from IHCs and OHCs. A possible explanation for the larger OHC contribution is a difference in low-pass-filtering membrane properties between IHCs and OHCs. The low-pass filtering cut-off frequencies for the IHCs are generally lower than those of the OHCs (Johnson et al., 2011), which results in a relative insensitivity of the ECoChG to the IHC AC voltages.

Animal studies correlating post-mortem histological counting of the hair cells to audiometric thresholds have shown that hair cell degeneration generally starts in the base and then proceeds to the apex. Laterally positioned hair cells are more vulnerable than those medially positioned. Hence, it is believed that degeneration generally progresses from base to apex, and affects lateral OHCs first and the medially positioned IHCs last (Dallos et al., 1972; Eric Lupo et al., 2011; Stebbins et al., 1979; Van Ruyven et al., 2005, 2004). Synaptic or retro-cochlear pathologies might cause hearing loss regardless of the status of hair cells in the cochlea (Hill et al., 2016).

Limitations of the model and future research

A challenge in modeling hair cell membrane behavior is the relatively sparse animal data available. In the present study the dependency of conductance parameters on the CF was determined from a few different data points only (Johnson et al., 2011). A wider range of data showing how the hair cell conductance depends on CF is desirable. Another limitation is the unusually large IHC responses to stimulus levels above 80 dB SPL compared to animal data (see appendix). Lastly, from the auditory peripheral model, only responses to hair cells with a CF higher than 125 Hz could be obtained, although hair cells with lower CFs might also contribute to the ECochG response. The current study focused on the CM response. Instead, the SP could perhaps also be used as a diagnostic marker of electrode position (Helmstaedter et al., 2018). This could be further evaluated with the here presented model. The model can also be extended with neural firing to simulate CAP and ANN responses, to disentangle these from hair cell responses. The model of the auditory periphery does include a nerve fiber model, which could simulate spiking, and hence, CAP and ANN responses could be modeled as well. For this purpose, single fiber contributions to the ECochG would have to be estimated first. The model developed here could also be used to predict extracochlear recordings, close to the round window. Effects of often used stimulation patterns, such as chirps or tone bursts, or newly suggested patterns such as partially noise-masked tones (Chertoff et al., 2012), could be modeled. By using the 3D model for this, also complex projections from the hair cells to the extracochlear electrode are taken into account.

APPENDIX

Comparison of simulated and recorded membrane voltages

Previously, it was shown that the relative dependency of IHC voltage on stimulus level and frequency is correctly predicted by the hair cell model (Zhang et al., 2001). In addition, this appendix shows qualitative similarities and discrepancies between simulated and previously recorded IHC and OHC voltages.

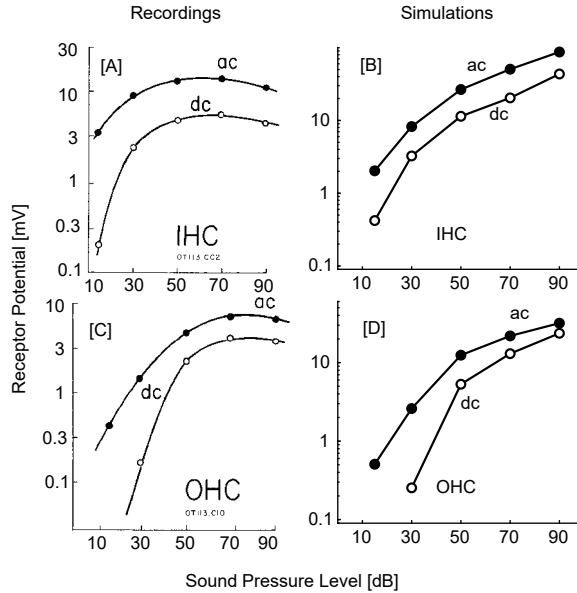


Figure 6.11. Measured [A&C] and simulated [B&D] input-output functions of intracellular responses to acoustic stimuli presented at 800 Hz. AC and DC responses are plotted for both IHCs [A&B] and OHCs [C&D]. AC responses were defined as the peak value of the fundamental component derived from the tone burst responses, while DC responses were defined as the mean of the response in the second half of the stimulation in both model and physiological data. The physiological recordings were obtained from Dallos (1985) [reprinted with permission].

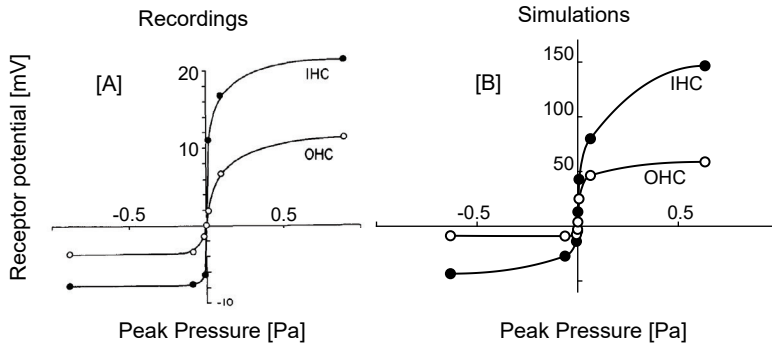


Figure 6.12. recorded [A] and simulated [B] max receptor potentials showing peak AC receptor potentials as a function of peak sound level, in response to stimulation at characteristic frequency (800Hz). The fit for simulations was done piecewise polynomial with constraints to the endpoints, the fit for the recordings is unknown. The physiological recordings were obtained from Dallos (1986) [reprinted with permission].

Figure 6.11 shows that the ratio between AC and DC response amplitudes is correctly simulated. The amplitudes of the simulated and recorded AC and DC components in both IHCs and OHCs increase with sound pressure level, but saturation is stronger in the recordings than in simulations. Figure 6.12 shows that the model successfully reproduces nonlinear behavior in both IHCs and OHCs. In both simulations, the absolute levels were comparable in response to the low stimulus levels, but up to a factor four larger in the simulations in response to high stimulus levels. An explanation for this is that the absolute response amplitudes are dependent on placement of the reference electrode. Overall, qualitative behavior of potentials of both types of hair cells in response to different stimulus levels is well described by the model.

CHAPTER 7

Discussion

Two models that can simulate acoustic responses of the implanted peripheral auditory system were presented in this thesis. One model describes responses of the auditory nerve to electrical stimulation, the other describes how responses to acoustic stimulation are recorded in a cochlear implant. In the first section of this discussion, both model designs are discussed. In the following section, the different outcome measures are discussed: single fiber action potential (SFAP), evoked compound action potential (ECAP). The SFAPs and ECAPs were calculated with the neural model, ECochG recordings were calculated with the cochlear model. In the section thereafter, the most important model parameters, and how they affect outcomes of objective measures are discussed. Limitations and suggestions for improved model design are discussed in the next section. The concluding sections describe alternative model applications and future research directions.

Model design

Neural response to electrical stimulation

With the first model responses of the auditory nerve to electrical pulse trains were simulated. It was built on an existing model of the cochlea and auditory nerve that simulates deterministic initial fiber thresholds in response to single pulses (Kalkman et al., 2015, 2014). The model was extended so that responses to pulse trains can be simulated. In the previous model, the initial thresholds were calculated with a realistic 3D geometric model of the cochlea and a biophysical active multi-nodal cable-neuron model of 32,000 nerve fibers (Frijns et al., 1994; Frijns and ten Kate, 1994; Kalkman et al., 2015). Thresholds could be calculated in response to predefined electrode configurations, pulse shapes, sizes and amplitudes, irrespective of spiking and stimulation history. In the current model, these initial thresholds were pre-calculated and stored in a database. To calculate responses to pulse trains, stochasticity and temporal components have to be described in a computationally efficient manner and with a limited parameter space. To achieve this, the pre-calculated thresholds were adjusted temporally and stochastically using a phenomenological approach. To accurately simulate temporal behavior in response to long duration pulse trains, long-term-adaptation components were introduced in the new model. It was shown that both a spiking-dependent adaptation and a stimulus-dependent adaptation (or accommodation) are required to correctly predict spike patterns. The resulting model is the first of its kind to include a combination of adaptation and accommodation. Stochasticity was implemented in the model as a relative spread (RS) on the threshold, by stochastic distributions of parameters over the fibers and by stochastic variation of the parameters in time. In a further refined version of the model, latency and jitter were implemented in the phenomenological part of the model. By having combined a biophysical approach with a phenomenological approach, this model can deal with both spatial and temporal effects in a computationally efficient manner. Because of this, single fiber action potentials (SFAPs) can be simulated for all nerve fibers in response to pulse trains. All single fiber responses together yield the pulse-train evoked

compound action potentials (ECAPs). To simulate these, the spike patterns were convolved with their contributions to the potentials recorded at each electrode contact.

Cochlear implant recordings of hair cell activity

The second model simulates how the implanted electrode records hair cell activity in response to sound, the intracochlear electrocochleography (ECochG). This model is a combination of two existing models; a model of hair cell activation (Zilany et al., 2014) and a 3D electrical conduction model (Kalkman et al., 2015) of the cochlea. Intracellular hair cell voltages were calculated with the hair cell activation model. The thus calculated intracellular voltages were similar to recordings from animal studies. Extracellular currents are calculated based on hair cell membrane resistances and capacitive low-pass filtering properties of the membrane. The 3D volume conduction model is used to calculate electrical impedances between hair cell dipoles at 3200 spatially different locations along the basilar membrane and each electrode contact. For the implanted electrode array two different designs and cochlear morphologies were used. Combining the extracellular hair cell currents with the impedances yielded simulations of the intracochlearly recorded ECochG.

Model outcomes

Responses of the peripheral auditory system either to acoustic or electrical stimulation can be recorded objectively with SFAP, ECAP and eCochG recordings, as elaborated in the introduction. Here, the ability of the models to simulate such recordings is evaluated. Single Fiber Action Potential (SFAP) recordings are made from individual neurons and can therefore be directly compared to simulated spike timings. The model of neural responses accurately simulated discharge rate I/O curves, post-stimulus time histograms (PSTH), period histograms (PH), and inter-spike interval histograms (IH), and their variances obtained from SFAP recordings (Bruce et al., 1999a; Javel et al., 1987; Litvak et al., 2001; Miller et al., 2008; Zhang et al., 2007; chapters 2 and 4) and in the case of amplitude modulated (AM) pulse trains also vector strengths (VS) and fundamental frequency (F0) amplitudes (Hu et al., 2010; Litvak et al., 2003b, 2003a; chapter 3). The simulated responses were in good agreement with animal data for continuous and amplitude modulated long-duration, pulse trains over a wide range of stimulus rates and amplitudes. The modulation detection thresholds, as interpreted by an ideal observer, inferred from the VS, yield realistic upper bounds when compared to data from human experiments (Shannon, 1992; chapter 3).

Simulated pulse-train-ECAP responses, to both short and long duration stimuli (chapter 5), replicated studies in both animals and humans (Carlyon and Deeks, 2015; Hughes et al., 2012; Jeng et al., 2009; Ramekers et al., 2015; chapter 5). Pulse train ECAP recordings show an alternation, which is replicated by the model. Modeled pulse train ECAPs showed that with the standard parameter settings, or with longer refractory periods when combined

with a larger stochasticity, describe the human data very well. Interpatient differences can now be explored with the model by investigating how parameters affect the pulse train ECAP response.

In chapter 6, intracochlear ECoChG simulations were compared to recordings from two different subjects. The model replicated characteristics seen in intracochlear ECoChG recordings in the temporal, spectral and spatial domains. Impedance calculations with the 3D volume conduction simulations demonstrate that the intracochlear ECoChG is a local measure of activation, although possibly sensitive to neighboring cochlear turns. In response to high stimulus levels, double peaks may occur which can either be contributed to cross-turn sensitivity, or to broad hair cell activation within the cochlea. Simulations of the hair cell response showed that increasing stimulus frequency results in a basal shift of the peak cochlear microphonic (CM) amplitude. The exact location on the array of the peak CM amplitude depended on cochlear geometry and electrode array type. Simulations of phase recordings showed that the recorded pattern becomes unreliable when the special sampling is too low.

Model parameters

As discussed in the previous section, the models and their average parameters are well equipped to replicate the different objective recordings of the auditory periphery to acoustic or electrical excitation. This section describes how recordings are affected by specific model parameters and how the parameters, and thus differences in recordings, might be related to hearing loss.

Neural adaptation and accommodation

Chapters 2 to 5 showed that adaptation must be implemented to correctly model auditory neuron spike rates in response to pulse trains. Adaptation decreased the discharge rate over time, and improved modulation following behavior. Only a few models of auditory nerve responses to electrical stimulation include adaptation (Negm and Bruce, 2008; Woo et al., 2009). Those models take a biophysical approach, where adaptation behavior is implemented in specific ion channels. Such models are important to provide further understanding of the origin of adaptation, but are too slow to be used to simulate spike trains in response to sound segments in a complete auditory nerve. Implementing adaptation using a phenomenological approach enabled fast simulations of neural responses to pulse trains. Spike-adaptation alone did not describe the long-term behavior; stimulus-dependent adaptation, sometimes referred to as accommodation, or sub-threshold adaptation, also had to be implemented. The time constant was assumed similar for both accommodation and adaptation. Biophysical studies have shown that there are at least a few different ion channel-types in spiral ganglion cells; fast voltage-gated sodium (Na_v) and delayed rectifier potassium (K_v) channels (Hodgkin and Huxley, 1952), but also low-threshold potassium (KLT) channels and hyperpolarization-activated

cation (HCN) channels (Negm and Bruce, 2008). These different channels invoke different currents flowing over the neural membrane which all may result in different forms of adaptation with different time scales. Because biologically it might very well be that different mechanisms underlie accommodation and spike-adaptation, different time constants for both processes could perhaps be physiologically more viable. Adaptation over different time scales can be modeled by a power-law. Power-law adaptation is suggested in general neuroscience (Fairhall et al., 2001) and is implemented in models of acoustic stimulation of the auditory periphery (Zilany et al., 2009; Zilany and Carney, 2010), but not in models of electrical stimulation. Chapter 4 shows that the adaptation is best described by a power-law, especially for long duration data. As suggested in literature, this power-law adaptation can be approximated with multiple exponentials, and the number of exponentials required to fit the data depended on the duration of stimulation to simulate. Chapter 5 shows that decreasing the magnitude of adaptation in the model produced increases in alternation of ECAP amplitude and response amplitude, as seen in deafened guinea pigs (Ramekers et al., 2015). In their study, Ramekers et al see an increased alternation depth of pulse-train ECAP in chronically deafened animals that is hypothesized to be related to altered refractoriness or jitter in hearing impaired animals. In chapter 5 this hypothesis was tested and it was shown that instead, decreasing the adaptation amplitude better reproduced recordings from the deafened animals. Thus, measurement of the pulse-train ECAP's alternation can provide a measure of adaptation, which might be related to hearing loss. Generally, explanations for the relation between hearing loss and neural behavior can be sought in axonal shrinkage, demyelination and progressive retraction of the peripheral axon (Leake and Hradek, 1988). To date, however, there is no exact biophysical explanation for any relation between hearing loss and decreased adaptation.

Refractoriness

Refractoriness has, by the use of two-pulse paradigms, been much more extensively studied than adaptation. Simulations in chapters 2 and 3 show that for longer duration stimulation, effects of refractoriness interplay with effects of accommodation and adaptation. Effects of refractoriness were mostly visible at short time scales, such as SFAP onset rates and initial rate decrements. Larger refractory parameters in the model lead to larger inter-spike intervals in the SFAP interval histograms. ECAP simulations showed that refractoriness affects the frequency at which alternation is maximal, alternation depth and, for short duration simulations, also the final response amplitude. Several previous studies show that refractory periods are longer in animals with hearing loss than in control animals (Rubinstein, 1995; Shepherd et al., 2004; Shepherd and Javel, 1997; Sly et al., 2007; Walton et al., 1995). Prolonged refractory time-constants are observed in demyelinated neurons (Waxman and Ritchie, 1993), of which the chronically deafened auditory nerve is an example (Leake and Hradek, 1988). Demyelinated nerve fibers have fewer potassium channels than myelinated fibers, which might result in a leakage of internodal potassium currents into the nodal regions and thus cause a prolongation of refractory time constants.

Stochasticity

Stochasticity was implemented in various parts of the neural model by using: a stochastic distribution of thresholds over all nerve fibers, a threshold variability, an internal variability of the refractoriness and a distribution of model parameters over the fibers. The relative stochasticity (RS) and the internal variability of the refractoriness were essential model attributes to obtain I/O curves similar to animal data in response to electrical pulse trains. Variation of RS affected the width of the peaks in the interval histograms obtained from simulated SFAPs. A lower RS resulted in slightly improved modulation following behavior and stronger phase-locking over time in response to low stimulus amplitudes. This can be explained by a more deterministic fiber more strongly relying on the exact stimulus amplitude to determine whether it fires or not. The model presented here shows that decreased stochasticity (i.e., reduced RS), or increased refractoriness of the nerve, may lead to increased alternation depths in the temporal ECAP, independent of stimulus rate. A psychophysical study by Carlyon and Deeks (2015) shows that patients with larger alternation depths in their ECAP responses perform worse on rate discrimination tasks. The simulations presented in chapter 5 suggest that CI wearers with better rate discrimination have auditory neurons with short refractory periods and strong stochastic behavior. Biophysically this can be understood as that stochasticity, or the RS of the threshold, depends on the myelination of the nerve, with demyelination reducing RS (Resnick et al., 2018).

Latency and jitter

For the SFAP simulations, latency and jitter were not implemented. This resulted in slightly later spike timings in the animal experiments than in the model simulations, visible in the post-stimulus time histograms. In the ECAP simulations latency and jitter were included. An increased latency induced a small delay in the ECAP responses. Jitter did not affect any of the output measures. Latency and jitter are important parameters when exact spike timing is of interest, such as in a model of ITD differences. Spike timing is, however, also affected by adaptation (Prescott and Sejnowski, 2008), and the exact location of the auditory neuron relative to the stimulus (Mino et al., 2004).

3D model

Both the neural model's responses to electrical stimulation and the hair cell model's responses to acoustic stimulation include a 3D model of the cochlea. It is demonstrated in chapter 2 that spike rate adaptation depends on the spatial location of the nerve fiber relative to the current source. Relative rate decreases, and thus the amount of adaptation, was largest at the borders of the stimulated area. The deterministic single pulse threshold distribution thus has a large effect on final firing patterns. The local sensitivity of the intracochlear ECoChG, as obtained with the 3D volume conduction model, was in line with a previous modeling study using a finite element approach (Teal and Ni, 2016) and with measurements made close to the hair cells (Dong and Olson, 2013; Fridberger et al., 2004), but contradicting other beliefs of wider fall-offs (Ayat et al., 2015; Charaziak et al., 2017; Davis et al., 1958; Tasaki and Fernández, 1952; v. Békésy, 1952, 1951; Whitfield and Ross,

1965). This local sensitivity implies that the intracochlearly located electrode contact is most sensitive to a small region of hair cells, located in closest proximity to the recording location. As a result of this local sensitivity of the intracochlear ECoChG, it is possible to measure acoustic tuning in the cochlea. For both types of models, it is thus of the utmost importance to include an accurate and realistic 3D volume conduction model.

Hair cell degeneration

In the intracochlear ECoChG simulations of chapter 6, different forms of hearing loss were modeled by implementing different degrees and types of hair cell degeneration. CM phase changes, as recorded with the intracochlear ECoChG, are suggested to indicate hair cell damage (Giardina et al., 2019; Koka et al., 2018), and most, but not all, data seems consistent with this theory (Tejani et al., 2019). Simulations with hair cell degeneration resulted in ECoChG responses that better resembled the recordings from subjects in terms of CM onset responses, higher harmonics, and the width of the tuning curve. Changes in the ECoChG recording in the temporal, spectral, and spatial domains were thus related to the degree and type of hair cell degeneration. Hence, it is concluded that the intracochlear ECoChG recording has the potential to elucidate on the type and degree of hair cell degeneration. Simulations show that OHCs are the main contributor to the intracochlear ECoChG response, in line with previous recordings from animal studies (Dallos, 1986, 1985, 1983; Dallos et al., 1972; Dallos and Cheatham, 1976; Davis et al., 1958; Russell et al., 1986). Animal studies correlating post-mortem histological counting of the hair cells to audiometric thresholds show that hair cell degeneration generally starts in the base and then proceeds to the apex. Laterally positioned hair cells are more vulnerable than those medially positioned. Hence, degeneration progresses from base to apex, and affects lateral OHCs first and the medially positioned IHCs last (Dallos et al., 1972; Eric Lupo et al., 2011; Stebbins et al., 1979; Van Ruyven et al., 2005, 2004). Despite this, the exact relation between audiogram and hair cell degeneration, especially in humans, remains unknown. Synaptic or retro-cochlear pathologies might cause hearing loss regardless of the status of hair cells in the cochlea (Hill et al., 2016). To verify the relationship between intracochlear ECoChG responses and hearing loss, further studies relating hair cell degeneration in humans to degree and etiologies of hearing loss are necessary.

Model design suggestions

Neural model parameters

Temporal and stochastic parameters are known to depend on fiber diameter and pulse shape (Lieberman and Oliver, 1984; Miller et al., 1999a; Resnick et al., 2018; Verveen, 1962; Woo et al., 2010; Zhang et al., 2007). These factors have not yet been included in the parameters of the phenomenological model, but could be included in a further refinement of this model. The RS was assumed to be independent of the time since a spike occurred, whereas some data suggest that RS depends on time since spike (Imennov and Rubinstein, 2009; Matsuoka et al., 2001). In response to some stimulation rates, SFAP

recordings may exhibit an increased sustained firing rate (Zhang et al., 2007), which can be hypothesized to be a result of integration effects, also referred to as summation or facilitation. In some ECAP recordings, increased amplitudes over the stimulus duration were observed (He et al., 2015), probably also related to integration. Such temporal integration was not implemented in the current model, because its exact dependency on pulse train characteristics such as rate and amplitude level needs to be investigated more thoroughly.

Hair cell model parameters

A challenge in modeling hair cell membrane behavior is the relatively sparse animal data available. Pujol et al. show that the outer hair cell length is correlated to the characteristic frequency in different species (Pujol et al., 1992). In the present study the dependency of conductance parameters on the characteristic frequency was determined from relatively sparse data (Johnson et al., 2011). A wider range of data recording how the hair cell conductance depends on characteristic frequency would be desirable. A limitation of the hair-cell model for the current application is the non-physiologically large IHC responses to stimulus levels above 80 dB SPL. From the auditory peripheral model, only responses to hair cells with a characteristic frequency larger than 125 Hz can be obtained, although hair cells with characteristic frequencies below 125 Hz might also influence the ECoHG response.

ECAP and the Unitary response

The exact unitary response, or contributions from each individual nerve fiber to the ECAP is unknown, especially for humans. Simulations in this thesis were done with a unitary response based on cat data (Miller et al., 1999b). Differences in fiber kinetics, neuron myelination, size and morphology between the cochleae of different species influence the contribution of each action potential. An important species-dependent factor is, for instance, that in humans the soma is unmyelinated, which effectively adds a large capacitance to the human auditory nerve: leading to altered spike propagation times along the nerve. For simulation of the human ECAP, a unitary response derived especially for the human situation would be desirable (Dong et al., 2018). To test sensitivity to the shape of the unitary response, simulations were repeated with an alternative unitary response (Versnel et al., 1992). With this different unitary response, the simulated normalized pulse-train ECAP responses were similar, thus such differences in shape of the unitary response would not influence the results reported in chapter 5.

Model applications

Recording adaptation in humans

The pulse train ECAP can be used as a measure of adaptation based on findings in chapter 5, as a decrease in adaptation magnitude produces an increased alternation and response amplitude in long duration simulations. First, the average refractory period of

the auditory nerve should be estimated based on a two-pulse paradigm ECAP recording, or by identification of the stimulus rate at which the ECAP alternation is maximal. After adjusting the model parameters of refractoriness accordingly, the adaptation amplitude can be altered so that recorded responses are best replicated. This will yield an indication of the adaptation amplitude. From such recordings, data on adaptation levels in patients can easily be obtained. This can be used to investigate the relationship between neural adaptation and outcomes on functional tests. Ultimately, information about the level of neural adaptation in an individual can be used to optimize settings in sound coding strategies.

Simulating other ECochG responses

The model of the eCochG responses presented in chapter 6 mainly investigated CM responses, but it can also be used to simulate intracochlear SP. With such simulations the eligibility of the SP as a diagnostic measure can be established and the origin of the SP response can be further elucidated on (Dallos and Cheatham, 1976; Davis et al., 1958; Durrant et al., 1998). In a similar approach to the ECAP simulations discussed above, after implementing neural responses, this eCochG model could also simulate compound action potential (CAP) and auditory nerve neurophonic (ANN) responses. This can be useful to evaluate how stimulus shape affects the intracochlear CAP response and ANN. The ANN is often believed to be reflected in the AC potentials in the summed response. Contrasting with this, the simulations presented in chapter 6 with only hair cells and no neurons simulated, also show an AC potential in the summed response. As another future application, the ECochG model developed here can be used to simulate the much more common extracochlear, round window, recordings. Responses to different stimulation patterns, such as chirps, clicks or tone bursts (Schoonhoven et al., 1995), or masked noises (Chertoff et al., 2012) could be modeled to better understand how these responses potentially differentiate between different types and degrees of hair cell degeneration. By combining simulations of the auditory periphery with simulations of the neural model, while incorporating electro-acoustic interactions, responses to an EAS system could also be simulated in future.

Towards model-based evaluation of sound coding strategies

Owing to the efficient implementation of spatial and temporal components, the model of responses to electrical pulse trains can be used to evaluate whole nerve responses to long duration sound segments. Simulated spike patterns in response to different stimuli, coded with different stimulation strategies, or from both ears in binaural stimulation, can now be compared. From these simulated neural responses, CI users' performance on tests as used in perceptual patient testing, such as minimal detection and identification tests, could be inferred with an interpretation model. Such simulations, whether with a basic interpretation, or a more complex perceptual interpretation model, can evaluate responses to different stimulation patterns, or sound coding strategies. Moreover, the

simulations could be used to investigate how inter-subject differences in auditory nerve characteristics will affect interpretation. These patient specific neural parameters, and related performance expectations, could yield patient specific recommendations for sound coding strategies. Whether used for optimizing sound coding strategies in general, or for personalization, the simulated spike trains have to be interpreted. In other words, spike trains have to be decoded to give information about the underlying stimuli. There are different approaches to evaluation of the information in, or to decode, these simulated spike trains.

One way to interpret spike trains would be to define a metric that can be calculated directly from the spike train, that quantifies embedded information. This outcome can be related to a stimulus. For example, a simple measure of modulation following behavior is the vector strength, which can be used to simulate modulation detection thresholds (Goldwyn et al., 2010; O'Brien et al., 2016; Xu and Collins, 2007; chapter 3). Another example of a metric that can be used to compare spike trains is cross-correlation, or coincidence counting (Heinz et al., 2001; Heinz and Swaminathan, 2009). Such measures can be very well used to compare binaural coincidence neurons for their interaural differences (Dietz, 2016). The cross-correlation metric does however, not take into account spatial effects, since only two neurons are compared. In modeling speech perception this will generally not suffice, because the whole nerve contains information about the stimulus. Also, for modeling localization in cochlear implant users, these metrics will probably not suffice. Due to differences in electrode placement and neural survival binaurally, the binaural coincidence neuron will receive unequal information. The cochlear implant recipient might use other cues for localization. Another example of a metric based on the spike pattern is using averaging in the spatial and temporal domains. For this, first an internal representation of a stimulus over time is defined from the spike patterns by a spatial averaging over all neurons and temporal windowing (Fredelake and Hohmann, 2012; Hamacher, 2004; Hines and Harte, 2012). Hereafter, this internal representation over time is compared to a reference representation by calculating the shortest Euclidean distance from the signal to the reference stimulus (Chiba and Sakoe, 1978). The temporal integration can be done by calculating average discharge rates over a steady or moving rectangular or asymmetric window, e.g. a running exponential integration window (McKay and McDermott, 1998). Instead of using time warping averaged spatially over all neurons, similarity can be assessed of the 2D representation. Here, the spatiotemporally averaged spike pattern is treated as an image, with the structural similarity index (Wang et al., 2004). In both metrics, representation with the smallest difference with the representation of the reference stimulus has the largest chance to be perceived as similar to the reference stimulus. All the metrics described here define a specific attribute of the spike train that should be evaluated. Its ability to predict psychophysical outcomes is largely dependent on the stimulus.

An alternative approach to interpreting spike patterns is the use of a neural network (Kell and McDermott, 2019). Neural network models have already been found useful in

speech recognition (Graves and Jaitly, 2014). For auditory sciences, neural networks often use spatiotemporally averaged spectrograms as inputs. From these, image classification features are extracted and used as inputs to the neural network. In a neural network, there are weights and layers connecting different aspects of the input to each other and to the output. In supervised learning, the weights of the different units that relate the output to the inputs are adjusted to minimize the error on a training set. This training set relates spectrograms to specific outputs. With this set, for example, the neural network can be trained to distinguish between two different sounds. Because in the training stage the desired output is known, this is referred to as a supervised learning deep neural network. Performance of deep learning neural networks is increasingly enhanced by introducing different levels of complexity such as multiple layers, pooling of input and optimized filtering operations. A specific class of neural networks, the spiking neural network, includes a temporal component and can be trained directly on spike trains simulated at the level of the auditory nerve (Paugam-Moisy and Bohte, 2012). Even though this is more directly applicable to the spike trains simulated in this thesis, its implementation is not straightforward because a more complex learning algorithm is required. So, it can be seen that there is a vast and growing variety of neural network designs, and there are many factors to consider when designing one for the current purpose.

Future perspectives

With an interpretation model, simulated spike trains can be compared for evaluating the effect of neural health, sound coding strategies, or binaural implants on the perceptual outcomes for cochlear implant users. This model can be used to test new sound coding strategies and to evaluate its performance in general. Sound coding strategies can be optimized for their expected performance on speech discrimination tasks, minimal just noticeable difference and detection tasks and optimal directional hearing. Moreover, patient specific performance, due to inter-individual differences in cochlear morphology and neural health, can also be modeled. Settings of the cochlear implant, its design, and its sound coding, can then be adjusted to realize an optimal performance for each individual. With this kind of modeling, the development of sound coding can be boosted, so that CI wearers will benefit more from their implants in the future.

CHAPTER 8

Samenvatting

In deze thesis zijn twee computermodellen ontwikkeld waarmee responsies op geluid na cochleaire implantatie kunnen worden nagebootst. Het eerste model simuleert het vuren van de gehoorzenuw in respons op elektrische pulstreinen. Het tweede model simuleert responsies van het perifere gehoororgaan op geluid zoals gemeten met een CI. Beide modellen kunnen gebruikt worden om geluidsoverdracht en objectieve metingen hiervan in CI-gebruikers te simuleren.

Cochleaire implantaten (CIs) zijn elektrische implantaten in het binnenoor waarmee het gehoor verbeterd kan worden bij mensen die geen of nog maar zeer weinig restgehoor hebben. De werking van deze implantaten in relatie tot het gehoororgaan wordt beschreven in **hoofdstuk 1**. Zoals ook in dat hoofdstuk beschreven wordt zijn sinds de introductie van de CI- resultaten met betrekking tot geluidsperceptie sterk verbeterd, maar recente ontwikkelingen hebben helaas niet geleid tot verdere verbetering. Het proces waarmee nieuwe ontwikkelingen kunnen worden getest is traag. Hieraan ten grondslag ligt dat het testen erg tijdrovend en vermoeiend is voor de patiënt en dat, ten gevolge van de relatief lage aantallen patiënten en de grote heterogeniteit van de populatie, het moeilijk is om een voldoende grote en representatieve testpopulatie te vinden. Om het proces te bespoedigen zou het gewenst zijn als nieuwe ontwikkelingen ook via een computersimulatie getest kunnen worden. Op deze manier zou veel sneller onderzocht kunnen worden of, op theoretische gronden, nieuwe ideeën voor geluidscodering, metingen en het ontwerp van het CI, kans van slagen hebben.

In **hoofdstukken 2 en 3** wordt een computermodel gepresenteerd waarmee simulaties van vuurpatronen van de gehoorzenuw in reactie op continue-amplitude (hoofdstuk II) en amplitude-gemoduleerde (hoofdstuk III) elektrische pulstreinen kunnen worden verkregen. In dit model is een driedimensionaal-volumegeleidingsmodel, eerder ontwikkeld in het Leidsch Universitair Medisch Centrum, uitgebreid met stochastiek, adaptatie en accommodatie. Dit complete model omvat zowel spatiële als temporele karakteristieken van de cochlea en de gehoorzenuw. Het model is gevalideerd door simulaties van single fiber action potentials (SFAPs) te vergelijken met gepubliceerde dierexperimenteel verkregen metingen. Pulstreinen met verschillende amplitudes, puls-frequenties, modulatiefrequenties en modulatiedieptes werden gebruikt. Het effect van neurale adaptatie- en stochastiek-parameters op vuurfrequentie en modulatie-specifiek volgedrag werd onderzocht. Gesimuleerde vuurpatronen toonden goede overeenstemming met de in dierexperimenten gemeten patronen. Dit toont aan dat het model karakteristiek gedrag van de zenuwvezels in respons op continue en amplitude-gemoduleerde pulstreinen goed weergeeft. Het effect van spatiële locatie van de zenuwvezel werd ook onderzocht. Daarbij werd gevonden dat adaptatie sterker is aan de rand van het gestimuleerde gebied dan in het centrum. Het gebruikte model is zeer compleet, het bevat zowel spatiële als (lange-duur) temporele elementen, en stochasticiteit op verschillende niveaus. Het model is gevalideerd voor pulstreinen van lange duur en een brede variatie van stimulusfrequenties, amplitudes en modulatieparameters. Het

model kan daarom gebruikt worden om zenuwresponsies op arbitraire input, en dus verschillende geluidscoderingsstrategieën, te evalueren.

In **hoofdstuk 4** is het model gebruikt om SFAPs te simuleren in reactie op pulstreinen met een lange duur. Hierbij is onderzocht welke wiskundige benadering van adaptatie het beste de werkelijke adaptatie van de gehoorzenuw op elektrische stimulatie beschrijft. Het is aangetoond dat in respons op pulstreinen van lange duur, een power-law functie de adaptatie beter beschrijft dan exponentiële functies. Deze power-law kan theoretisch benaderd worden door een som van exponenten, welke gefit kan worden op de power-law in een laag-dimensioneel parametrische ruimte. Hoe langer de duur van de stimulus, hoe meer exponenten benodigd zullen zijn voor een adequate fit; een simulatie van 400 ms vereiste minimaal 2 exponenten, een simulatie van 10 minuten vereiste 7 exponenten.

De eerder beschreven SFAP kan slechts worden gemeten in een enkele zenuwvezel, terwijl de gehoorzenuw uit ongeveer 30.000 zenuwvezels bestaat. De electrically evoked compound action potential (ECAP) is de respons van de complete gehoorzenuw op elektrische stimulatie. In **hoofdstuk 5** wordt deze ECAP in respons op pulstreinen gesimuleerd. Het is bekend dat deze pulstrein-ECAP een alternerend patroon laat zien. Hoe dit patroon precies afhangt van stimulus- en neuron-parameters is onbekend. Om dit te onderzoeken zijn responsies op pulstreinen met verschillende rates en amplitudes gesimuleerd, voor vezels met verschillende eigenschappen. De gesimuleerde responsies lieten een goede gelijkens zien met gepubliceerde data uit mens- en dierexperimenteel onderzoek. Ook het patroon van alternaties werd correct gesimuleerd, deze laatste werd duidelijk beïnvloed door de eigenschappen van de vezel. Deze informatie zou gebruikt kunnen worden om uit de pulstrein-ECAP te distilleren wat de temporele en stochastische eigenschappen van de gehoorzenuw zijn. Zulke eigenschappen zijn mogelijk gerelateerd aan de functionele staat van de zenuw en hebben invloed op hoe de zenuw reageert op pulstreinen, en zijn daarmee van groot belang voor optimaal horen met een CI.

In **hoofdstuk 6** is het tweede model gepresenteerd, waarmee electrocochleography (ECochG) metingen, zoals intracochleair gemeten, gesimuleerd kunnen worden. Met de intracochleaire ECochG kunnen responsies op akoestische stimulatie gemeten worden. Het is tot op heden onbekend hoe gehoorverlies en bijvoorbeeld de morfologie van de cochlea en het elektrode design zich verhouden tot deze meting. Om hier meer inzicht in te krijgen werden deze factoren getest met een computermodel. Dit model bouwt voort op twee bestaande modellen; een eerder ontwikkeld haarcel model, en het driedimensionaal volumegeleidingsmodel van de cochlea. Deze twee modellen werden gecombineerd om de potentialen uit te rekenen zoals gemeten zouden worden op de verschillende locaties van de elektrode-contacten. Simulaties werden vergeleken met intracochleaire ECochG metingen van twee CI-dragers. Bij zowel simulaties als metingen resulteerde een hogere stimulus frequentie in een meer basale locatie van de maximale amplitude. De simulaties toonden aan dat de intracochleaire ECochG vooral gevoelig is voor dichtbij gelokaliseerde haarcellen, maar ook voor haarcellen die ongeveer een

winding hoger in de cochlea liggen. Door verschillende niveaus van haarceldegeneratie te modelleren konden verschillen tussen metingen in beide CI-dragers verklaard worden.

Tot slot worden de belangrijkste resultaten bediscussieerd in **hoofdstuk 7**. De invloed van model parameters op gesimuleerde responsies op geluid of pulstreinen wordt besproken. Aanbevelingen voor verbeteringen en ideeën voor klinische toepassingen van de gepresenteerde modellen worden gegeven. Daarnaast wordt beschreven welke route bewandeld zou kunnen worden om de voorspelde vuurpatronen klinisch te interpreteren. De modellen gepresenteerd in deze thesis zullen hier de input voor kunnen leveren doordat hiermee de responsies van de gehoorzenuw op geluid gesimuleerd kunnen worden.

Bibliography

- Abbas, P.J., 1984. Long-term adaptation in hearing impaired ears. *Hear. Res.* 14, 29–38. [https://doi.org/10.1016/0378-5955\(84\)90066-2](https://doi.org/10.1016/0378-5955(84)90066-2)
- Abbas, P.J., Rubinstein, J.T., Miller, C.A., Matsuoka, A.J., Robinson, B.K., 1999. Final Report The Neurophysiological Effects of Simulated Auditory Prosthesis Stimulation. Response.
- Al Muhaimed, H., Al Anazy, F., Hamed, O., Shubair, E., 2010. Correlation between NRT measurement level and behavioral levels in pediatric cochlear implant patients. *Int. J. Pediatr. Otorhinolaryngol.* 74, 356–360. <https://doi.org/10.1016/j.ijporl.2009.12.017>
- Antunes, F.M., Nelken, I., Covey, E., Malmierca, M.S., 2010. Stimulus-specific adaptation in the auditory thalamus of the anesthetized rat. *PLoS One* 5, 1–15. <https://doi.org/10.1371/journal.pone.0014071>
- Arnesen, A.R., Osen, K.K., 1978. The cochlear nerve in the cat: topography, cochleotopy, and fiber spectrum. *J. Comp. Neurol.* 178, 661–78. <https://doi.org/10.1002/cne.901780405>
- Avissar, M., Wittig, J.H., Saunders, J.C., Parsons, T.D., 2013. Refractoriness enhances temporal coding by auditory nerve fibers. *J. Neurosci.* 33, 7681–90. <https://doi.org/10.1523/JNEUROSCI.3405-12.2013>
- Ayat, M., Teal, P.D., Searchfield, G.D., Razali, N., 2015. Cochlear microphonic broad tuning curves. *AIP Conf. Proc.* 1703. <https://doi.org/10.1063/1.4939325>
- Badenhorst, W., Malherbe, T.K., Hanekom, T., Hanekom, J.J., 2015. Development of a voltage dependent current noise algorithm for conductance based stochastic modelling of auditory nerve fibre populations in compound models, in: Conference on Implantable Auditory Prostheses. Pacific Grove, CA.
- Barlow, H.B., 1961. Possible Principles Underlying the Transformations of Sensory Messages, in: *Sensory Communication*. pp. 217–234.
- Ben-Avraham, D., Havlin, S., 1991. *Diffusion and Reactions in Fractals and Disordered Systems*, Cambridge University Press. Springer Berlin Heidelberg. <https://doi.org/10.1007/978-3-642-51435-7>
- Benda, J., Herz, A.V.M., 2003. A universal model for spike-frequency adaptation. *Neural Comput.* 15, 2523–2564. <https://doi.org/10.1162/089976603322385063>
- Blair, N.T., Bean, B.P., 2003. Role of Tetrodotoxin-Resistant Na⁺ Current Slow Inactivation in Adaptation of Action Potential Firing in Small-Diameter Dorsal Root Ganglion Neurons. *J. Neurosci.* 23, 10338–10350. <https://doi.org/10.1523/jneurosci.23-32-10338.2003>
- Bohte, S.M., 2012. Efficient Spike-Coding with Multiplicative Adaptation in a Spike Response Model. *Adv. Neural Inf. Process. Syst.* 25 1844–1852.
- Boulet, J., White, M.W., Bruce, I.C., 2016. Temporal Considerations for Stimulating Spiral Ganglion Neurons with Cochlear Implants. *JARO - J. Assoc. Res. Otolaryngol.* 17, 1–17. <https://doi.org/10.1007/s10162-015-0545-5>
- Boyle, P.J., Bchner, A., Stone, M.A., Lenarz, T., Moore, B.C.J., 2009. Comparison of dual-time-constant and fast-acting automatic gain control (AGC) systems in cochlear implants. *Int. J. Audiol.* 48, 211–221. <https://doi.org/10.1080/14992020802581982>
- Brenner, N., Bialek, W., De Ruyter Van Steveninck, R., 2000. Adaptive rescaling maximizes information transmission. *Neuron* 26, 695–702. [https://doi.org/10.1016/S0896-6273\(00\)81205-2](https://doi.org/10.1016/S0896-6273(00)81205-2)
- Briaire, J.J., Frijns, J.H.M., 2005. Unraveling the electrically evoked compound action potential. *Hear. Res.* 205, 143–56. <https://doi.org/10.1016/j.heares.2005.03.020>

- Briaire, J.J., Frijns, J.H.M., 2000. Field patterns in a 3D tapered spiral model of the electrically stimulated cochlea. *Hear. Res.* 148, 18–30. [https://doi.org/10.1016/S0378-5955\(00\)00104-0](https://doi.org/10.1016/S0378-5955(00)00104-0)
- Bruce, I.C., 1997. Spatiotemporal coding of sound in the auditory nerve for cochlear implants.
- Bruce, I.C., Erfani, Y., Zilany, M.S.A., 2018. A phenomenological model of the synapse between the inner hair cell and auditory nerve: Implications of limited neurotransmitter release sites. *Hear. Res.* 360, 40–54. <https://doi.org/10.1016/j.heares.2017.12.016>
- Bruce, I. C., Irlicht, L.S., White, M.W., O'Leary, S.J., Dynes, S.B., Javel, E., Clark, G.M., Irlicht, L.S., O'Leary, S.J., Dynes, S.B., Javel, E., Clark, G.M., 1999a. A stochastic model of the electrically stimulated auditory nerve: pulse-train response. *IEEE Trans. Biomed. Eng.* 46, 630–7. <https://doi.org/10.1109/10.764939>
- Bruce, I.C., Sachs, M.B., Young, E.D., 2003. An auditory-periphery model of the effects of acoustic trauma on auditory nerve responses. *J. Acoust. Soc. Am.* 113, 369–388. <https://doi.org/10.1121/1.1519544>
- Bruce, I. C., White, M.W., Irlicht, L.S., O'Leary, S.J., Dynes, S., Javel, E., Clark, G.M., 1999b. A stochastic model of the electrically stimulated auditory nerve: single-pulse response. *IEEE Trans. Biomed. Eng.* 46, 617–629. <https://doi.org/10.1109/10.764938>
- Calloway, N.H., Fitzpatrick, D.C., Campbell, A.P., Iseli, C., Pulver, S., Buchman, C.A., Adunka, O.F., 2014. Intracochlear electrocochleography during cochlear implantation. *Otol. Neurotol.* 35, 1451–1457. <https://doi.org/10.1097/MAO.0000000000000451>
- Campbell, L., Bester, C., Iseli, C., Sly, D., Dragovic, A., Gummer, A.W., O'Leary, S.J., 2017. Electrophysiological evidence of the basilar-membrane travelling wave and frequency place coding of sound in cochlear implant recipients. *Audiol. Neurotol.* 22, 180–189. <https://doi.org/10.1159/000478692>
- Campbell, L., Kaicer, A., Briggs, R., O'Leary, S.J., 2015. Cochlear response telemetry: Intracochlear electrocochleography via cochlear implant neural response telemetry pilot study results. *Otol. Neurotol.* 36, 399–405. <https://doi.org/10.1097/MAO.0000000000000678>
- Campbell, L.J., Sly, D.J., O'Leary, S.J., 2012. Prediction and control of neural responses to pulsatile electrical stimulation. *J. Neural Eng.* 9, 026023. <https://doi.org/10.1088/1741-2560/9/2/026023>
- Carlyon, R.P., Deeks, J.M., 2015. Combined neural and behavioural measures of temporal pitch perception in cochlear implant users. *J. Acoust. Soc. Am.* 138, 2885–2905. <https://doi.org/10.1121/1.4934275>
- Carney, L.H., 1993. A model for the responses of low-frequency auditory-nerve fibers in cat. *J. Acoust. Soc. Am.* 93, 401–417. <https://doi.org/10.1121/1.405620>
- Cartee, L.A., van den Honert, C., Finley, C.C., Miller, R.L., 2000. Evaluation of a model of the cochlear neural membrane. I. Physiological measurement of membrane characteristics in response to intrameatal electrical stimulation. *Hear. Res.* 146, 143–52.
- Charaziak, K.K., Shera, C.A., Siegel, J.H., 2017. Using cochlear microphonic potentials to localize peripheral hearing loss. *Front. Neurosci.* 11. <https://doi.org/10.3389/fnins.2017.00169>
- Chen, F., Zhang, Y., 2007. An integrate-and-fire-based auditory nerve model and its response to high-rate pulse train. *Neurocomputing* 70, 1051–1055. <https://doi.org/10.1016/j.neucom.2006.09.001>
- Chertoff, M.E., Earl, B.R., Diaz, F.J., Sorensen, J.L., 2012. Analysis of the cochlear microphonic to a low-frequency tone embedded in filtered noise. *J. Acoust. Soc. Am.* 132, 3351–3362. <https://doi.org/10.1121/1.4757746>

- Choudhury, B., Fitzpatrick, D.C., Buchman, C.A., Wei, B.P., Dillon, M.T., He, S., Adunka, O.F., 2012. Intraoperative Round Window Recordings to Acoustic Stimuli From Cochlear Implant Patients. *Otol. Neurotol.* 33, 1507–1515. <https://doi.org/10.1097/MAO.0b013e31826dbc80>
- Clague, H., Theunissen, F., Miller, J.P., 1997. Effects of Adaptation on Neural Coding by Primary Sensory Interneurons in the Cricket Cercal System. *J. Neurophysiol.* 77, 207–220. <https://doi.org/10.1152/jn.1997.77.1.207>
- Clark, G.M., Clark, J.C.M., 2013. The evolving science of cochlear implants. *JAMA* 310, 1225–6. <https://doi.org/10.1001/jama.2013.278142>
- Clay, K.M., Brown, C.J., 2007. Adaptation of the electrically evoked compound action potential (ECAP) recorded from nucleus CI24 cochlear implant users. *Ear Hear.* 28, 850–861. <https://doi.org/10.1097/AUD.0b013e318157671f>
- Cohen, L.T., 2009. Practical model description of peripheral neural excitation in cochlear implant recipients: 3. ECAP during bursts and loudness as function of burst duration. *Hear. Res.* 247, 112–21. <https://doi.org/10.1016/j.heares.2008.11.002>
- Dalbert, A., Pfiffner, F., Rössli, C., Thoele, K., Sim, J.H., Gerig, R., Huber, A.M., 2015. Extra- and intracochlear electrocochleography in cochlear implant recipients. *Audiol. Neurotol.* 20, 339–348. <https://doi.org/10.1159/000438742>
- Dallos, P., 1986. Neurobiology of cochlear inner and outer hair cells: Intracellular recordings. *Hear. Res.* 22, 185–198.
- Dallos, P., 1985. Response characteristics of mammalian cochlear hair cells. *J. Neurosci.* 5, 1591–1608. <https://doi.org/10.1523/JNEUROSCI.05-06-01591.1985>
- Dallos, P., 1984. Some electrical circuit properties of the organ of Corti. II. Analysis including reactive elements. *Hear. Res.* 14, 281–291. [https://doi.org/10.1016/0378-5955\(84\)90055-8](https://doi.org/10.1016/0378-5955(84)90055-8)
- Dallos, P., 1983. Some electrical circuit properties of the organ of Corti. I. Analysis without reactive elements. *Hear. Res.* 12, 89–119. [https://doi.org/10.1016/0378-5955\(83\)90120-X](https://doi.org/10.1016/0378-5955(83)90120-X)
- Dallos, P., Billone, N.C., Durrant, J.D., Wang, C. -y., Raynor, S., 1972. Cochlear Inner and Outer Hair Cells: Functional Differences. *Science* (80-.). 177, 356–358. <https://doi.org/10.1126/science.177.4046.356>
- Dallos, P., Cheatham, M.A., 1976. Production of cochlear potentials by inner and outer hair cells. *J. Acoust. Soc. Am.* 60, 510–512. <https://doi.org/10.1121/1.381086>
- Davis, H., Deatherage, B.H., Rosenblut, B., Fernandez, C., Kimura, R., Smith, C.A., 1958. Modification of cochlear potentials produced by streptomycin poisoning and by extensive venous obstruction. *Laryngoscope* 68, 596–627. <https://doi.org/10.1002/lary.5540680341>
- de Ruyter van Steveninck, R.R., Zaagman, W.H., Mastebroek, H.A.K., 1986. Adaptation of transient responses of a movement-sensitive neuron in the visual system of the blowfly *Calliphora erythrocephala*. *Biol. Cybern.* 54, 223–236. <https://doi.org/10.1007/BF00318418>
- de Vos, J.J., Biesheuvel, J.D., Briaire, J.J., Boot, P.S., van Gendt, M.J., Dekkers, O.M., Fiocco, M., Frijns, J.H.M., 2017. Use of Electrically Evoked Compound Action Potentials for Cochlear Implant Fitting. *Ear Hear.* <https://doi.org/10.1097/AUD.0000000000000495>
- Dean, I., Harper, N.S., McAlpine, D., 2005. Neural population coding of sound level adapts to stimulus statistics. *Nat. Neurosci.* 8, 1684–1689. <https://doi.org/10.1038/nn1541>

- Dekker, D.M.T., Briaire, J.J., Frijns, J.H.M., 2014. The impact of internodal segmentation in biophysical nerve fiber models. *J. Comput. Neurosci.* 37, 307–315. <https://doi.org/10.1007/s10827-014-0503-y>
- Dhanasingh, A., Jolly, C., 2017. An overview of cochlear implant electrode array designs. *Hear. Res.* 356, 93–103. <https://doi.org/10.1016/j.heares.2017.10.005>
- Djourno, A., Eyries, C., 1957. Auditory prosthesis by means of a distant electrical stimulation of the sensory nerve with the use of an indwelt coiling. *Presse Med.* 65, 1417.
- Dong, W., Olson, E.S., 2013. Detection of cochlear amplification and its activation. *Biophys. J.* 105, 1067–1078. <https://doi.org/10.1016/j.bpj.2013.06.049>
- Dong, Y., Briaire, J.J., Frijns, J.H.M., 2018. Unravelling the Neural Firing Properties Underlying Human eCAPs through an Extended Deconvolution Method, in: OMAI 2018. p. 172.
- Doyle, J.H., Doyle, J.B., Turnbull, F.M., 1964. Electrical Stimulation of Eighth Cranial Nerve. *Arch. Otolaryngol.* 80, 388–391.
- Drennan, W.R., Rubinstein, J.T., 2008. Music perception in cochlear implant users and its relationship with psychophysical capabilities. *J. Rehabil. Res. Dev.* 45, 779–89. <https://doi.org/10.1682/JRRD.2007.08.0118>
- Drew, P.J., Abbott, L.F., 2006. Models and properties of power-law adaptation in neural systems. *J. Neurophysiol.* 96, 826–33. <https://doi.org/10.1152/jn.00134.2006>
- Durrant, J.D., Wang, J., Ding, D.L., Salvi, R.J., 1998. Are inner or outer hair cells the source of summing potentials recorded from the round window? *J. Acoust. Soc. Am.* 104, 370. <https://doi.org/10.1121/1.423293>
- Dynes, S.B., 1996. Discharge Characteristics of Auditory Nerve Fibers for Pulsatile Electrical Stimuli. *Dep. Phys.*
- Dynes, S.B., Delgutte, B., 1992. Phase-locking of auditory-nerve discharges to sinusoidal electric stimulation of the cochlea. *Hear. Res.* 58, 79–90. [https://doi.org/10.1016/0378-5955\(92\)90011-B](https://doi.org/10.1016/0378-5955(92)90011-B)
- Eggermont, J.J., 2017. Ups and downs in 75 years of electrocochleography. *Front. Syst. Neurosci.* 11, 1–21. <https://doi.org/10.3389/fnsys.2017.00002>
- Epping, W.J.M., 1990. Influence of adaptation on neural sensitivity to temporal characteristics of sound in the dorsal medullary nucleus and torus semicircularis of the grassfrog. *Hear. Res.* 45, 1–13. [https://doi.org/10.1016/0378-5955\(90\)90178-R](https://doi.org/10.1016/0378-5955(90)90178-R)
- Eric Lupo, J., Koka, K., Thornton, J.L., Tollin, D.J., 2011. The effects of experimentally induced conductive hearing loss on spectral and temporal aspects of sound transmission through the ear. *Hear. Res.* 272, 30–41. <https://doi.org/10.1016/j.heares.2010.11.003>
- Fairhall, A.L., Lewen, G.D., Bialek, W., de Ruyter van Steveninck, R.R., 2001. Efficiency and ambiguity in an adaptive neural code. *Nature* 412, 787–792. <https://doi.org/10.1038/35090500>
- Ferraro, J.A., Arenberg, I.K., Hassanein, R.S., 1985. Electrocochleography and Symptoms of Inner Ear Dysfunction. *Arch. Otolaryngol.* 111, 71–74. <https://doi.org/10.1001/archotol.1985.00800040035001>
- Fletcher, H., Munson, W.A., 1933. Loudness, Its Definition, Measurement and Calculation*. *Bell Syst. Tech. J.* 12, 377–430. <https://doi.org/10.1002/j.1538-7305.1933.tb00403.x>
- Fontenot, T.E., Giardina, C.K., Fitzpatrick, D.C., 2017. A Model-Based Approach for Separating the Cochlear Microphonic from the Auditory Nerve Neurophonic in the Ongoing Response Using Electrocochleography. *Front. Neurosci.* 11, 1–18. <https://doi.org/10.3389/fnins.2017.00592>

- Forgues, M., Koehn, H.A., Dunnon, A.K., Pulver, S.H., Buchman, C.A., Adunka, O.F., Fitzpatrick, D.C., 2014. Distinguishing hair cell from neural potentials recorded at the round window. *J. Neurophysiol.* 111, 580–593. <https://doi.org/10.1152/jn.00446.2013>
- Frankenhaeuser, B., Huxley, A.F., 1964. The Action Potential in the Myelinate Nerve Fiber of *Xenos Laevis* as computed on the basis of Voltage Clamp Data. *J. Physiol.* 171, 302–15.
- Fredelake, S., Hohmann, V., 2012. Factors affecting predicted speech intelligibility with cochlear implants in an auditory model for electrical stimulation. *Hear. Res.* 287, 76–90. <https://doi.org/10.1016/j.heares.2012.03.005>
- Fridberger, A., De Monvel, J.B., Zheng, J., Hu, N., Zou, Y., Ren, T., Nuttall, A., 2004. Organ of corti potentials and the motion of the basilar membrane. *J. Neurosci.* 24, 10057–10063. <https://doi.org/10.1523/JNEUROSCI.2711-04.2004>
- Frijns, J.H.M., Briaire, J.J., Grote, J.J., 2001. The importance of human cochlear anatomy for the results of modiolus-hugging multichannel cochlear implants. *Otol. Neurotol.* 22, 340–9.
- Frijns, J.H.M., Briaire, J.J., Schoonhoven, R., 2000. Integrated use of volume conduction and neural models to simulate the response to cochlear implants. *Simul. Pract. Theory* 8, 75–97. [https://doi.org/10.1016/S0928-4869\(00\)00008-2](https://doi.org/10.1016/S0928-4869(00)00008-2)
- Frijns, J.H.M., de Snoo, S.L., Schoonhoven, R., 1995. Potential distributions and neural excitation patterns in a rotationally symmetric model of the electrically stimulated cochlea. *Hear. Res.* 87, 170–186. [https://doi.org/10.1016/0378-5955\(95\)00090-Q](https://doi.org/10.1016/0378-5955(95)00090-Q)
- Frijns, J.H.M., Kalkman, R.K., Vanpoucke, F.J., Bongers, J.S., Briaire, J.J., 2009. Simultaneous and non-simultaneous dual electrode stimulation in cochlear implants: evidence for two neural response modalities. *Acta Otolaryngol.* 129, 433–9. <https://doi.org/10.1080/00016480802610218>
- Frijns, J.H.M., Mooij, J., ten Kate, J.H., 1994. A quantitative approach to modeling mammalian myelinated nerve fibers for electrical prosthesis design. *IEEE Trans. Biomed. Eng.* 41, 556–66. <https://doi.org/10.1109/10.293243>
- Frijns, J.H.M., ten Kate, J.H., 1994. A model of myelinated nerve fibres for electrical prosthesis design. *Med. Biol. Eng. Comput.* 32, 391–398. <https://doi.org/10.1007/BF02524690>
- Fu, Q., 2002. Temporal processing and speech recognition in cochlear implant users. *Neuroreport* 13, 1635–9. <https://doi.org/10.1097/00001756-200209160-00013>
- Fuller, C.D., Galvin, J.J., Maat, B., Free, R.H., Baskent, D., 2014. The musician effect: does it persist under degraded pitch conditions of cochlear implant simulations? *Front. Neurosci.* 8, 1–16.
- Fusi, S., Drew, P.J., Abbott, L.F., 2005. Cascade models of synaptically stored memories. *Neuron* 45, 599–611. <https://doi.org/10.1016/j.neuron.2005.02.001>
- Gantz, B.J., Turner, C.W., 2010. Combining acoustic and electrical hearing. *Laryngoscope* 113, 1726–1730. <https://doi.org/10.1097/00005537-200310000-00012>
- Giardina, C.K., Brown, K.D., Adunka, O.F., Buchman, C.A., Hutson, K.A., Pillsbury, H.C., Fitzpatrick, D.C., 2019. Intracochlear electrocochleography: Response patterns during cochlear implantation and hearing preservation. *Ear Hear.* 40, 833–848. <https://doi.org/10.1097/AUD.0000000000000659>
- Gibson, W.P.R., 1983. Diagnostic Significance of Transtympanic Electrocochleography in Ménière's Disease. *Oto-Rhino-Laryngology Tokyo* 26, 629–633. <https://doi.org/10.11453/orltohyo1958.26.629>

- Gibson, W.P.R., Moffat, D.A., Ramsden, R.T., 1977. Clinical electrocochleography in the diagnosis and management of menière's disorders. *Int. J. Audiol.* 16, 389–401. <https://doi.org/10.3109/00206097709071852>
- Goldberg, J.M., Brown, P.B., 1969. Response of binaural neurons of dog superior olivary complex to dichotic tonal stimuli: some physiological mechanisms of sound localization. *J. Neurophysiol.* 32, 613–36. https://doi.org/10.1007/978-1-4612-2700-7_3
- Goldstein, M.H., Kiang, N.Y. -S., 1958. Synchrony of Neural Activity in Electric Responses Evoked by Transient Acoustic Stimuli. *J. Acoust. Soc. Am.* 30, 107–114. <https://doi.org/10.1121/1.1909497>
- Goldwyn, J.H., Bierer, S.M., Bierer, J.A., 2010a. Modeling the electrode-neuron interface of cochlear implants: effects of neural survival, electrode placement, and the partial tripolar configuration. *Hear. Res.* 268, 93–104. <https://doi.org/10.1016/j.heares.2010.05.005>
- Goldwyn, J.H., Rubinstein, J.T., Shea-Brown, E., 2012. A point process framework for modeling electrical stimulation of the auditory nerve. *J. Neurophysiol.* 108, 1430–52. <https://doi.org/10.1152/jn.00095.2012>
- Goldwyn, J.H., Shea-Brown, E., Rubinstein, J.T., 2010b. Encoding and decoding amplitude-modulated cochlear implant stimuli—a point process analysis. *J. Comput. Neurosci.* 28, 405–24. <https://doi.org/10.1007/s10827-010-0224-9>
- Goychuk, I., Hänggi, P., 2004. Fractional diffusion modeling of ion channel gating. *Phys. Rev. E - Stat. Physics, Plasmas, Fluids, Relat. Interdiscip. Top.* 70, 9. <https://doi.org/10.1103/PhysRevE.70.051915>
- Haenggeli, A., Zhang, J.S., Vischer, M.W., Pelizzone, M., Rouiller, E.M., 1998. Electrically evoked compound action potential (ECAP) of the cochlear nerve in response to pulsatile electrical stimulation of the cochlea in the rat: effects of stimulation at high rates. *Audiology* 37, 353–371. <https://doi.org/10.3109/00206099809072989>
- Hamacher, V., 2004. Signalverarbeitungsmodelle des elektrisch stimulierten Gehörs - PhD Thesis. Technische Hochschule Aachen.
- Harris, M.S., Riggs, W.J., Giardina, C.K., O'Connell, B.P., Holder, J.T., Dwyer, R.T., Koka, K., Labadie, R.F., Fitzpatrick, D.C., Adunka, O.F., 2017. Patterns Seen During Electrode Insertion Using Intracochlear Electrocochleography Obtained Directly Through a Cochlear Implant. *Otol. Neurotol.* 38, 1415–1420. <https://doi.org/10.1097/MAO.0000000000001559>
- Hartmann, R., Topp, G., Klinke, R., 1984. Discharge patterns of cat primary auditory fibers with electrical stimulation of the cochlea. *Hear. Res.* 13, 47–62. [https://doi.org/10.1016/0378-5955\(84\)90094-7](https://doi.org/10.1016/0378-5955(84)90094-7)
- Hay-McCutcheon, M.J., Brown, C.J., Abbas, P.J., 2005. An analysis of the impact of auditory-nerve adaptation on behavioral measures of temporal integration in cochlear implant recipients. *J. Acoust. Soc. Am.* 118, 2444–57. <https://doi.org/10.1121/1.2035593>
- He, S., Abbas, P.J., Doyle, D. V., McFayden, T.C., Mulherin, S., 2015. Temporal Response Properties of the Auditory Nerve in Implanted Children with Auditory Neuropathy Spectrum Disorder and Implanted Children with Sensorineural Hearing Loss. *Ear Hear.* 397–411. <https://doi.org/10.1097/AUD.0000000000000254>
- Heffer, L. F., Sly, D.J., Fallon, J.B., White, M.W., Shepherd, R.K., O'Leary, S.J., 2010. Examining the auditory nerve fiber response to high rate cochlear implant stimulation: chronic sensorineural hearing loss and facilitation. *J. Neurophysiol.* 104, 3124–35. <https://doi.org/10.1152/jn.00500.2010>

- Heffer, Leon F, Sly, D.J., Fallon, J.B., White, M.W., Shepherd, R.K., O'Leary, S.J., 2010. Examining the auditory nerve fiber response to high rate cochlear implant stimulation: chronic sensorineural hearing loss and facilitation. *J. Neurophysiol.* 104, 3124–35. <https://doi.org/10.1152/jn.00500.2010>
- Helmstaedter, V., Lenarz, T., Erfurt, P., Kral, A., Baumhoff, P., 2018. The Summating Potential Is a Reliable Marker of Electrode Position in Electrocochleography. *Ear Hear.* 39, 687–700. <https://doi.org/10.1097/AUD.0000000000000526>
- Hill, K., Yuan, H., Wang, X., Sha, S.H., 2016. Noise-induced loss of hair cells and cochlear synaptopathy are mediated by the activation of AMPK. *J. Neurosci.* 36, 7497–7510. <https://doi.org/10.1523/JNEUROSCI.0782-16.2016>
- Hodgkin, A.L., Huxley, A.F., 1952. A quantitative description of membrane current and its application to conduction and excitation in nerve. *J. Physiol.* 117, 500–544. <https://doi.org/10.1113/jphysiol.1952.sp004764>
- Holden, L.K., Finley, C.C., Firszt, J.B., Holden, T.A., Brenner, C., Potts, L.G., Gotter, B.D., Vanderhoof, S.S., Mispagel, K., Heydebrand, G., Skinner, M.W., 2013. Factors Affecting Open-Set Word Recognition in Adults With Cochlear Implants. *Ear Hear.* 34, 342–360. <https://doi.org/10.1097/AUD.0b013e3182741aa7>
- Hong, R.S., Rubinstein, J.T., 2003. High-rate conditioning pulse trains in cochlear implants: Dynamic range measures with sinusoidal stimuli. *J. Acoust. Soc. Am.* 114, 3327. <https://doi.org/10.1121/1.1623785>
- Horne, C.D.F., Sumner, C.J., Seeber, B.U., 2016. A Phenomenological Model of the Electrically Stimulated Auditory Nerve Fiber : Temporal and Biphasic Response Properties. *Front. Comput. Neurosci.* 10, 1–17. <https://doi.org/10.3389/fncom.2016.00008>
- House, W.F., Urban, J.P.E., 1973. Long Term Results of Electrode Implantation and Electronic Stimulation of the Cochlea in Man. *Ann. Otol. Rhinol. Laryngol.* 82, 504–517.
- Housley G.D., Ashmore, J.F., 1992. Ionic Currents of Outer Hair Cells Isolated from the Guinea-Pig Cochlea. *Physiology* 73–98.
- Hu, N., Miller, C.A., Abbas, P.J., Robinson, B.K., Woo, J., 2010. Changes in auditory nerve responses across the duration of sinusoidally amplitude-modulated electric pulse-train stimuli. *J. Assoc. Res. Otolaryngol.* 11, 641–56. <https://doi.org/10.1007/s10162-010-0225-4>
- Huarte, A., Ramos, A., Morera, C., Garcia-Ibáñez, L., Battmer, R., Dillier, N., Wesarg, T., Müller-Deile, J., Hey, M., Offeciers, E., von Wallenberg, E., Coudert, C., Killian, M., 2014. Evaluation of neural response telemetry (NRT™) with focus on long-term rate adaptation over a wide range of stimulation rates. *Cochlear Implants Int.* 15, 136–144. <https://doi.org/10.1179/1754762814Y.0000000063>
- Hughes, M.L., Baudhuin, J.L., Goehring, J.L., 2014. The relation between auditory-nerve temporal responses and perceptual rate integration in cochlear implants. *Hear. Res.* 316, 44–56. <https://doi.org/10.1016/j.heares.2014.07.007>
- Hughes, M.L., Brown, C.J., Abbas, P.J., Wolaver, A.A., Gervais, J.P., 2000. Comparison of EAP thresholds with MAP levels in the nucleus 24 cochlear implant: data from children. *Ear Hear.* 21, 164–74. <https://doi.org/10.1097/00003446-200004000-00010>

- Hughes, M.L., Castioni, E.E., Goehring, J.L., Baudhuin, J.L., 2012. Temporal response properties of the auditory nerve: data from human cochlear-implant recipients. *Hear. Res.* 285, 46–57. <https://doi.org/10.1016/j.heares.2012.01.010>
- Imennov, N.S., Rubinstein, J.T., 2009. Stochastic population model for electrical stimulation of the auditory nerve. *IEEE Trans. Biomed. Eng.* 56, 2493–501. <https://doi.org/10.1109/TBME.2009.2016667>
- Javel, E., Tong, Y.C., Shepherd, R.K., Clark, G.M., 1987. Responses of cat auditory nerve fibers to biphasic electrical current pulses. *Ann. Otol. Rhinol. Laryngol.* 96, 26–30.
- Jeng, F.C., Abbas, P.J., Hu, N., Miller, C.A., Nourski, K. V., Robinson, B.K., 2009. Effects of temporal properties on compound action potentials in response to amplitude-modulated electric pulse trains in guinea pigs. *Hear. Res.* 247, 47–59. <https://doi.org/10.1016/j.heares.2008.10.007>
- Johnson, S.L., Beurg, M., Marcotti, W., Fettiplace, R., 2011. Prestin-Driven Cochlear Amplification Is Not Limited by the Outer Hair Cell Membrane Time Constant. *Neuron* 70, 1143–1154. <https://doi.org/10.1016/j.neuron.2011.04.024>
- Kalkman, R.K., Briaire, J.J., Dekker, D.M.T., Frijns, J.H.M., 2014. Place pitch versus electrode location in a realistic computational model of the implanted human cochlea. *Hear. Res.* 315, 10–24. <https://doi.org/10.1016/j.heares.2014.06.003>
- Kalkman, R.K., Briaire, J.J., Frijns, J.H.M., 2016. Stimulation strategies and electrode design in computational models of the electrically stimulated cochlea: An overview of existing literature. *Netw. Comput. Neural Syst.* 27, 107–134. <https://doi.org/10.3109/0954898X.2016.1171412>
- Kalkman, R.K., Briaire, J.J., Frijns, J.H.M., 2015. Current focussing in cochlear implants: An analysis of neural recruitment in a computational model. *Hear. Res.* 322, 89–98. <https://doi.org/10.1016/j.heares.2014.12.004>
- Kandel, E., Schwartz, J., 2000. *Principles of Neural Science*, 5th ed. McGraw-Hill Education - Europe.
- Kidd, G., Mason, C.R., Feth, L.L., 1984. Temporal integration of forward masking in listeners having sensorineural hearing loss. *J. Acoust. Soc. Am.* 75, 937–944. <https://doi.org/10.1121/1.390558>
- Koka, K., Riggs, W.J., Dwyer, R., Holder, J.T., Noble, J.H., Dawant, B.M., Ortmann, A., Valenzuela, C. V., Mattingly, J.K., Harris, M.M., O'Connell, B.P., Litvak, L.M., Adunka, O.F., Buchman, C.A., Labadie, R.F., 2018. Intra-Cochlear Electrocochleography During Cochlear Implant Electrode Insertion Is Predictive of Final Scalar Location. *Otol. Neurotol.* 39, e654–e659. <https://doi.org/10.1097/MAO.0000000000001906>
- Koka, K., Saoji, A.A., Attias, J., Litvak, L.M., 2017a. An objective estimation of air-bone-gap in cochlear implant recipients with residual hearing using electrocochleography. *Front. Neurosci.* 11, 1–7. <https://doi.org/10.3389/fnins.2017.00210>
- Koka, K., Saoji, A.A., Litvak, L.M., 2017b. Electrocochleography in Cochlear Implant Recipients With Residual Hearing. *Ear Hear.* 38, e161–e167. <https://doi.org/10.1097/AUD.0000000000000385>
- Kotak, V.C., 2005. Hearing Loss Raises Excitability in the Auditory Cortex. *J. Neurosci.* 25, 3908–3918. <https://doi.org/10.1523/JNEUROSCI.5169-04.2005>
- Laneau, J., Wouters, J., Moonen, M., 2004. Relative contributions of temporal and place pitch cues to fundamental frequency discrimination in cochlear implantees. *J. Acoust. Soc. Am.* 116, 3606–3619. <https://doi.org/10.1121/1.1823311>
- Leake, P.A., Hradek, G.T., 1988. Cochlear pathology of long term neomycin induced deafness in cats. *Hear. Res.* 33, 11–33. [https://doi.org/10.1016/0378-5955\(88\)90018-4](https://doi.org/10.1016/0378-5955(88)90018-4)

- Liberman, M.C., Oliver, M.E., 1984. Morphometry of intracellularly labeled neurons of the auditory nerve: correlations with functional properties. *J. Comp. Neurol.* 223, 163–176. <https://doi.org/10.1002/cne.902230203>
- Litvak, L., Delgutte, B., Eddington, D., 2001. Auditory nerve fiber responses to electric stimulation: Modulated and unmodulated pulse trains. *J. Acoust. Soc. Am.* 110, 368. <https://doi.org/10.1121/1.1375140>
- Litvak, L.M., Delgutte, B., Eddington, D.K., 2003a. Improved temporal coding of sinusoids in electric stimulation of the auditory nerve using desynchronizing pulse trains. *J. Acoust. Soc. Am.* 114, 2079. <https://doi.org/10.1121/1.1612493>
- Litvak, L.M., Smith, Z.M., Delgutte, B., Eddington, D.K., 2003b. Desynchronization of electrically evoked auditory-nerve activity by high-frequency pulse trains of long duration. *J. Acoust. Soc. Am.* 114, 2066–2078. <https://doi.org/10.1121/1.1612492>
- Liu, W., Edin, F., Atturo, F., Rieger, G., Löwenheim, H., Senn, P., Blumer, M., Schrott-Fischer, A., Rask-Andersen, H., Glueckert, R., 2015. The pre- and post-somatic segments of the human type I spiral ganglion neurons – Structural and functional considerations related to cochlear implantation. *Neuroscience* 284, 470–482. <https://doi.org/10.1016/j.neuroscience.2014.09.059>
- Liu, Y.H., Wang, X.J., 2001. Spike-frequency adaptation of a generalized leaky integrate-and-fire model neuron. *J. Comput. Neurosci.* 10, 25–45. <https://doi.org/10.1023/A:1008916026143>
- Loeb, G.E., 1990. Cochlear prosthetics. *Annu. Rev. Neurosci.* 13, 357–371.
- Loquet, G., Pelizzone, M., Valentini, G., Rouiller, E.M., 2004. Matching the neural adaptation in the rat ventral cochlear nucleus produced by artificial (electric) and acoustic stimulation of the cochlea. *Audiol. Neuro-Otology* 9, 144–159. <https://doi.org/10.1159/000077266>
- Lorenzi, C., Gilbert, G., Carn, H., Garnier, S., Moore, B.C.J., 2006. Speech perception problems of the hearing impaired reflect inability to use temporal fine structure. *Proc. Natl. Acad. Sci. U. S. A.* 103, 18866–18869. <https://doi.org/10.1073/pnas.0607364103>
- Macherey, O., Carlyon, R.P., van Wieringen, A., Wouters, J., 2007. A dual-process integrator-resonator model of the electrically stimulated human auditory nerve. *J. Assoc. Res. Otolaryngol.* 8, 84–104. <https://doi.org/10.1007/s10162-006-0066-3>
- Madison, D. V., Nicoll, R.A., 1984. Control of the repetitive discharge of rat CA1 pyramidal neurones in vitro. *J. Physiol.* 354, 319–331.
- Mammano, F., Ashmore, J.F., 1996. Differential expression of outer hair cell potassium currents in the isolated cochlea of the guinea-pig. *J. Physiol.* 496, 639–646. <https://doi.org/10.1113/jphysiol.1996.sp021715>
- Mandalà, M., Colletti, L., Tonoli, G., Colletti, V., 2012. Electrocochleography during cochlear implantation for hearing preservation. *Otolaryngol. - Head Neck Surg. (United States)* 146, 774–781. <https://doi.org/10.1177/0194599811435895>
- Matsuoka, A.J., Abbas, P.J., Rubinstein, J.T., Miller, C.A., 2000. The neuronal response to electrical constant-amplitude pulse train stimulation: Evoked compound action potential recordings. *Hear. Res.* 149, 115–128. [https://doi.org/10.1016/S0378-5955\(00\)00172-6](https://doi.org/10.1016/S0378-5955(00)00172-6)
- Matsuoka, A.J., Rubinstein, J.T., Abbas, P.J., Miller, C.A., 2001. The effects of interpulse interval on stochastic properties of electrical stimulation: models and measurements. *IEEE Trans. Biomed. Eng.* 48, 416–24. <https://doi.org/10.1109/10.915706>

- McKay, C.M., Chandan, K., Akhoun, I., Siciliano, C., Kluk, K., 2013. Can ECAP Measures Be Used for Totally Objective Programming of Cochlear Implants? *J. Assoc. Res. Otolaryngol.* 14, 879–890. <https://doi.org/10.1007/s10162-013-0417-9>
- McNeal, D.R., 1976. Analysis of a model for excitation of myelinated nerve. *IEEE Trans. Biomed. Eng.* 23, 329–37.
- Mensi, S., Hagens, O., Gerstner, W., Pozzorini, C., 2016. Enhanced Sensitivity to Rapid Input Fluctuations by Nonlinear Threshold Dynamics in Neocortical Pyramidal Neurons. *PLoS Comput. Biol.* 12, 1–38. <https://doi.org/10.1371/journal.pcbi.1004761>
- Miller, C.A., Abbas, P.J., Robinson, B.K., 2001. Response properties of the refractory auditory nerve fiber. *J. Assoc. Res. Otolaryngol.* 2, 216–232. <https://doi.org/10.1007/s101620010083>
- Miller, C.A., Abbas, P.J., Robinson, B.K., Rubinstein, J.T., Matsuoka, A.J., 1999a. Electrically evoked single-fiber action potentials from cat: Responses to monopolar, monophasic stimulation. *Hear. Res.* 130, 197–218. [https://doi.org/10.1016/S0378-5955\(99\)00012-X](https://doi.org/10.1016/S0378-5955(99)00012-X)
- Miller, C.A., Abbas, P.J., Rubinstein, J.T., 1999b. An empirically based model of the electrically evoked compound action potential. *Hear. Res.* 135, 1–18. [https://doi.org/10.1016/S0378-5955\(99\)00081-7](https://doi.org/10.1016/S0378-5955(99)00081-7)
- Miller, C.A., Hu, N., Zhang, F., Robinson, B.K., Abbas, P.J., 2008. Changes across time in the temporal responses of auditory nerve fibers stimulated by electric pulse trains. *J. Assoc. Res. Otolaryngol.* 9, 122–37. <https://doi.org/10.1007/s10162-007-0108-5>
- Mino, H., Rubinstein, J.T., Miller, C.A., Abbas, P.J., 2004. Effects of Electrode-to-Fiber Distance on Temporal Neural Response with Electrical Stimulation. *IEEE Trans. Biomed. Eng.* 51, 13–20. <https://doi.org/10.1109/TBME.2003.820383>
- Mistrič, P., Mullaley, C., Mammano, F., Ashmore, J., 2009. Three-dimensional current flow in a large-scale model of the cochlea and the mechanism of amplification of sound. *J. R. Soc. Interface* 6, 279–91. <https://doi.org/10.1098/rsif.2008.0201>
- Mittal, R., Panwar, S., 2009. Correlation between intra-operative high rate neural response telemetry measurements and behaviourally obtained threshold and comfort levels in patients using Nucleus 24 cochlear implants. *Cochlear Implant. Int. An Interdiscip. J.* 10, 103–111. <https://doi.org/10.1002/cii.366>
- Morrison, A.W., Gibson, W.P.R., Beagley, H.A., 1976. Transtympanic electrocochleography in the diagnosis of retrocochlear tumours. *Clin. Otolaryngol. Allied Sci.* 1, 153–167. <https://doi.org/10.1111/j.1365-2273.1976.tb00868.x>
- Negm, M.H., Bruce, I.C., 2014. The Effects of HCN and KLT Ion Channels on Adaptation and Refractoriness in a Stochastic Auditory Nerve Model. *IEEE Trans. Biomed. Eng.* 9294, 1–12. <https://doi.org/10.1109/TBME.2014.2327055>
- Negm, M.H., Bruce, I.C., 2008. Effects of I(h) and I(KLT) on the response of the auditory nerve to electrical stimulation in a stochastic Hodgkin-Huxley model. *Conf. Proc. IEEE Eng. Med. Biol. Soc.* 2008, 5539–5542. <https://doi.org/10.1109/IEMBS.2008.4650469>
- O'Brien, G.E., Imennov, N.S., Rubinstein, J.T., 2016. Simulating electrical modulation detection thresholds using a biophysical model of the auditory nerve. *J. Acoust. Soc. Am.* 139. <https://doi.org/10.1121/1.4947430>

- O'Brien, G.E., Rubinstein, J.T., 2016. The development of biophysical models of the electrically stimulated auditory nerve: Single-node and cable models. *Netw. Comput. Neural Syst.* 6536, 1–22. <https://doi.org/10.3109/0954898X.2016.1162338>
- Paintal, A.S., 1966. The influence of diameter of medullated nerve fibres of cats on the rising and falling phases of the spike and its recovery. *J. Physiol.* 184, 791–811. <https://doi.org/10.1113/jphysiol.1966.sp007948>
- Parkins, C.W., 1989. Temporal response patterns of auditory nerve fibers to electrical stimulation in deafened squirrel monkeys. *Hear. Res.* 41, 137–168. [https://doi.org/10.1016/0378-5955\(89\)90007-5](https://doi.org/10.1016/0378-5955(89)90007-5)
- Pozzorini, C., Naud, R., Mensi, S., Gerstner, W., 2013. Temporal whitening by power-law adaptation in neocortical neurons. *Nat. Neurosci.* 16, 942–948. <https://doi.org/10.1038/nn.3431>
- Pozzorini, C.A., 2014. Computational principles of single neuron adaptation PAR 6461.
- Prescott, S.A., Sejnowski, T.J., 2008. Spike-rate coding and spike-time coding are affected oppositely by different adaptation mechanisms. *J. Neurosci.* 28, 13649–61. <https://doi.org/10.1523/JNEUROSCI.1792-08.2008>
- Pujol, R., Lenoir, M., Ladrech, S., Tribillac, F., Rebillard, G., 1992. Correlation Between the Length of Outer Hair Cells and the Frequency Coding of the Cochlea. *Audit. Physiol. Percept.* 45–52. <https://doi.org/https://doi.org/10.1016/B978-0-08-041847-6.50011-3>
- Ramekers, D., Versnel, H., Strahl, S.B., Klis, S.F.L., Grolman, W., 2015. Recovery characteristics of the electrically stimulated auditory nerve in deafened guinea pigs: Relation to neuronal status. *Hear. Res.* 321, 12–24. <https://doi.org/10.1016/j.heares.2015.01.001>
- Ramekers, D., Versnel, H., Strahl, S.B., Smeets, E.M., Klis, S.F.L., Grolman, W., 2014. Auditory-nerve responses to varied inter-phase gap and phase duration of the electric pulse stimulus as predictors for neuronal degeneration. *J. Assoc. Res. Otolaryngol.* 15, 187–202. <https://doi.org/10.1007/s10162-013-0440-x>
- Reilly, J.P., Freeman, V.T., Larkin, W.D., 1985. Sensory effects of transient electrical stimulation—evaluation with a neuroelectric model. *IEEE Trans. Biomed. Eng.* 32, 1001–11. <https://doi.org/10.1109/TBME.1985.325509>
- Relkin, E.M., Doucet, J.R., 1997. Is loudness simply proportional to the auditory nerve spike count? *J. Acoust. Soc. Am.* 101, 2735–2740. <https://doi.org/10.1121/1.418561>
- Resnick, J.M., O'Brien, G., Rubinstein, J.T., 2018. Simulated auditory nerve axon demyelination alters sensitivity and response timing to extracellular stimulation. *Hear. Res.* 361, 121–137. <https://doi.org/10.1016/j.heares.2018.01.014>
- Rosen, S., 1992. Temporal information in speech: acoustic, auditory and linguistic aspects. *Philos. Trans. R. Soc. Lond. B. Biol. Sci.* 336, 367–373. <https://doi.org/10.1098/rstb.1992.0070>
- Rubinstein, J.T., 1995. Threshold fluctuations in an N sodium channel model of the node of Ranvier. *Biophys. J.* 68, 779–785. [https://doi.org/10.1016/S0006-3495\(95\)80252-3](https://doi.org/10.1016/S0006-3495(95)80252-3)
- Rubinstein, J.T., Wilson, B.S., Finley, C.C., Abbas, P.J., 1999. Pseudospontaneous activity: Stochastic independence of auditory nerve fibers with electrical stimulation. *Hear. Res.* 127, 108–118. [https://doi.org/10.1016/S0378-5955\(98\)00185-3](https://doi.org/10.1016/S0378-5955(98)00185-3)
- Russell, I.J., Cody, A.R., Richardson, G.P., 1986. The responses of inner and outer hair cells in the basal turn of the guinea-pig cochlea and in the mouse cochlea grown in vitro. *Hear. Res.* 22, 199–216. [https://doi.org/10.1016/0378-5955\(86\)90096-1](https://doi.org/10.1016/0378-5955(86)90096-1)

- Russell, I.J., Sellick, P.M., 1977. Tuning properties of cochlear hair cells. *Nature* 267, 858–860. <https://doi.org/10.1038/267858a0>
- Scheidt, R.E., Kale, S., Heinz, M.G., 2010. Noise-induced hearing loss alters the temporal dynamics of auditory-nerve responses. *Hear. Res.* 269, 23–33. <https://doi.org/10.1016/j.heares.2010.07.009>
- Schoonhoven, R., Detgemen, D.F., van Oosterom, A., Dautzenberg, G.F.M., 1988. The Inverse Problem in Electroneurography - I: Conceptual Basis and Mathematical Formulation. *IEEE Trans. Biomed. Eng.* 35, 769–777.
- Schoonhoven, R., Fabius, M.A.W., Grote, J.J., 1995. Input/output curves to tone bursts and clicks in extratympanic and transtympanic electrocochleography. *Ear Hear.* 16, 619–630. <https://doi.org/10.1097/00003446-199512000-00008>
- Schoonhoven, R., Prijs, V.F., Grote, J.J., 1996. Response thresholds in electrocochleography and their relation to the pure tone audiogram. *Ear Hear.* <https://doi.org/10.1097/00003446-199606000-00009>
- Schwarz, J.R., Eikhof, G., 1987. Na currents and action potentials in rat myelinated nerve fibres at 20 and 37 degrees C. *Pflugers Arch.* 409, 569–77.
- Schwarz, J.R., Reid, G., Bostock, H., 1995. Action potentials and membrane currents in the human node of Ranvier. *Pflugers Arch.* 430, 283–92.
- Shannon, R. V., 1992. Temporal modulation transfer functions in patients with cochlear implants. *J. Acoust. Soc. Am.* 91, 2156–2164. <https://doi.org/10.1121/1.403807>
- Shepherd, R.K., Javel, E., 1997. Electrical stimulation of the auditory nerve. I. Correlation of physiological responses with cochlear status. *Hear. Res.* 108, 112–144. [https://doi.org/10.1016/S0378-5955\(97\)00046-4](https://doi.org/10.1016/S0378-5955(97)00046-4)
- Shepherd, R.K., Roberts, L.A., Paolini, A.G., 2004. Long-term sensorineural hearing loss induces functional changes in the rat auditory nerve. *Eur. J. Neurosci.* 20, 3131–3140. <https://doi.org/10.1111/j.1460-9568.2004.03809.x>
- Shera, C.A., Guinan, J.J., Oxenham, A.J., 2002. Revised estimates of human cochlear tuning from otoacoustic and behavioral measurements. *Proc. Natl. Acad. Sci. U. S. A.* 99, 3318–3323. <https://doi.org/10.1073/pnas.032675099>
- Simmons, F.B., Mongeon, C.J., Lewis, W.R., Huntington, D.A., 1964. Electrical Stimulation of Acoustical Nerve and Inferior Colliculus. *Arch. Otolaryngol.* 79, 559–568.
- Sly, D.J., Heffer, L.F., White, M.W., Shepherd, R.K., Birch, M.G.J., Minter, R.L., Nelson, N.E., Wise, A.K., O’Leary, S.J., 2007. Deafness alters auditory nerve fibre responses to cochlear implant stimulation. *Eur. J. Neurosci.* 26, 510–522. <https://doi.org/10.1111/j.1460-9568.2007.05678.x>
- Snel-Bongers, J., Briaire, J.J., Van Der Veen, E.H., Kalkman, R.K., Frijns, J.H.M., 2013. Threshold levels of dual electrode stimulation in cochlear implants. *JARO - J. Assoc. Res. Otolaryngol.* 14, 781–790. <https://doi.org/10.1007/s10162-013-0395-y>
- Spoendlin, H., Schrott, A., 1989. Analysis of the human auditory nerve. *Hear. Res.* 43, 25–38. [https://doi.org/10.1016/0378-5955\(89\)90056-7](https://doi.org/10.1016/0378-5955(89)90056-7)
- Stebbins, W.C., Hawkins, J.E., Johnsson, L.G., Moody, D.B., 1979. Hearing thresholds with outer and inner hair cell loss. *Am. J. Otolaryngol. Neck Med. Surg.* 1, 15–27. [https://doi.org/10.1016/S0196-0709\(79\)80004-6](https://doi.org/10.1016/S0196-0709(79)80004-6)

- Stocks, N.G., Allingham, D., Morse, R.P., 2002. The application of Suprathreshold stochastic resonance to cochlear implant coding. *Fluct. Noise Lett.* 02, L169–L181. <https://doi.org/10.1142/S0219477502000774>
- Strahl, S.B., Ramekers, D., Nagelkerke, M.M.B., Schwarz, K.E., Spitzer, P., Klis, S.F.L., Grolman, W., Versnel, H., 2016. Assessing the Firing Properties of the Electrically Stimulated Auditory Nerve Using a Convolution Model. pp. 143–153. https://doi.org/10.1007/978-3-319-25474-6_16
- Stypulkowski, P.H., Van den Honert, C., 1984. Physiological properties of the electrically stimulated auditory nerve. I. Compound action potential recordings. *Hear. Res.* 14, 205–223. [https://doi.org/10.1016/0378-5955\(84\)90051-0](https://doi.org/10.1016/0378-5955(84)90051-0)
- Takanen, M., Bruce, I.C., Seeber, B.U., 2016. Phenomenological modelling of electrically stimulated auditory nerve fibers: A review. *Netw. Comput. Neural Syst.* 27, 157–185. <https://doi.org/10.1080/0954898X.2016.1219412>
- Talbot, K.N., Hartley, D.E.H., 2008. Combined electro-acoustic stimulation: a beneficial union? *Clin. Otolaryngol.* 33, 536–545. <https://doi.org/10.1111/j.1749-4486.2008.01822.x>
- Tasaki, I., Davis, H., Eldredge, D.H., 1954. Exploration of cochlear potentials in guinea pig with a microelectrode. *J. Acoust. Soc. Am.* 26, 765–773. <https://doi.org/10.1121/1.1907415>
- Tasaki, I., Fernández, C., 1952. Modification of Cochlear Microphonics and Action Potentials by KCl Solution and by Direct Currents. *J. Neurophysiol.* 15, 497–512. <https://doi.org/10.1152/jn.1952.15.6.497>
- Teal, P.D., Ni, G., 2016. Finite element modelling of cochlear electrical coupling. *J. Acoust. Soc. Am.* 140, 2769–2779. <https://doi.org/10.1121/1.4964897>
- Tejani, V., Abbas, P.J., Brown, C.J., 2017. Relationship between Peripheral and Psychophysical Measures of Amplitude Modulation Detection in CI Users. *Ear Hear.* 91, 2401. <https://doi.org/10.1097/AUD.0000000000000417>
- Tejani, V.D., Carroll, R.L., Abbas, P.J., Brown, C.J., 2019. Impact of stimulus frequency and recording electrode on electrocochleography in Hybrid cochlear implant users. *Hear. Res.* 384, 107815. <https://doi.org/10.1016/j.heares.2019.107815>
- Teka, W., Stockton, D., Santamaria, F., 2016. Power-Law Dynamics of Membrane Conductances Increase Spiking Diversity in a Hodgkin-Huxley Model. *PLoS Comput. Biol.* 12, 1–23. <https://doi.org/10.1371/journal.pcbi.1004776>
- Toib, A., Lyakhov, V., Marom, S., 1998. Interaction between duration of activity and time course of recovery from slow inactivation in mammalian brain Na⁺ channels. *J. Neurosci.* 18, 1893–903. <https://doi.org/10.1523/jneurosci.5392-08.2009>
- v. Békésy, G., 1952. DC Resting Potentials Inside the Cochlear Partition. *J. Acoust. Soc. Am.* 24, 72–76. <https://doi.org/10.1121/1.1906851>
- v. Békésy, G., 1951. DC Potentials and Energy Balance of the Cochlear Partition. *J. Acoust. Soc. Am.* 23, 576–582. <https://doi.org/10.1121/1.1906807>
- van den Honert, C., Stypulkowski, P.H., 1987. Temporal response patterns of single auditory nerve fibers elicited by periodic electrical stimuli. *Hear. Res.* 29, 207–22.
- van der Jagt, A.M.A., Kalkman, R.K., Briaire, J.J., Verbist, B.M., Frijns, J.H.M., 2017. Variations in cochlear duct shape revealed on clinical CT images with an automatic tracing method. *Sci. Rep.* 7, 1–9. <https://doi.org/10.1038/s41598-017-16126-6>

- van Gendt, M.J., Briaire, J.J., Frijns, J.H.M., 2019. Effect of neural adaptation and degeneration on pulse-train ECAPs: A model study. *Hear. Res.* 377, 167–178. <https://doi.org/10.1016/j.heares.2019.03.013>
- van Gendt, M.J., Briaire, J.J., Kalkman, R.K., Frijns, J.H.M., 2017. Modeled auditory nerve responses to amplitude modulated cochlear implant stimulation. *Hear. Res.* 351, 19–33. <https://doi.org/10.1016/j.heares.2017.05.007>
- van Gendt, M.J., Briaire, J.J., Kalkman, R.K., Frijns, J.H.M., 2016. A fast, stochastic, and adaptive model of auditory nerve responses to cochlear implant stimulation. *Hear. Res.* 341, 130–143. <https://doi.org/10.1016/j.heares.2016.08.011>
- Van Ruijven, M.W.M., De Groot, J.C.M.J., Klis, S.F.L., Smoorenburg, G.F., 2005. The cochlear targets of cisplatin: An electrophysiological and morphological time-sequence study. *Hear. Res.* 205, 241–248. <https://doi.org/10.1016/j.heares.2005.03.023>
- Van Ruijven, M.W.M., De Groot, J.C.M.J., Smoorenburg, G.F., 2004. Time sequence of degeneration pattern in the guinea pig cochlea during cisplatin administration. A quantitative histological study. *Hear. Res.* 197, 44–54. <https://doi.org/10.1016/j.heares.2004.07.014>
- van Schoonhoven, J., Sparreboom, M., van Zanten, Bert G A Scholten, R.J.P.M., Mylanus, E.A.M., Dreschler, W.A., Grolman, W., Maat, B., 2013. The Effectiveness of Bilateral Cochlear Implants for Severe-to-Profound Deafness in Adults: A Systematic Review. *Otol. Neurotol.* 34, 190–198.
- Vellinga, D., Briaire, J.J., Van Meenen, D.M.P., Frijns, J.H.M., 2017. Comparison of Multipole Stimulus Configurations With Respect to Loudness and Spread of Excitation. *Ear Hear.* 38, 487–496. <https://doi.org/10.1097/AUD.0000000000000416>
- Versnel, H., Prijs, V.F., Schoonhoven, R., 1992. Round-window recorded potential of single-fibre discharge (unit response) in normal and noise-damaged cochleas. *Hear. Res.* 59, 157–170. [https://doi.org/10.1016/0378-5955\(92\)90112-Z](https://doi.org/10.1016/0378-5955(92)90112-Z)
- Verveen, A.A., 1962. Axon diameter and fluctuation in excitability. *Acta Morphol. Neerl. Scand.* 5, 79–85.
- Verveen, A.A., Derksen, H.E., 1968. Fluctuation phenomena in nerve membrane. *Proc. IEEE* 56, 906–916. <https://doi.org/10.1109/PROC.1968.6443>
- Vilin, Y.Y., Ruben, P.C., 2001. Slow inactivation in voltage-gated sodium channels: Molecular substrates and contributions to channelopathies. *Cell Biochem. Biophys.* 35, 171–190. <https://doi.org/10.1385/CBB:35:2:171>
- Walton, J.P., Frisina, R.D., Meierhans, L.R., 1995. Sensorineural hearing loss alters recovery from short-term adaptation in the C57BL/6 mouse. *Hear. Res.* 88, 19–26. [https://doi.org/10.1016/0378-5955\(95\)00093-J](https://doi.org/10.1016/0378-5955(95)00093-J)
- Wark, B., Lundstrom, B.N., Fairhall, A., 2007. Sensory adaptation. *Curr. Opin. Neurobiol.* 17, 423–429. <https://doi.org/10.1016/j.conb.2007.07.001>
- Waxman, S.G., Ritchie, J.M., 1993. Molecular dissection of the myelinated axon. *Ann. Neurol.* 33, 121–136. <https://doi.org/10.1002/ana.410330202>
- Wen, B., Wang, G.I., Dean, I., Delgutte, B., 2009. Dynamic range adaptation to sound level statistics in the auditory nerve. *J Neurosci* 29, 13797–13808. <https://doi.org/10.1523/JNEUROSCI.5610-08.2009>
- Westen, A.A., Dekker, D.M.T., Briaire, J.J., Frijns, J.H.M., 2011. Stimulus level effects on neural excitation and eCAP amplitude. *Hear. Res.* 280, 166–76. <https://doi.org/10.1016/j.heares.2011.05.014>

- Whitfield, I.C., Ross, H.F., 1965. Cochlear-Microphonic and Summating Potentials and the Outputs of Individual Hair-Cell Generators. *J. Acoust. Soc. Am.* 126, 126–131. <https://doi.org/10.1121/1.1909586>
- Wilson, B.S., Finley, C.C., Lawson, D.T., Wolford, R.D., Eddington, D.K., Rabinowitz, W.M., 1991. Better speech recognition with cochlear implants. *Nature*. <https://doi.org/10.1038/352236a0>
- Wilson, B.S., Finley, C.C., Lawson, D.T., Zerbi, M., 1997. Temporal representations with cochlear implants. *Am. J. Otol.*
- Wilson, B.S., Finley, C.C., Zerbi, M., Lawson, D.T., 1994. Seventh Quarterly Progress Report. Speech Processors for Auditory Prostheses, NIH.
- Wojtczak, M., Oxenham, A.J., 2010. Recovery from on- and off-frequency forward masking in listeners with normal and impaired hearing. *J. Acoust. Soc. Am.* 128, 247–256. <https://doi.org/10.1121/1.3436566>
- Won, J.H., Drennan, W.R., Nie, K., Jameyson, E.M., Rubinstein, J.T., 2011. Acoustic temporal modulation detection and speech perception in cochlear implant listeners. *J. Acoust. Soc. Am.* 130, 376–88. <https://doi.org/10.1121/1.3592521>
- Woo, J., Miller, C.A., Abbas, P.J., 2010. The dependence of auditory nerve rate adaptation on electric stimulus parameters, electrode position, and fiber diameter: a computer model study. *J. Assoc. Res. Otolaryngol.* 11, 283–96. <https://doi.org/10.1007/s10162-009-0199-2>
- Woo, J., Miller, C.A., Abbas, P.J., 2009. Biophysical Model of an Auditory Nerve Fiber With a Novel Adaptation Component. *IEEE Trans. Biomed. Eng.* 56, 2177–2180. <https://doi.org/10.1109/TBME.2009.2023978>
- Wouters, J., Mcdermott, H.J., Francart, T., 2015. Sound coding in cochlear implants: from electric pulses to hearing. *IEE Signal Process. Mag.* 32, 67–80. <https://doi.org/10.1109/MSP.2014.2371671>.
- Xu, H., Kotak, V.C., Sanes, D.H., 2007. Conductive Hearing Loss Disrupts Synaptic and Spike Adaptation in Developing Auditory Cortex. *J. Neurosci.* 27, 9417–9426. <https://doi.org/10.1523/JNEUROSCI.1992-07.2007>
- Xu, Y., Collins, L.M., 2007. Predictions of Psychophysical Measurements for Sinusoidal Amplitude Modulated (SAM) Pulse-Train Stimuli From a Stochastic Model. *IEEE Trans. Biomed. Eng.* 54, 1389–1398. <https://doi.org/10.1109/TBME.2007.900800>
- Yang, H., Woo, J., 2015. Effect of axon diameter and electrode position on responses to sinusoidally amplitude-modulated electric pulse-train stimuli. *Biomed. Eng. Lett.* 5, 124–130. <https://doi.org/10.1007/s13534-015-0181-3>
- Zeng, F.-G., 2017. Challenges in Improving Cochlear Implant Performance and Accessibility. *IEEE Trans. Biomed. Eng.* 64, 1662–1664. <https://doi.org/10.1109/TBME.2017.2718939>
- Zeng, F.G., 2004. Trends in Cochlear Implants. *Trends Amplif.* 8, 1–34. <https://doi.org/10.1177/108471380400800102>
- Zeng, F.G., Rebscher, S., Harrison, W. V., 2008. Cochlear Implants: System Design, Integration and Evaluation. *IEEE Rev Biomed Eng.* January, 115–142. <https://doi.org/10.1109/RBME.2008.2008250.Cochlear>
- Zhang, F., Anderson, J., Samy, R., Houston, L., 2010. The adaptive pattern of the late auditory evoked potential elicited by repeated stimuli in cochlear implant users. *Int. J. Audiol.* 49, 277–285. <https://doi.org/10.3109/14992020903321759>

- Zhang, F., Benson, C., Murphy, D., Boian, M., Scott, M., Keith, R., Xiang, J., Abbas, P.J., 2013. Neural adaptation and behavioral measures of temporal processing and speech perception in cochlear implant recipients. *PLoS One* 8, 1–13. <https://doi.org/10.1371/journal.pone.0084631>
- Zhang, F., Miller, C.A., Robinson, B.K., Abbas, P.J., Hu, N., 2007. Changes across time in spike rate and spike amplitude of auditory nerve fibers stimulated by electric pulse trains. *JARO - J. Assoc. Res. Otolaryngol.* 8, 356–372. <https://doi.org/10.1007/s10162-007-0086-7>
- Zhang, X., Heinz, M.G., Bruce, I.C., Carney, L.H., 2001. A phenomenological model for the responses of auditory-nerve fibers: I. Nonlinear tuning with compression and suppression. *J. Acoust. Soc. Am.* 109, 648–670. <https://doi.org/10.1121/1.1336503>
- Zilany, M.S.A., Bruce, I.C., 2006. Modeling auditory-nerve responses for high sound pressure levels in the normal and impaired auditory periphery. *J. Acoust. Soc. Am.* 120, 1446. <https://doi.org/10.1121/1.2225512>
- Zilany, M.S.A., Bruce, I.C., Carney, L.H., 2014. Updated parameters and expanded simulation options for a model of the auditory periphery. *J. Acoust. Soc. Am.* 135, 283–286. <https://doi.org/10.1121/1.4837815>
- Zilany, M.S.A., Bruce, I.C., Nelson, P.C., Carney, L.H., 2009. A phenomenological model of the synapse between the inner hair cell and auditory nerve: long-term adaptation with power-law dynamics. *J. Acoust. Soc. Am.* 126, 2390–2412. <https://doi.org/10.1121/1.3238250>
- Zilany, M.S.A., Carney, L.H., 2010. Power-law dynamics in an auditory-nerve model can account for neural adaptation to sound-level statistics. *J. Neurosci.* 30, 10380–10390. <https://doi.org/10.1523/JNEUROSCI.0647-10.2010>

List of publications

List of publications

van Gendt, M.J., Siebrecht, M., Briaire, J.J., Bohte, S.M., Frijns, J.H.M., 2020. Short and long-term adaptation in the auditory nerve stimulated with high-rate electrical pulse trains are better described by a power law. *Hear. Res.* 398 108090

van Gendt, M.J., Briaire, J.J., Frijns, J.H.M., 2019. Effect of neural adaptation and degeneration on pulse-train ECAPs: A model study. *Hear. Res.* 377, 167–178

van Gendt, M.J., Briaire, J.J., Kalkman, R.K., Frijns, J.H.M., 2017. Modeled auditory nerve responses to amplitude modulated cochlear implant stimulation. *Hear. Res.* 351, 19–33

van Gendt, M.J., Briaire, J.J., Kalkman, R.K., Frijns, J.H.M., 2016. A fast, stochastic, and adaptive model of auditory nerve responses to cochlear implant stimulation. *Hear. Res.* 341, 130–143.

van Gendt, M.J., Koka, K., Kalkman, R.K., Stronks, H.C., Briaire, J.J., Litvak, L.M., Frijns, J.H.M., 2020. Simulating intracochlear electrocochleography with a combined model of acoustic hearing and electric current spread in the cochlea. *J. Acoust. Soc. Am.* 147, 2049-2060.

de Vos, J.J.; Biesheuvel, J.D.; Briaire, J.J., Boot, P.S., **van Gendt, M.J.**, Dekkers, O.M., Fiocco, M., Frijns, J.H.M. 2018. Use of electrically evoked compound action potentials for cochlear implant fitting: a systematic review. *Ear Hear.* 39, 401-411.

van Gendt, M.J., Boyen, K., de Kleine, E., Langers D.R.M., van Dijk, P. 2012. The relation between perception and brain activity in gaze-evoked tinnitus. *J. of Neurosc.* 32(49) 17528-17539

Dankwoord

Dankwoord

Een pandemie eronder krijgen, een kind opvoeden, een marathon rennen, een promotie-onderzoek doen, we kunnen het niet alleen.

Geachte professor Frijns, beste Johan, bedankt voor de bezielde en inspirerende begeleiding. Beste co-promotor Jeroen, bedankt voor alle levendige discussies en gezellige overlegmomenten.

Voor de samenwerking, het meedenken en hulp bij het uitwerken wil ik ook graag bedanken: Sander Bohte, Michael, Randy, Chris en John. Volkmar, Paddy, Leo & Kanth, thank you for the collaboration, and providing me the opportunity to get a peak of the going around at a CI manufacturer.

Lieve collega's, in het bijzonder mijn kamergenootjes, de research buddies en de AC-collega's, bedankt voor de fijne samenwerking en de soms ook nodige afleiding. Ik kijk er naar uit om de komende jaren nog veel meer van dit mooie werk samen met jullie te mogen doen.

Paranimfen, lieve Jelmer ik ga wel alle vragen over Matlab doorpassen. Lieve Christina, sit beside me, have a drink, ... Wat een jaren, en wat heerlijk om te weten dat jullie naast me staan.

Lieve familie en vrienden, in het bijzonder GJ, Marjolein, pap en mam, dank voor jullie onaflatende support. Lieve Obe, dankje, we hebben het wel een beetje samen gedaan he 😊. Lieve Bauke, dankjewel voor de glans die je mijn proefschrift, mijn PhD-jaren, en mijn leven hebt gegeven.

Zonder jullie was het niet gelukt, maar, nog belangrijker, ook veel minder leuk geweest.

Curriculum Vitae

Curriculum Vitae

Margriet van Gendt (24-09-1984) is geboren in Alphen aan den Rijn te Nederland. In 2002 behaalde zij haar VWO-diploma in Natuur&Techniek en Natuur&Gezondheid aan het Ashram College. Ze behaalde haar Bachelor (2007) en Master (2009) in Biomedical Engineering aan de Universiteit Twente, waar zij afstudeerde op magnetocardiography aan de vakgroep lage temperaturen. Van 2009 tot 2013 volgde zij de opleiding tot klinisch fysicus – audioloog bij Pento en het Universitair Medisch Centrum Groningen. Daar onderzocht ze gaze-evoked tinnitus met een fMRI studie. Ze startte in 2014 met haar promotieonderzoek aan het Leids Universitair Medisch Centrum (LUMC), het eerste jaar voltijds, de jaren erna combineerde ze haar PhD-studie met een deeltijdfunctie als klinisch fysicus - audioloog in het centrum voor audiologie en hoorimplantaten in het LUMC, Leiden (CAHIL). Ze verkreeg de Basis Kwalificatie Onderwijs (BKO) in 2019. Na afloop van haar promotieonderzoek is haar aanstelling als klinisch fysicus - audioloog in het CAHIL van het LUMC uitgebreid, daarnaast werkt ze aan een onderzoeksproject over de diagnose van tinnitus aan het Erasmus Medisch Centrum Rotterdam. Ze is getrouwd met Bauke Bekkering, samen hebben ze een zoon Obe (2019).

